ROCKET STUDIES OF THE LOWER THERMOSPHERE

by

Giovanni Bibbo, PhD (University of Rome, Italy.)

Department of Physics
University of Adelaide

A thesis submitted to the University of Adelaide

for the

Degree of Doctor of Philosophy

September, 1977

Awarded August 1978

Corrections for the thesis entitled "Rocket Studies of the Lower Thermosphere" by G. Bibbo.

The corrections are as follow:

(a) the label of the abscissa axis of fig 3.4 (between pages 85 and 86) which is missing should be:

$$\overline{\sigma}_{eff}(x10^{-22}m^2)$$

(b) Equation (3.39) on page 94, i.e.,

$$n(0) + n(0_2) = 0.21n_T$$

is incorrect and should be:

$$\tfrac{1}{2}n(0) + n(0_2) = 0.21n_T$$

As a consequence, the atomic oxygen number densities calculated using the incorrect formula are a factor of two lower. These densities which are shown on figures 3.15 (solid line) and 3.16 (line (g)) have to be modified as shown on the attached figures 3.15 and 3.16.

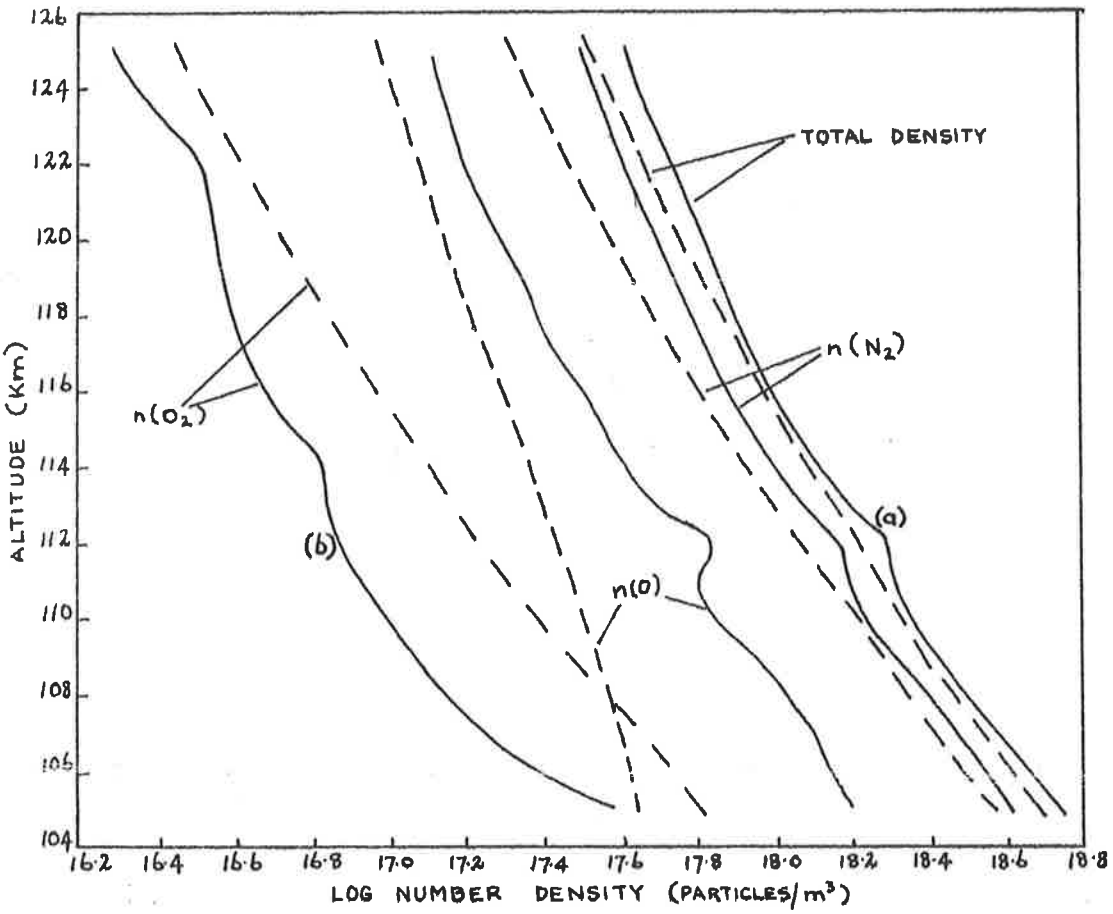

FIG 3·15: NUMBER DENSITY OF THE MAJOR ATMOSPHERIC CONSTITUENTS; (– – –) mean CIRA (1972) DENSITIES, (——) CALCULATED $n(O)$ AND $n(N_2)$.
(a) n_T FROM X-RAY DATA
(b) $n(O_2)$ FROM ION CHAMBER DATA.

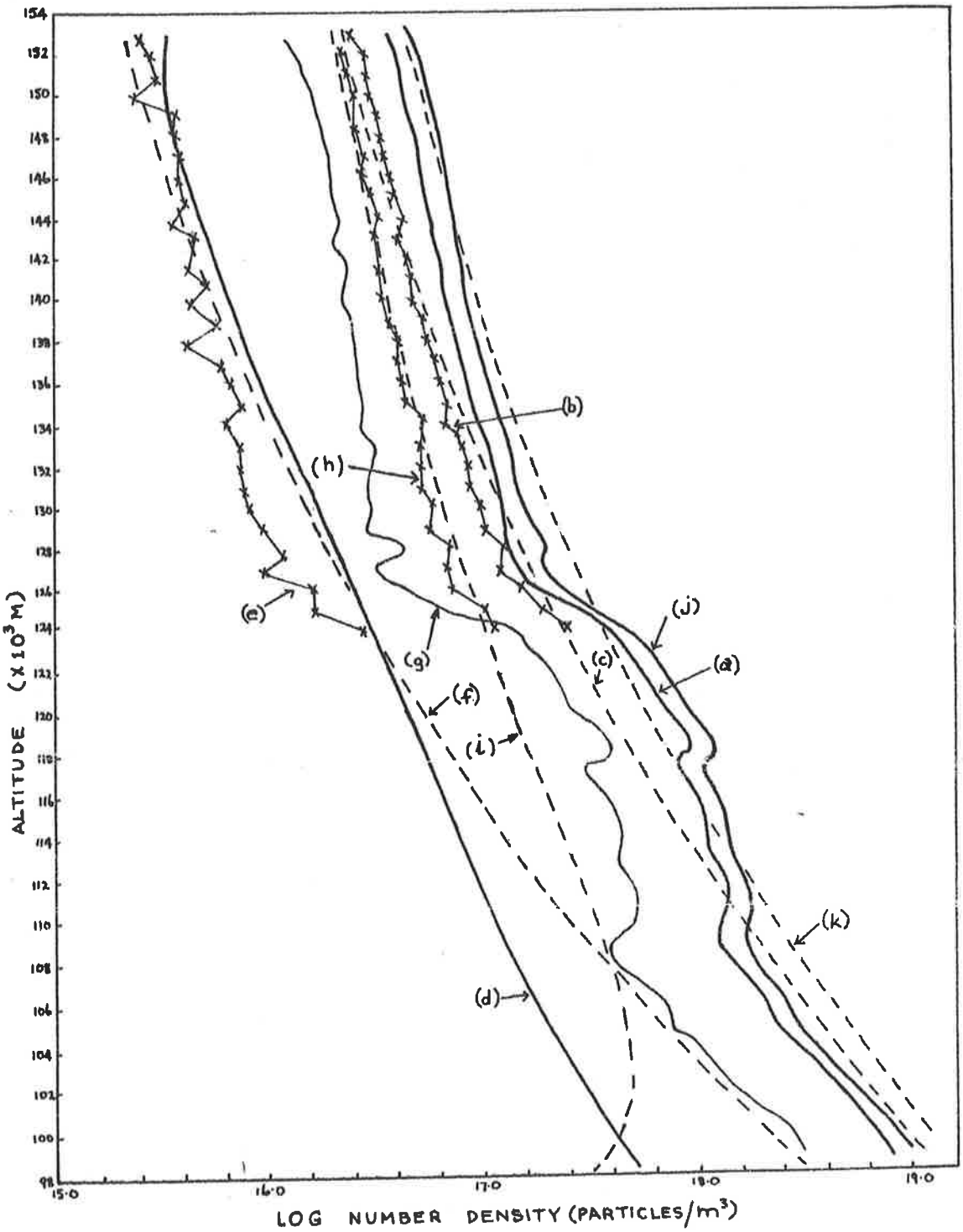
ALTITUDE (X 10³ M)
LOG NUMBER DENSITY (PARTICLES/m³)
15·0
16·0
17·0
18·0
19·0
(a)
(b)
(c)
(d)
(e)
(f)
(g)
(h)
(i)
(j)
(k)

REPLY TO THE COMMENTS IN THE EXAMINERS' REPORT OF THE THESIS

ENTITLED 'ROCKET STUDIES OF THE LOWER THERMOSPHERE'

BY G. BIBBO

1. [redacted]

Chapter I: Review of Present State of Knowledge

p. 7 This section deals with the classification of the neutral atmosphere so that it is implied that the particles are neutral.

pp. 18 and 21 The author does not state that E_s is only a night-time phenomenon but merely that the night-time E-region is characterized by the presence of the E_s layer at an altitude of about 100 Km. Daytime E_s does occur and in fact has been measured (see, for example, Hall, J.E., 1973. Planet. Space Sci., 21, 119) but is not extensively measured, studied and modelled as the night-time E_s. The study of the daytime E_s seems to be overshadowed by the study of other daytime phenomena which occur in this region.

p. 18 The meaning of the term 'ionic recombination' is as stated by Prof. Kaiser.

p. 28 The statement '.....the thermal energy distribution of the electron gas is larger that the Maxwellian functions' should read "....the velocity distribution of the electron gas is larger than the Maxwellian function".

Chapter III: E.U.V. and X-ray Data Analysis

The total density profile has been recalculated using the $n(O)$, $n(N_2)$ and $n(O_2)$ values determined with the iterative process and is presented in section 3.2.8 on page 99.

p. 78 It appears that the detectors after being subjected to stress by the vibrations and acceleration of the powered part of the flight require about a minute or more before they settle down.

pp 93 and 94 The revised values for $n(O)$ and $n(N_2)$ were calculated, using the equation:

$$\tfrac{1}{2}n(O) + n(O_2) = 0.21n_T \qquad (1)$$

where the total particle content is taken as:

$$n_T = \tfrac{1}{2}n(O) + n(O_2) + n(N_2)$$

This is because the X-radiation does not distinguish between the atomic and molecular form of oxygen, i.e., the absorption cross-section of atomic oxygen $\sigma(O)$ is equal to half of that of O_2, i.e.,

$$\sigma(O) = \tfrac{1}{2}\sigma(O_2)$$

The argument of Prof Kaiser is correct only in the region where $\sigma(O) \neq \tfrac{1}{2}\sigma(O_2)$, i.e., in the E.U.V. region and in this case:

$$n_T = n(O) + n(O_2) + n(N_2)$$

The difference between Prof. Kaiser's formula:

$$0.6n(O) + n(O_2) = 0.21n_T$$

and the one used by the author:

$$0.5n(O) + n(O_2) = 0.21n_T$$

is not very significant and as already mentioned in this section of the thesis the assumption that equation (1) is satisfied from $\sim$90 to 150 Km is not a valid one since it does not allow for the fact that above about 120 Km the atmospheric constituents are in a state of gravitational equilibrium. This assumption arose from the fact that having measured $n(O_2)$ and n_T on the same rocket flight the author wanted to see whether it was possible to calculate $n(O)$ and $n(N_2)$ profiles. Three methods were used to do this (see this section) and one of the methods was by using equation (1).

The revised $n(O)$ and $n(N_2)$ values agree better with those of CIRA at altitudes greater than about 122 - 124 Km than the orginal values while the original values agree better with CIRA at altitudes less than these heights. This effect is mainly an artefact resulting for the fact that measured $n(O_2)$ values for altitudes less than 122 - 124 Km are less than those of CIRA values. Again the author must stress the fact that as stated on page 94 this method does not yield satisfactory values for $n(O)$ and $n(N_2)$.

3.2.7 The value used for Z_o was 159 Km.

The $n(N_2)$ values used to calculate the temperature profile in this section (3.2.7) are those determined using the iterative procedure in which the equation system (3.30) is solved simultaneously so that this section does not warrant any modification.

Chapter V: Mass Spectrometer Payloads

All the development of the instruments described in this thesis has been done by the author

Chapter VI: Photo-Electron Spectra

Similar results are obtained with the Aerobee's electron spectrometer.

2. [redacted]

The X-ray data for SL 1207 were analyzed using both the gaussian fit with m = 3, 4, 5 and 6 and the least square polynomial fit of orders from 4 to 15, but unfortunately, in the case of polynomial fit, the author has included in the thesis only the data determined with the 6th order polynomial (see Fig 3.2). The density profiles obtained with the gaussian fit of m = 3, 4 and 5 (fig 3.6) are highly structured. When the polynomial fit method was used this structure

appears only with high order polynomials (>8th order). It was found that a 12th order polynomial gave the same structure as that obtained with the gaussian fit of m = 6. This unfortunately again was not included in the thesis. Thus both methods can be used equally well, i.e., a gaussian fit with a small value of m and a polynomial of high order. Both the polynomial and gaussian fit have end effects which produce artificial structure in the density profile. However, the end effects are larger for the polynomial fit than for the gaussian one, especially if a gaussian fit of small m is used and in the case of the gaussian fit the end effect can be eliminated while this is not the case for the polynomial fit. Thus, the gaussian fit is a better method of analysis than the polynomial one.

The profile of the integrated X-ray flux calculated from the gaussian density data of m = 6 (fig 3.8) does not show fine structure because the density data profile has been fairly smoothed, i.e., m = 6 (fig3.7). If, on the other hand, the X-ray flux obtained from the density profile with m = 3 or 4 was used then the resulting flux would have more fine structure and fit better with the X-ray raw data. From an altitude of 128 to 134 Km the data were not presented and this was to avoid the end effect in the density profiles.

During the days of 22nd, 23rd and 24th of April 1974 no major solar flares were observed. Subflares occurred at 01^h26^m, 06^h12^m and 13^h46^m U.T. on the 22nd, at 20^h44^m U.T. on the 23rd and at 12^h55^m and 17^h18^m U.T. on 24th April 1974 (Solar-Geophysical Data prompt reports, May 1974. Number 357-Part 1). SL 1207 was launched at 01^h03^m U.T. on the 23rd of April, 1974, so that it is unlikely that there was a variation of the X-ray flux during the rocket flight. However, if this had occurred then the wavelike structure would have appeared in the X-ray density data but not in the E.U.V. ones since the variation of E.U.V. radiation with solar activity is very small (practically negligible) and this is not the case (see fig 3.13).

CONTENTS

CHAPTER II SOFT X-RAYS AND EXTREME ULTRAVIOLET EXPERIMENTS

CHAPTER III E.U.V. AND X-RAY DATA ANALYSIS

CHAPTER IV MASS SPECTROMETER EXPERIMENT

CHAPTER V MASS SPECTROMETER PAYLOADS

SUMMARY

This thesis is primarily concerned with the study of the lower thermosphere region of the earth's atmosphere, a region in which although the occurring aeromic phenomena are fairly well understood there are still uncertainties in many parameters needed to describe the morphology of the region. The uncertainties are to be found mainly in the:

(a) concentration of the atmospheric constituents, particularly those of the atomic, ionic and minor species.

(b) intensities of the solar flux in the extreme ultraviolet (E.U.V.) and X-ray spectral regions and in its temporal variation.

(c) overall dynamics of the atmosphere.

(d) reaction rates necessary for the understanding of the chemistry and photochemistry of the atmosphere.

These uncertainties arise mainly because this region (altitude 90 - 200 Km) is above the balloon ceiling (>35 Km) and below most of the satellites' paths except for the few short-lived satellites with a low perigee ($\approx$135 Km). Therefore the lower thermosphere is a region accessible only by rocket borne probes and the difficulties are in the fact that since the advent of rockets and satellites for atmospheric and space research only very few payloads have been adequately instrumentated to measure simultaneously the necessary parameters of the neutral and ionized species and the physical or chemical phenomena resulting from their mutual interactions. This lack of fundamental data coupled with the fact that it is not possible to simulate the upper atmosphere in

the laboratory has made the task of understanding the many processes involved in the aeronomic phenomena not an easy one.

In this dissertation a series of rocket borne experiments flown from the Woomera Rocket Range during the period from late 1972 to early 1977 are described and the data from the earlier flights are presented. The experiments are:

(a) X-ray and E.U.V. detectors which measured the attenuation of the E.U.V. and X-ray solar flux in the atmosphere as a function of the altitude from which it has been possible to derive the densities of the neutral constituents.

(b) electrostatic energy spectrometers used to measure the energy spectrum of the photoelectrons and ions.

(c) neutral and ion quadrupole mass spectrometers for the determination of the composition and concentration of both the neutral and the ionized components of the atmosphere in the altitude range of interest.

During the course of this work the author has been involved with 10 rocket firings but, unfortunately, due mainly to technical problems associated with the vehicles, successful flights have been few. The rocket vehicles which were available and the experiments prepared and flown by the author on these vehicles have been:

(1) four Cockatoos, rocket vehicles carrying X-ray detector experiments to an altitude of 130 - 135 Km.

(2) two Lorikeets, vehicles each carrying a neutral mass spectrometer to an altitude of about 140 Km.

(3) two Skylarks, rockets, the first carrying only

X-ray detectors while the second carried X-ray detectors, a grazing incidence spectrometer and an electrostatic energy analyzer to measure the photoelectron energy spectra.

(4) one Super-Chief vehicle carrying an electrostatic energy analyzer to measure the energy spectra of the superthermalized electrons and conjugate photoelectrons in the night-time ionosphere.

(5) one Aerobee rocket. This vehicle which was successfully launched on the 22nd of February, 1977, carried X-ray detectors, an ion and a neutral mass spectrometer, a high resolution (2%) 127^{o} electrostatic analyzer and an ion and electron retarding potential analyzer.

Out of all of these flights only three firings have been successful: the two Skylarks and the Aerobee flights. The results from the Skylarks are presented in the thesis, while those of the Aerobee will be published in the near future in scientific journals.

The total density of the lower thermosphere derived from the solar X-ray measurements on the first Skylark and those determined from the X-ray and E.U.V. (grazing incidence spectrometer) absorption measurements with the instruments flown on the second Skylark vehicle are presented in chapter III while the results from the electrostatic energy analyzer experiment aboard the second Skylark are presented in chapter VI. However, samples of the Aerobee's preliminary data are also presented and are illustrated in Appendix B. The X-ray and E.U.V. absorption experiments are described in detail in chapter II, and those of the mass spectrometers in chapter IV and V.

PREFACE

This thesis contains no material which has been accepted for the award of any other degree or diploma in any University. To the best of the author's knowledge and belief it contains no material previously published or written by another person, except where due reference is made in the text.

G. BIBBO

SEPTEMBER, 1977.

ACKNOWLEDGEMENTS

The author would like to thank all the persons involved with the preparation and launching of the rocket vehicles and, in particular, the Upper Atmospheric Research group of Weapons Research Establishment, Salisbury, for launching the Cockatoo and Lorikeet vehicles, the personnel of the British Aircraft Corporation for launching the Skylark vehicles and the team from the Goddard Space Flight Center for launching the Aerobee rocket.

Thanks are due to Messrs R. Walker and R. Hurn of the Department of Physics for building the flight electronics, Mr A. Jones, formerly of the Department of Physics, for designing and supervising the building of the Lorikeet mass spectrometer payloads and Mr S. Dowden, also formerly of the Department of Physics, for making the proportional counters.

Thanks are also due to the staff of the Physics Department's workshop for their assistance in building the apparatus and instruments involved in this work and, particularly, Mr G. Eames for building most of the instruments of the Skylark 1207 and Aerobee payloads.

The author appreciates the help given to him by Mr D. L. Swingler of the Chemical Physical Division, C.S.I.R.O., Clayton, Victoria, in making the mass spectrometer instrument functional and Dr R. C. Schaeffer, formerly of the Department of Physics, for pointing out a different method of smoothing of the rocket data.

Finally, the author would like to thank Dr B. H. Horton, his supervisor, most sincerely for his enthusiasm, guidance and encouragement during the course of this work and also for his critical reading of the manuscript. Thanks are also due to Professor J. H. Carver for his directorship of the

Space Research Group.

The rocket program was financed through the grants to the University of Adelaide from the Australian Research Grants Committee.

The author gratefully acknowledges the financial support provided by the Commonwealth Postgraduate Research Award and a full-time deomonstrating position with the University of Adelaide.

Special thanks and appreciation are due to Ms H. A. Polgreen for her patience in typing this thesis and tracing the drawings.

CHAPTER I

REVIEW OF THE PRESENT STATE OF KNOWLEDGE OF THE LOWER THERMOSPHERE.

1.1.1 INTRODUCTION

The earth's atmosphere, a sea of gases enveloping the whole planet, extends from the earth's surface to altitudes of thousands of kilometers where it thins out into the interplanetary space. The atmosphere is part of man's environment and its physical, chemical and dynamical phenomena do not only protect him from the lethal solar and cosmic radiations, but also provide him with such necessity as rain and hence sustenance. In the lower atmosphere, the atmospheric phenomena, mainly in the form of cloud formation, rain, snow, wind, storms, etc., and visible optical displays from the upper atmosphere such as auroras in high geomagnetic latitudes, have been the object, perhaps of curiosity, for millenia and scientific study for centuries, for man's habitat is directly affected by such phenomena as rain, snow, wind and storms. The upper atmosphere, on the other hand, has been outside man's reach until 1901 when Marconi succeeded in receiving in Newfoundland a radio signal transmitted from Cornwall (U.K.). But the advancement in the knowledge of the upper atmosphere did not really start until rockets and satellites became available after World War II. Then, with the direct probing of the upper atmosphere with rocket and satellite borne instruments, it became evident that the upper atmosphere supports a broad range of intricate physical and chemical phenomena. Since the early sounding rocket experiments, through the increasing understanding of the physi-

cal and chemical processes and the development of more sophisticated observational instruments to measure the atmospheric parameters, advances in the knowledge of the atmosphere has been rapid and exciting.

The atmosphere below about 100 Km is composed mainly of N_2, O_2, Ar, and CO_2 and its relative composition remains constant with altitude, but decreasing approximately exponentially. However, above about 100 Km departure from the exponential behaviour occurs as a result of atmospheric heating and composition variation arising from the interaction of the atmospheric constituents with energetic solar radiation. This radiation ionizes and excites the atmospheric constituents and the energy given to the atmosphere in these two processes is partly released by photon emission (such as airglows) and partly stored in the atmosphere as heat energy through a chain of sophisticated physical and chemical processes. The photodissociation of molecular oxygen into atomic oxygen in the altitude region above about 100 Km by solar radiation with wavelengths less than 2424Å and the ionization of the atomic and molecular gas species by solar extreme ultraviolet and X-ray radiation give rise not only to a change in the composition of the upper atmosphere above 100 Km, but also to the formation of a multiconstituent plasma which extends from an altitude of about 50 Km to, perhaps, thousands of kilometers, called the "IONOSPHERE".

The ionosphere is comprised of minor constituents of the upper atmosphere, free electrons and ions. The free electron component has the important property of reflecting, under suitable conditions, the "long", "medium" and "short" electromagnetic waves used for broadcasting and radio communication. Thus, the ionosphere, because of its property of providing worldwide radio communication, has been subjected to intense

theoretical study since the first transatlantic radio communication in 1901 and probing by radio sounding methods since the classic experiments of Appleton and Barnett (1925) and Breit and Tuve (1926).

1.1.2 THE STRUCTURE OF THE ATMOSPHERE AND ITS CLASSIFICATION

The penetration of the solar radiation at different altitudes in the earth's atmosphere depends on the atmospheric composition and on the energy of the incident radiation. This is because in the interaction of the radiation with the atmospheric constituents the most energetic radiation ionizes the molecular and atomic species and the less energetic radiation dissociates molecules and excites the atoms and the molecules to various higher energy levels. However, these primary interactions are only the initial reactions of a long and complex chain of processes. The secondary reactions that may follow are: the recombination of ions and electrons, recombination and re-arrangement of atoms and molecules, re-emission of radiation, etc. All these reactions may lead to the display of optical phenomena, formation of the ionosphere (free electrons and ions) and may alter the identities, densities and distributions of the neutral and ionized molecular and atomic species, etc. Different processes occur predominantly at different heights in the atmosphere and when it comes to understanding a particular phenomenon it is practically impossible to consider the whole chain of processes occurring throughout the atmosphere which gives rise to that phenomenon. It is more convenient to consider a simple model of the processes and then elaborate on it so that the basic phenomenon is fully explained. Thus, in the understanding of the aeronomic phenomena it has been useful to divide the atmosphere into regions in which the character is determined by only a few processes.

There are a number of ways in which the gross structure of the atmosphere can be described and each leads to a classification of the altitude region in a way that is

appropriate to the physical processes taking place there. The classifications found in the literature are based on the atmospheric temperature profile, chemical composition and electron concentration of the ionosphere. These classifications neglect the horizontal and temporal variations in the physical processes and only consider the vertical component of the spatial variations of the processes. The outlined divisions of the atmosphere are shown in fig. 1.1 for the neutral atmosphere and in fig. 1.2 for the ionosphere.

(a) Classification based on the thermal property of the atmosphere.

This classification is based on the temperature profile of the atmosphere which in turn gives some indication of the height at which solar energy is deposited. Thus, using the temperature as a parameter, it is possible to divide the atmosphere into several regions which are:

(1) Troposphere. This is a lower region which starts at the surface of the earth and extends to a level called "Tropopause" at an average altitude which varies between 18 Km at the equator and about 8 Km at the poles. In this region the temperature decreases with altitude (about 6^{o}/Km) to a minimum at the tropopause since the principal source of heat of the region is the earth's surface.

(2) Stratosphere. This region extends from the tropopause up to a level called "stratopause" at an altitude of about 50 Km. It is characterized by a rise in temperature to a maximum at the stratopause. This rise in temperature is caused largely by the absorption of solar U.V. radiation by ozone. Ozone in this region

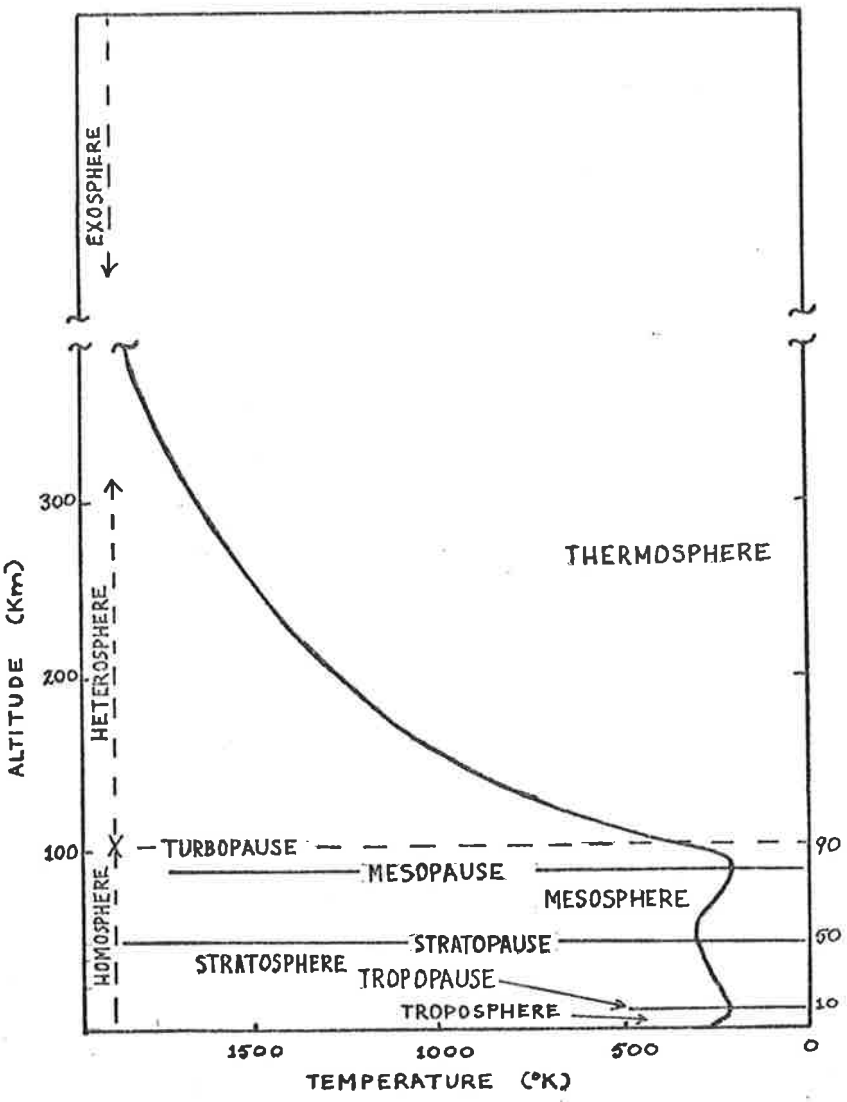

FIG. 1·1: SCHEMATIC REPRESENTATION OF THE NEUTRAL ATMOSPHERIC REGIONS. (After Whitten and Poppoff (1971)).

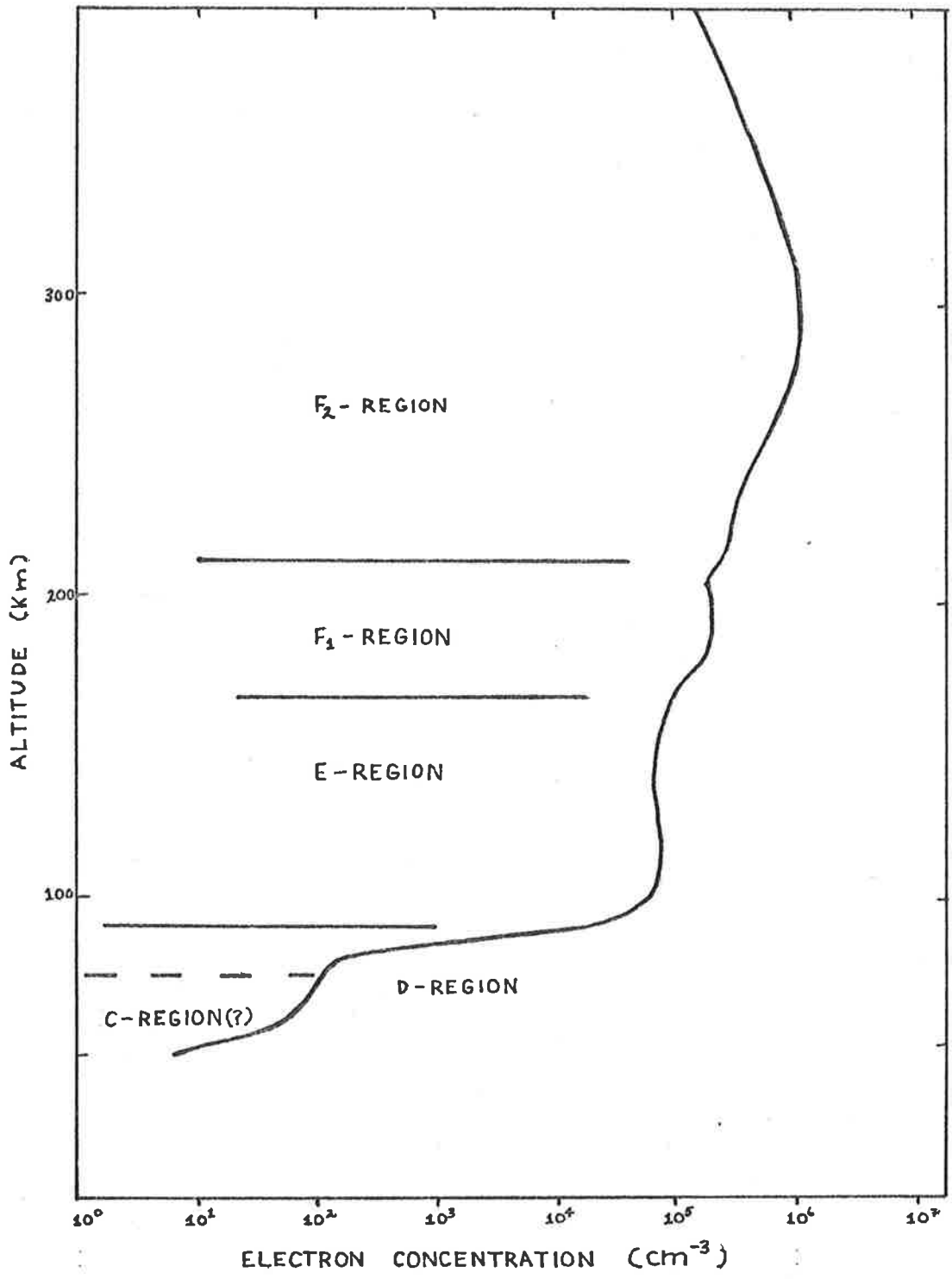

FIG. 1·2: SCHEMATIC REPRESENTATION OF IONOSPHERIC REGIONS (After Whitten and Poppoff (1971)).

is very important, even though it is a minor constituent, never more than about 1 part in 10^5 of the atmosphere at these heights, for it is not only responsible for a temperature increase with height but also protects us from solar U.V. radiation.

(3) Mesosphere. The mesosphere is a region between the stratopause (50 Km) and the "mesopause" at an altitude between 80 and 90 Km and it is characterized by a decrease of temperature with altitude. It is a region more complex than the stratosphere or troposphere because of the oxidation and hydration processes and the penetration of the U.V. radiation which dissociates polyatomic molecules. The chemical reactions which result are manifested in airglow emissions and formation of a diverse number of minor constituent gases which are important in the thermal balance and ionization state of the mesosphere.

(4) Thermosphere. It starts at the mesopause and is characterized by a temperature which increases monotonically with altitude up to a height between about 300 and 400 Km. Above that the temperature is independent of height where it ceases to be properly definable somewhere between 800 and 2000 Km. The thermosphere extends from about 80 Km to approximately 500 to 800 Km. The large temperature gradient of this region results mainly through the absorption of solar E.U.V. and to a lesser degree from charged particle influx and chemical

reactions and to the fact that in this region there is a lack of any effective means of thermal emission. However, the fact that the temperature gradient depends on the absorption of solar E.U.V. has many consequences in the sense that the heat budget of the thermosphere is related to variations of the solar energy and hence subjected to diurnal, seasonal, geographical, etc., variations.

In the thermosphere at altitudes above about 120 Km the particles are in diffusive equilibrium while at heights below about 100 Km they are in a state of mixing equilibrium and since diffusion enhances the concentration of the light constituents (atoms) relative to the heavy constituents (molecules) the predominant species above a certain height are in the atomic form.

(5) Exosphere or Protosphere. This is a region above the thermosphere and is characterized by the fact that the mean free path of the particles is so large that the particles move on ballistic trajectories. Furthermore, since the collision between particles is infrequent their velocity distribution functions is no longer Maxwellian, and the temperature of the region is undefinable.

The exosphere is almost fully ionized and the predominant constituents are the light elements helium and hydrogen. At altitudes less than about 2000 Km the concentration of the neutral particles is still greater than that of

the ions but for altitudes greater than about 2000 Km the ions become dominant and their behaviour is no longer governed by the earth's gravitational field but rather by the earth's magnetic field and the region is called the "magnetosphere" which may extend to between 9 and 15 earth's radii. Particles entering the exosphere from the thermosphere with sufficient energy are able to escape from the earth's gravitational field; however, for temperatures found in the thermosphere, the escape is limited only to hydrogen and helium.

(b) Classification based on the Chemical Composition.

(1) Homosphere. The homosphere extends from the surface of the earth to an altitude of about 100 - 120 Km, called the "turbopause", and encompasses the three regions, troposphere, stratosphere and mesosphere, and part of the lower thermosphere. This is a region in which the predominant atmospheric constituents (the content by volume of which is N_2, 78.1%; O_2, 20.9%; Ar, 0.9%; and CO_2, 0.03%) are thoroughly mixed through turbulence and convection. The concentration of these constituents decreases approximately exponentially with altitude but their relative composition is kept approximately constant by the mixing processes. The region also contains trace constituents such as water vapour and ozone which are not all homogeneously distributed.

(2) Heterosphere. This is a region which extends from the turbopause up to the exosphere where

the particles follow ballistic trajectories under the influence of gravity alone and it is characterized by the fact that the atmospheric constituents are in diffusive equilibrium in which atoms and molecules move about as independent particles. The chemical composition of the region changes with height not only by the diffusion processes but also by the chemical and photochemical reactions which remove and produce various atomic and molecular species.

The transition from one region to another is usually not easily defined. For instance, it is very difficult to say where the homosphere finishes and the heterosphere starts or where the thermosphere ends and the exosphere begins, but there is usually a gradual transition from one to the next region

(c) Classification according to the electron concentration of the atmosphere.

The ionosphere can be divided into about three distinct regions according to the different production and loss processes which occur. The regions are (fig 1.2):

(1) D-region, which covers the altitude range from about 50 - 60 to approximately 80 to 90 Km. There is sometimes mentioned in the literature the existence of another distinct region below about 75 Km which has been designated as the "C-layer". The evidence of this C-layer has come mainly from the study of the propagation of low frequency radio waves but this can probably be considered best as part of the D-region.

(2) E-region, which extends from the top of the

D-region (80 - 90 Km) to an altitude of about 130 - 160 Km.

(3) F-region, which begins at the E-region (130 to 160 Km) is frequently divided into two regions, F_1 and F_2. It has no well defined upper limit, but the region above the F_2 peak is usually referred to as the topside ionosphere. The F_2 peak has the highest electron density of the ionosphere and occurs at heights varying from about 250 to 500 Km while the F_1-ledge is usually found at about 180 Km.

1.2 SOLAR RADIATION

The sun is the prime energy source of all the aeronomical and meteorological phenomena occurring throughout the terrestrial atmosphere.

The solar radiation can be thought to consist mainly of two components:

(a) the visible and near visible radiation which is emitted by the solar disk or photosphere.

(b) radiation of short wavelengths which comprises the extreme ultraviolet (E.U.V.) radiation and X-rays and is emitted mainly by the active regions of the solar disk (principally by the chromosphere and corona).

The emission of visible and near visible radiation, which resembles the radiation emitted by a black body having a temperature of about 5800^{o}K and containing a large number of absorption lines (Fraunhofer lines) caused by the relatively cooled gas in the upper photosphere, has been observed to be very constant with time. In fact no periodic variations greater than about 0.2% have been observed (Whitten and Poppoff (1965)). This is not the case for the E.U.V. and X-ray radiations. For X-rays not only the intensity varies rapidly from day to day in accordance with the solar activity (Kreplin (1961) and Kreplin et al (1962)) but even during a quiet sun period the emission is neither constant in time nor evenly distributed across the solar disk and the magnitude of the variation is a function of the wavelength (Kreplin (1961)). In a review of solar X-ray emission over a period of 17 years, Mandel'stam (1965) found that during a quiet sun period the emission in the spectral region from about 2 to 10 Å varied by a factor of 1000, while in the region 8 - 20 Å by a factor of 100 and in the spectral region 44 - 100 Å by a factor less

than about 10. However, during a flare the X-ray flux can be enhanced by a factor of 10^5, 10^4, and 10^3 respectively for the three mentioned spectral regions.

Solar E.U.V. radiation and X-rays are totally absorbed in the upper atmosphere and, as a consequence, these radiations can only by measured with rockets or satellites and in the case of ultraviolet radiation (U.V.) with balloon borne instruments. It is this portion of the radiation of the solar spectrum which is responsible for the upper atmospheric aeronomical phenomena, and hence of interest in this work, even though it only represents less than about 10^{-3} of the total solar radiation (Whitten and Poppoff (1971)). Detailed quantitative measurements of the solar E.U.V. flux has been made mainly by Hinteregger and his co-workers (Hinteregger et al (1965) and Hinteregger (1970) and Manson (1974)). The detailed structure of the solar spectrum from the visible to the X-ray region is, to date, fairly well known but there are still uncertainties in the absolute value of the E.U.V. flux. In fact, in the literature there is still discussion as to the absolute value of the E.U.V. flux (Roble and Dickinson (1973) and Prasad and Furman (1974)).

The Solar X-ray spectrum has been observed with numerous rocket and satellite experiments such as Manson (1972) and Wolff (1974) (see the paper of Walker (1972) for further reference) and, again, the uncertainties are in the absolute fluxes.

1.3.1 THE FORMATION OF THE IONOSPHERIC REGIONS

The ionosphere, as already mentioned, is a region of the upper atmosphere which contains free electrons and ions and is formed by the action of incident ionizing radiation upon the earth's atmosphere. Most of this is of solar origin but effects due to non solar radiation may be observed. The behaviour and the structure of the ionosphere is, therefore, closely related with that of the neutral atmosphere, and the solar ionizing radiation.

Prior to the era of rocket and satellite experiments the knowledge of the physical parameters of the ionsophere was limited by the need to deduce the nature of the fundamental processes from ground based radio reflection and propagation techniques' data. This led to exaggerate the importance of the free electrons in the ionosphere in the sense that the study of the ionsophere involved mainly the detection and interpretation of the manner in which the free electron varied with height. Thus, the deduction obtained from these radio wave experiments were always incomplete since it was impossible to know accurately the spectrum of the ionizing radiation, and the ionic and even the neutral composition of the upper atmosphere. With the coming of the space age and hence the feasibility of in situ measurements of the ionic and neutral structure of the atmosphere and the spectral distribution of the ionizing solar radiation, it has been possible to extensively modify and improve the earlier models of the ionosphere. Today, it can be said that the principal processes associated with the E, F, topside and to a lesser extent the D-region are reasonably well understood, although difficulties associated with reaction rates still exist but mainly because of the great diffuclties related to the laboratory experiments when it comes to simulate the upper atmosphere.

1.3.2 THE D-REGION

The D-region is, perhaps, the most complex region of the ionosphere and one of the most interesting of the whole atmosphere for it supports a wide range of physical and chemical phenomena. It is a region the chemistry of which is dominated by the presence of minor neutral constituents such as NO and water vapour. These minor constituents coupled with the energetic ionizing radiation give rise to complex ion-interchange and electron attachment and detachment reactions leading to the formation of negative, positive and cluster ions. It is the least understood region partly because of the complexity of the processes and partly because of difficulties which still have to be overcome in making in situ measurements of the region.

The absorption of the ionizing radiation in the atmosphere is governed by the absorption cross sections of the major constituents and if these cross sections are greater than about 10^{-19} cm^2 this radiation is absorbed at higher altitudes in the E and F regions. The D-region, being the lowest lying region, is thus produced by the most penetrating of the ionizing radiation such as:

(1) solar X-rays having wavelengths less than about 10 Å which ionize all the constituents.

(2) radiation with wavelengths greater than 910 Å, since for these wavelengths the absorption cross section of O_2 is very irregular (Hudson (1971)) and thus permitting the penetration of the radiation in some spectral windows. This radiation is hydrogen Lyman -α which ionizes lower ionization potential molecules such as NO and radiation with wavelengths less than 1118 Å which ionize the metastable molecular oxygen,

$O_2(a^1\Delta g)$.

(3) very energetic (>BeV) charged particles of the galactic cosmic radiation, celestial X-rays and precipitating charged energetic particles in the auroral zones.

The solar X-rays contribution is extremely variable due to their association with solar flares and hence it is expected that the ionization of this region is to some extent related to the solar activity. In fact, in the auroral region there is an enhanced ionization following a large proton solar flare and enhanced solar X-ray emission during the flare. It has also been reported that enhanced ionization of the D-region at mid-latitude is associated with magnetic activity (Bourne et al (1968)).

At night the electron concentration is reduced practically to zero in the D-region and to a very small value in the E and F_1 region. This loss in the electron concentration results from the formation of negative ions by the three bodied electron attachment to molecules or atoms (see Banks and Kockarts (1973)). The nocturnal ionization radiation of this region is:

(1) galactic cosmic radiation

(2) celestial X-rays (e.g. Ananthakrishnan et al (1969), Edwards et al (1969) and Francey (1970)).

(3) precipitating energetic particles (Tulinov et al (1969), Potemra and Zmuda (1970), Manson and Merry (1971) and Manson (1971)).

The modelling of the D-region has been hindered by the lack of information on such parameters as the concentration of the minor constituents, composition of the positive and negative ions and their relative concentration and there is still some uncertainty of the chemical reactions involving

the positive and negative ions and electron constituents. Both positive and negative ions in the D-region have been measured by mass spectrometers but there are difficulties in the conversion of the measured ion mass peaks into number densities for various reasons which are explained in the works of Arnold et al (1971) and Ferguson and Fehsenfeld (1969). As a consequence, the number densities of the positive ions measured by Narcisi and Baily (1965), Goldberg and Aikin (1971), Narcisi et al (1972), Johannessen and Krankowsky (1974) and Zbinden et al (1975), and those of the negative ions measured by Narcisi et al (1971) and Arnold et al (1971) are only indicative. Furthermore, the mass spectrum of both the positive and the negative ions in the D-region, because of the presence of large clusters of hydrated ions, could be much more complex than the one that has been detected. In fact, according to Narcisi (1970) and other workers it is possible that the existance of heavier ion clusters than those identified with mass spectrometers, because the heavier ion clusters have low energy of dissociation, can easily be broken up by the shockwaves surrounding the rocket vehicle in its flight in the region.

The most critical neutral constituents of the D-region are NO (Whitten and Poppoff (1971), water vapour, metastable O_2 ($a'\Delta g$) and to a less extent atomic oxygen and hydrogen. Nitric oxide has been measured by many authors such as Barth (1964, 1966), Pearce (1969), Meira (1971), Tisone (1973) and Zalpuri et al (1974), but there is still some discussion (Mitra and Rowe (1974)) as to its actual concentration in the D-region, while the water vapour and the atomic oxygen and hydrogen are as difficult to measure as the concentration of the ionic composition.

Despite the lack of quantitative observational data, the chemistry of the D-region has been discussed in detail by

many authors (such as Donahue (1972), Krankowsky et al (1972), Niles et al (1972)) and several attempts have been made to model it, calculating the positive or negative ion densities or both. These models are presented by such authors as Nicolet and Aikin (1960), Mitra (1968), Radicella (1968), LeLevier and Branscomb (1968), Thomas (1971), Keneshea and Swider (1972), Hunt (1971, 1973), Turco and Sechrist (1972), Rowe et al (1974) and many others in which they used the latest rate reactions available in the literature.

Only two sets of measurements of negative ions in the D-region have been published (Narcisi et al (1971) and Arnold et al (1971)). The ions tentatively found are CO_3^-, NO_3^-, CO_4^-, HCO_3^-, NO_2^-, Cl^-, O_2^-, O^-, $NO_3^-.(H_2O)$, $CO_3^-.(H_2O)$ and $NO_2^-.(HNO_2)$. Not all of these ions have been observed on the same flight and by the two groups of experimenters. In fact, from the flight of Narcisi et al (1971) NO_3^- is dominant while CO_3^- results as the major ion from the Arnold experiment. Arnold et al (1971) also detected unexpected ions like Cl^-, HCO_3^-, NO_3^-, HNO_3, $NO_2^-.(HNO_2).H_2O$ which are absent from the results of Narcisi et al (1971).

In the case of the positive ion composition of the D-region, the picture is slightly simpler, and to date it is generally accepted that the dominant ions of the D-region are NO^+ followed by O_2^+ but below about 85 Km the ion composition is dominated by the water cluster ions $H^+.(H_2O)_n$; n = 1,2,3, which disappear at about an altitude of 90 Km. There also exists a metallic region between about 90 and 110 Km having a broad maximum at heights of 93 - 96 Km which is dominated by the presence of Mg^+ and Fe^+ ions with smaller concentrations of Na^+, Al^+, Si^+, K^+ and Ca^+ ions. The chemistry of the metal ions in the D-region is described by Ferguson (1972) and Zbinden et al (1975).

1.3.3 THE E-REGION

The simplicity of the chemistry coupled with the easiness of which in situ measurements can be conducted in this region, in comparison with those of the D-region, and lack of important transport effects as in the F-region makes the E-region, probably, one of the best understood part of the ionosphere. The behaviour of this region has been studied and modelled by many authors, for example, Ratcliffe and Weeks (1960), Belrose (1965), Yonezawa (1966), Harris and Tohmatsu (1972), Banks and Kockarts (1973), etc., and is characterized by the dominance of NO^+ and O_2^+ ions, the absence of negative ions (Fehsenfeld et al (1967)) and the presence at night of a thin ($\approx$1 Km thick) layer of enhanced electron concentration which usually occurs at an altitude of about 100 Km, called the sporadic-E layer or simply Es. The negative ions, although they are still produced by radiative attachment, are being rapidly destroyed by ionic recombination and in daylight by photodetachment.

The daytime mid-latitude E-region is produced by the ionization of;

(1) molecular oxygen by solar soft X-rays with wavelengths in the spectral region from about 31 to 100 Å, hydrogen Lyman-β (1025·7 Å), carbon III (977 Å) emission line and the hydrogen Lyman continuum from 911 Å to about 800 Å.

(2) molecular nitrogen by soft X-rays (31 - 100 Å).

(3) atomic oxygen by soft X-rays and the hydrogen Lyman continuum.

while in the auroral zones another source of ionization may be the precipation of energetic particles (Manson and Merry (1971)).

Mass spectrometer measurements (Holmes et al (1965),

Johnson (1972), Narcisi et al (1972), Johannessen and Krankowsky (1974), Zbinden et al (1975) and others) indicate that the major ion of the E-region is NO^+ followed by O_2^+ and O^+ while N_2^+ is a minor ion even though the initial ions produced by the ionizing radiation are N_2^+ and O_2^+ (Keneshea et al (1970)). The presence of N_2^+ in minute quantities in the E-region can be explained by the fact that its ionizing radiation is absorbed at higher altitudes, in the F-region, and by the fast reactions which convert N_2^+ to NO^+. The chemistry of the E-region can be fully explained by the following chain reaction (Keneshea et al (1970), Johnson (1972), Hunt (1973), etc).

$$N_2^+ + O \longrightarrow NO^+ + N \; ; \; k_1 = 1{\cdot}4 \times 10^{-10} \text{ cm}^3/\text{sec} \qquad (1.1)$$

(Fehsenfeld et al (1970)).

$$N_2^+ + O_2 \longrightarrow O_2^+ + N_2 \; ; \; k_2 = 6{\cdot}4 \times 10^{-7} \times T_i^{-1{\cdot}67} \text{cm}^3/\text{sec} \qquad (1.2)$$

(Dunkin et al (1968)).

$$O^+ + O_2 \longrightarrow O_2^+ + O \; ; \; k_3 = 3{\cdot}4 \times 10^{-10} \times T_i^{-0{\cdot}48} \text{cm}^3/\text{sec} \qquad (1.3)$$

(Smith and Fouracre (1968)).

$$O^+ + N_2 \longrightarrow NO^+ + N \; ; \; k_4 = 3{\cdot}6 \times 10^{-10} \times T_i^{-1{\cdot}0} \text{cm}^3/\text{sec} \qquad (1.4)$$

(Dunkin et al (1968)).

$$O_2^+ + NO \longrightarrow NO^+ + O_2 \; ; \; k_5 = 6{\cdot}3 \times 10^{-10} \text{cm}^3/\text{sec} \qquad (1.5)$$

(Fehsenfeld et al (1970)).

$$O_2^+ + N \longrightarrow NO^+ + O \; ; \; k_6 = 1{\cdot}8 \times 10^{-10} \text{cm}^3/\text{sec} \qquad (1.6)$$

(Fehsenfeld et al (1969)).

$$O_2^+ + e^- \longrightarrow O + O \; ; \; k_7 = 6{\cdot}69 \times 10^{-5} \times T_e^{-1} \text{ cm}^3/\text{ sec} \qquad (1.7)$$

(Zipf (1970)).

$$NO^+ + e^- \longrightarrow N + O \; ; \; k_8 = 1{\cdot}23 \times 10^{-4} \times T_e^{-1} \text{cm}^3/\text{sec} \qquad (1.8)$$

(Biondi (1969))

$$N_2^+ + e^- \longrightarrow N + N \; ; \; k_9 = 2{\cdot}9 \times 10^{-7} \text{cm}^3/\text{sec} \qquad (1.9)$$

(Biondi (1969))

The values of the reaction constants k_1 through to k_9 are the latest values found in the literature although they

may not necessarily be the best values.

Since the primary ions are produced by the interaction of the solar ionizing radiation with the neutral constituents, it is expected that the ionic composition varies with the solar zenith angle and to some extent with solar activity. This is because of the variability of the X-ray and, to a much lesser extent, the extreme ultraviolet spectrum of the sun with solar activity. In fact, Danilov (1970, 1972a), from surveys of published experimental data on the ionic composition of the atmosphere in the altitude region 100 - 200 Km, found that there is a well pronounced diurnal variation of the absolute concentration of the ions NO^+, O_2^+, O^+, etc. Furthermore, he found that in the E-region the ratio NO^+/O_2^+ not only increased from day to night but also with magnetic activity. This diurnal variation of the E-region has been qualitatively studied by a number of authors such as Ogawa and Tohmatsu (1966), Monro (1970), Keneshea et al (1970), Swider (1972) and Hunt (1973).

At sunset a general reduction of the ion density takes place at all altitudes with NO^+ remaining still the major ion (Holmes et al (1965)). The existence of the nocturnal E-region is due to the presence of resonance scattering of Lyman-α and Lyman-β in the hydrogen corona of the earth and, to a lesser extent, to resonance scattered HeI and HeII lines. In fact, computations by different authors have shown that the night time ionization results from:

(1) Lyman-α which ionizes NO at altitudes below about 100 Km (Swider (1965)).

(2) Lyman-β which ionizes molecular oxygen in the altitude rang 100 - 130 Km (Ogawa and Tohmatsu (1966) and Tohmatsu and Wakai (1970)).

(3) HeI (584 Å) and HeII (304 Å) which ionize all constituents at altitudes above about 150 Km (Young et al (1971) and Tohmatsu and Wakai (1970)).

This nocturnal resonant radiation has been observed photometrically by such experimenters as Young et al (1971), Ogawa and Tohmatsu (1971) and Paresce et al (1973)).

The normal features of the mid-latitude night time E-region can be explained by the effect of the night sky resonant E.U.V. radiation but for the irregular features such as the sporadic E-layer; the explanation has to be sought elsewhere. Moreover, the causes of the formation of the sporadic E-layer vary with latitude and current theory is that at mid-latitude it is caused by wind-shears (Whitehead (1961, 1967), Axford (1963, 1967) and Chimonas and Axford (1968)), while at high latitudes by particle precipitation and at the equatorial region by plasma instabilities arising from the equatorial electorject (Whitten and Poppoff (1971)).

The wind-shears theory is corroborated by the mass spectrometer measurements of the ionic composition of the E-region (Aikin et al (1974), Holmes et al (1965), Zhlood'ko (1971) and others) which show the existence of a layer of long lived (Ferguson and Fehsenfeld (1962) and Swider (1968)) metallic ions which are probably of meteoritic origin (Lehman and Wagner (1966)) in the altitude region 90 - 100 Km, coupled with the numerical modelling of these ions by MacLead et al (1975). Further support of the wind shear hypothesis comes from the works of Layzer (1972), Kato et al (1972) and Harper et al (1975) which compared available observational data with theory.

1.3.4 THE F_1-REGION.

In the lower ionosphere the local production and loss processes of ionization predominate over the transport processes and, as a consequence, the structure of the ionosphere at heights less than about 200 Km is determined by the photochemical processes. At altitudes greater than about 200 Km this is not the case. At these altitudes the chemical loss rates of the ions are comparable to their diffusion rates through the neutral gas and the transport mechanisms begin to influence the concentrations of the ions and electrons (Whitten and Poppoff (1971)). This is true for the molecular ions and atomic ions during daylight, but at night for the atomic ion species both diffusion and vertical drifts induced by winds or electric fields have to be considered (Schunk and Walker (1973) and Bothe (1974)). This is because at night there is practically no production of ions and the transport processes of atomic oxygen ions determine the ionic composition and density of the F-region at heights less than about 200 Km since the loss rate of the atomic oxygen ions is much slower than that of the molecular ion species (Banks and Kockarts (1973)).

For the purpose of this work it is then convenient to divide the F-region into two regions, F_1 and F_2, and consider only the F_1- region since the author is mainly interested in the lower part of the ionosphere, i.e., for altitudes less than about 200 Km.

The F_1-region is characterized (1) by the presence of the F_1-ledge which usually occurs in the altitude range 150 - 200 Km on the underside of the F_2-layer, and (2) by the fact that the principal ion produced is the atomic oxygen ion while the main electron disappearance process is dissociative recombination with molecular ions (reactions (1·7), (1·8) and

(1·9)). This is because the radiative recombination reaction

$$O^+ + e^- \longrightarrow O + h\nu \qquad (1.10)$$

is very slow. In fact, Whitten and Poppoff (1971) for the reaction (1.10) quote a value for the rate constant of $10^{-12} cm^3/sec$ which is at least a factor of 100 slower than the charge exchange reactions of O^+ with N_2 and O_2 (reactions (1.3) and (1.4).

The features of the F_1-ledge are (a) that it merges into the F_2-layer during the night and sometimes even during the day and cannot be observed as a separate layer at such times; it appears mainly at mid-latitude and more frequently at sunspot minimum than sunspot maximum; and (c) it is more liable to appear as a separate layer in summer than in winter and near noon than near sunset or sunrise (for further details see the works of Yonezawa (1966) and Rishbeth (1974)). The formation of the F_1-ledge is due to the presence of molecular ions in the F_1-region. The chemistry of the F_1-region is similar to that of the E-region and the reactions (1.1) through to (1.9) describe it adequately. The molecular ion, NO^+, is still the major ion at altitudes less than about 170 Km during the day and at altitudes less than about 220 Km during the night while the atomic oxygen ion, O^+, predominates at heights greater than 170 Km during the day and at heights greater than 220 Km at night (Holmes et al (1965) and Johnson (1972) and others). During the day the F_1-region ionosphere is formed by the ionizing solar radiation of wavelengths between about 100 and 910 $\mathring{A}$ which ionizes all constituents, whereas at night the F_1-region is maintained by the ionization produced by the HeI (584 $\mathring{A}$) and HeII (304 $\mathring{A}$) scattered resonant radiation from the night sky (Tohmatsu and Wakai (1970) and Young et al (1971)), and from the diffusion of O^+ from higher

levels (Walker and McElroy (1966) and Rishbeth (1968)).

In the E and F region the ratio NO^+/O_2^+ depends strongly upon the density of nitric oxide, NO, and a number of authors, such as Koshelev and Belinskaya (1974), Oliver (1974) and Golshan and Sechrist (1975), have used the measured NO^+/O_2^+ ratio to calculate the number density of NO, which is a minor constituent throughout the atmosphere.

The ratio, NO^+/O_2^+, is a function of the solar activity (Danilov (1972a) and Mitra and Barnejee (1972)) and it increases with solar activity. This increase can be related to the increase in the concentration of the minor constituents NO and atomic nitrogen (Mitra and Banejee (1972)), however, when the ratio NO^+/O^+ is considered, its increase with solar activity cannot be interpreted entirely on the basis of changes in the neutral composition but requires an increase in the value of the rate constant of the reaction

$$O^+ + N_2 \longrightarrow NO^+ + O \qquad (1.11)$$

and hence an increase in the vibration temperature of the neutral gas (Mitra and Banejee (1972) and Banks et al (1974)).

1.3.5 THE PHOTOELECTRONS

The photoionization of the atmospheric constituents by solar ionizing radiation converts a certain amount of solar energy into the kinetic energy of the released electrons. The initial energy spectrum of the photoelectrons is fairly complex and generally reflects the gross feature of the spectral distribution of the ionizing radiation and the relative neutral composition of the upper atmosphere. This complexity results from the highly structured solar E.U.V. and X-ray spectrum and from the neutral molecules or atoms which may have several internal energy states above the ground state, which as a consequence, depending upon the energy of the incident photon and the ionization cross sections for the different energy states of the particles, the resulting photoelectron can have one of the several possible energies.

The photoelectrons and their effects on the neutral atmosphere and ionosphere have been studied theoretically in many different contexts for a number of years. Their energy distribution as a function of altitude and in many cases as a function of the solar zenith angle has been calculated by such authors as Cicerone and Bowhill (1971), Krinberg et al (1974), Schlegel (1974), Mantas and Bowhill (1975) and Victor et al (1976), and measured by Shea et al (1968), Doering et al (1970), Knudsen and Sharp (1972), Maier and Rao (1972), Hays and Sharp (1973) and Mukai and Hirao (1973). The theoretical and measured energy spectra of the photoelectrons agree fairly well at different altitudes, although the measured spectra have less structure and this is because of the limited resolution of the employed measuring instruments. There are, however, difficulties when it comes to comparing theoretical and experimental results because of ~~the~~ still uncertainties in the values of the solar flux, excitation and ionization

cross sections of the various energy states of the particles and densities of the neutral and ionized constituents. Another problem is that at heights less than about 300 Km the production rate of the photoelectrons is strongly dependent on the geographical latitude, local time and solar conditions and to date the few measurements reported in the literature have been made at different latitudes and solar zenith angles. Perhaps, the best comparison between a theoretical and measured energy distribution of the equilibrium photoelectrons is that reported by Victor et al (1976). In their calculations, the authors used neutral atmospheric and ionospheric parameters and solar ionizing fluxes measured by instruments flown on the Atmospheric Explorer-C satellite and then compared their results with the photoelectron fluxes observed on the same satellite.

The initial kinetic energies of the photoelectrons are much greater than those of the neutral and ionized atmospheric constituents and, as a consequence, they cause a number of aeronomical phenomena by supplying energy to the neutral and ionized gases and ambient thermal electrons, or at high altitudes by escaping along the geomagnetic field lines into the magnetosphere.

In the ionosphere the photoelectrons exist in a state of equilibrium and their energy spectrum is different from that of the initial photoelectrons. It has less structure. This is because the photoelectrons as soon as they are created lose their energy very quickly through the following processes (Banks (1966), Dalgarno and Degges (1968), Stubbe and Varnum (1972), Chandra and Sinha (1973), etc.):

(a) elastic collisions with ions and neutral particles.

(b) rotational and vibrational excitation of N_2

and O_2.

(c) electronic excitation of atomic oxygen.

(d) fine structure excitation of atomic oxygen.

In addition, in the E and F-regions, another process which may need to be considered is the heating or cooling of the electron gas by the dissociative recombination of electrons with NO^+ and O_2^+ ions, although the effect is very small, the order of a few per cent (Hamlin and Myers (1974)). On the whole, under normal ionospheric conditions, the most important loss process is the fine structure excitation of atomic oxygen and the least important is elastic collisions of photoelectrons with the neutral constituents (Chandra and Sinha (1973)).

Expressions for the thermalization and energy transfer rates of the fast electrons have been reported in the literature by a number of authors such as Hoegy et al (1965), Banks (1966), Dalgarno and Degges (1968), Schunk and Hays (1971), Stubbe and Varnum (1972), Cicerone et al (1973) and Mantas (1974). However, it appears that some of these theoretical expressions underestimate the energy loss by about 70% (Schunk and Hays (1971)).

In the upper atmosphere, the dominant contribution to the energy loss rate for photoelectrons having energy above about 6 eV is from electronic excitation of atomic oxygen, molecular oxygen and molecular nitrogen, while in the energy range from about 2 eV to about 6 eV vibrational excitation of N_2 is the main energy sink. Below about 2 eV the energy loss process is continuous principally by collision of the photoelectrons with ions and electrons and a number of relatively slow resonant rotational and vibrational excitations of O_2 and N_2 (Hoegy et al (1965), Banks (1969), Dalgarno et al (1963) and Ashihara and Takayanagi (1974)).

In the final stages of photoelectron thermalization, a substantial amount of energy is given to the ambient electron gas which increases the electron temperature, T_e, above that of the neutral and ion gases. This is particularly true at heights above about 150 Km whereas below this level the electron gas is in thermal equilibrium with the neutral gas, i.e., $T_e = T_n$ where T_n is the temperature of the neutral gas. Furthermore, at altitudes less than about 250 Km, the thermal energy distribution of the electron gas is larger than the Maxwellian function, but above this height, because of the overwhelming electron-electron collisions, the distribution becomes very close to the Maxwellian (Ashihara and Takayanagi (1974)). In the case of the ion gas, it is in thermal equilibrium with the neutral gas at altitudes up to about 250 Km where the ion gas is rapidly cooled by the neutral atmosphere. Above this level the temperature of the ion gas, T_i, increases with height, taking up an intermediate value between T_n and T_e and approaching T_e at altitudes above about 1000 Km (for further details see the articles of Banks (1969)).

At altitudes less than about 250 Km the photoelectrons deposit their energy locally, but above this level transport mechanisms have to be considered (Hanson (1963)). In fact, Mantas and Bowhill (1975) in their theoretical derivation of the energy spectrum of the photoelectrons found that the energy distribution is isotropic at heights below about 250 Km but anisotropic in pitch angle and energy above this level, implying that above 250 Km transport mechanisms are important and that there is a net upward photoelectron current. In fact, it is possible for photoelectrons produced at altitudes greater than about 250 Km to escape from the ionosphere into the magnetosphere (Hanson (1963)) by spiralling along the geomagnetic field lines and, if sufficiently

energetic, to reach the conjugate ionosphere where they deposit their energy. Detailed calculations of the flux of the photoelectrons escaping the ionosphere has been reported by a number of authors such as Nisbet (1968), Cicerone and Bowhill (1971), Schlegel (1974) and Mantas and Bowhill (1975).

1.4 DISPLAY OF OPTICAL PHENOMENA IN THE UPPER ATMOSPHERE.

The optical phenomena that occur in the upper atmosphere are of two types: airglows and auroras. Auroras occur mainly in the auroral zones although sometimes they are visible at the mid-latitude, while the airglows are generally widespread and always present, though in varying degree. The auroras are quite bright and hence visible by the naked eye; the airglows, on the other hand, are too feeble to be observed with the naked eye.

Both of these phenomena have been extensively studied theoretically and measured with both ground based equipments and rocket and satellite borne instruments. Through the years a large body of information has been built in the literature about these phenomena and any detailed review of the subject here is beyond the scope of this thesis. For detailed information the reader is referred to such comprehensive works on the subject as those reported by Wallace and McElroy (1966), Jones (1971), Whitten and Poppoff (1971) and a collections of scientific papers on auroras, the compilation of which is edited by McCormac and Omholt (1969).

1.5.1 THE NEUTRAL UPPER ATMOSPHERE

For the purpose of this thesis the author is mainly interested in the upper atmospheric region from about 90 to about 200 Km and, therefore, the properties of the lower thermosphere will be reviewed here.

The lower thermosphere comprises the top part of the homosphere and the lower part of the heterosphere and hence a transition region in which the constituents are neither in mixing nor in diffusive equilibrium. The transition region is a region between the homosphere and the heterosphere in which the atmospheric constituents change gradually from a state of turbulent mixing (homosphere) to one of gravitational diffusion (heterosphere) and in accordance with the definition of Colegrove et al (1966) the height at which the vertical component of the eddy mixing coefficient is equal to the molecular diffusion coefficient of the species in question is the turbopause.

The height of the turbopause is very important in the study of the upper atmosphere, particularly, in the elaboration of theoretical models. This is because the values of the atmospheric parameters at this height give the boundary conditions for the equations in question in the models.

It is expected that, because of the mass difference of the various constituents, their corresponding heights of the turbopause would be different. But, unfortunately because of the experimental difficulties in determining the concentration of the reactive gases, such as atomic oxygen, it is more convenient to assume the turbopause to be the same for all gases, except the light constituents, helium and hydrogen, and to derive the turbopause from mass spectrometers' measurements of the number density of the non reactive gases, argon and molecular nitrogen. From a survey of the ratios $n(Ar)/n(N_2)$

obtained from mass spectrometers, von Zahn (1970) found that the average height of the turbopause was 101 Km.

It is expected that the level of the turbopause will be subjected to variation such as latitudinal, seasonal and diurnal, although Kasprzak et al (1968) found that the diurnal variation is very small, only of 2 Km. They found that the height of the turbopause was 100 and 102 Km during the day and night respectively. However, Noxon and Johanson (1972), in seeking an explanation for the seasonal change of O_2 inferred from the excess 6300 $\mathring{A}$ twilight intensity, have suggested that the variation of the O_2 concentration may involve a systematic seasonal change in the altitude of the turbopause. The variability of the turbopause has been briefly discussed by Champion (1969).

1.5.2 COMPOSITION OF THE LOWER THERMOSPHERE

The lower thermosphere is only accessible by rockets and satellites having a low perigee and since the advent of these vehicles numerous measurements have been made of the composition and density of the region. The measurements have shown that the principal constituents of the region are N_2, O, and O_2, where N_2 is the major specie at altitudes less than about 150 - 170 Km and atomic oxygen above this level.

Different techniques have been employed to determine the composition and density of the upper atmosphere but, unfortunately, each technique has its merits and drawbacks. The techniques employed are mainly:

(1) Mass spectrometers. The number density of all species have been measured by this method (Offermann and Grossmann (1973), Nier et al (1976) and many others. (See the review of von Zahn (1970) and Offermann (1974) for a more complete bibliography).

(2) U.V. and E.U.V. extinction method. This technique has been largely used to determine the concentration of O_2 (Felske et al (1972), Roble and Norton (1972), Hays and Roble (1973), Norton and Roble (1974), Weeks (1974), etc) and of the major gases N_2, O and O_2 (Hall et al (1965), Timothy et al (1972). etc). In fact, it is a method which has been extensively used by the Space Research Group of the University of Adelaide to measure O_2 densities in the upper mesosphere and lower thermosphere by means of rocket borne ion chambers responding to U.V. radiation (Carver et al (1964,1969, 1977a, 1977b)). These types of measurements have been

carried out by the Adelaide Group since its its inception in the early sixties (Horton (1977)).

(3) Decay of the orbit of satellites. This method measures total mass density of the atmospheric gases. (For references the reader is referred to the review of Moe (1973)).

In the case of atomic oxygen, in addition to the

(4) $O(^1S - ^1D)$ airglow green line emission. (Donahue et al (1973), Offermann and Drescher (1973), and others).

(5) Nitric oxide chemical release method. (Philbrick et al (1974), Good and Golomb (1973), etc).

two novel methods

(6) silver film sensors (Henderson (1974), and a

(7) rocket-borne resonance lamp. (Dickinson et al (1974).

have been used to determine its concentration.

A few values of the measured densities of O_2, O and N_2 gases by different methods are listed in table 1.1, 1.2 and 1.3 respectively. A detailed comparison of the measured data of the density of the atmsopheric gases by different experimental groups is not really possible because the data may be subjected to temporal and spatial variation (see section 1.5.4). Even so, von Zahn (1970) from a review of composition measurements with mass spectrometers and E.U.V. extinction methods reached the conclusion that mass spectrometric and E.U.V. extinction measurements agree quite well for the molecular species N_2 and O_2 but differ significantly for atomic oxygen. This is because in the ion source of the mass spectrometers, atomic oxygen reacts chemically with the fila-

Table 1.1

NUMBER DENSITY OF O_2 IN PARTICLES/CC

Reference	150 Km	200 Km	Comments
Norton and Roble (1974)	$\sim 3 \times 10^9$	$\sim 2 \times 10^8$	U.V. absorption values from their graphed results.
Oppenheimer et al (1976)		$(1 - 2) \times 10^8$	From daytime ion chemistry of O_2^+
Nier et al (1974)		$\sim 3.5 \times 10^8$	Mass spectrometer with their new ion source (from their graphed values).
Ackerman et al (1974)	1.9×10^9 3.33×10^9		U.V. absorption. mass spectrometer (from graphed values)
Offermann and Grossmann (1973)	1.62×10^9	1.12×10^8	mass spectrometer with cryogenic ion source
Nier et al (1976)	3.1×10^9	2.4×10^8	mass spectrometers
Timothy et al (1972)	4.4×10^9	3×10^8	E.U.V. extinction (from graphed values)
von Zahn (1970)	2.5×10^9		average value from review of mass spectrometer and E.U.V. data
CIRA (1972)	2.9×10^9	2×10^8	mean CIRA (1972)

Table 1.2

CONCENTRATION OF ATOMIC OXYGEN AT 120 KM

Reference	Conc. in particles/cc	Comments
Dickinson et al (1974)	$\sim 1.3 \times 10^{11}$	Rocket-borne U.V. resonant lamp (from graphed values)
Donahue et al (1973)	$(1.5 - 5) \times 10^{10}$	Airglow of green line
Henderson (1974)	$\sim 5 \times 10^{10}$	Silver film sensor (from graphed values)
Good and Golomb (1973)	$\sim 6 \times 10^{10}$	NO release (from graphed values)
Philbrick et al (1974)	$\sim 9 \times 10^{10}$	Average value from 3 different methods (from graphed values)
Offermann and Grossmann (1973)	1×10^{11}	Mass spectrometer with cooled ion source
Timothy et al (1972)	$\sim 1 \times 10^{11}$	E.U.V. extinction (from graphed values)
CIRA (1972)	1.4×10^{11}	mean CIRA (1972)

Table 1.3

CONCENTRATION OF N_2 AT 150 KM

Reference	particles/cc	Comments
Ackerman et al (1974)	3.7×10^{10} 3.4×10^{10}	Mass spectrometers Two flights
Nier et al (1976)	2.9×10^{10}	Mass spectrometer
Timothy et al (1972)	$\sim 3 \times 10^{10}$	E.U.V. extinction (from graphed values)
von Zahn (1970)	2.6×10^{10}	Average value from mass spectrometers and E.U.V. data
mean CIRA (1972)	2.7×10^{10}	

ment and walls to form such impurity gases as CO_2, CO, NO, N_2O, etc. (see Chapter IV) and as a result mass spectrometers not only give a small value of the concentration of atomic oxygen but the values determined by different experimental groups are different. To minimize the loss of atomic oxygen in the ion source Offermann and Grossmann (1973) have used a cryogenic ion source. They found that the number density of atomic oxygen with this novel type of ion source was considerably higher than any previous mass spectrometer experiment while the density of molecular oxygen was low. In fact, the measured ratio of $n(O)/n(O_2)$ at 150 Km was 13.6, a value much higher than the 9.2 proposed by von Zahn (1970). Nier et al (1976) have flown on the Atmospheric Explorer-C satellite a mass spectrometer with an ion source which according to the authors (Hayden et al (1974)) is capable of discriminating particles which suffer wall collisions with the ion source, and, hence, to detect only those particles coming directly from the ambient atmosphere. From this mass spectrometer the authors found a density for atomic oxygen a factor of about 2.5 less than that of Offermann and Grossmann (1973) at 150 Km while their concentration of molecular oxygen was about a factor of 2 higher. At present it is not possible to say which set of values represent best the concentration of atomic oxygen in the upper atmosphere as there are several experiments which support high values and quite a number which support low values of atomic oxygen concentration. For instance, the value of Henderson (1974) using silver film sensors favours a low value while that of Dickinson et al (1974) supports a high value. (For further detail on the discussion of high and low values for the density of atomic oxygen the reader is referred to the work of Nier et al (1976)).

In the case of molecular oxygen even though to a certain extent the mass spectrometer and E.U.V. extinction are in harmony the spread in the individual results is much larger than for the non reactive gases, such as molecular nitrogen and argon. In fact, Ackerman et al (1974) determined the concentration of O_2 by two methods, mass spectrometer and U.V. absorption, and found that the two measured density values agreed well at low altitudes ($<$ 120 Km) but not at altitudes greater than about 120 Km. The O_2 number densities determined with mass spectrometers were much greater than those obtained by U.V. absorption. They attributed the difference in the two values to the recombination of atomic oxygen in the ion source of the mass spectrometer.

The minor constituents of the lower thermosphere are principally Ar, NO, CO_2, CO, He and hydrogen and the difficulties in measuring the concentration of these gases lie mainly in the limited sensitivity of the instruments. Argon can be measured well with mass spectrometers at low altitudes but the mass spectrometer data for the gases NO, CO_2, and CO are not reliable because these gases are produced as impurites at the hot filament of the ion source, although Offermann and Grossmann (1973) employing the cryogenic ion source have claimed to have measured the true ambient CO_2 concentration. It has been possible to determine the concentration of NO from the measured ratio of NO^+/O_2^+ with ion mass spectrometers (Oliver (1974), Golshan and Sechrist (1975), etc) and in the low altitudes from the observation of the resonant radiation of the γ-bands of NO (Barth (1966), and Meira (1971)).

In conclusion, it can be said that even though a large number of measurements have been made with different teachniques there still remains the fundamental problem of knowing the actual concentration of atomic oxygen in the lower thermosphere.

1.5.3 ATMOSPHERIC MODELS.

There have been a large number of models of the upper atmosphere which take into account the temporal and spatial variation of the atmospheric parameters such as density and temperature. Some of these models have been purely theoretical while others empirical or semi-empirical. In fact, prior to the rocket or satellite era the atmospheric models were based entirely on theoretical assumptions while with the availibility of high altitude rockets and satellites the construction of the models were closely connected with the experimental observations and, as a consequence, empirical and semi-empirical models have resulted.

Basically, the upper atmospheric models are based on the solution of the following equation of continuity:

$$\frac{\partial n_i}{\partial t} + \nabla.(n_i.\vec{V}_i) = P_i - L_i \qquad (1.12)$$

where n_i is the number density, $\vec{V}_i$ is the macroscopic velocity and P_i and L_i are, respectively, the production and loss rates per unit volume for the i^{th} constituent. Equation (1.12) is a time-dependent three-dimensional equation and its numerical intergration is still not possible, even, with today's powerful digital computers. Thus, it is still impossible to construct atmospheric models which are able to represent in detail all the aeronomical phenomena. Theoretical models can be constructed, but, only by introducing simplifying assumptions.

The first comprehensive theoretical model of the upper atmosphere is that of Harris and Priester (1962). In this model the authors succeeded in describing the structure of the upper atmosphere in accordance with the experimental data available at that time, although, this was only achieved by introducing in the model, in addition to the solar

E.U.V. heat input, a hypothetical "second heat source". In a later work Harris and Priester (1965) reported an improved version of the orginal model, but unfortunately, even in this case, they were not able to replace the "second heat source".

The orginal model of Harris and Priester (1962) may have its drawbacks, but it has been a very important model for two reasons:

(a) the COSPAR International Reference Atmosphere 1965 which has been used extensively for years by the international scientific community is based on this model.

(b) the model has lead to the development of more complex models such as the two-dimensional model of Lagos and Mahoney (1967) and Dickinson et al (1968).

Volland and Mayr (1970) have also developed a two dimensional model of the upper atmosphere, but they approached the problem in a completely different way from that of Lagos and Mahoney (1967) or Dickinson et al (1968). In fact, they treated the diurnal density variations of the thermosphere in terms of atmospheric waves.

More recently, attempts have been made to develop three-dimensional models such as Friedman (1970) and Volland and Mayr (1972).

Models have played a major role in the understanding of the upper atmosphere, in the sense that the elaboration of some of the models has been based on assumptions derived from experimental data, while, in turn, these models have been used to process and refine the experimental data. This iterative process has continued to date with the subsequent result that there exists in the literature quite a few empirical models such as the COSPAR International Reference

Atmosphere of 1961, 1965, and 1972, respectively, U.S. Standard Atmosphere (1962) and its supplements (1966) and Jacchia (1971) revised model, although some of these models or part of them have become obsolete.

All the above mentioned models assume that above a certain level, the turbopause, the atmospheric constituents are in diffusive equilibrium. However, the works of Shimazaki (1968) and Oran and Strobel (1976) showed that for atomic oxygen and molecular oxygen this is not the case. In fact, Shimazaki (1968) found that if he assumed in his model that O_2 and atomic oxygen were in diffusive equilibrium at altitudes greater than 120 Km, then their concentrations at 500 Km would be in error by 31.2% and 14.5% respectively. Similarly, Oran and Strobel (1976) found that above 200 Km the O_2 concentrations are about 20 - 35% less than the diffusive concentrations given by the Jacchia (1971) model atmosphere, while the concentrations of atomic oxygen are enhanced by about 10%. The low values of the concentration of O_2 seem to be supported by the rocket measurements of Weeks (1975).

1.5.4 THERMOSPHERIC VARIATIONS

The thermosphere is a region in which U.V. and E.U.V. radiations are absorbed and, consequently, its energy budget and, hence, its composition, density and temperature are strongly related to any variation in the emission of the solar U.V. and E.U.V. radiations. The available observational data reveal that the atmospheric parameters are subject to several types of variations. These variations have been classified as:

(1) periodical variations such as

(a) diurnal variation due to the rotation of the earth on its axis (period, one day).

(b) variation of the solar radiation due to the rotation of the sun on its axis (period, 27 days).

(c) semi-annual variation (period, 6 months).

(d) seasonal - latitudinal variations due to the revolution of the earth around the sun.

(e) variations with the solar cycle (period, 11 years).

(2) sporadic variations such as

(f) variations due to the daily change in the activity on the solar disk (sunspots).

(g) variations due to geomagnetic activity.

(h) rapid density fluctuations which are probably due to gravity waves.

Of all the above mentioned variations only the diurnal, seasonal and the variation due to geomagnetic activity and solar cycle will be discussed briefly here.

(1) Diurnal Variation. Satellite drag data indicate that the air mass density has a maximum

value at 14.00 hours local time (L.T.) and a minimum at 03.00 hours L.T. The amplitude of the diurnal variation of the mass density and hence of the individual neutral constituents of the upper atmosphere is fairly large and is a function of the altitude. In fact, Danilov (1972b) from the analysis of published results of 50 rocket flights, found that the ratio of the concentration of the daytime N_2 to the concentration of the night-time N_2, $n(N_2)$ day/$n(N_2)$night, increased from a factor of 1.4 at 140 Km to a factor of 2 at 200 Km with a maximum occurring at 14.00 hours L.T. Similarly, for atomic oxygen he found that the ratio n(O)day/n(O)night was 2.3 for moderate solar activity and 3.6 for low solar activity at 200 Km height with the diurnal maximum occurring at 13.00 - 14.00 hours L.T. This diurnal variation of atomic oxygen is supported by the incoherent scatter measurements of Alcayde et al (1972). Such measurements indicate that the diurnal variation of atomic oxygen has a similar phase as the one deduced by Danilov (1972b) from the rocket data but with a maximum/minimum density ratio larger than 2 at 120 Km.

In the case of O_2, the diurnal variation is asymmetric with respect to the local noon and the maximum concentration of O_2 occurs 4 - 5 hours earlier then that of N_2 or atomic oxygen. Offermann (1974) from the analysis of rocket experiments data deduced

that the ratio $n(O_2)_{max}/n(O_2)_{min}$ is about 1.5 at 150 Km while Parker and Stewart (1972) and May (1973) from U.V. absorption experiments on the Ariel 3 satellite found that the density variation of O_2 yielded a morning/evening ratio of about 1.25 and 1.16, respectively, at low latitudes and at 180 Km altitude.

(2) Seasonal Variation. For the seasonal variation there have been a large number of measurments both from ground based and from rocket or satellite borne instruments and only the most recent published results will be mentioned here.

In the case of molecular nitrogen, Offermann (1974) found that at low altitude (120 Km) the seasonal variation is such that there is a summer minimum and that the concentration of N_2, $n(N_2)$, is 12% less in summer than in winter, but at higher altitudes the trend is reversed. In fact, Offermann (1974) found no detectable seasonal variation at 150 Km and a summer maximum instead of the summer minimum at 200 Km with a small amplitude variation. More recently, Mauersberger et al (1976) from the data of the mass spectrometer flown on the Atmosphere Explorer-C satellite deduced that there is an enhancement of N_2 in summer and the ratio of $n(N_2)$ for summer/winter is 1.3 at 200 Km, increasing to 2.5 at 300 Km and still increasing to 6.2 at 450 Km.

For atomic oxygen the seasonal variation is such that the maximum concentration

occurs in the winter hemisphere. In fact, Alcayde et al (1974) and Johnson (1973) found that the winter/summer ratio of the concentration of atomic oxygen, n(O), at 120 Km is 1.5 while Scialom (1974) found a ratio of about 2 at the same height. However, the data of Mauersberger et al (1976) indicate that there is a substantial winter enhancement of n(O) at low altitude but the effect decreases with increasing altitudes and at 350 Km there is a "crossover", leading to an enhancement of atomic oxygen in summer rather than in winter at high altitudes. Furthermore, in an analysis of rocket borne mass spectrometer and 5577 Å night airglow photometer data below 110 Km, Offermann and Drescher (1973) found a seasonal variation in the peak of the atomic oxygen profile at 95 Km with a maximum occurring in summer. They also found a seasonal vertical movement of the atomic oxygen peak, its location being at lower altitudes in summer than in winter.

Considering the seasonal variation of molecular oxygen, it is found that there is a large discrepancy between mass spectrometer measurement and U.V. absorption and incoherent scatter measurements. In general, the mass spectrometer results show a much smaller seasonal variation than either U.V. absorption or incoherent scatter observations. In fact, at the altitude of 120 Km the U.V. absorption measurements of Noxon and Johanson (1972) and Roble and Norton (1972) indicate that there is an enhancement of

O_2 in summer with a summer/winter density ratio of about 3, while this ratio at 100 Km as determined by the U.V. experiment of Norton and Warnock (1968) is 1.5. On the other hand, Sialom (1974), by applying a photochemical model of the F_1 region to the incoherent scatter ionic composition data, found a summer/winter ratio of 4 at 120 Km. However, Offermann (1974), from the analysis of a large number of mass spectrometer plus a few U.V. measurements, found that there is a negligible seasonal variation of O_2 at 150 and 200 Km altitudes while at 120 Km he found a winter rather than summer enhancement, with a winter/summer O_2 density ratio of 1.3, in contrast to the U.V. and incoherent data, although he cautions the reader that this winter enhancement at 120 Km may be accidental resulting from a large scattering in O_2 data.

Similarly, at the altitude of 200 Km, Alcayde et al (1974), from incoherent scatter data, found a large summer/winter density ratio of 6, while the O_2 densities as determined by Oppenheimer et al (1976) from the daytime chemistry of O_2^+ ions, Nier et al (1976) from the mass spectrometer data and by Offermann (1974) indicate only a very small seasonal variation at this height.

(3) Variation due to geomagnetic acivity. The effect of a geomagnetic distrubance on the atmospheric parameters has been studied at length and measured by many researchers such as DeVries (1972),

Jacchia et al (1967, 1976), Roemer (1971, 1974), Waldteufel et al (1972) and May (1973), and from their study it is possible to draw the following conclusions:

(a) That there is a general increase in density with the onset of geomagnetic activity.

(b) Even the smallest variation in geomagnetic activity is reflected in atmospheric variations.

(c) There is a certain time lag between the onset of a magnetic disturbance and the beginning of density increase, the time lag being longer at low latitudes than at high latitudes, although Roemer (1971) failed to detect this feature.

It appears that not all the neutral constituents are enhanced with geomagnetic activity. In fact, while the density of the heavy atmospheric constituents such as N_2, O_2 and Ar are increased with geomagnetic activity the concentration of atomic oxygen decreases (Danilov (1972b) and Alcayde et al (1974)).

(4) Variations with solar cycle. Waldteufel et al (1972) found that atomic oxygen exhibits a solar cycle variation and that its concentration increased by a factor of 1.7, at 120 Km, from solar minimum to solar maximum.

1.6 CONCLUSION

In this review chapter, the author has only attempted to review the aeronomical phenomena, the parameters of which have been measured in his rocket experiments. To date the author has measured total lower thermospheric density, composition and density of both the neutral and ionized species of the lower thermosphere and the energy spectra of ions and fast electrons. However, not all the data will be presented in this thesis.

It has not been possible to review all the aeronomical phenomena presented in this chapter to any great depth or detail; however, whenever possible the author has extracted the information from the latest works reported in the literature. The magnitude of the literature, which is to be found in scientific journals, has made it practically impossible to mention all the authors who have participated in the advancement of the knowledge of the upper atmosphere.

CHAPTER II

SOFT X-RAYS AND EXTREME ULTRAVIOLET EXPERIMENTS

2.1.1 AIM OF THE SOFT X-RAYS AND EXTREME ULTRAVIOLET EXPERIMENTS

The aim of these experiments is to measure the solar X-ray and E.U.V. (Extreme Ultraviolet) fluxes, as a function of altitude in the earth's atmosphere by means of rocket-borne instruments and to determine from the measured fluxes the composition and total particle density in the upper mesosphere and lower thermosphere.

2.1.2 THE QUANTA INSTRUMENTS

The instruments which will be described in this chapter are the proportional counters, which respond to X-rays in the spectral regions from 1 to 20 Å and from 44 to 60 Å, and a grazing incidence spectrometer employed for measuring the E.U.V. fluxes.

The proportional counter may be thought of as a transducer which converts the energy associated with a quanta or charged particle into a proportional quantity of charge. It also acts as a linear amplifier with a gain up to 10^5 or more. The counter consists basically of two co-axial cylinders, the center one, the anode, being usually of a thin stretched wire, insulated from the outsider cylinder by two glass or ceramic to metal seals (fig 2.1). If a voltage V (volts) is applied between the anode and cathode, of radii a and b respectively, then the electric field inside the counter, at a distance X from the anode is:

$$E = \frac{V}{X} \cdot \ell n b/a \qquad (2.1)$$

On the side of the outer cylinder there is a window, usually of aluminium, beryllium or plastic films. The counter is filled with a mixture of inert and quenching gases, such as a mixture of 10% methane and 90% argon, commercially known as P-10. A combination of the window's material and the filling gas will determine the spectral response region of the counter.

The grazing incidence spectrometer employs a concave grating as a dispersive element of the solar E.U.V. fluxes and the dispersed, nearly monochromatic radiations after passing through the exit slits, positioned on the Rowland circle of the grating, are detected with channeltrons. The channeltrons are discussed in some detail in chapter IV.

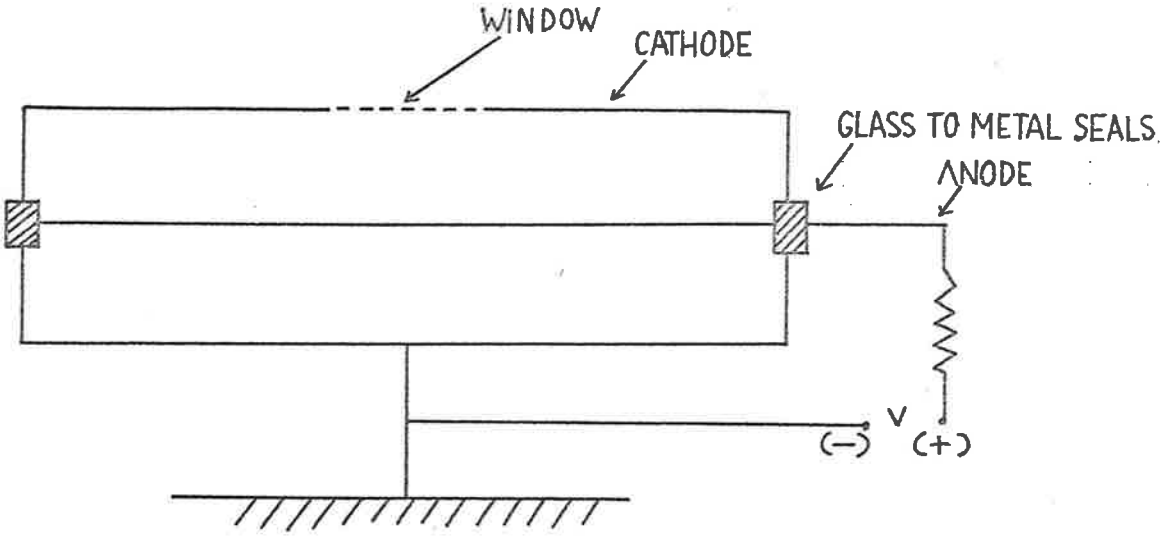

FIG. 2·1. SCHEMATIC VIEW OF A PROPORTIONAL COUNTER.

2.1.3 OPERATION OF PROPORTIONAL COUNTERS

The classical gas filled radiation detectors are the ionization chamber, the proportional counter and the Geiger counter. These detectors have been used in atomic and nuclear physics research since the first decade of this century (Rutherford and Geiger (1908)), and yet it is only since the early forties that their principles of operation have been understood.

The theory and operation of a proportional counter are discussed by Rose and Korff (1941), Korff (1948), Rossi and Staub (1949), Wilkinson (1950), Curran and Craggs (1949), Zastawny (1966) and Hendricks (1972).

When an X-ray passes through the gas, it is absorbed by an atom of the gas, causing the emission of a photoelectron with kinetic energy:

$$K.E. = h\nu - E_K \qquad (2.2)$$

where $h\nu$ is the energy of the incident photon and E_K, the potential energy of the K shell of the atom of the gas involved in the emission, which in the case of argon is 2.98 KeV. The vacancy created in the K shell may be filled by one of the L-electrons and two things may happen:

(a) the energy of the L electron in jumping from the L to the K shell is emitted as a characteristic $K\alpha$ X-ray of energy E_K, called fluorescent X-ray.

(b) the $K\alpha$ X-ray, instead of leaving the atom, is absorbed by the L shell and an electron, called the Auger electron, is emitted.

The electron vacancies that exist after step (a) or (b) are filled by similar processes which continue with the emission of L, M, N, etc., X-rays and Auger electrons until a highly charged positive ion remains (Fink et al (1966)).

The ejected photo-electrons and the Auger electrons produce secondary ionization until the energy of every free electron falls below the ionization potential of the filling gas which for P-10 gas is 26.2 eV. The accelerating electric field applied between the anode and cathode is strong enough for the free electrons to acquire sufficient energy between collisions with the neutral particles so that an electron avalanche results within a few diameters of the anode wire, the charge of which is proportional to the incident photon energy.

Not all of the fluorescent X-rays are re-absorbed by the gas and the K radiation that escapes gives rise to a second peak (escape peak) at an energy $(h\nu - E_K)$. For argon gas this escape peak is at $(h\nu - 2.98)$ KeV and is shown in fig. 2.2. The fluorescence yield is not the same for all gases. In fact, Fink et al (1966) found experimentally that the fluorescence yield for argon is 11%, while for krypton and xenon is 65% and 85% respectively. The latter two gases have very large escape peaks and consequently krypton and xenon are not as suitable as argon for the proportional counter's filling gases.

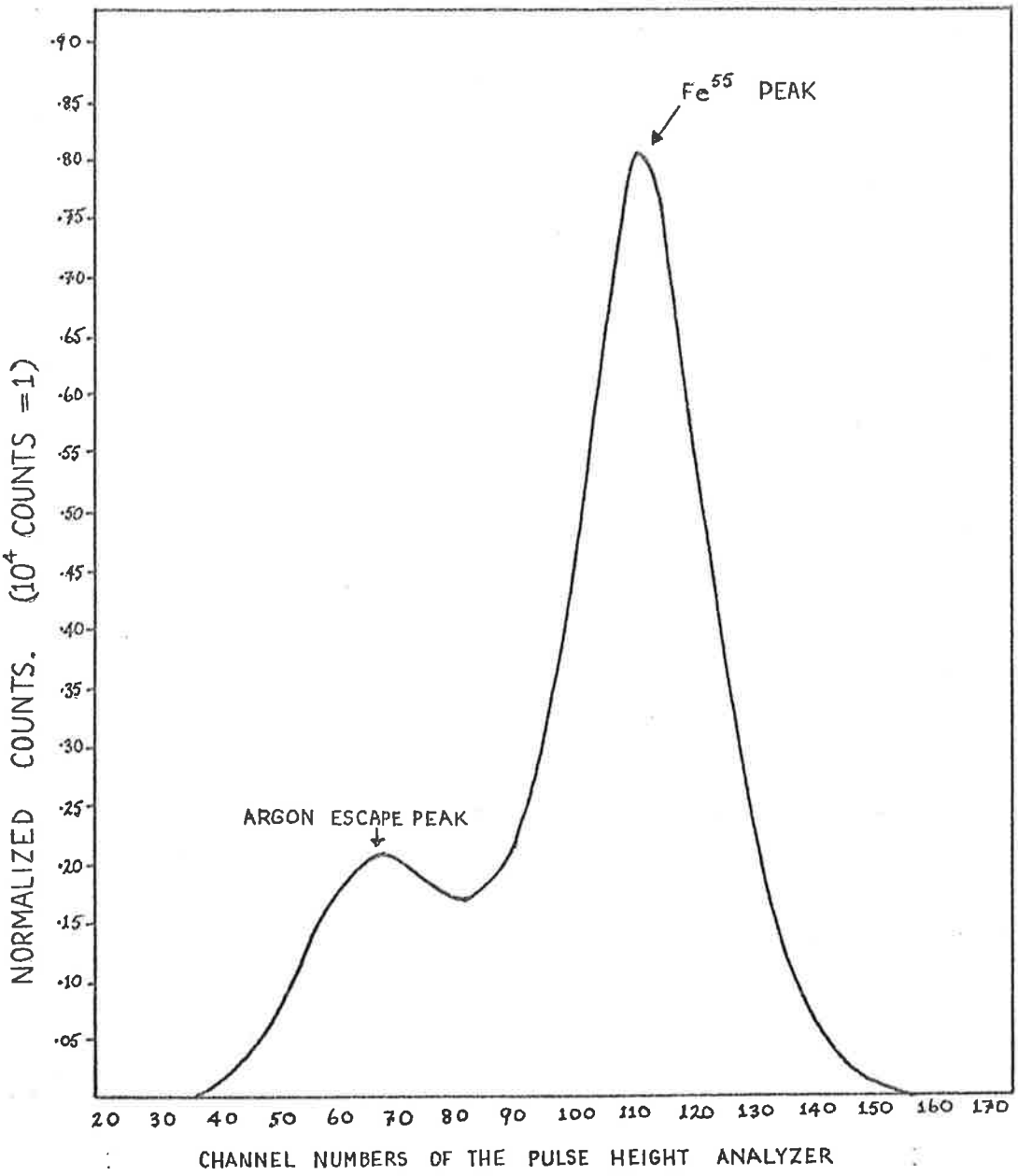

FIG. 2·2: A FLIGHT PROPORTIONAL COUNTER SPECTRUM OF Fe^{55} X-RAY SOURCE.

2.1.4 GAS GAIN OF THE PROPORTIONAL COUNTERS

Various authors have studied the gas multiplication process in proportional counters and succeeded in deriving theoretical expressions for its value. The general accepted formula for the gas gain, A, was derived by Rose and Korff (1941) which was later improved by Curran and Craggs (1949). A different formula was given by Kiser (1960) and more recently Zastawny (1966) derived the following expression:

$$\frac{\ell nA}{pr_a S_a} = K + B(\ell nS_a/S_o + S_o/S_a - 1) \qquad (2.3)$$

where $S_a = X_a/p$ and $S_o = X_o/p$, X_a, X_o being the intensity of the electric field at the anode and where the gas multiplication occurs, p the gas pressure in the counter and K and B are constants which are characteristic of the filling gas.

The problem of using any of the theoretical expressions for A is that A is a complex function of the anode and cathode radii, applied voltage, gas pressure and the nature of the gas, and in these formulas appear constants which can only be calculated when A is already known, so that A can only be determined experimentally.

2.1.5 GAIN SHIFT WITH COUNTING RATE

The output pulse amplitude of a proportional counter depends not only on the energy of the incident radiation but also on its intensity, and the higher the intensity the smaller the pulse height. The pulse height decreases exponentially with the counting rate (Fergason (1966)), and, because of this, a proportional counter cannot be used to measure the energy of the incident radiation with great accuracy if the counting rate is too high.

The shift in gain with counting rate is mainly due to the positive ions space charge formed near the anode wire which causes a lowering of the electric field near the anode and consequently the gain. This space charge is set up because the multiplication in a proportional counter takes place very close to the anode, and since the positive ions have relatively low mobilities by the time another pulse starts forming the positive ions of the last pulse are still within the region of multiplication which produce a screening effect around the anode, i.e., the positive ions space charge has the effect of reducing the electric field in the vicinity of the anode. This screening effect depends on the anode voltage (Burkhalter et al (1966)) and the diameter of the anode (Spielberg (1967)). But, according to Spielberg (1967), part of the gain shift with the counting rate is due to "adsorbed gases, perhaps debris from counter avalanches, on the wire surface, which are momentarily released during the electron collection process, and are subsequently capable of capturing electrons during succeeding avalanches, thereby reducing the average pulse height".

2.1.6 ENERGY RESOLUTION

The energy resolution of the proportional counter is limited basically by two factors:

(a) variation in the number of ions produced by the incident radiation and

(b) fluctuation in the number of ion pairs formed in the avalanche (variation in the gain A).

If it is assumed that there is no interaction between the ionization produced by the incident radiation, and that resulting from the avalanche, the probability theory (Charles and Cook (1968)) shows that the fluctuation in the pulse is mainly due to the fluctuation in the number of primary ion pairs and not in the gain A. The fluctuations (a) and (b) are in general difficult to separate, but Curran and co-workers (1949) have shown experimentally that they can in fact be separated and the variations in A can be studied experimentally by observing the pulse spectrum produced by the release of a single electron with zero energy within the counter, while the fluctuations in the number of ion pairs produced by the incident radiation cannot be studied experimentally because the number of ions is not large enough to be measured accurately, especially if the counter is used to detect soft X-ray and U.V.(ultraviolet radiation).

The distribution of the pulse shape is very complex, especially if one tries to incorporate in his theory all the factors which affect the electron avalanche such as the nature of the gas mixture, photo-electric effect, space charge, and uniformity of the anode wire. The simplest analysis of the pulse distribution was made by Snyder (1947) and improved by Curran and his co-workers (1949) in which they assumed that the electrons were always in equilibrium with the electric field within the counter. Byrne (1962) has reconsidered the

problem theoretically, taking into account the previous history of the electron, and has derived the following expression for the avalanche distribution:

$$P(A) = A^{(1/b - 1)}.e^{-A/ab} \qquad (2.4)$$

where a and b are constants which can be determined experimentally. More recent works, especially those of Gold and Bennet (1966) and Carver and Mitchell (1967) in which they used various gases and mixtures, seems to support the complex nature of the avalanche distribution.

However, the energy resolution of the counter (as already mentioned) depends mainly on the fluctuation of the number of ion pairs produced by the incident radiation. Fano (1947) was the first to consider the problem and has found that the relative standard deviation $(\sigma_p/\bar{p})$ of the distribution of the pulse is proportional to $E^{-\frac{1}{2}}$, where E is the energy of the incident radiation. However, experimentally Bisi and Zappa (1955) found that in the energy range 2 - 66 KeV the relative standard deviation does not obey the law $E^{-\frac{1}{2}}$, but

$$(\sigma_p/\bar{p}) = 0.138/E^{0.395} \qquad (2.5)$$

and the energy spectra approximates a Gaussian distribution at energy $E>2$ KeV. Various other authors have found that the energy distribution is Gaussian (Pontecorvo (1950), while for energy $E<2$ KeV, the distribution is Poissonian (Campbell and Ledingham (1966)).

2.1.7 PULSE SHAPE

The most important property of a proportional counter, apart from the gas gain multiplication, is the fact that the electron avalanche is formed very close to the anode wire (within a few microns of the anode), and consequently the pulse size is independent of the position at which the incident radiation ionizes the gas, i.e. there is a very small chance that the primary ionization is produced in the multiplication region.

The pulse of a proportional counter results mainly from the motion of the positive ions away from the anode, and thus to calculate its shape the behaviour of positive ions must be known. The contribution of the electrons to the pulse height is very small. The mobilities of positive ions are about 1000 times smaller than those of electrons (Wilkinson (1950)), and since the ions have to travel a greater distance than electrons to be collected, the duration of the pulse due to positive ions is longer than that due to electrons. This means that if a proportional counter is used as as a fast counting detector, the output pulse must be strongly differentiated. However, this differentiation has the effect of reducing the pulse height, and then it becomes important to avoid contaminating the filling gas with electro-negative gases which capture electrons forming stable negative ions, the low mobilities of which reduce the pulse height still further.

2.1.8 PROPORTIONALITY

In a gas filled tube a complex relationship exists between the voltage applied to the tube and the current flowing through it. In fact, if an ionizing agent (β particles, X-rays, etc.) enters the volume between the two electrodes of the tube and if the anode voltage is gradually increased from zero to a certain maximum voltage, the current-voltage characteristic of the tube passes through several distinct regions. The region in which the electric field is strong enough to cause amplification in the gas by ionization is called the "proportional region", and it is in this region that proportional counters operate. The region is characterized by the fact that the gas amplification is independent of the initial number of ion-electron pairs produced and hence the output pulse height is always proportional to the initial ionization.

However, if the initial ionization is considerable, or the proportional counter is operated with a high gas gain, the charge per pulse can become large enough to reduce the electric field in the region of the anode and so reduce the gas multiplication. Hanna and co-workers (1949) established a critical value for the gain A and energy E of the incident radiation such that when the product $A.E \geqslant 10^8$, the proportional counter loses its proportionality. They found that the pulse height is proportional to the energy E as long as $A.E < 10^8$ eV. Hence, if say $E = 6 \times 10^3$ eV then in order for the counter to preserve its proportionality A must be less than 1.7×10^4.

The proportionality of a flight proportional counter is shown in fig. 2.3. In this figure the relative pulse height (pulse heights have been normalized such that the pulse heights from Fe^{55} X-rays source is equal to one) is plotted as a function of X-ray energy for an anode voltage of 1.8 KV.

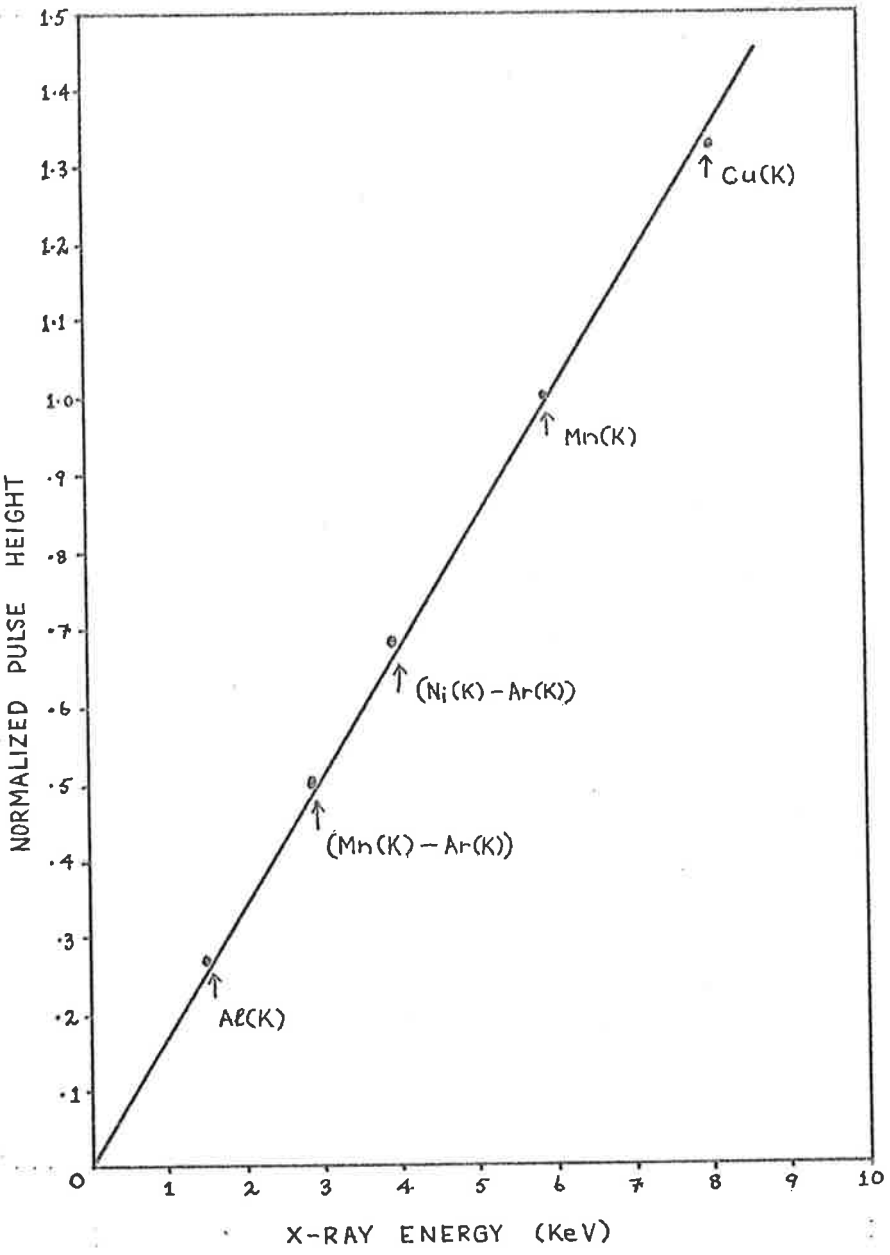

FIG. 2·3: PULSE HEIGHT AS A FUNCTION OF X-RAY ENERGY FOR A FLIGHT PROPORTIONAL COUNTER. The voltage applied to the anode was 1800 volts.

2.1.9 LIFETIME AND AGING EFFECTS

One of the factors which determines the life of a proportional counter (Korff (1948)) is the decomposition of the quenching gas. For instance, if a cylindrical proportional counter of length 4 cm and diameter 2.5 cm is considered and filled with P-10 at a pressure of one atmosphere, then the total number of CH_4 molecules in the counter is 5.4×10^{19}. If a gain of 10^4 is assumed and X-rays of energy of 6 KeV are used, then the lifetime of the counter is 2.7×10^{13} counts which means that after 2.7×10^{13} counts all the CH_4 molecules will be decomposed.

In practice, the counter changes its characteristics long before this happens. In fact, den Boggende et al (1969) observed that after about 10^8 counts the counter starts showing aging effects. The symptom is that the resolution of the counter deteriorates and the gaussian pulse distribution becomes asymmetric, and in the case of hard X-rays a second peak develops on the lower energy side of the main peak, while for soft X-rays the distribution broadens.

The lifetime depends also on such factors as counting rate, gas gain, gas composition and contamination. For example, for P-10 gas the counter shows the aging effect after about 10^8 counts, while for Ar + CO_2 mixture this appears only after approximately 10^{10} counts (den Boggende et al (1969)).

The lifetime of the flight proportional counters was of the order of six weeks (see section 2.1.19), irrespective of whether they were left on counting or not for a long period of time. The counters had polypropylene windows of thickness 15 μm and it is evident from table 2.2, section 2.1.14, that the high permeability of the window material to oxygen and water vapour is the cause of the short lifetime expectancy of the counters.

2.1.10 FILLING GAS AND WALL MATERIAL

Ideally, the wall material for a proportional counter should be chosen so that the photo-electric absorption coefficients are as low as possible. Therefore, the material should be of low atomic number such as beryllium or aluminium but, unfortunately, aluminium does not solder or seal easily so that copper is used instead.

However, the filling gas should be of high atomic number so that the photo-electric effect is as large as possible. This is because the mean free path of the radiation in the counter must be less than the dimension of the counter body to avoid the radiation from reaching the inner wall, which gives rise to spurious pulses. For this reason xenon is preferred since the absorption coefficients of xenon are higher than those of argon, but when the escape peaks and mobilities of the positive ions are considered, xenon is not as suitable as argon.

The gas generally employed in filling the counters is a mixture of approximately 10% methane and approximately 90% argon, known commercially as P-10. In Australia this gas is prepared by C.I.G. (Australia) and its composition is given in table 2.1.

The electronegative gases present in the filling gas capture electrons which have the effect of reducing the lifetime and the gain of the counter. It can be easily calculated (Wilkinson (1950)) that if less than 1% of the electrons in the avalanche are to suffer capture, the presence of electro-negative gases such as O_2, H_2O and Cl_2, must be less than one part in 10^4. From table 2.1, it follows then that the commercial grade P-10 gas available in Australia is sufficiently pure to be used in the counters.

Table 2.1

COMPOSITION OF C.I.G. COMMERCIAL GRADE P-10

USED IN FILLING PROPORTIONAL COUNTERS

Component Gas	Concentration
Methane (CH_4)	9 - 11%
Ethane (C_2H_6)	1000 volumes per 10^6
Nitrogen (N_2)	850 " " "
Propane (C_3H_8)	125 " " "
Carbon Dioxide (CO_2)	125 " " "
Hydrogen (H_2)	1 " " "
Oxygen (O_2)	20 " " "
Water Vapour (H_2O)	25 " " " in full cylinder at 15°C
	60 " " " in 10% full cylinder at 15°C
	900 " " " in 5% full cylinder at 15°C
Argon	~ 90%

2.1.11 UNIFORMITY OF ANODE WIRE

Gas multiplication in the counter depends mainly on the strength of the electric field in the neighbourhood of the anode wire (within about 3 or 4 anode diameters), and is therefore important that the wire should be of uniform diameter, smooth and free from prominences which may cause local ionization and hence spurious pulses.

O'Boyle (1965) has shown that die imperfection of the wire can be removed by subjecting it to an alternating electric field at high temperature (1900^{o}K) in a vacuum for several hours. This operation will practically remove microscopic bits of dust, and any sharp points. The DC fields, however, seem to have the opposite effect.

The anode wire of the manufactured detectors, used to measure the absorption of the solar X-ray fluxes as a function of altitude in the atmosphere, was of tungsten and had a diameter of 50μm. Visual observation of the wire under a microscope revealed that it was smooth and free from any prominences or sharp points so that it was not subjected to an AC field.

2.1.12 END EFFECTS

In a proportional counter, the electric field near the ends of the anode is different from that near the center. The lines of force are not radial and the field strength is weaker and reaches its normal value only at some distance from the ends. This causes the gas gain to decrease gradually toward either end of the wire producing a lower energy trail in the energy spectrum, and reaches its normal value only at a distance from the ends equal to the diameter of the cathode cylinder (Curran and Craggs (1949)). Thus, a proportional counter, of a cylindrical geometry, in order to have a flat gain response, requires its length to be at least three times its diameter.

These end effects can be eliminated in different ways (Cockroft and Curran (1951)) and in cases where the counters do not need large window areas they are not so important since the majority of the photo-electrons are produced near the window at the center of the counter. This is the situation of the rocket-borne detectors which were used to measure solar X-ray fluxes and since the sun is a strong source of X-rays the required window area was only 50 mm^2 (section 2.1.17). Therefore, the end effects were not considered.

2.1.13 GAS PRESSURE AND ANODE VOLTAGE

For a proportional counter operating in the proportional region a number of pressures-voltages combinations are possible for which the gas gain is the same. For example, for the rocket-borne proportional counters manufactured in the Department of Physics, University of Adelaide, the gas gain was the same whether the counters were filled with P-10 at a pressure of one atmosphere and had an applied anode voltage of 2.4 KV or filled at 55 cm of Hg with anode voltage of 1.8 KV. Fig. 2.4 shows the gas gain of a flight proportional counter as a function of the anode voltages for different pressures of the P-10 filling gas.

The flight proportional counters, ideally, should have a gas gain as high as possible in order to discriminate the background noise level from the signal and at the same time a low anode voltage so as to minimize the possibility of a high voltage corona occurrence during the rocket flight. To stop ~~the coroning~~ corona in of the high voltage power supply, it has been found that if the high voltage is less than 2 KV it is sufficient to pot the power supply with araldite or red silastic potting compounds, while if the high voltage is greater than 2 KV it becomes necessary to place the high voltage power supply in a pressurized box. On the Cockatoo vehicles there was no room available for the pressurized box so that it was decided to fill the counters at a pressure of 55 cm of Hg and apply to their anodes a voltage of 1.8 KV. With this gas pressure and applied anode voltage the gas gain was sufficiently high such that when larger vehicles (Skylarks and Aerobee) became available it was found unnecessary to increase the anode voltage in order to increase the gain.

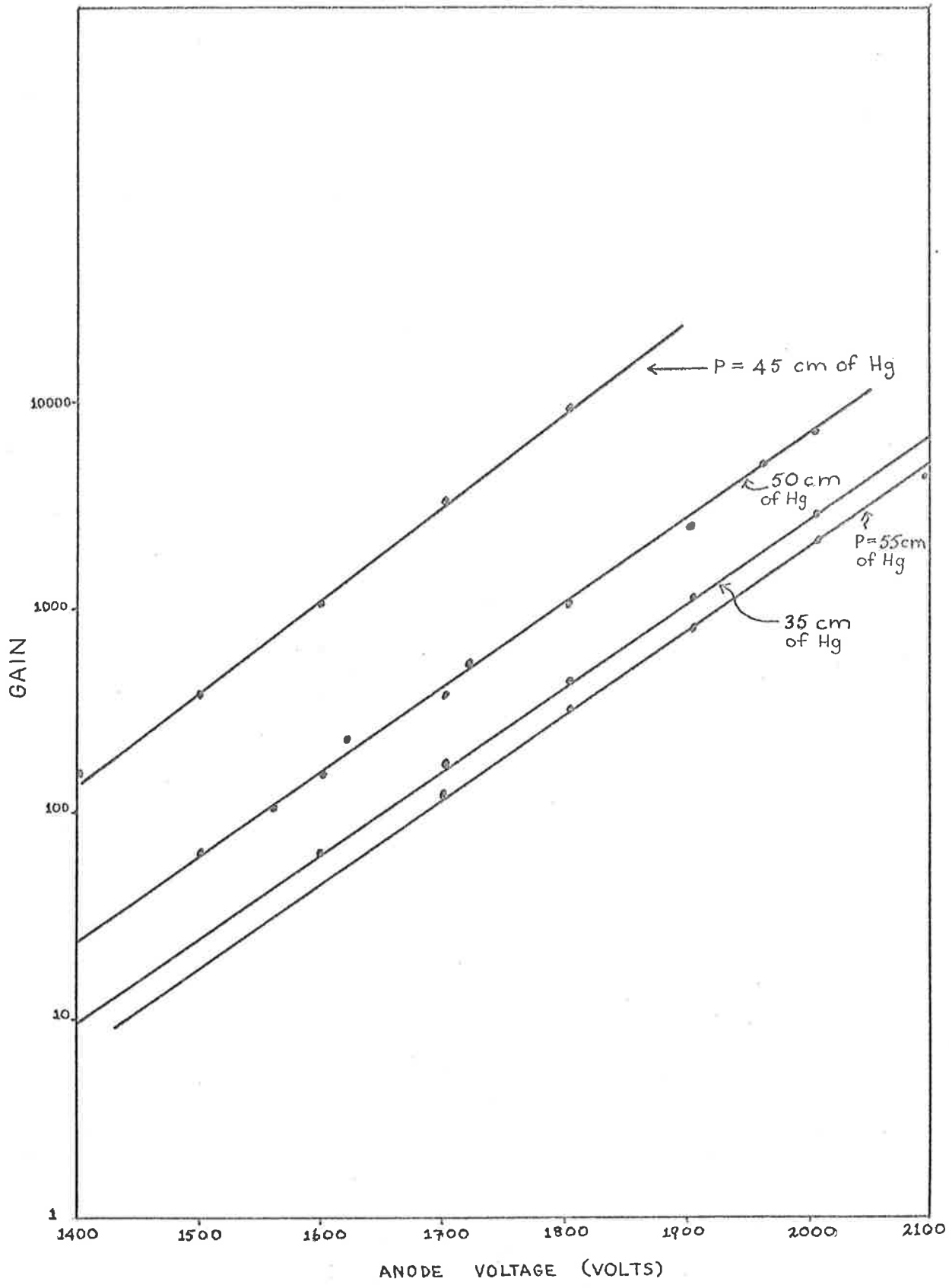

FIG. 2·4 COCKATOO'S PROPORTIONAL COUNTER'S GAS GAIN AS A FUNCTION OF THE APPLIED HIGH VOLTAGE FOR DIFFERENT PRESSURES OF THE FILLING GAS MIXTURE.

2.1.14 WINDOW MATERIALS

The window materials used on the proportional counters are mainly aluminized plastic films. These are polypropylene (propafilm) and melinex (mylar) which are both made by I.C.I. (Australia). Table 2.2 gives the property of these plastic films. The aluminium film on the plastic material was of the order of 100 nm. The window material was fastened to the body of the counter with silver araldite and with the aluminium film towards the counter, so as to avoid any field distortion in the window region due to the fact that plastic materials are insulators.

Table 2.2

PROPERTIES OF I.C.I. PLASTIC FILMS

Trade Name	Melinex "S"	Propafilm "O"
Formula	$(C_{10}H_8O_4)_n$	$(CH_2)_n$
Synonym	Polyethylene Terephthalate	polypropylene
Density (gram/cm^3)	1.395 - 1.405	0.91
Available thickness (μm)	8.9 (35 G) 12.7 (50 G)	15 (60 G) 20 (80 G)
Tensile strength (Kg/cm^2)	>1750	1750 - 2100
Elongation at break (%)	60 - 110	50 - 85
Melting Point (^oC)	~ 265	170
Permeability to:		
O_2	210	3000 - 3400 (1)
N_2	-	600 - 1200 (1)
CO_2	-	8000 - 10000 (1)
water vapour	42	8 - 10 (2) 2 - 3 (3)

(1) cm^3/m^2 in 24 hours at 25°C and 1 atmospheric differential pressure

(2) gram/m^2 in 24 hours at 38°C and 90% r.h. (relative humidity)

(3) gram/m^2 in 24 hours at 25°C and 75% r.h.

2.1.15 STOPPING POWER OF PLASTIC FILMS

The proportional counters are sensitive to any energetic ionizing agent (X-rays, α and β particles, etc.) and since for the purpose of this work the detectors are used to measure solar X-ray fluxes, it is essential that the window material stops the energetic atmospheric electrons and protons from entering the counter, thereby giving rise to background pulses which cannot be easily discriminated against the signal X-ray pulses.

The stopping power of plastic films is fairly high; for example, a polypropylene film, thickness 15 microns, will stop all the electrons of energy less than 25 KeV from entering the counter, while for protons this energy limit is above 1 MeV. These energy limits are calculated from the data of Berger and Seltzer (1964).

The number of electrons with energy E greater than 25 KeV and protons of $E > 1$ MeV in the height range of 90 to 150 Km is very small so that the background noise resulting from the atmospheric electrons and protons is negligible.

2.1.16 COUNTER'S EFFICIENCY

The detection of X-rays by a proportional counter is determined by the X-ray transmission of the window material and the absorption by the gas. The probability that the X-ray passes through the window material of thickness X (gm/cm^2) without being absorbed is:

$$T = \exp(-\mu_\omega X_\omega) \qquad (2.6)$$

while the probability that the X-ray is absorbed by the gas is given by:

$$I = I_o(1 - \exp(-\mu_g X_g)) \qquad (2.7)$$

so that the efficiency of the counter is;

$$\varepsilon(\lambda) = \exp(-\mu_\omega(\lambda).X_\omega).(1 - \exp(-\mu_g(\lambda).x_g)) \qquad (2.8)$$

where μ_ω and μ_g are, respectively, the mass absorption of the window material and of the filling gas.

Fig 2.5 shows the efficiency of the counter filled at a pressure of 55 cm of Hg with P-10 gas and having a polpropylene window of thickness $15x10^{-4}$ cm. The mass absorption coefficients used are from those tabulated by Henke and Elgin (1970).

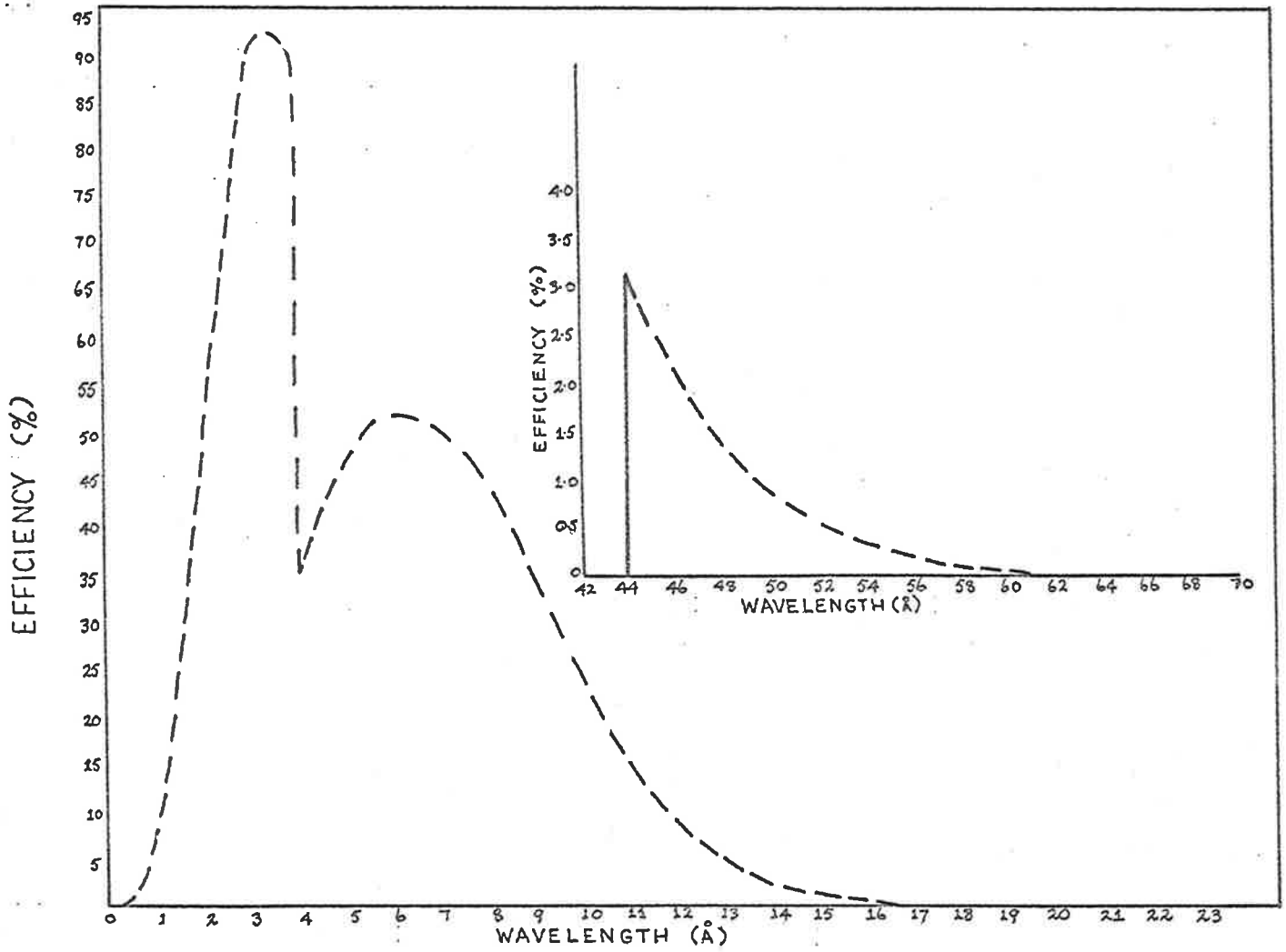

FIG. 2·5: EFFICIENCY OF A FLIGHT PROPORTIONAL COUNTER.

2.1.17 WINDOW SIZE

The emission of X-rays from the sun can vary by a factor of about 1000 over a short period of time even during a quiet sun period so that it is not possible to estimate the size of the window area very accurately.

Mandel'stam (1965) gives values of the solar X-ray emission in three spectral regions over a period of about 17 years. These values are for the quiet sun period:

- region I: (2 - 10 Å) 10^6 - 10^3 counts/sec.cm^2.
- region II: (8 - 20 Å) 10^7 - 10^5 counts/sec.cm^2
- region III: (44 - 60 Å) 10^8 - 10^7 counts/sec.cm^2

In these spectral regions the efficiency of the counter is about 89%, 12% and 1%, respectively, so that the proportional counter has to deal with about 10^5 counts/sec.cm^2. The counter has a maximum counting rate of about 5×10^4 counts/sec. and hence the area of its window must be about 50 mm^2. The flight proportional counters had 3 holes of 4.5 mm diameter as windows, illustrated in fig 2.6, or 3 holes of 4mm diameter, as shown in photograph 2.1.

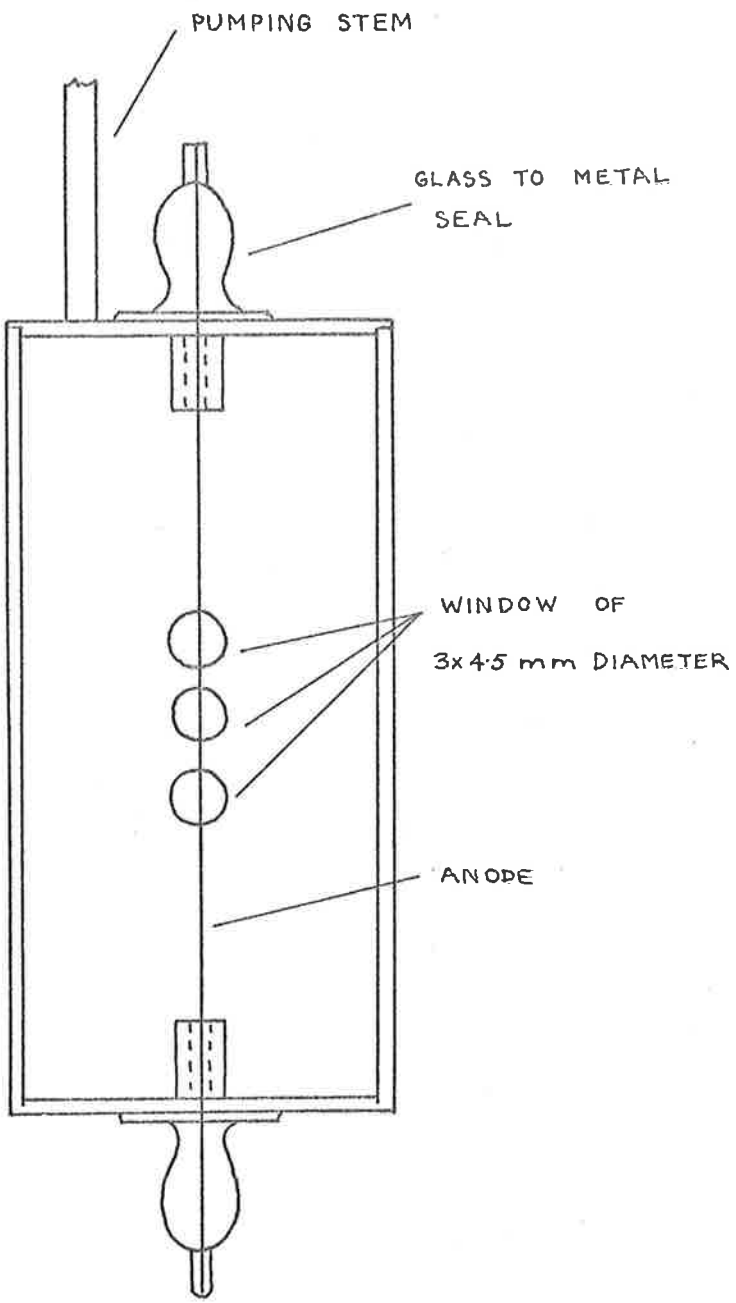

FIG 2·6: CROSS-SECTIONAL VIEW OF A PROPORTIONAL COUNTER.

Photograph 2.1: Proportional Counters flown on the Aerobee vehicle.

10
20
30
40
50
60
70
80
90
100
110
120
130
140
150

2.1.18 ANODE WIRE'S RESONANT FREQUENCIES

According to B.A.C. (British Aircraft Corporation) specifications, components to be flown on Skylark rockets must be tested under random vibrations in the frequency band 30 - 2000 c/s with an applied acceleration force of $4g$.

The well known D'Alembert equation for a vibrating string is given by:

$$\frac{\partial^2 y(x,t)}{\partial x^2} - \frac{1}{v^2}\cdot\frac{\partial^2 y(x,t)}{\partial t^2} = 0 \qquad (2.9)$$

where $v = \sqrt{\tau/\mu}$ and τ is tension of the string and μ is the linear density (mass/length).

If the anode is subjected to an acceleration of $4g$, then the initial conditions of the equation (2.9) are:

$$\begin{cases} \dot{y}(x,0) = 0 \\ \ddot{y}(x,0) = -4g \\ y(0,t) = 0 \\ y(\ell,t) = 0 \end{cases} \qquad (2.10)$$

where ℓ is the length of the string.

The solution of the equation (2.9) is:

$$y(t) = \frac{4g}{\omega_n^2}\cdot\cos\omega_n t \qquad (2.11)$$

where $\omega_n = n\pi v/\ell$

If the anode wire has a diameter of 5×10^{-3} cm and length 5 cm and is stretched by applying a weight of 250 grams to it, then its tension, τ, is 2.45×10^5 dynes. The anode is of tungsten of density 19.35 grams/cm^3 so that $\mu = 3.78\times10^{-4}$ grams/cm. Then:

$$v = 2.55\times10^4 \text{ cm/sec}, \qquad (2.12)$$

$$\omega_n = 1.6\times10^4 n \text{ rad/sec} \qquad (2.13)$$

$$y(t) = \frac{1.5\times10^{-5}}{n}\cdot\cos\omega_n t \qquad (2.14)$$

Under these conditions the maximum displacement that the anode

wire suffers is:

$$y_{max.} = 1.5 \times 10^{-5} \text{cm} \tag{2.15}$$

and its resonant frequencies are:

$$\nu = \frac{n}{2\ell}\sqrt{\frac{\tau}{\mu}} \tag{2.16}$$

For the above value of τ and μ

$$\nu \approx 3.3 \times 10^{3} n \text{ Hz} \tag{2.17}$$

From this, it follows that the resonant frequencies of the anode are outside the Skylark resonant frequency band.

2.1.19 PREPARATION OF THE COUNTERS

The first set of rocket-borne proportional counters which were flown on the Skylark rocket, SL 1005, launched from Woomera on December 11th, 1972, were made of copper tubing of 2.5 cm diameter and length of 5 cm. The end plates and the two anode glass to metal seals were soldered using high temperature silver solder.

The bodies were then first chemically and then ultrasonically cleaned with isopropyl alcohol and baked at 150^{o} for 24 hours. They were then pumped with a diffusion pump for about 24 hours, flushed three times with P-10 gas and filled at the required pressure. All these proportional counters had a pumping stem of 3 mm diameter and their expected lifetime was three weeks.

It was later found that be increasing the diameter of the pumping stem, their lifetime increased. In fact, when a pumping stem of 6 mm was used instead of the 3 mm one, the expected lifetime doubled. With a pumping stem of 10 cm long it was observed that if the stem had a diameter of 3 mm the counter could be pumped down to a pressure of 2×10^{-4} torr, while if it had a stem of 6 mm diameter it could be pumped to a pressure of 1×10^{-4} torr over a period of 3 hours. Even though the counters were flushed several times with P-10 gas before they were finally filled a difference of only a factor of two in their final vacuum pressure was critical to their lifetime expectancy. As a consequence, the counters from then on were made with a pumping stem of 6 mm diameter.

The later types of proportional counters which were flown on Skylark, SL 1207, Cockatoo and Aerobee rockets were made of aluminium tubing of the same diameter as the copper ones and put together with silver araldite. The expected lifetime of these counters was at least six weeks.

The proportional counters have been flown on rocket vehicles of different types and sizes (Skylarks, Cockatoos), but unfortunately because of a lack of space the counters had to be always short in length (50 mm, only twice their diameter). With the availability of the Aerobee rocket and hence more space, it has been possible to increase the length and hence the volume of the counters. The counters which were flown on the Aerobee, photograph 2.1, had the ideal length to diameter ratio of three to one with the resulting effect of increased gain and lifetime.

2.1.20 THE FLIGHT PROPORTIONAL COUNTERS

During the course of this work proportional counters have been flown on four Cockatoo rockets, designated C4007, C4009, C4017 and C4018, two Skylarks, SL1005 and SL1207, and on the Aerobee, 13.123IS vehicles.

Since the Cockatoo vehicles were spin stabilized, spinning at a rate between 8 and 11 rev/sec and to some extent coning it was necessary to know the angle response of the counters along both the longitudinal and transversal directions. This response is shown in fig. 2.7. The Skylarks and Aerobee vehicles were sun stabilized and therefore it was not necessary to determine the angle response of the counters.

The counters were all filled with P-10 gas at a pressure of 55 cm of Hg and had a high voltage of 1.8 KV applied to their anodes. The pre-amplifier of the counters is shown in fig. 2.8. Both the Cockatoo and Skylark vehicles had a FM/AM 24 channel telemetry system which only accepted analog voltage in the range -3 to +3 volts and hence the pulses from the comparator of fig. 2.8 were fed into binary counters and then into a digital to analog convertor to provide a suitable output analog voltage acceptable by the telemetry. The Aerobee, however, had a digital input PCM telemetry system and in this case the pulses from the comparator of the pre-amplifier were fed directly into the input of the telemetry.

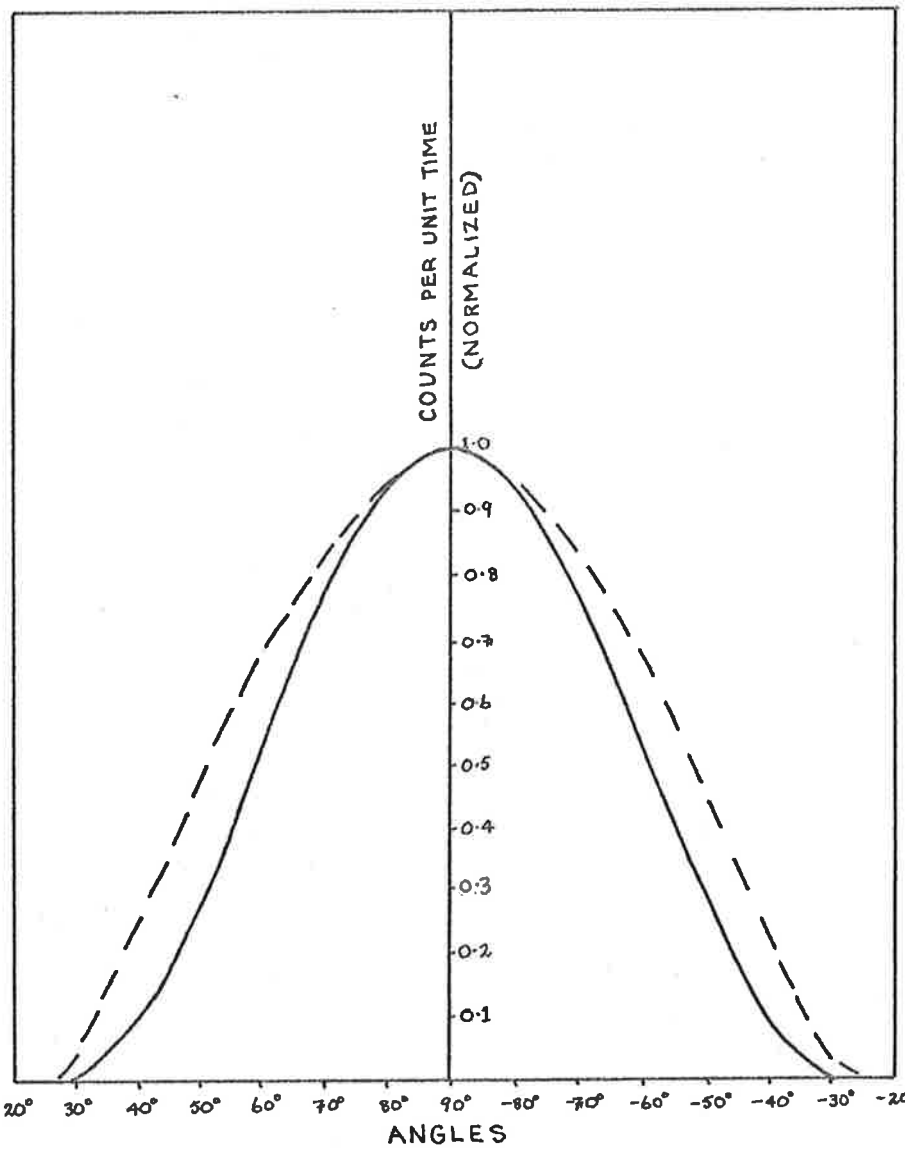

FIG. 2·7 LONGITUDINAL (——) AND TRANSVERSAL (– – –) ANGLE RESPONSE FOR THE COCKATOO'S PROPORTIONAL COUNTERS.

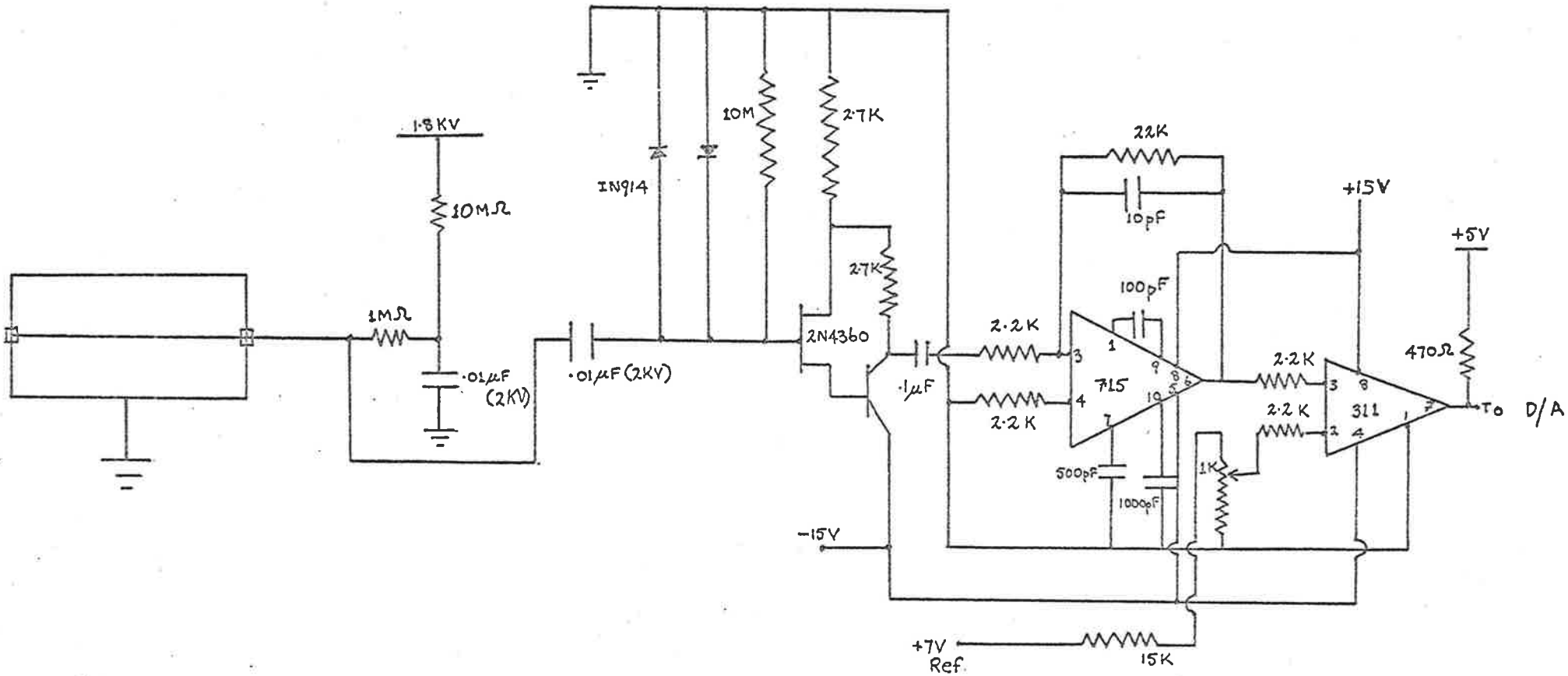

FIG 2·8: PRE-AMPLIFIER FOR X-RAY PROPORTIONAL COUNTERS.

2.2 THE GRAZING INCIDENCE SPECTROMETER

In the past several years a number of grazing incidence spectrometers have been successfully flown on rockets and, from the observed atmospheric attenuation of the nearly monochromatic solar fluxes as a function of altitude, the atmospheric composition at the time and place of the flight could be deduced.

A small non-scanning grazing incidence spectrometer, employing as a dispersing element a concave grating of radius of curvature of 390 mm, was flown on SL1207 vehicle. The entrance and exit slits were positioned on the Rowland circle such that the angle of incidence was 80^{o}. The spectral region of interest was between 200 and 1000 Å and three wavelengths were selected. These were the strong helium lines at 303.8 and 584 Å and the hydrogen continium at 850 Å. The choice of the wavelength 850 Å was a technical rather than a scientific one in the sense that three quanta detectors had to be fitted in the small space assigned for the spectrometer experiment.

The entrance slit of the spectrometer was 8 mm long and 75 μm wide while the three exit slits were 10 mm long and 100 μm wide. As detectors for the quanta, three channeltrons were used. These channeltrons, designated B413BL and made by Mullard Pty Ltd (U.K.) at the author's request, had as input apertures slits of length 15 mm and internal width of 1 mm instead of the ordinary 70 degrees funnels.

At the time of the SL1207 flight it was not possible to calibrate the instrument absolutely in the laboratory due to the unavailability of a suitable light source for the lines 584 and 303.8 Å so that its efficiency was only approximately estimated. But for the purpose of this work it was sufficient since the author's interest lies in the determination of the atmospheric composition and not in the study of the solar

fluxes at these wavelengths.

With the aid of an autocollimator the spectrometer was aligned with the A.C.U. (altitude control unit) detector which was a sun pointing device capable of pointing the axis of the vehicle on to the sun with an accuracy of 2 arc minutes. The SL1207 payload, which fully assembled is shown in photograph 2.2, was a shared payload, the primary experimenter being the University College, London (U.K.).

Photograph 2.2: Skylark 1207 fully assembled payload.

(Courtesy of B.A.C.)

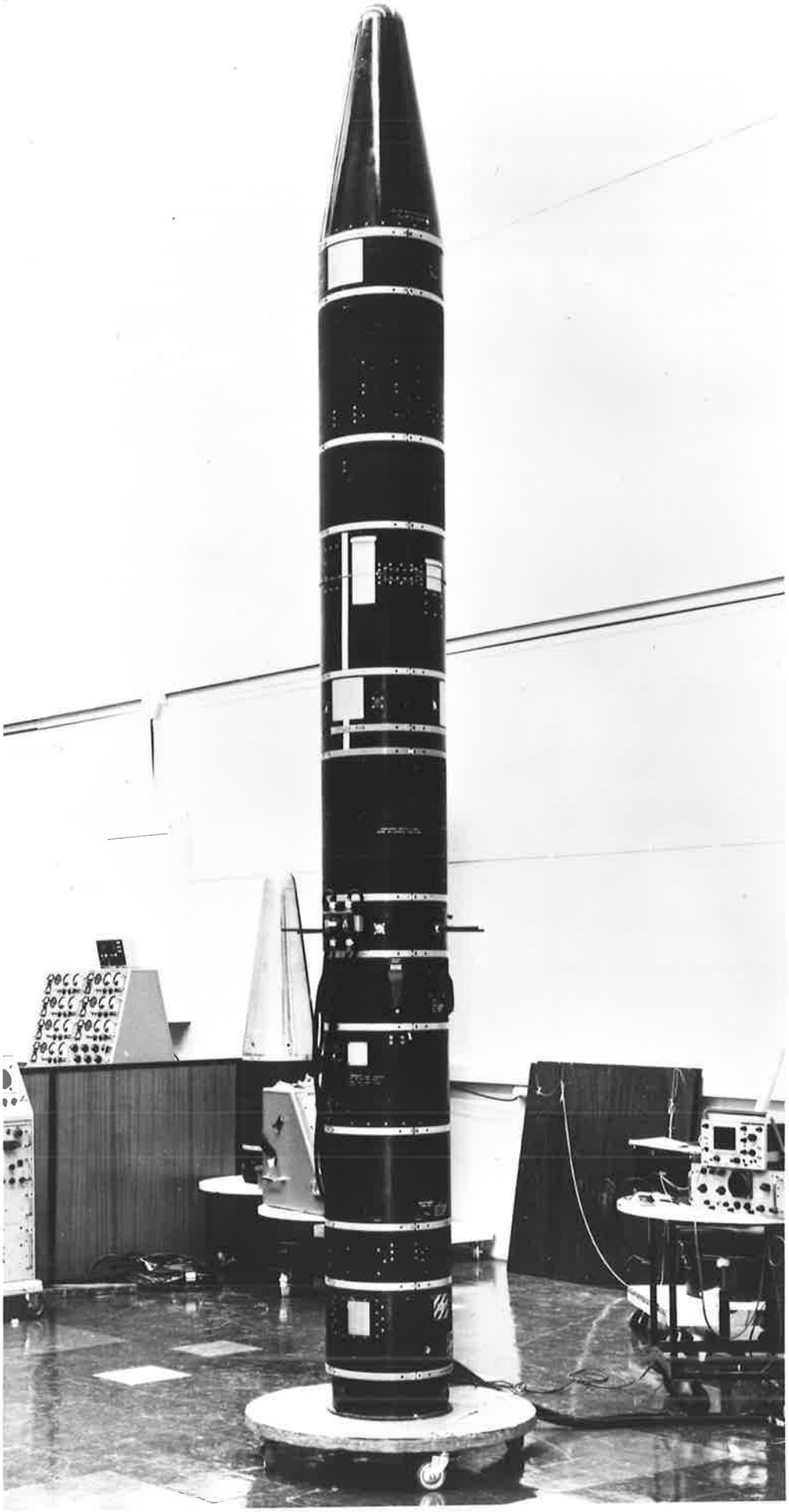

2.3 SOLAR X-RAYS AND E.U.V. ATMOSPHERIC EXTINCTION

Solar X-rays and E.U.V. fluxes have been measured as a function of altitude in the terrestrial atmosphere since the later nineteen forties for the purpose of determining the composition and total density of the atmosphere. But in order to make the best use of the sensitivity of the quanta detectors, which in the case of the proportional counters means selecting the correct type of window material and filling gas while for a non-scanning E.U.V. spectrometer selecting the wavelengths of radiation such that in both cases the absorption is maximum in the altitude region of interest, it is necessary to know "a priori" the attenuation of the solar fluxes in the atmosphere.

The attenuation of the solar radiation in the atmosphere follows the Beer-Lambert law and for a monochromatic radiation of wavelength, λ, and zero solar zenith angle is given by:

$$I(\lambda,h) = I_o(\lambda).\exp(-\tau(\lambda,h)) \qquad (2.18)$$

where $I_o(\lambda)$ is the radiation incident at the top of the atmosphere while $\tau(\lambda,h)$ is the optical depth, i.e:

$$\tau(\lambda,h) = \sum_1^m {}_i\sigma_i(\lambda).\int_h^\infty n_i(z)dz \qquad (2.19)$$

In equation (2.19), $\sigma_i(\lambda)$ and $n_i(z)$ are the cross-section and number density, respectively, of the i^{th} atmospheric constituent. The attenuation factor, $A(\lambda,h,\chi)$, at an altitude, h, and for a solar zenith angle, χ, is given by:

$$\begin{aligned} A(\lambda,h,\chi) &= I(\lambda,h,\chi)/I_o(\lambda,h) \\ &= \exp(-\tau(\lambda,h).F(\chi,H)) \end{aligned} \qquad (2.20)$$

where $F(\chi,H)$ is the optical depth factor which for solar zenith angles less than about 80^o is simply equal to $\sec\chi$ while

for zenith angles greater than 80^{o}, the expression is more complicated, as it depends on the density scale height, H, of the atmosphere as well as χ (see Swider (1964) for further details).

With the application of equations (2.19) and (2.20) the attenuation of the solar radiation in the atmosphere for various wavelengths and solar zenith angles has been computed. The attenuation curves for wavelengths of 3, 6, 9, 12, 15 and 44 $\mathring{A}$ for a zero zenith angle are shown in fig 2.9 while for 3 and 9 $\mathring{A}$, 15, 303.8, 584.3 and 850 $\mathring{A}$ for different solar zenith angles are shown in figs 2.10, 2.11, 2.12, 2.13 and 2.14, respectively.

In the expression (2.19) the values of the number densities, $n_i(z)$, used are from CIRA (1972) while those of the absorption cross sections are from Henke and Elgin (1970) for the X-ray region and from those tabulated by Stolarski and Johnson (1972) for the E.U.V. spectral region.

The proportional counters with polypropylene window and filled with P-10 gas respond to soft X-rays of wavelengths from 1 to 20 $\mathring{A}$ and the overall attenuation which is calculated from the expression:

$$A_T(h,\chi) = \frac{\int_1^{20} \varepsilon(\lambda).\exp(-\tau(\lambda,h).\sec\chi).d\lambda}{\int_1^{20} \varepsilon(\lambda).d\lambda} \qquad (2.21)$$

where $\varepsilon(\lambda)$ is the detector's efficiency, is shown in fig 2.15.

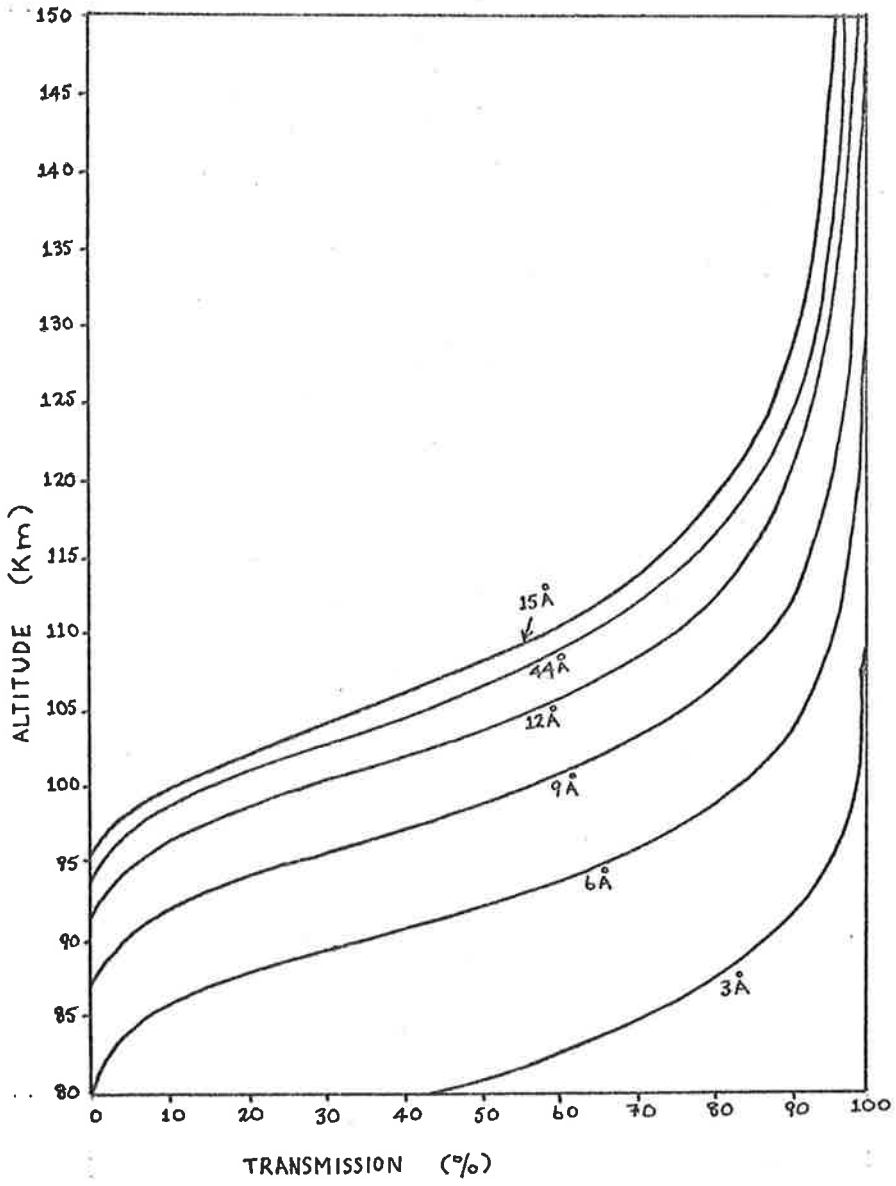

FIG. 2·9: ATMOSPHERIC TRANSMISSION FOR X-RAYS OF WAVELENGTHS 3, 6, 9, 12, 15 AND 44 ANGSTROMS FOR A ZERO ZENITH ANGLE OF THE SUN.

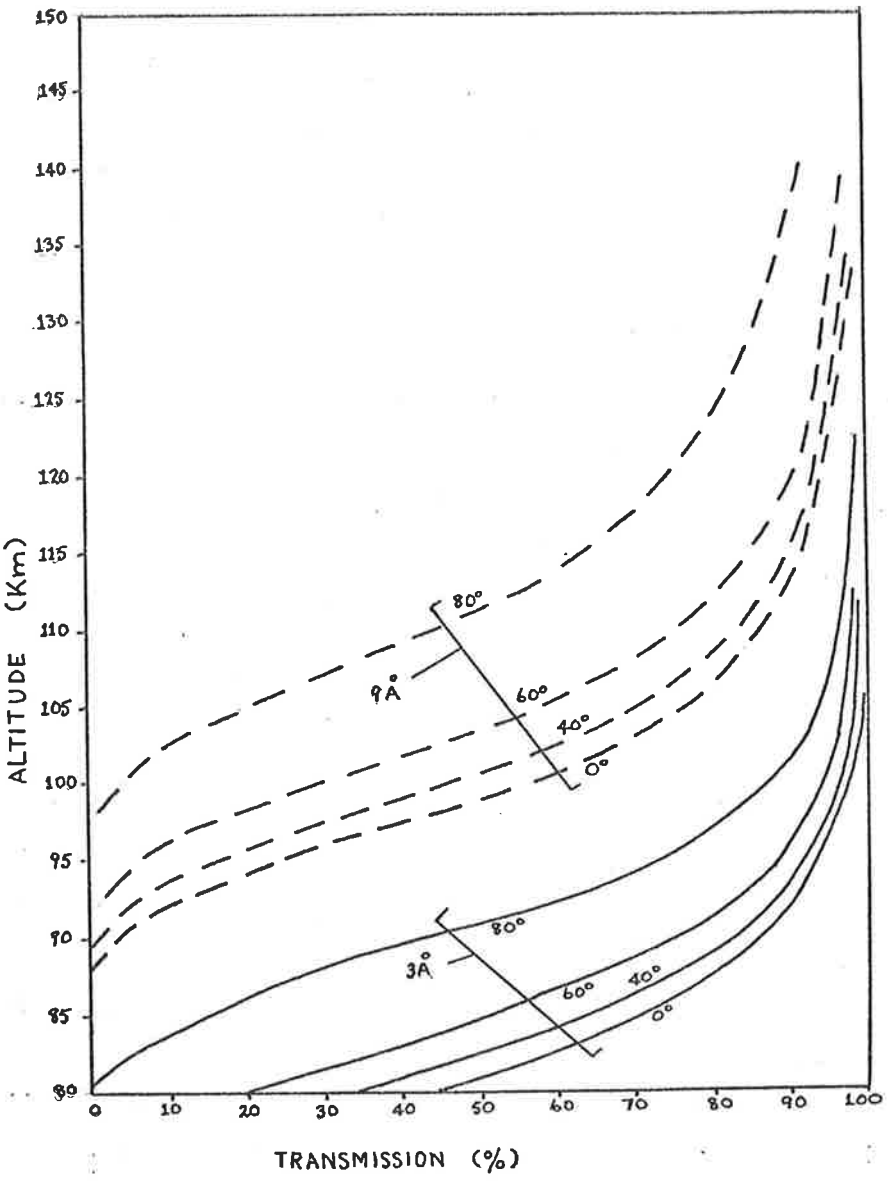

FIG. 2·10 ATMOSPHERIC TRANSMISSION FOR X-RAYS OF WAVELENGTHS 3 Å (solid lines) AND 9 Å (broken lines) FOR DIFFERENT ZENITH ANGLES OF THE SUN.

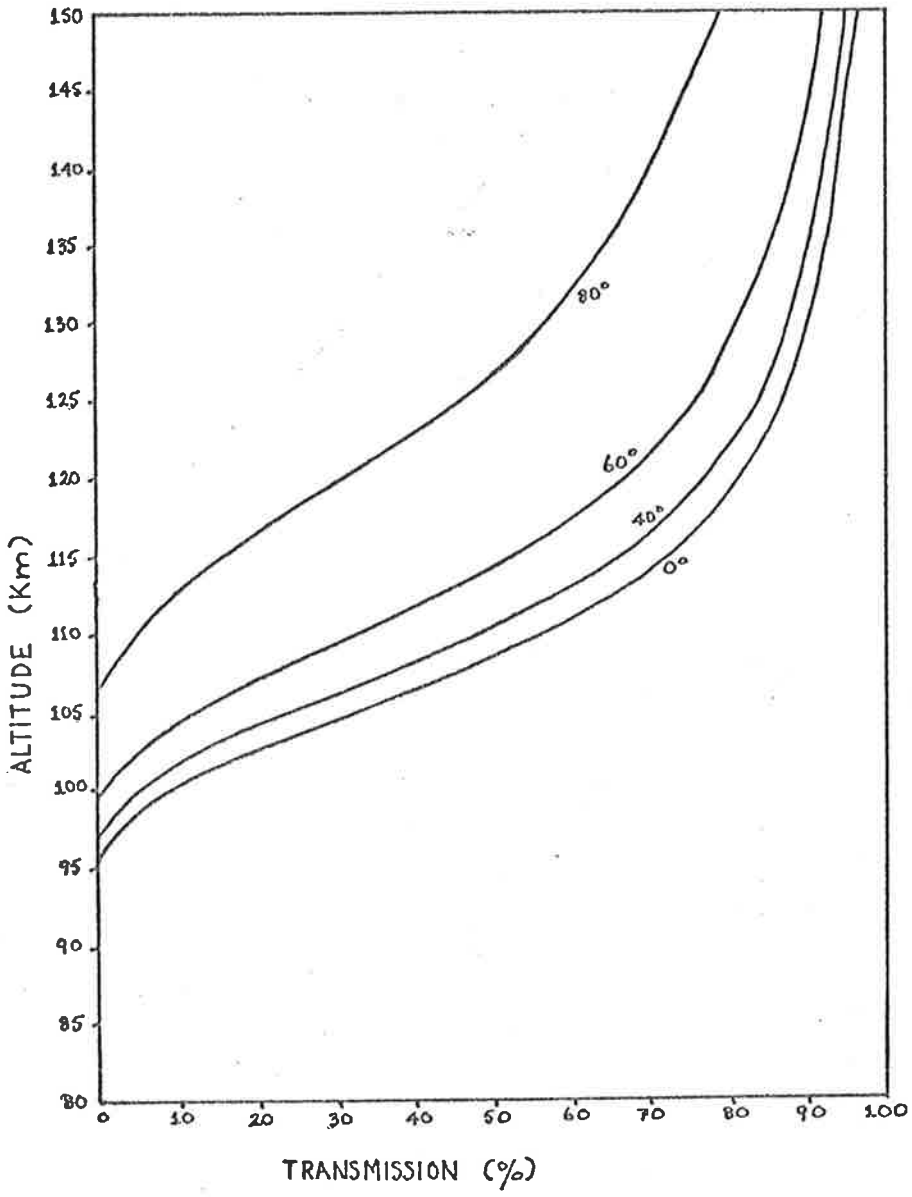

FIG. 2·11: ATMOSPHERIC TRANSMISSION FOR 15 Å X-RAYS FOR DIFFERENT SOLAR ZENITH ANGLES.

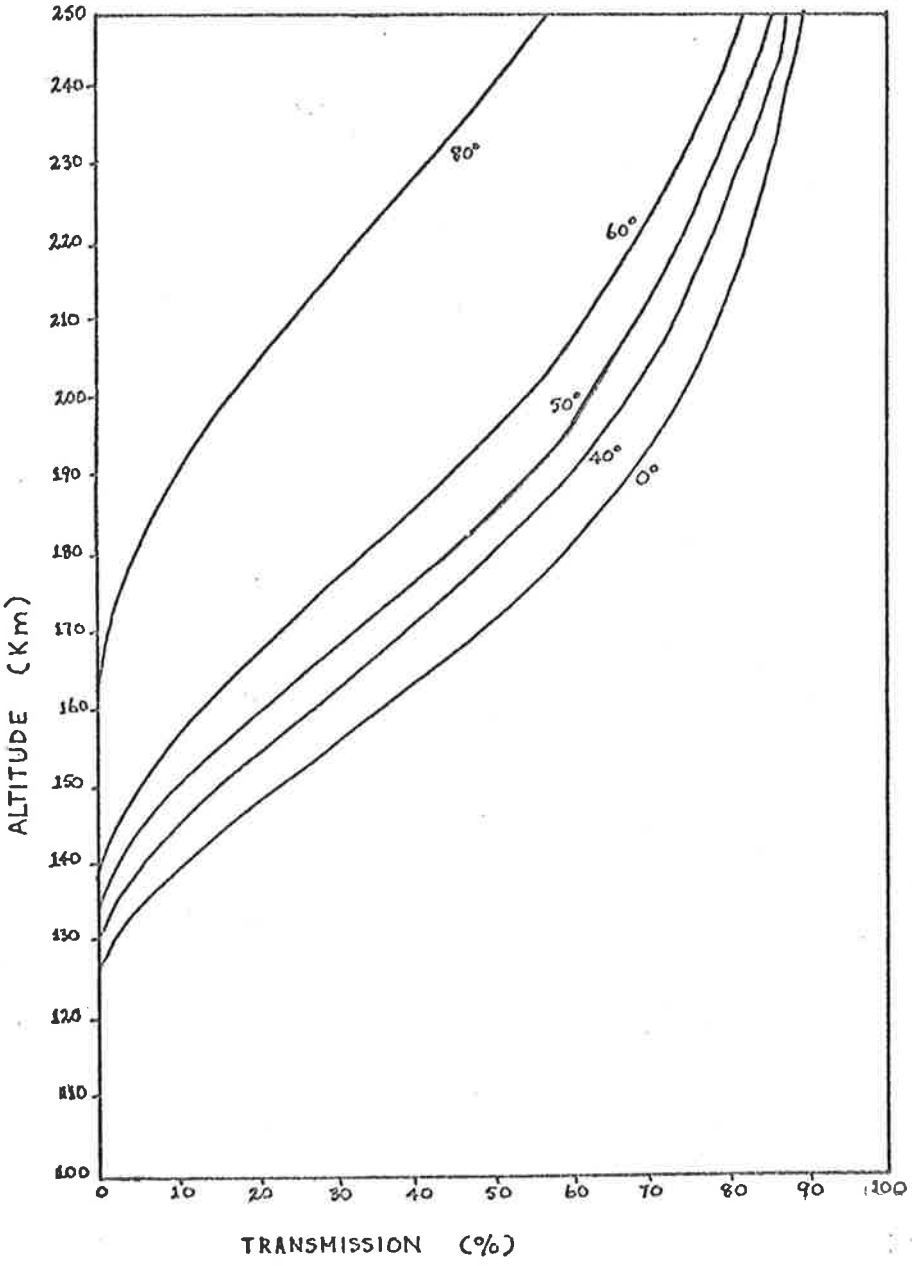

FIG. 2·12: TRANSMISSION THROUGH THE ATMOSPHERE OF THE 303·8 Å RADIATION FOR DIFFERENT SOLAR ZENITH ANGLES.

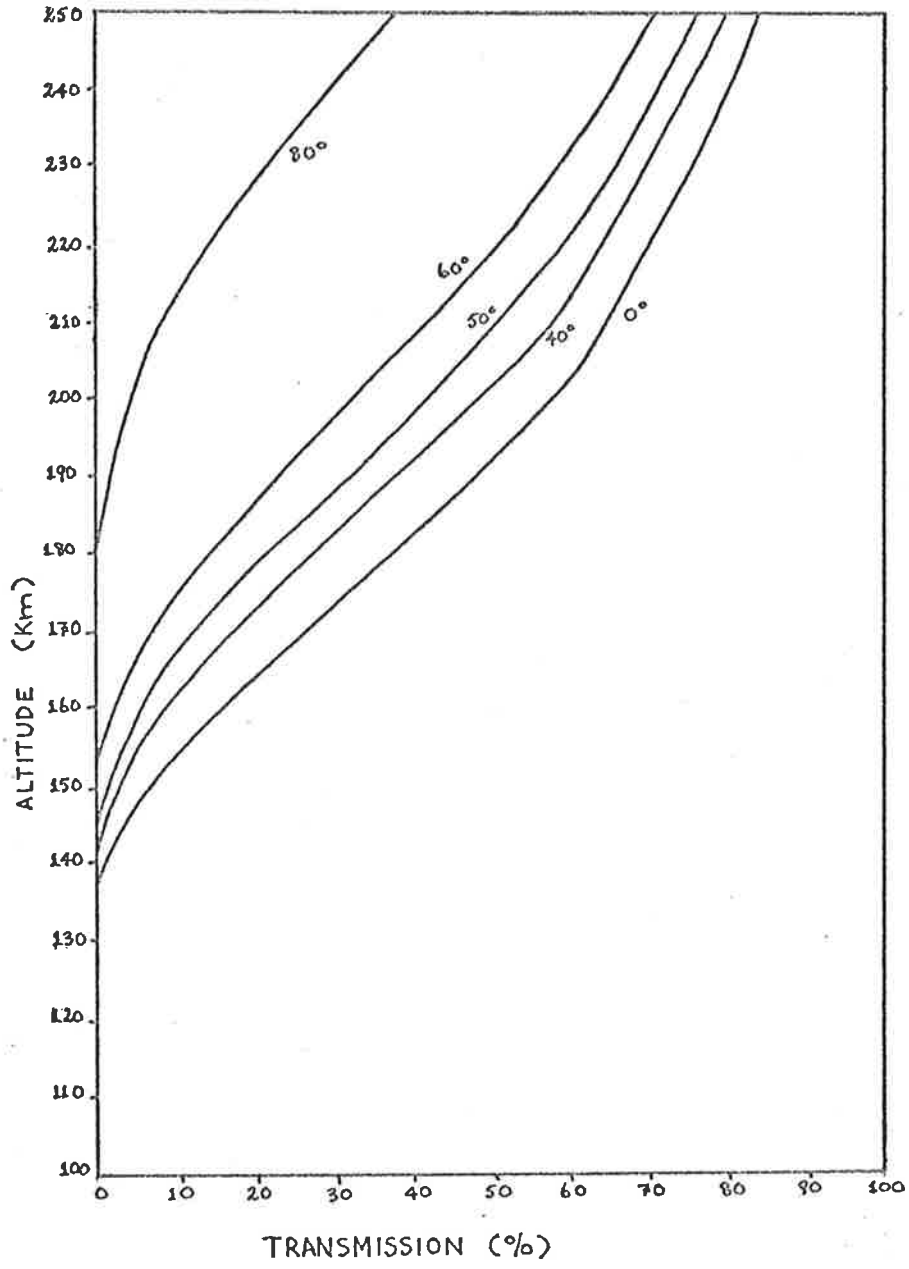

FIG. 2·13: ATMOSPHERIC TRANSMISSION OF THE 584·3 Å RADIATION FOR DIFFERENT SOLAR ZENITH ANGLES.

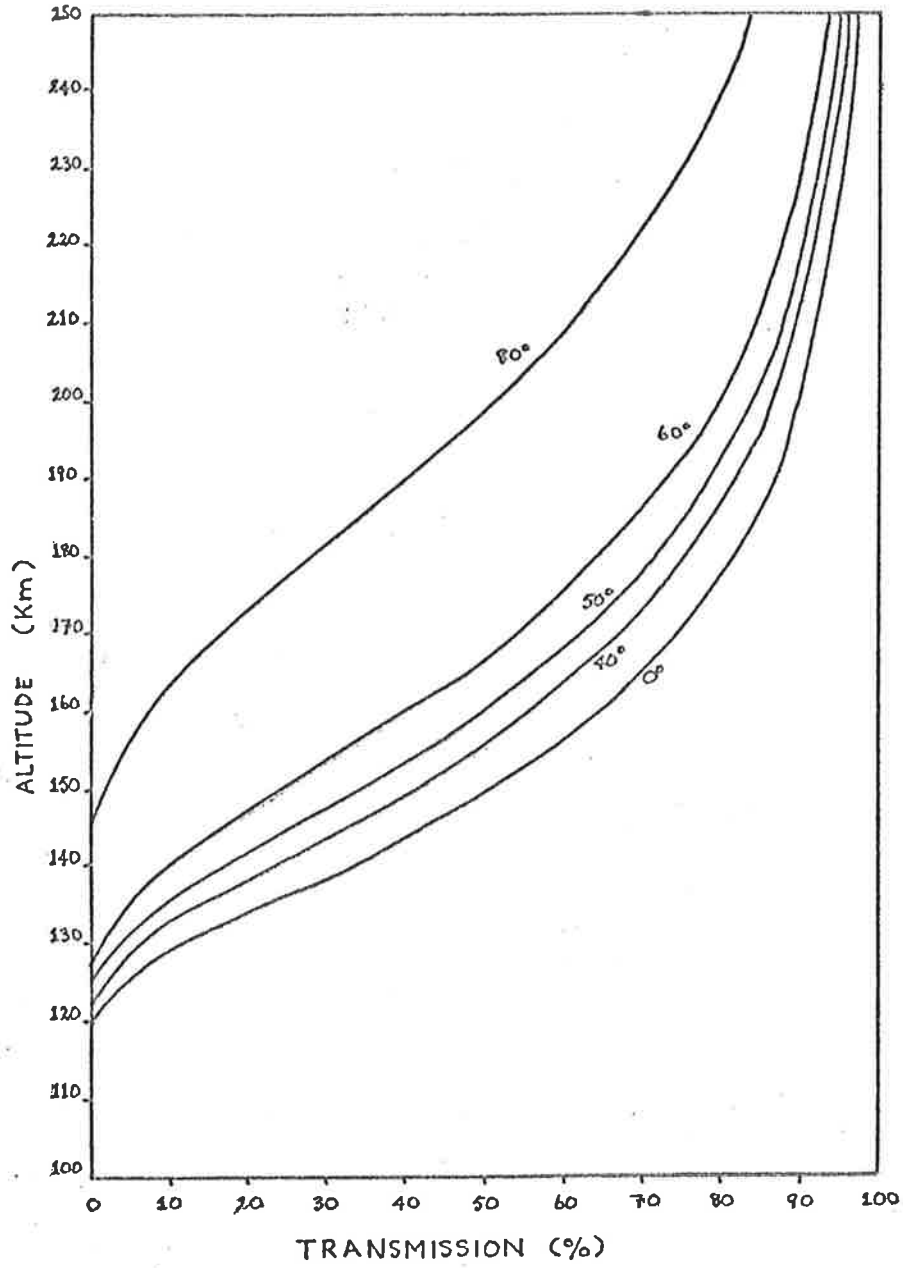

FIG. 2·14: ATMOSPHERIC TRANSMISSION OF THE 850 Å RADIATION FOR DIFFERENT ZENITH ANGLES OF THE SUN.

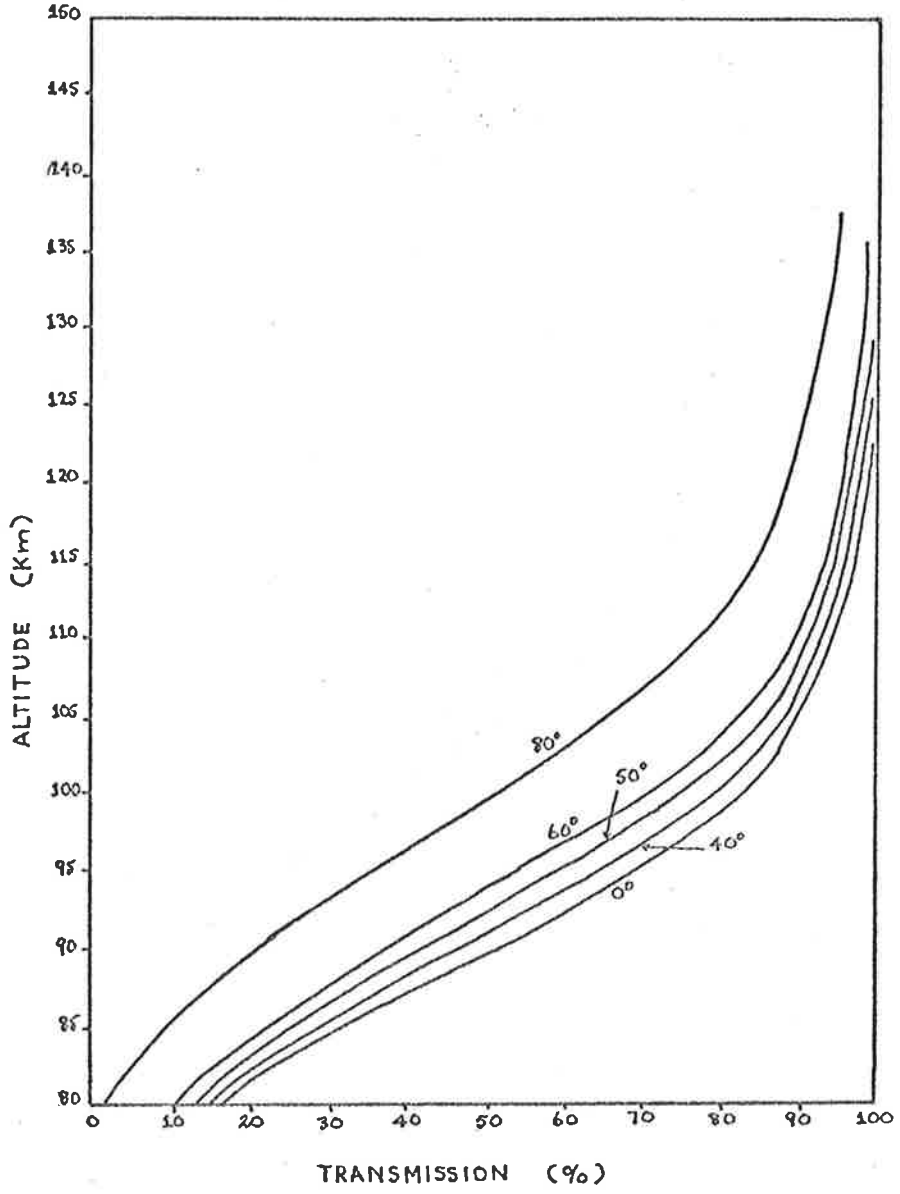

FIG. 2·15: ATMOSPHERIC TRANSMISSION FOR THE OVERALL RESPONSE OF THE FLIGHT PROPORTIONAL COUNTERS FOR DIFFERENT SOLAR ZENITH ANGLES.

CHAPTER III

E.U.V. AND X-RAY DATA ANALYSIS

3.1.1 INTRODUCTION

A series of rocket payloads have been prepared by the Space Group of the University of Adelaide during the years 1971 to 1976 for the purpose of studying the earth's lower thermosphere under different conditions and time of the day. The author's participation in this rocket program has involved the development and flying of a number of diverse instruments on different types of rocket vehicles.

In this chapter will be presented the analysis of the rocket data of the optical part of the author's payloads, namely the E.U.V. and X-ray detectors described in the previous chapter.

3.1.2 TYPES OF ROCKET PAYLOADS

The rocket vehicles which carried the E.U.V. and X-ray detectors were principally of two types:

(a) spin stabilized. These vehicles with the assigned name of "Cockatoo" had two stage solid fuel motors and were capable of taking a payload of cylindrical shape of 127 mm in diameter and about 17 Kg in weight to an altitude greater than 130 Km. The vehicles were developed by the former Australian Department of Supply under the aegis of the Weapons Research Establishment, Salisbury, South Australia.

(b) sun stabilized. These vehicles were the Skylark 1005 and 1207 payloads and the Aerobee 13.123IS rocket. Because of the size of the vehicles, they had the inbuilt sopistication of being able to point a certain part of the payload towards the sun and keeping the three axes of the vehicle fixed, within a certain accuracy, with respect to this position for a large part of the flight.

The author participated in the preparation of four Cockatoo payloads designated C4007, C4009, C4017 and C4018. These vehicles which were launched in pairs, morning and afternoon flights, carried instruments aimed at measuring the diurnal variation of the density of the neutral upper atmosphere in the altitude region of interest. The pairs were C4009 and C4007 which were launched, respectively, at 08^h20^m and 17^h25^m Australian Central Standard Time (C.S.T.) on October 2nd, 1974, and C4018 and C4017 which were launched at 9^h15^m and 16^h55^m C.S.T., respectively, on April 29th, 1975.

The Skylark 1005 vehicle was launched at 9^h30^m C.S.T.

on December 11th, 1972, while Skylark 1207 was launched at 10^h33^m C.S.T. on April 23rd, 1974. The Aerobee 13.123IS was launched at 6^h36^m C.S.T. on February 22nd, 1977. The solar zenith angles at the time of launch of these vehicles were 37.9^o, 50^o and 85^o for the Skylark 1005 and 1207 and the Aerobee payloads, respectively.

All the mentioned vehicles carried X-ray detectors while Skylark 1207 carried also a non scanning three channel grazing incidence spectrometer. Moreover, these vehicles have all been launched from the Woomera Rocket Range situated at latitude $30^o35'$S and longitude $136^o31'$E.

3.1.3 ROCKET DATA

The X-ray detectors flown on Skylarks 1005 and 1207 functioned satisfactorily on the down leg part of the flight but were noisy on the up-leg. Unfortunately, the X-ray detectors flown on the Cockatoo vehicles were very noisy both on the up and down leg of the flight. These counters behaved as though under the atmospheric vacuum the filling gas of the counter leaked through the windows or other parts of the body of the counters from the filling pressure of 550 torr to a pressure of a few torr where the counters discharged under the applied high voltage of 1.8 KV. This behaviour was noted in some of the counters in the laboratory when they were prepared for flight. The preparation involved the filling and testing of the counters and then placing them under a vacuum of 10^{-2} torr for about half an hour. After this time, the counters were tested again and selected for flight. The same procedure was used to select the flight counters for the Cockatoo, the Skylark and Aerobee vehicles.

Of the two Cockatoo pairs of vehicles, the X-ray detectors on C4007 discharged while for C4009 the door came off at launch and the heat generated during flight burned the window of the proportional counters. For C4017 there was a malfunction in the second stage motor and the flight was abortive and again on C4018 the detectors discharged. On the second pair of the Cockatoo vehicles extra care was taken to ensure that the counters did not produce a leak during flight. In this case, the counters were placed under vacuum and tested several times but, again, the discharge repeated during flight. On the other hand, the same type of counters flown on the sun-stabilized vehicles functioned satisfactorily so that is was concluded that the erratic behaviour of the detectors flown on the Cockatoos was somehow related to the high spinning rates

and high initial launch acceleration of these vehicles and the stress imposed on the electrode structure of the counters. In fact, the resulting spinning rate of C4007 was 8.6 rev/sec, of C4009 8.4 rev/sec and C4018 11 rev/sec and the launch acceleration was about 100g as compared with about 15g of the large sun-stabilized vehicles.

The payload 1207, in addition to the X-ray detector, carried a three channel grazing incidence spectrometer which measured as a function of altitude the attenuation of solar E.U.V. radiation at three different wavelengths, namely, 304, 584 and 850 Å. Unfortunately, the channels that measured the HeI (584 Å) and HeII (304 Å) lines saturated during part of the flight while the other channel functioned well on both the up and down-leg.

In this chapter will be presented the analysis of the rocket data of the down-leg flights of the Skylarks 1005 and 1207 for the X-ray detectors and for the up and down-leg part of the flight for the 850 Å channel of the grazing incidence spectrometer. The data from the X-ray detector flown on the Aerobee will not be presented here.

3.2.1 METHOD OF ANALYSIS

As already mentioned in Chapter II, the attenuation of the solar radiation in the atmosphere follows the Beer-Lambert law which for monochromatic radiation of wavelength, λ, and zero solar zenith angle is expressed by equation (2.18). If this attenuation is measured with an instrument having a narrow spectral bandwidth, $\Delta\lambda$, and if the absorption cross-sections of the atmospheric species are constant in this spectral bandwidth, then for solar zenith angle, χ, less than about 85^{o}, equation (2.18) can be rewritten in the form:

$$I_{\lambda}(\Delta\lambda,h) = I_{o\lambda}(\Delta\lambda).\exp\left[-\sec\chi.\sum_{i}^{n}\sigma_{i\lambda}(\Delta\lambda).\int_{h}^{\infty}n_{i}(z)dz\right] \qquad (3.1)$$

where $I_{\lambda}(\Delta\lambda,h)$ and $I_{o\lambda}(\Delta\lambda)$ are the measured solar fluxes at a wavelength, λ, in the spectral band, $\Delta\lambda$, and at height, h, and at the top of the atmosphere, respectively, while $\sigma_{i\lambda}(\Delta\lambda)$ and $n_{i}(z)$ are, respectively, the absorption cross-section and number density of the i^{th} constituent of the atmosphere.

If the atmosphere is divided into shells separated by a distance, Δh, then, by differentiating the expression (3.1) with respect ot the height parameter, h, the total number density, $n_{T}(h)$, at a height, h, is given by:

$$n_{T}(h) = \Delta I_{\lambda}(\Delta\lambda,h)/\left[\bar{\sigma}_{eff}.\sec\chi.I_{\lambda}(\Delta\lambda,h).\Delta h\right] \qquad (3.2)$$

where $\Delta I_{\lambda}(\Delta\lambda,h)$ is the difference between the solar fluxes at height levels, h, and, $h + \Delta h$, and:

$$n_{T}(h) = \sum_{i}^{n}n_{i}(h) \qquad (3.3)$$

The mean weighted effective absorption cross-section, $\bar{\sigma}_{eff}(h)$, appearing in equation (3.2) is given by:

$$\bar{\sigma}_{eff}(h) = \frac{\int_{\lambda}^{\lambda+\Delta\lambda}\sigma_{eff}(\lambda,h).\varepsilon(\lambda).\phi(\lambda,h).d\lambda}{\int_{\lambda}^{\lambda+\Delta\lambda}\varepsilon(\lambda).\phi(\lambda,h).d\lambda} \qquad (3.4)$$

where the effective cross-section, $\sigma_{eff}(\lambda,h)$ is:

$$\sigma_{eff}(\lambda,h) = \sum_{1}^{n} {}_{i}\sigma_{i}(\lambda).n_{i}(h) / \sum_{1}^{n} {}_{i}n_{i}(h) \qquad (3.5)$$

which has to be calculated by using the number density data, $n_i(h)$, of the atmospheric species from a reference model of the upper atmosphere such as CIRA (1972), and $\varepsilon(\lambda)$ is the efficiency of the instrument while:

$$\phi(\lambda,h) = \phi_o(\lambda).\exp(-\sec\chi.\sum_{1}^{n} {}_{i}\sigma_{i}(\lambda).\int_{h}^{\infty} n_i(z)dz) \qquad (3.6)$$

The symbol, $\phi_o(\lambda)$, represents the solar flux incident at the top of the atmosphere of wavelengths within the instrument's spectral band. The flux, $\phi_o(\lambda)$, may not necessarily be equal to the measured flux, $I_{o\lambda}(\Delta\lambda)$, which represents the average flux over the band width, $\Delta\lambda$. The two fluxes are the same only if the instrument measures nearly monochromatic radiation as in the case of the grazing incidence spectrometer.

In equations (3.1) and (3.2) by approximating the optical path depth factor as $\sec\chi$, the values of the calculated number densities, $n_T(h)$, will be in error by no more than 1% for $\chi < 73^\circ$ which becomes 5% at $\chi = 82^\circ$ and 10% at $\chi = 85^\circ$ (Weeks and Smith (1968)).

Having computed the values of $\overline{\sigma}_{eff}(h)$ as a function of the height of interest, the problem of converting the rocket data into number densities becomes merely a matter of numerically differentiating the profile curve of the measured attenuation of the solar radiation, i.e., it is a matter of solving equation (3.2).

In this work two different methods have been used in the reduction of the rocket raw data. One method simply deals with the least square fit of a high order polynomial to the raw data and then differentiating the resulting polynomial to calculate the number density profile with the aid of equa-

tion (3.2). The second method which has been suggested to the author by Dr R. C. Schaeffer will be described in some detail henceforth.

This method involves fitting a gaussian distribution as a weight factor to the rocket raw data and to create new data points at constant height intervals. Hence, if $I_{i\lambda}(\Delta\lambda, z_i)$ is the measured solar radiation at a height, z_i, then the new datum point at a height, z_n, is:

$$I_{n\lambda}(\Delta\lambda, z_n) = \sum_{1}^{k} {}_i\omega_i \cdot I_{i\lambda}(\Delta\lambda, z_i) / \sum_{1}^{k} {}_i\omega_i \qquad (3.7)$$

where ω_i is the weight factor which is of the form:

$$\omega_i = \exp(-x_i^2) \qquad (3.8)$$

where

$$x_i = (z_n - z_i)/dz \qquad (3.9)$$

and dz being the "weight criteria".

In the present work the weight criteria, dz, is set such that if z_n and z_{n+1} are the heights at which two adjacent datum points are created and indicating with:

$$\Delta z_o = z_{n+1} - z_n \qquad (3.10)$$

then, at a height half way between z_n and z_{n+1}, the weight factor (fig 3.1) is set such that $\omega_i = 0.5$. It follows, then, that:

$$\ell n 0.5 = x_i^2 = -\Delta z_o^2 / 4 d_z^2 \qquad (3.11)$$

so that

$$dz = 0.6 \Delta z_o \qquad (3.12)$$

Thus, if $\Delta z_o = 500m$

$$dz = 300m \qquad (3.13)$$

and

$$\omega_i = \exp\left[-((z_n - z_i)/300)^2\right] \qquad (3.14)$$

where z_n and z_{n+1} are both in meters.

Equation (3.2) can then be written in the form

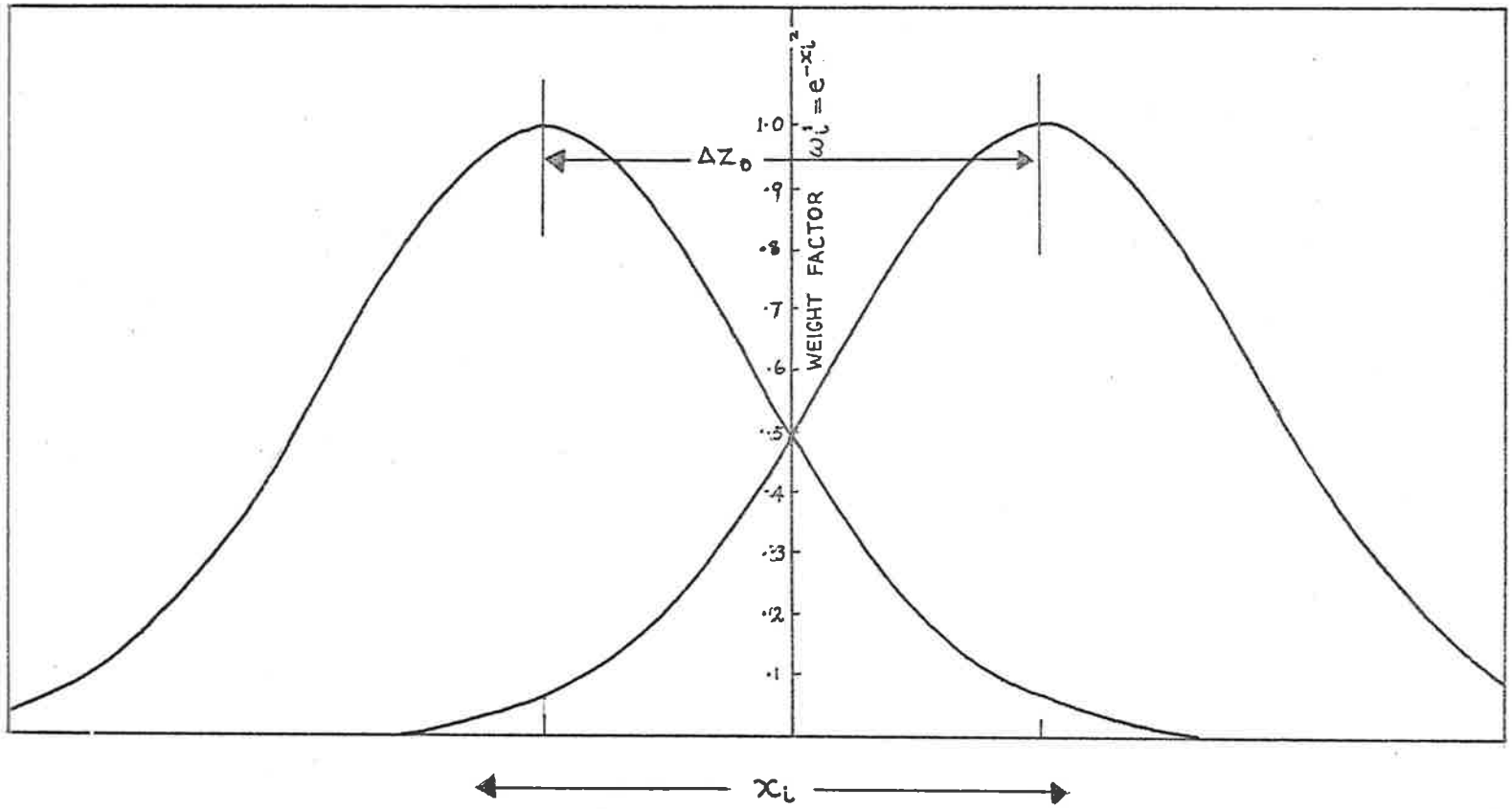

FIG. 3·1: WEIGHT FACTOR ω_i AS A FUNCTION OF x_i

$$n_T(h) = g(h)/\left[\bar{\sigma}_{eff}(h).\sec\chi.I_\lambda(\Delta\lambda,h)\right] \qquad (3.15)$$

where the weighted gradient, $g(h)$, is given by:

$$g(h) = \sum_1^\ell {}_n\omega_n' . g_n(h) / \sum_1^\ell {}_n\omega_n' \qquad (3.16)$$

and $I_\lambda(\Delta\lambda,h)$ is the created datum point at a height, h. The gradient, $g_n(h)$, appearing in equation (3.16) is given by:

$$g_n(h) = \left[I_\lambda(\Delta\lambda,h) - I_{n\lambda}(\Delta\lambda,z_n)\right]/(h - z_n) \qquad (3.17)$$

while the parameter, ω_n' (figure 3.2), is the differentiated weight factor of ω_i, i.e.,

$$\omega_n' = 2x_n.\exp(-x_n^2) \qquad (3.18)$$

In this case:

$$x_n = (h - z_n)/dh = m.\Delta z_o/dh \qquad (3.19)$$

where dh is termed as the "height resolution" and m, which is an integer, indicates the position of the n^{th} datum point from the datum point in consideration.

The maximum value of ω_n' occurs when:

$$dh = \sqrt{2}m.\Delta z_o \qquad (3.20)$$

so that for m = 1 the maximum weight in calculating $g(h)$ and hence $n_T(h)$ is given to the two adjacent points to the datum point in consideration while for m = 2 the next two points have the maximum weight. Thus, by varying the value of m, dh (the height resolution) varies and hence the amount of smoothness introduced in the final data of the number densities. The parameter, m, then represents the "degree of smoothness" of the density data.

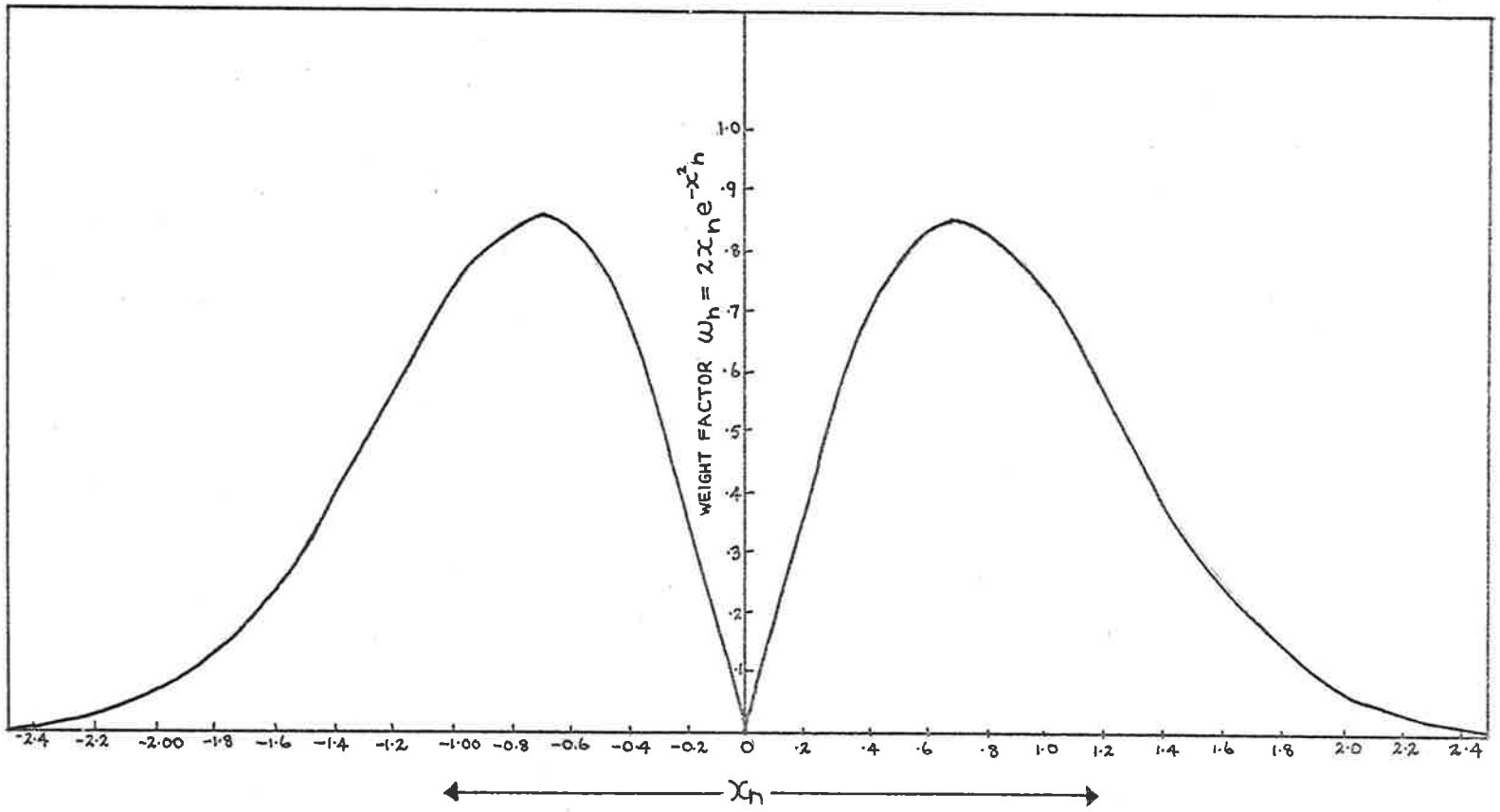

FIG 3·2: WEIGHT FACTOR ω_n' AS A FUNCTION OF x_n

3.2.2 X-RAY ABSORPTION CROSS-SECTIONS

In order to calculate the density of the neutral upper atmosphere from the X-ray data, equation (3.2) has to be used. Thus, it becomes necessary to determine the value of the mean weighted effective absorption cross-section, $\bar{\sigma}_{eff}(h)$, as a function of altitude in the altitude range of interest. The X-ray detectors which have been flown on the two Skylarks and on the Aerobee vehicles had a spectral band width response of about 20 Å. However, in this wavelength band the absorption cross-sections of the atmospheric constituents and the solar X-ray emission fluxes are not constant so that $\bar{\sigma}_{eff}(h)$ has to be calculated using equation (3.4). But, before $\bar{\sigma}_{eff}(h)$ can be computed the parameters $\sigma_{eff}(\lambda,h)$, $\varepsilon(\lambda)$ and $\phi(\lambda,h)$ have to be known.

The absorption of X-rays in the upper atmosphere is mainly due to the major gas species which at the height of interest are N_2, O_2 and O. Thus, equation (3.5) can be written in the form:

$$\sigma_{eff}(\lambda,h) = \frac{\sigma_\lambda(N_2).n(N_2) + \sigma_\lambda(O_2).n(O_2) + \sigma_\lambda(O).n(O)}{n(N_2) + n(O_2) + n(O)} \qquad (3.2)$$

where $\sigma_\lambda(N_2)$, $\sigma_\lambda(O_2)$, $\sigma_\lambda(O)$ and $n(N_2)$, $n(O_2)$ and $n(O)$ are, respectively, the absorption cross-sections and densities of the constituents N_2, O_2 and O. The values of $n(N_2)$, $n(O_2)$ and $n(O)$ used in this work are from the mean CIRA (1972) while $\sigma_\lambda(N_2)$ and $\sigma_\lambda(O_2)$ are from the tabulated data of Henke and Elgin (1970) and the absorption cross-section of atomic oxygen is taken as:

$$\sigma_\lambda(O) = \tfrac{1}{2}.\sigma_\lambda(O_2) \qquad (3.32)$$

The efficiency, $\varepsilon(\lambda)$, of the X-ray detectors is shown in fig 2.5 on a linear-linear scale. From this figure it is seen that the detectors respond to X-rays of wavelengths

from less than 1 to greater than 17 Å and in the spectral region from about 44 to 62 Å. The X-rays in the region from 44 to 62 Å have been discriminated electronically during the flight of the vehicles so that only X-rays in the spectral region from about 1 to 20 Å have to be considered.

The large spectral response band width of the X-ray detectors presents certain difficulties in the reduction of the X-ray data. This is because the solar X-ray fluxes vary not only in time, but also by different amounts in the different parts of the X-ray spectral region (see section 1.2) and, as a consequence, at any time the spectral solar X-ray flux, $I_o(\lambda)$, incident at the top of the atmosphere is not known. Solar X-ray fluxes have been measured extensively with rocket and satellite borne instruments but, mainly, by broad band detectors such as proportional or Geiger counters. High resolution spectrometric measurements of the solar X-ray fluxes have been made utilizing crystal spectrometers but, unfortunately, only in a limited X-ray spectral region. For example, Wolff (1974) using a rocket borne crystal spectrometer measured the solar spectra in the 1.8 to 5.3 Å region under quiescent conditions. Thus, in calculating $\overline{\sigma}_{eff}(h)$, for the solar X-ray flux, $\phi_o(\lambda)$, which appear in equation (3.6), theoretical fluxes calculated by Mewe (1972) have been used.

Mewe (1972) has calculated the lines and continuum solar X-ray emission fluxes from 1 to 60 Å at an interval of 1 Å for different solar electron temperatures. These fluxes for a temperature of 5×10^6 °K are shown in fig 3.3.

In this work the absorption cross-sections, $\overline{\sigma}_{eff}(h)$, have been calculated as a function of height for X-ray fluxes corresponding to different solar electron temperatures and are shown in fig 3.4. Using the determined values of $\overline{\sigma}_{eff}(h)$ the total number density have, then, been computed from the X-ray

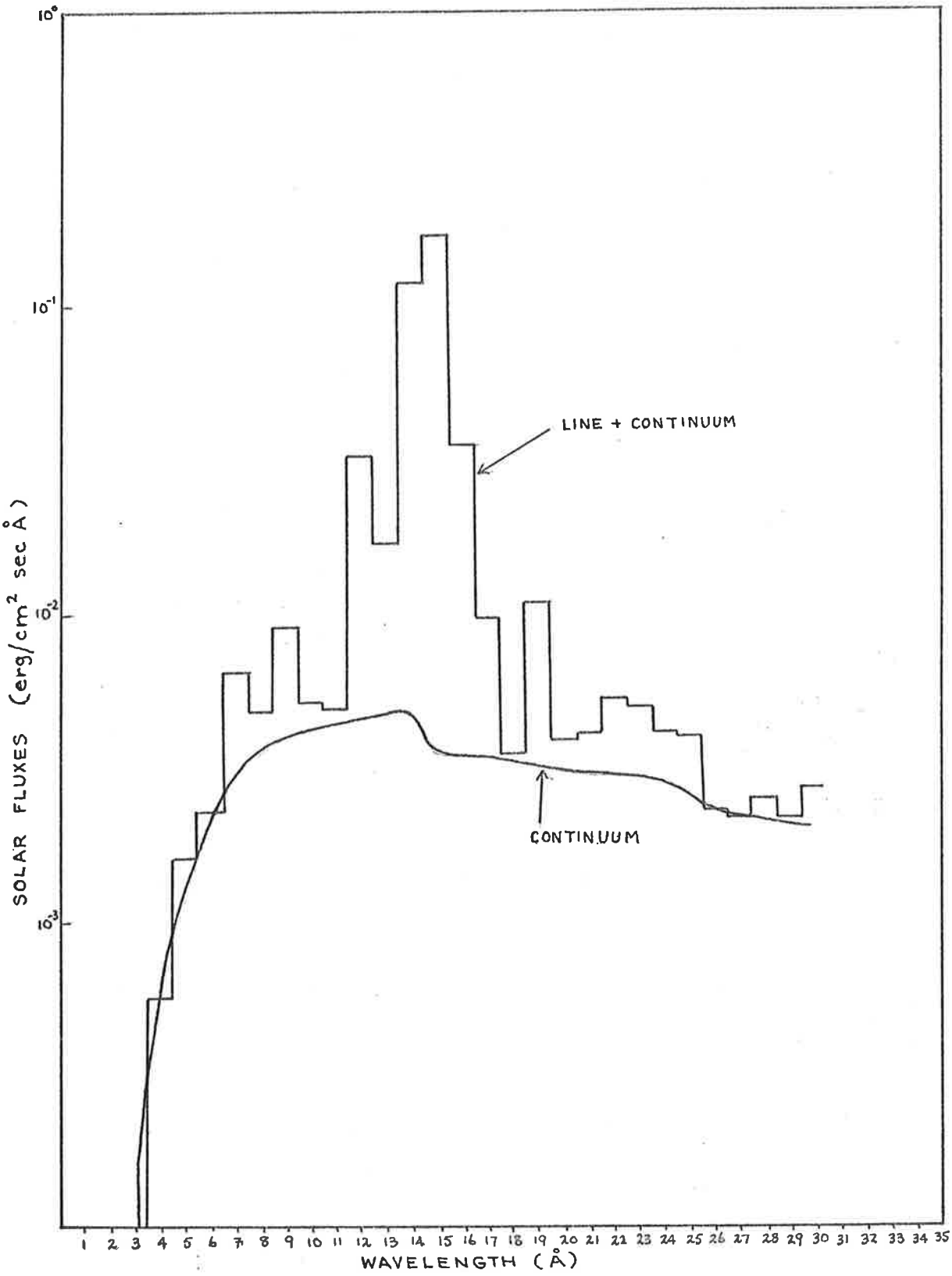

FIG 3·3: CONTINUUM AND LINE EMISSION OF X-RAY FLUXES FOR A SOLAR ELECTRON TEMPERATURE OF 5×10^6 °K (After Mewe (1972)).

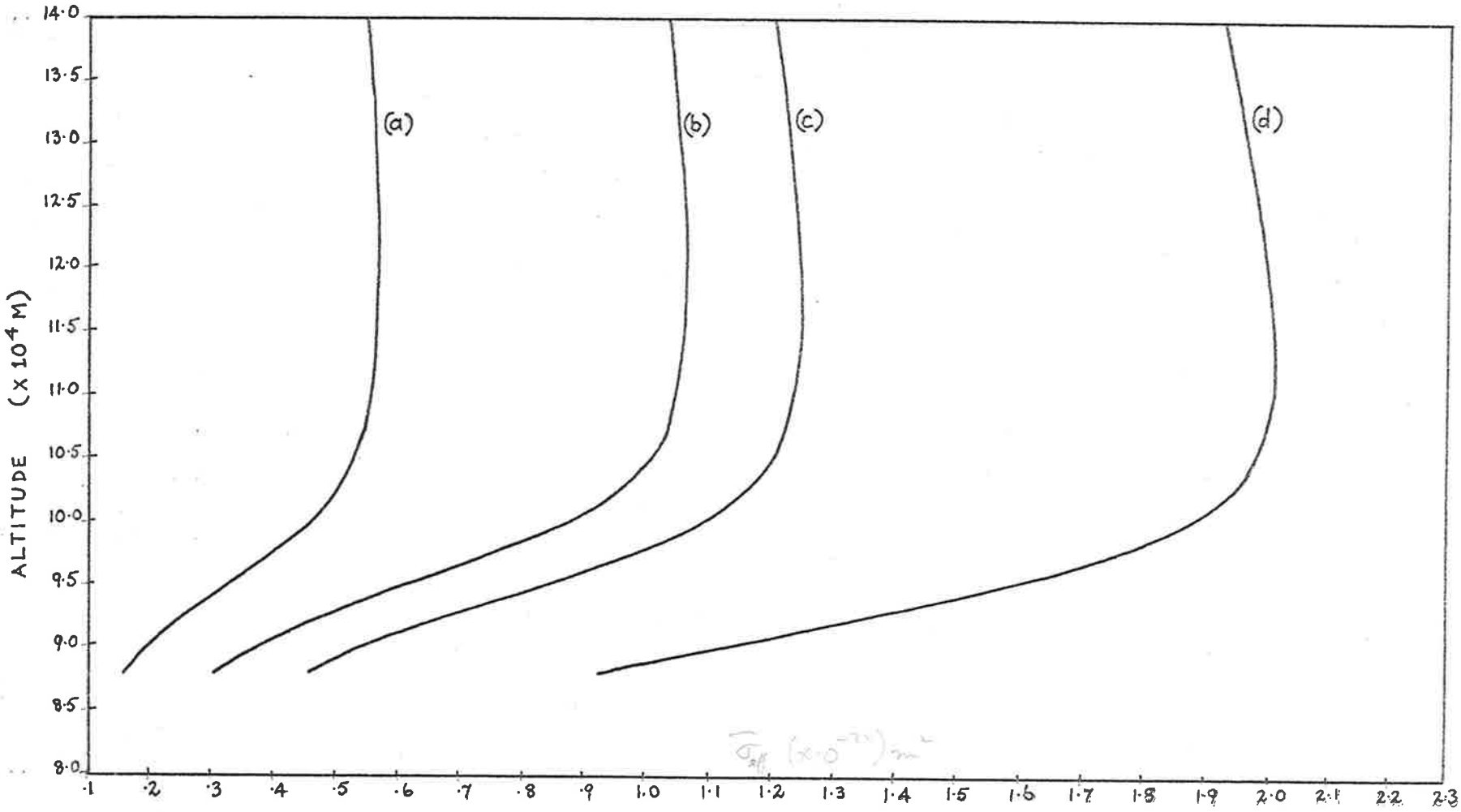

FIG 3·4: THE WEIGHTED EFFECTIVE ABSORPTION CROSS-SECTIONS, $\bar{\sigma}_{eff}$, AS A FUNCTION OF ALTITUDE FOR THE SOLAR X-RAY FLUXES AT THE ELECTRON TEMPERATURES.
(a) $T = 10 \times 10^6$ °K (b) $T = 5 \times 10^6$ °K (c) $T = 3 \times 10^6$ °K (d) $T = 1 \times 10^6$ °K.

fluxes measured with the detectors on the two Skylark flights. It has been found that the cross-sections for which the resulting number densities compared favourably with those of the mean CIRA (1972) reference atmospheric model were those determined with the use of $\bar{\sigma}_{eff}(h)$ calculated for the electron temperature of 5×10^6 ^oK and 3×10^6 ^oK for the solar X-ray fluxes measured furing the flight of Skylark 1207 and 1005 vehicles, respectively. The 1207 flight took place when the sun was fairly active in which the geomagnetic planetary three-hour-range index, K_p, was 5^- while during the Skylark 1005 flight the sun was fairly quiet, K_p being only 2^-. Thus, there was an enhancement of X-ray fluxes during the time of flight of Skylark 1207 and the enhancement was not constant across the instrumental spectral band region, but was larger at shorter wavelengths. For this reason the data from the Skylark 1207 give a better result when the absorption cross-section calculated for a solar electron temperature of 5×10^6 ^oK is used as compared with that of 3×10^6 ^oK.

The solar X-ray emission fluxes have also been simulated by those emitted by a multitemperature model of the sun, but the resulting densities did not compare satisfactorily with those of the mean CIRA (1972) so that this model was disregarded.

3.2.3 X-RAY DATA ANALYSIS

The gaussian fit method discussed in section (3.2.1) has been applied to calculate the total number density as a function of height from the X-ray raw data of both Skylark 1005 and 1207 flights. In both cases the new data points were created at height intervals of:

$$\Delta z_o = 500 \text{ meters} \qquad (3.23)$$

and the total number densities were calculated for a degree of smoothness of m = 3, 4 and 5 for Skylark 1005 data and for m = 3, 4, 5 and 6 for those of Skylark 1207. These density data are shown with the mean CIRA (1972) data in fig 3.5 for the Skylark 1005 flight and in fig 3.6 for the Skylark 1207 flight and for degree of smoothness of the data of m = 3, 4 and 5.

In the case of the X-ray data of the Skylark 1207 flight the total number densities have also been determined by differentiation of a 6^{th} order polynomial which has been least square fit to the X-ray raw data. The number densities have been calculated as discussed in section (3.2.1) and shown in fig 3.7. In this figure are presented also the total number density determined with a gaussian fit to the raw data of degree of smoothness of m = 6 and the mean CIRA (1972) for comparison.

The density data from the least square polynomial fit well with the gaussian fit of m = 6, although the gaussian fit shows slightly more structure. The gaussian fit appears to be a superior method of data reduction than the polynomial fit so that for the rest of this chapter the density data determined with the method of least square polynomial fit to the raw data will not be presented.

To ensure that the wave-like structure in the density data of the 1207 flight which are shown in figures 3.6 and

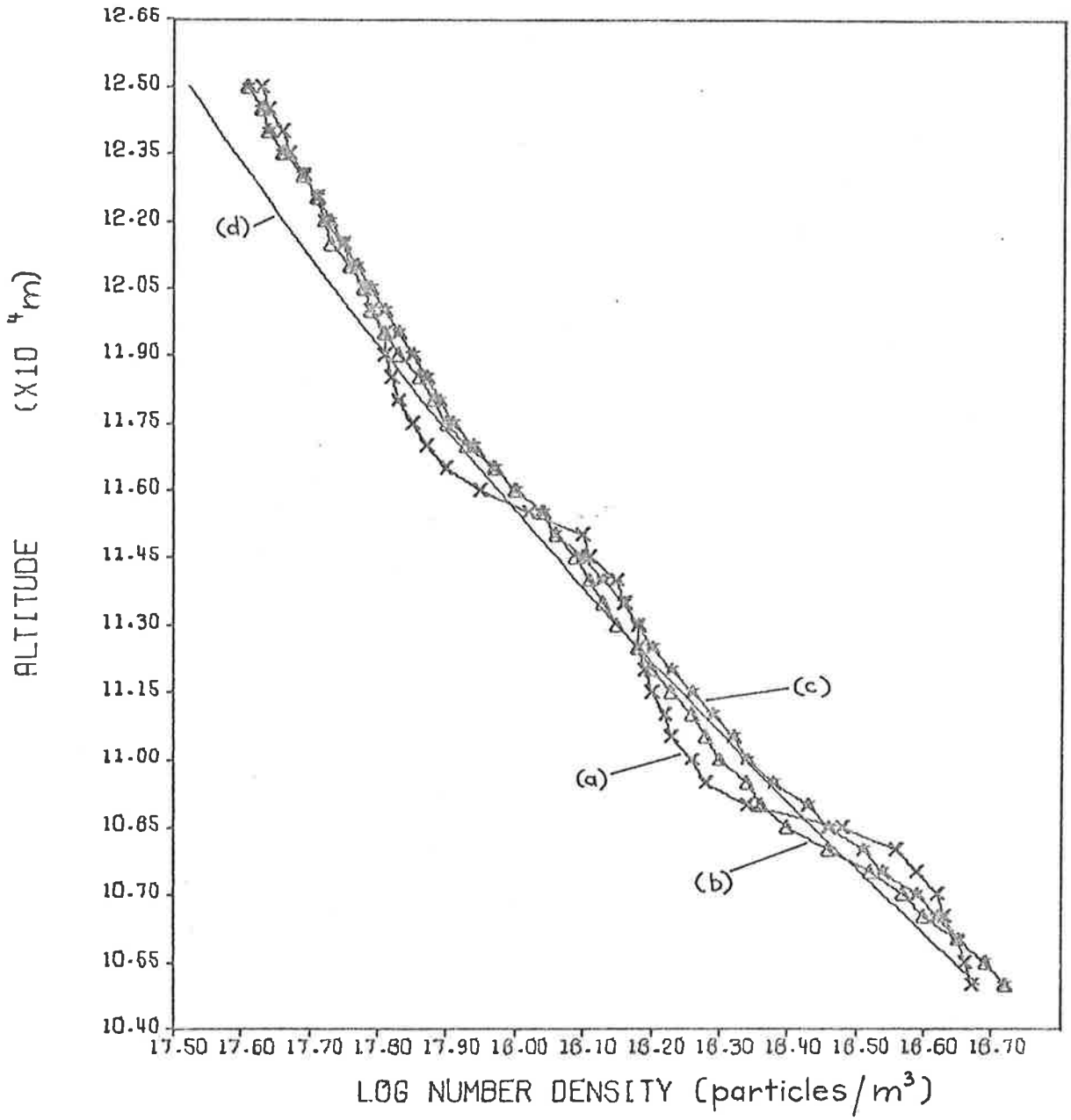

FIG 3.5: TOTAL NUMBER DENSITY AS A FUNCTION OF ALTITUDE DETERMINED FROM THE SKYLARK 1005 X-RAY DATA FOR A DEGREE OF SMOOTHNESS:
(a) m = 3
(b) m = 4
(c) m = 5
and (d) mean CIRA (1972).

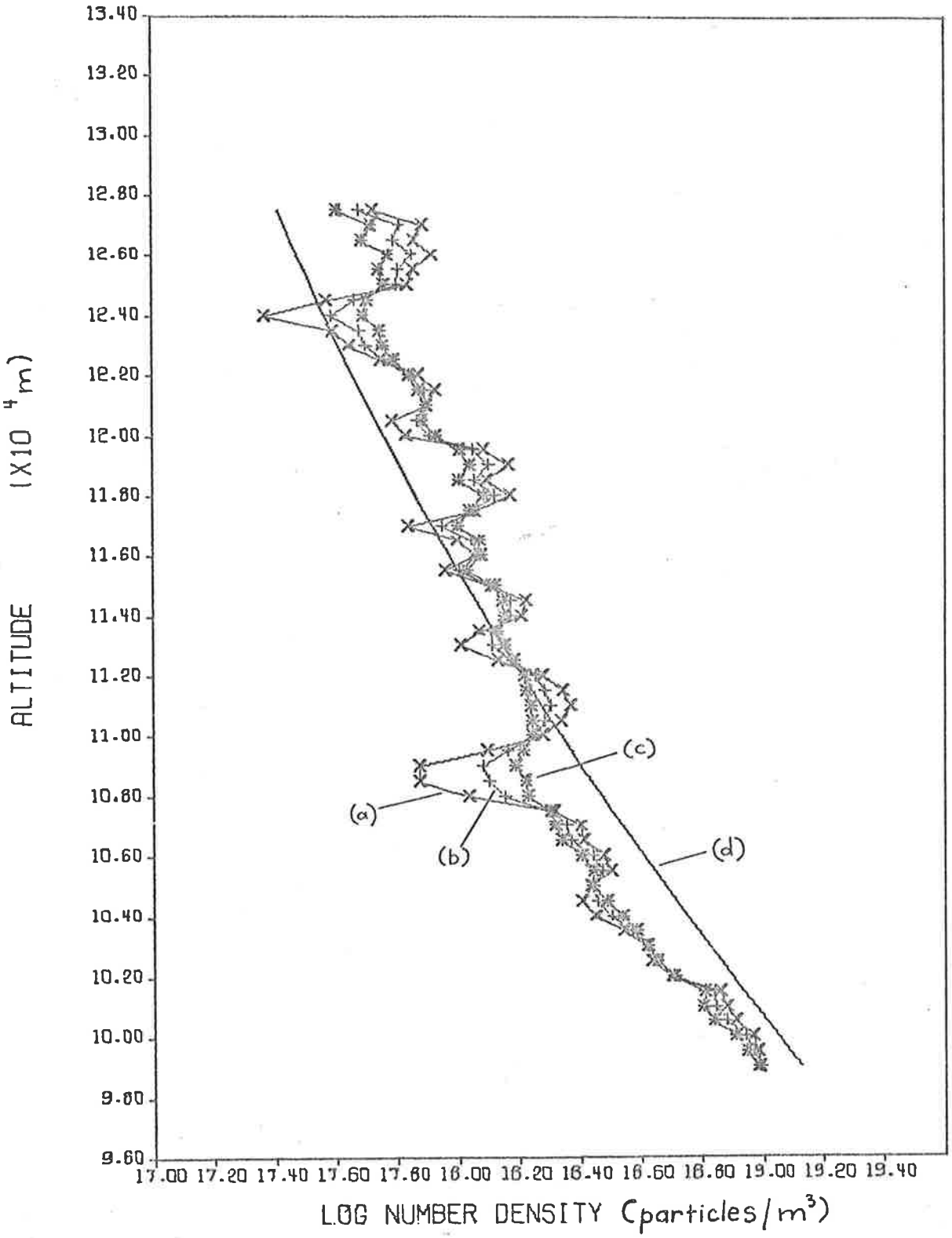

FIG 3.6: TOTAL NUMBER DENSITY AS A FUNCTION OF ALTITUDE FOR THE DEGREE OF SMOOTHNESS OF THE SKYLARK'S 1207 X-RAY DATA OF (a) m = 3
(b) m = 4
(c) m = 5
(d) CIRA (1972)

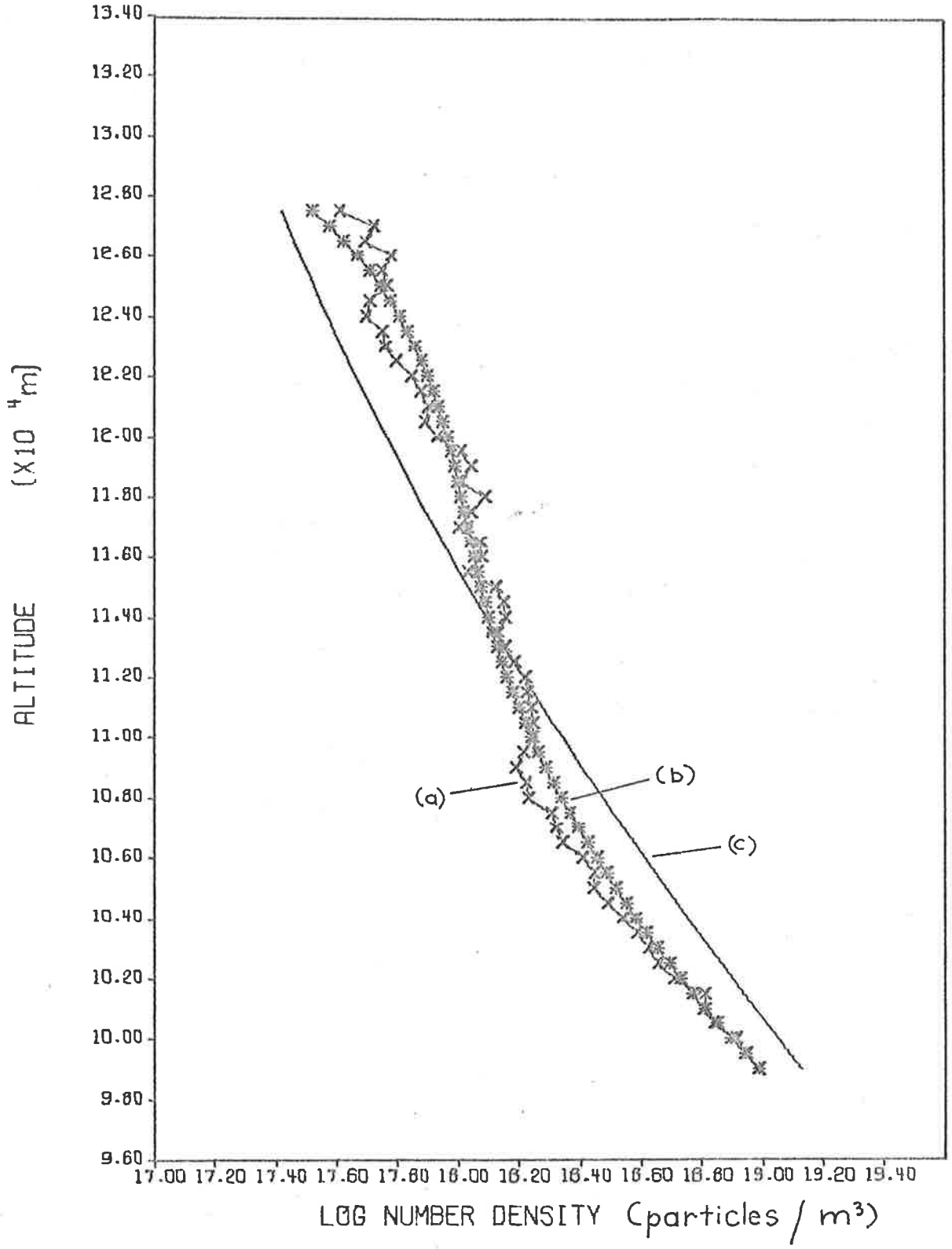

FIG 3·7: TOTAL NUMBER DENSITY (SKYLARK 1207):
(a) m = 6
(b) polynomial fit
(c) mean CIRA (1972)

3.7 is not due to an artefact introduced by the method of analysis of the raw data, equation (3.2) has been used in reverse to create from the calculated density data, $n_T(h)$, the profile of the X-ray flux, $I_\lambda(\Delta\lambda,h)$, being attenuated in the upper atmosphere. Equation (3.2), then, becomes:

$$I_\lambda(\Delta\lambda,h) = I_\lambda(\Delta\lambda,h+\Delta h)/(\bar{\sigma}_{eff}(h).\sec\chi.n_T(h).\Delta h+1) \qquad (3.24)$$

where $I_\lambda(\Delta\lambda,h+\Delta h)$ is the created solar flux at a height level of $h+\Delta h$.

The profile of the integrated X-ray flux has been calculated from the total number density, $n_T(h)$, of a gaussian fit of m = 6 and from the density data of the mean CIRA (1972). These integrated fluxes are shown in figure 3.8 in which the X-ray raw data fluxes are also presented for comparison. From this figure it can be seen that the integrated flux calculated from the gaussian fit density data fit well with the X-ray raw data while the flux determined from the density data of CIRA (1972) does not.

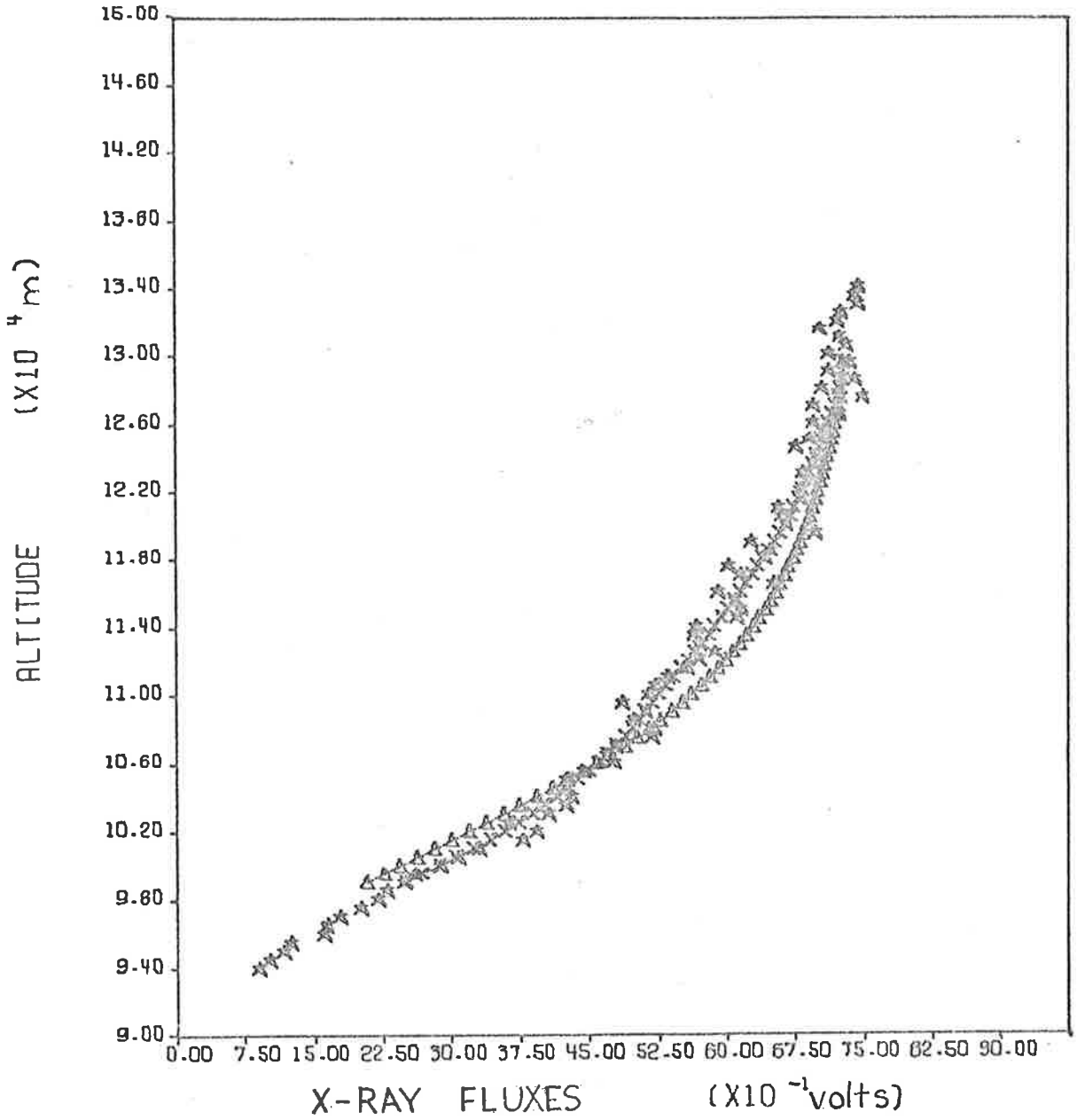

FIG 3·8: SKYLARK 120† (☆) X-RAY RAW DATA, (+++) INTEGRATED FLUX AND (Δ–Δ) INTEGRATED FLUX FROM MEAN CIRA (1972) DENSITY DATA

3.2.4 E.U.V. DATA REDUCTION

In the case of the grazing incidence spectrometer the spectral bandwidth of the instrument for the solar radiation of wavelength 850 Å was only about 2 Å so that from equation (3.4) it is reasonable to assume that:

$$\overline{\sigma}_{eff}(h) = \sigma_{eff}(h) \tag{3.25}$$

Furthermore, the absorption of the solar radiation is mainly due to the major atmospheric constituents which in the height of interest are principally N_2, O and O_2. Thus:

$$n_T = n(N_2) + n(O) + n(O_2) \tag{3.26}$$

and hence:

$$\sigma_{eff} = (\sigma(N_2).n(N_2) + \sigma(O).n(O) + \sigma(O_2).n(O_2))/n_T \tag{3.27}$$

For the radiation of wavelength of 850 Å the values of the absorption cross-sections used are those tabulated by Stolarski and Johnson (1972) and are:

$$\begin{aligned} \sigma(N_2) &= 7.5\times10^{-22}\ m^2 \\ \sigma(O_2) &= 9.3\times10^{-22}\ m^2 \\ \sigma(O) &= 1.8\times10^{-22}\ m^2 \end{aligned} \tag{3.28}$$

while the number densities of N_2, O and O_2 used are those from the tabulated mean CIRA (1972) reference atmospheric model. The calculated effective absorption cross-section, $\sigma_{eff}(h)$, as a function of altitude is shown in fig 3.9.

The method of data analysis used is that of the gaussian fit in which the new data points are created every 500 meters. The total number densities have been calculated for both the upleg and downleg part of the flight of the Skylark 1207 vehicle and for different degrees of smoothness. The total density profiles so calculated are shown in fig 3.10 for the upleg part of the flight and in fig 3.11 for the downleg. In

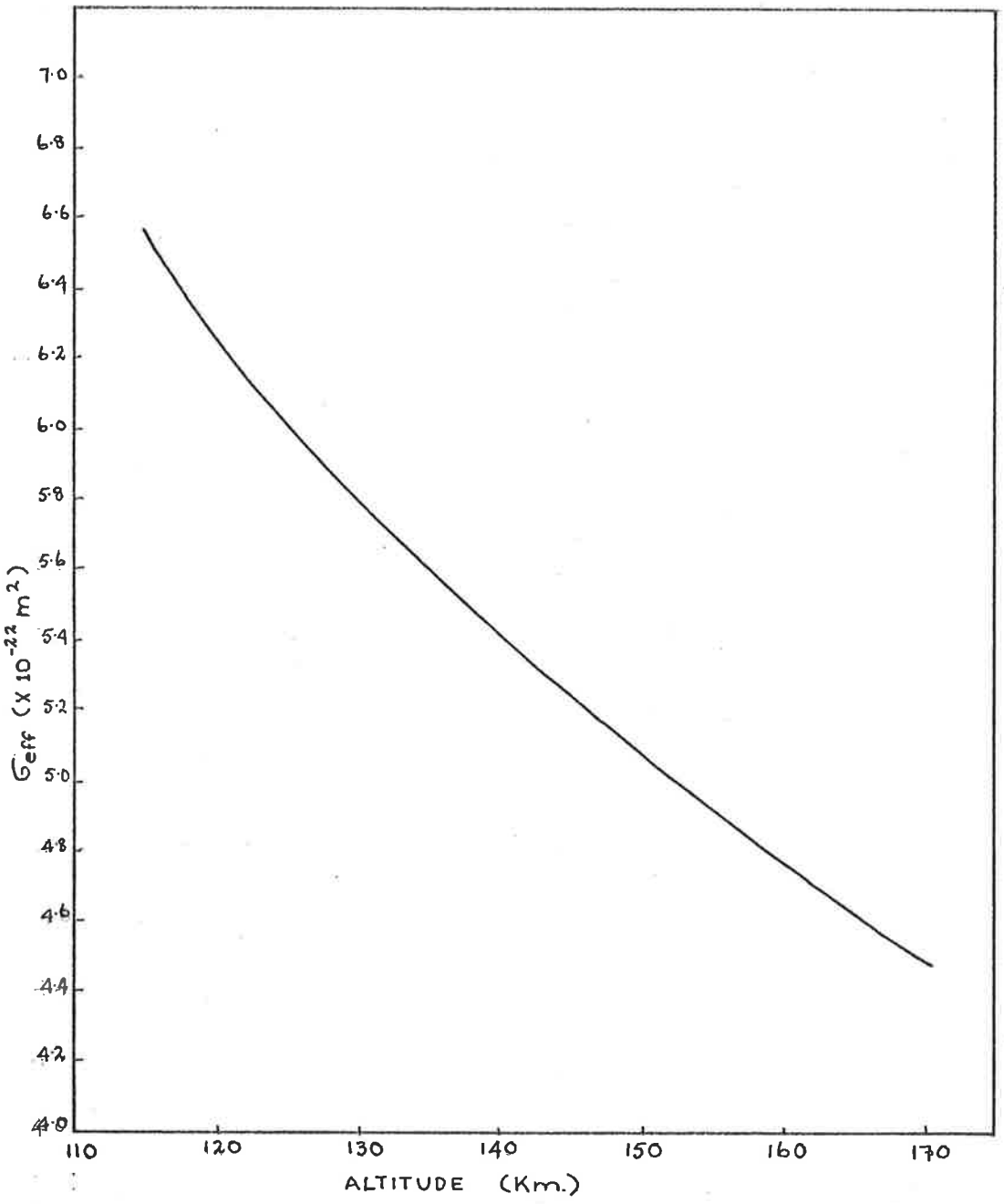

FIG 3·9 : EFFECTIVE ABSORPTION CROSS-SECTION AS A FUNCTION OF ALTITUDE FOR 850 Å RADIATION.

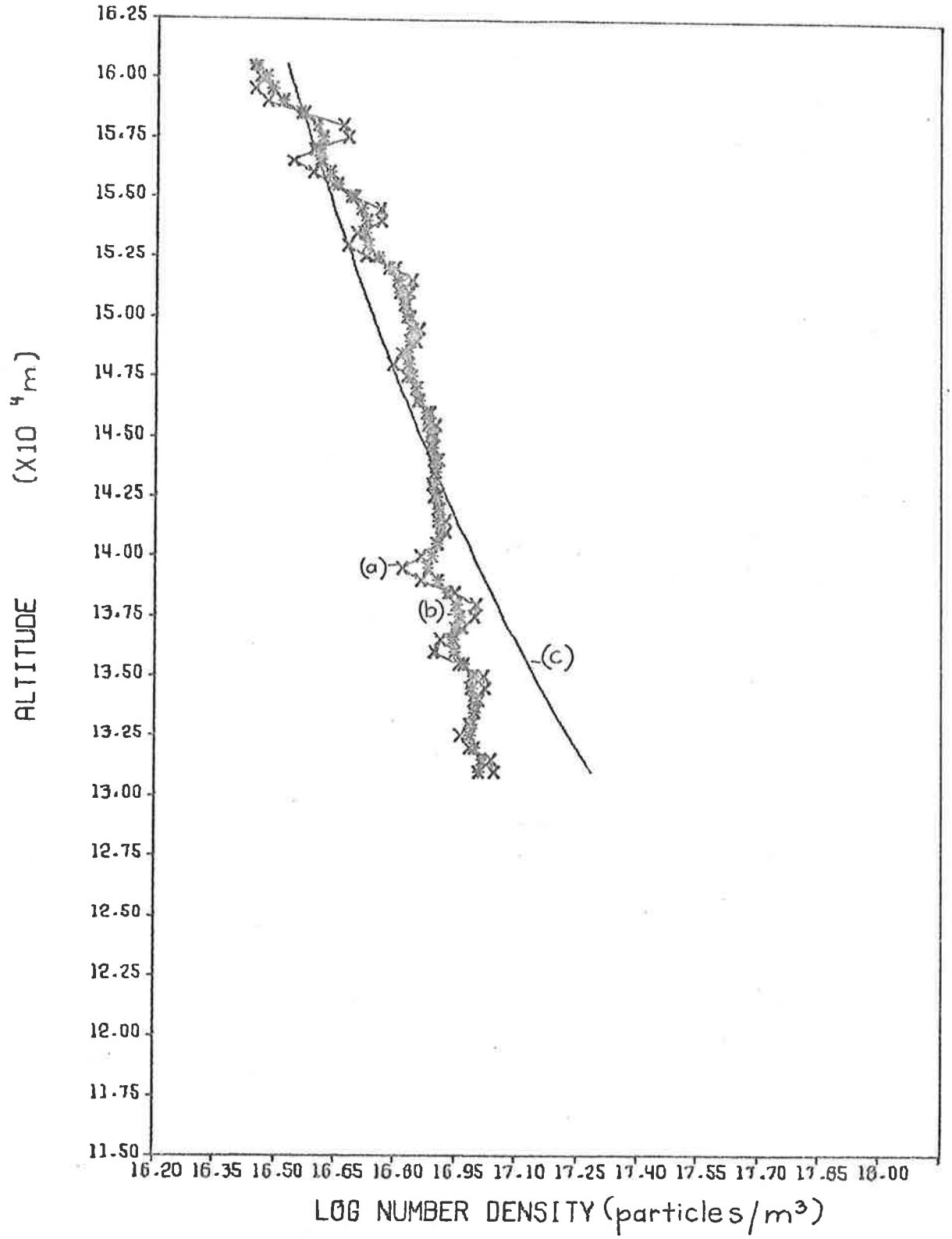

FIG 3·10: TOTAL NUMBER DENSITY FROM 850 Å DATA (UPLEG):
(a) $m = 2$
(b) $m = 4$
and (c) mean CIRA (1972)

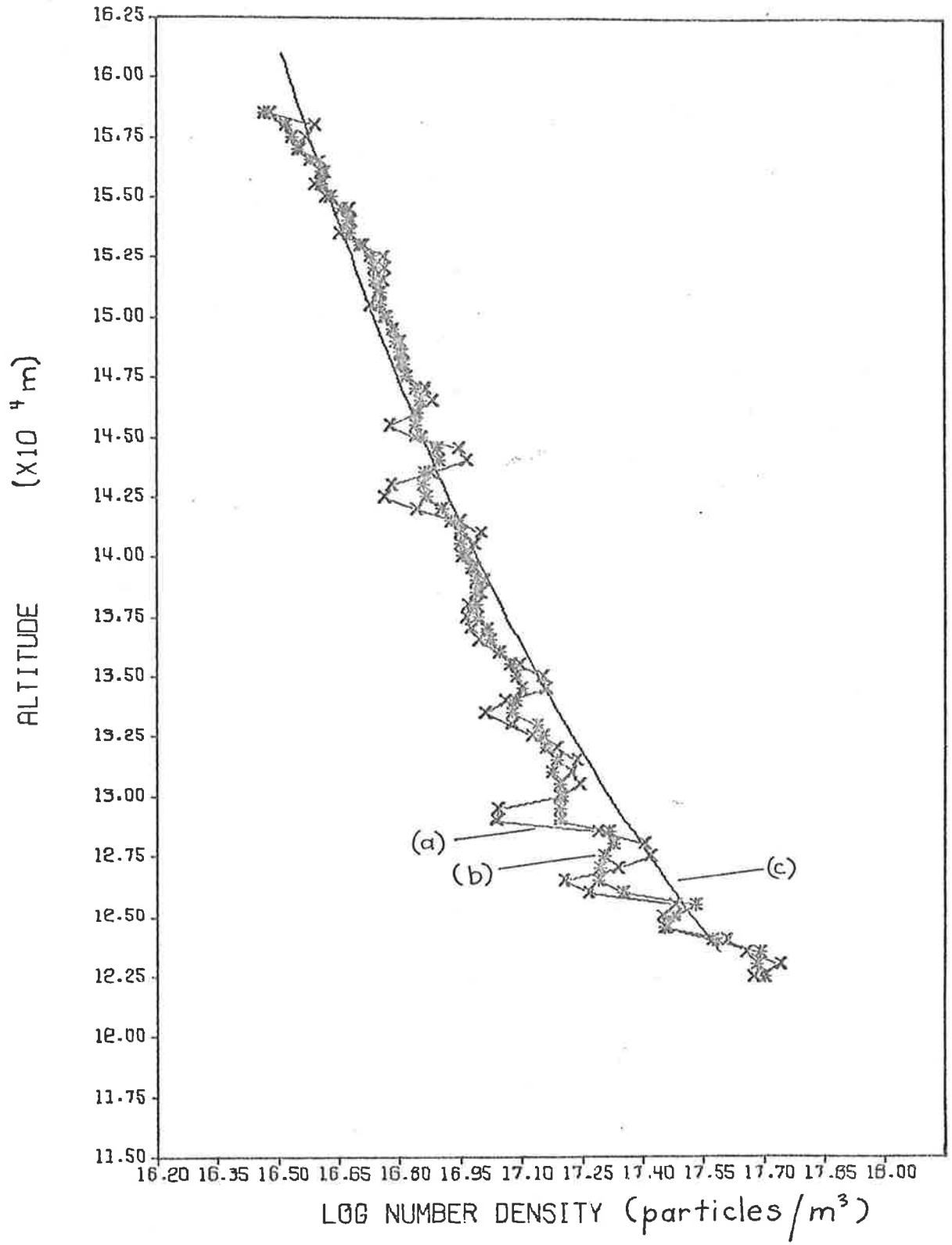

FIG 3·11: TOTAL NUMBER DENSITY FROM 850 Å DATA (DOWNLEG)
(a) m = 2
(b) m = 4
and (c) mean CIRA (1972)

these figures are presented the density profiles for the degree of smoothness of m = 2 and m = 4 only of the gaussian fit and the mean CIRA (1972) densities for comparison.

As in the previous section, to check that the wave-like structure of the total density profiles of figures 3.10 and 3.11 are not due to the method of analysis equation (3.24) is used to determine the solar flux profiles from the down-leg density profile with m = 4 and from the mean CIRA (1972) densities. The flux profiles are shown in fig 3.12.

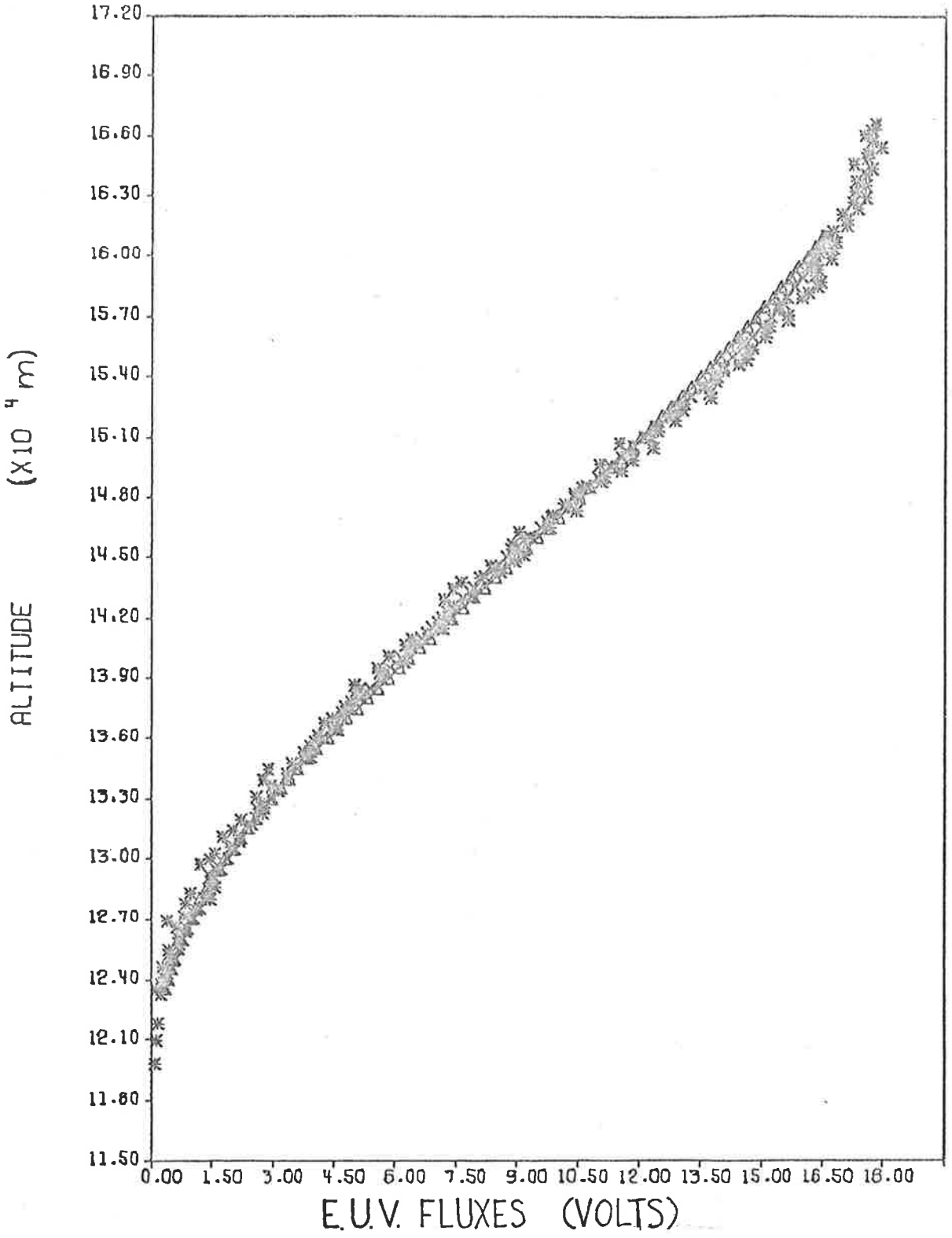

FIG 3·12: DOWNLEG (✳) 850 Å RAW DATA, (++) INTEGRATED FLUX, (△—△) INTEGRATED FLUX FROM MEAN CIRA (1972) DENSITY DATA.

3.2.5 DISCUSSION OF THE DENSITY RESULTS

The total number density data determined from the X-ray fluxes measured on 1005 flight, and which are shown in fig 3.5, agree well with the mean CIRA (1972) densities for altitudes less than about 119 Km. Above this height the measured densities deviate from those of CIRA (1972) and this is due to the fact that above about 120 Km heights for small solar zenith angles ($<60^{o}$) and for X-rays in the spectral band 1 - 20 $\mathring{A}$ the atmosphere becomes optically thin, i.e., the decrease in the attenuation coefficient with height is very small. A similar effect is shown in fig 3.13 in the altitude region between about 120 and 129 Km for the total densities determined from the X-ray data of the 1207 flight.

In the case of the 1207 flight the general profiles of the density data determined from the X-ray fluxes (fig 3.6) and from the E.U.V. fluxes (fig 3.10 and 3.11) agree satisfactorily with the mean CIRA (1972) density profile but are oscillatory in nature. The oscillatory structure is best seen in fig 3.13 in which are presented the measured densities for both the up and downleg parts of the flight and for m = 5. The wave-like structure in the present results is not introduced by the method of analysis (see sections 3.2.3 and 3.2.4) and cannot be instrumental because of the agreement in the positions of the density bulges which have been measured by two different types of instruments (X-ray and E.U.V.) and on the up and downleg of the flight. Furthermore, wave perturbations in the density profiles have been observed by a number of experimenters such as Faire et al (1970, 1973), Subbaraya et al (1972) and Weeks (1974), although their observations were confined mainly to altitudes less than about 110 Km.

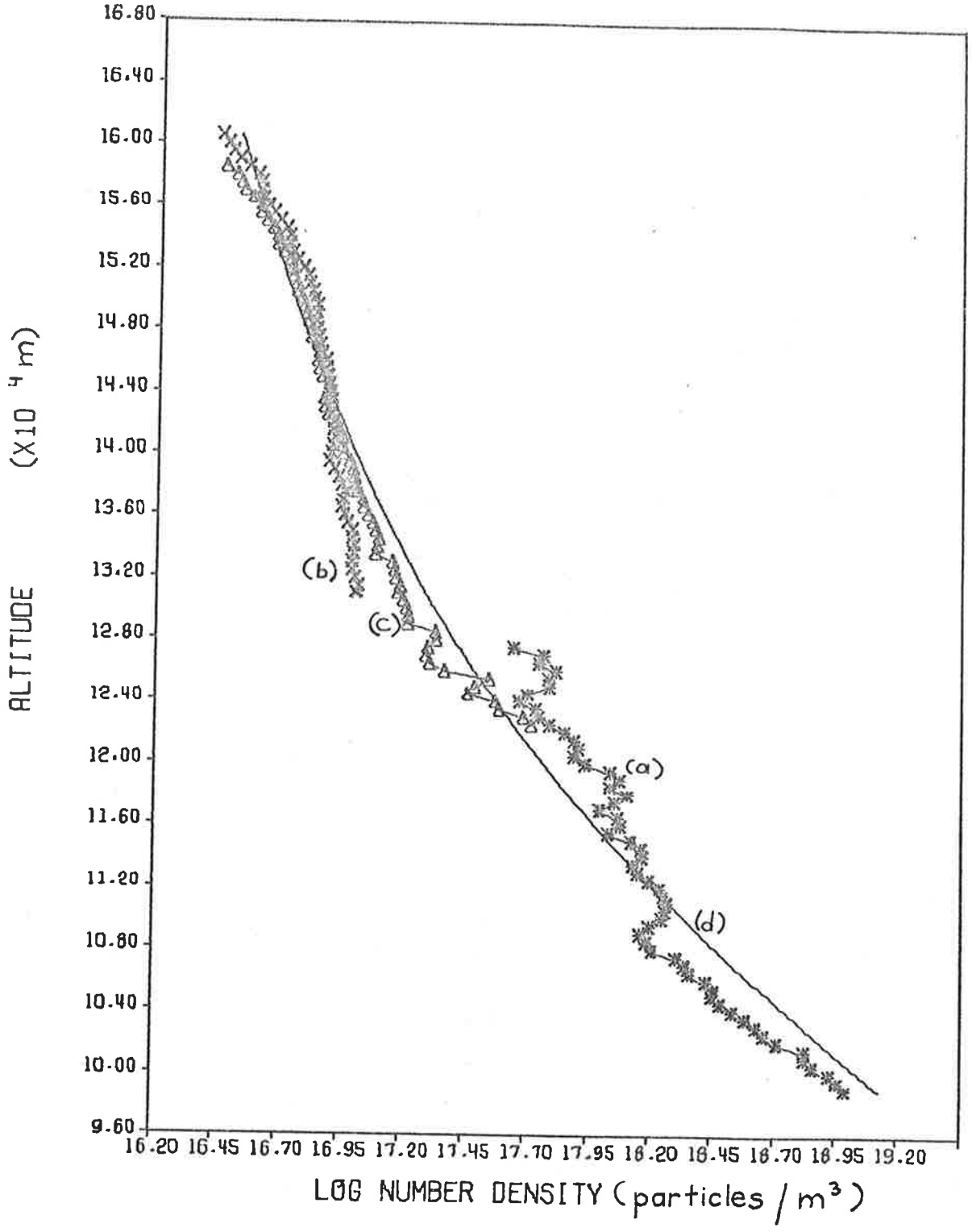

FIG 3·13: TOTAL DENSITY DETERMINED FROM:
(a) X-RAY DATA (DOWNLEG)
(b) E.U.V. DATA (UPLEG)
(c) E.U.V. DATA (DOWNLEG)
and (d) mean CIRA (1972).

The percentage departure of the present results from the mean CIRA (1972) data (fig 3.14) indicate that the wavelength of the oscillations in the density profiles has a magnitude of about 28 Km at low altitudes (<130 Km) but increasing to about 40 Km for altitudes higher than 140 Km, and the amplitude of the oscillations are larger on the upleg than on the downleg. This trend in which the wavelength of the oscillations increase with height has also been observed by Zimmerman and Marcos (1967). Furthermore, the value of the wavelength, 28 Km, of the wavelike fluctuations of the present results agree favourably with the 30 Km value determined by Rosenberg et al (1973) for the same heights, i.e., for altitudes less than about 125 Km.

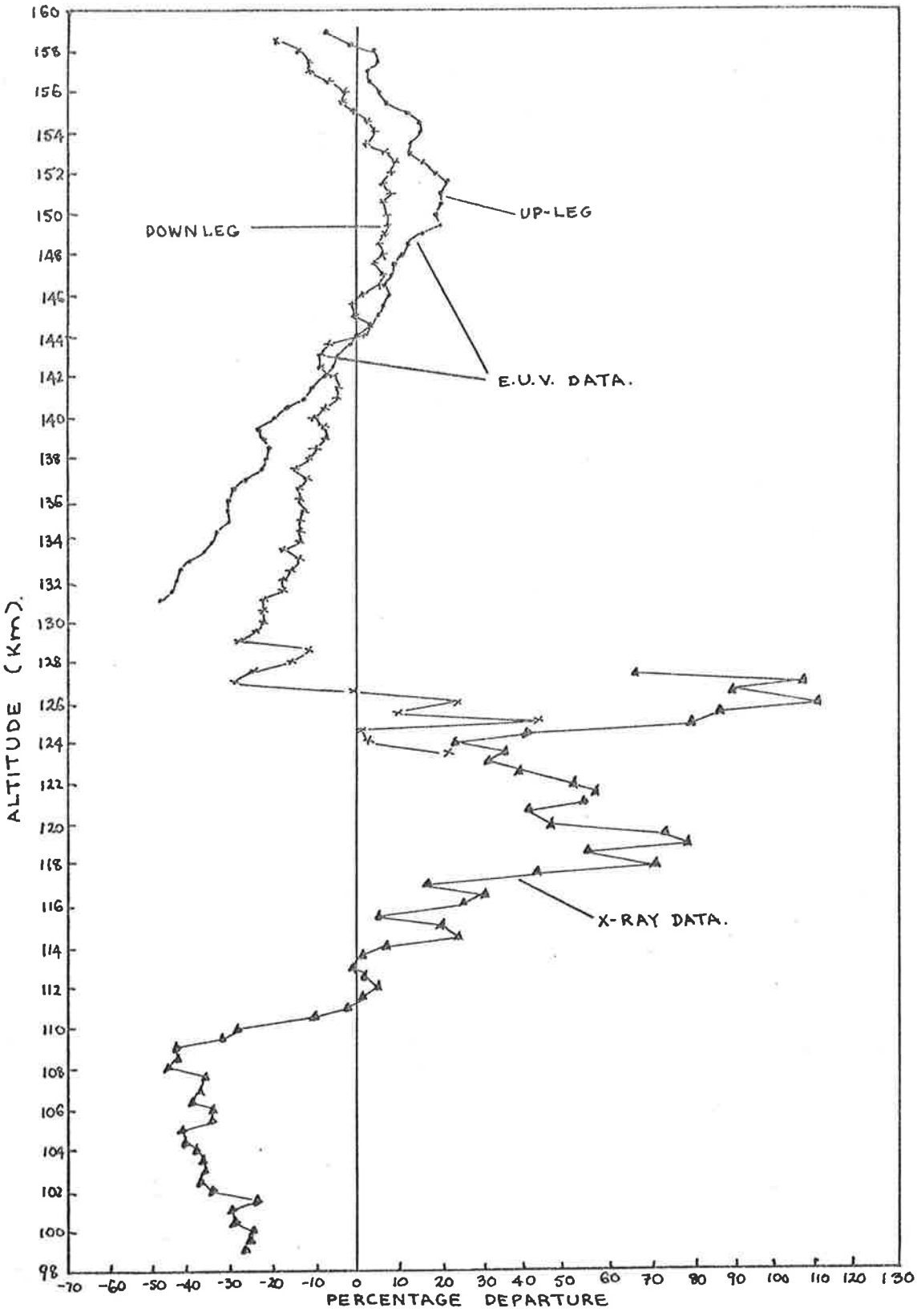

FIG 3·14: PERCENTAGE DEPARTURE OF TOTAL NUMBER DENSITIES SHOWN IN FIG 3·14 FROM THE MEAN CIRA (1972) DENSITY DATA.

3.2.6 NUMBER DENSITY OF THE MAJOR ATMOSPHERIC CONSTITUENTS

In the sections (3.2.3 and 3.2.4) the total number densities have been computed as a function of height from the attenuation coefficients of the X-ray and E.U.V. radiation in the upper atmosphere. In this section are presented the number densities as a function of altitude of the major atmospheric constituents, i.e., N_2, O and O_2, which have been derived from the measured total number densities. These densities have been derived with the use of two different methods.

On the Skylark 1005 and 1207 vehicles, in addition to the author's experiments, were as part of the payloads ion chamber detectors which were prepared by another member of the Space Group, Ms L. A. Davis. The ion chambers were of two types, namely:

(a) quartz-triethylamine which were sensitive to U.V. radiation in the spectral region from 1540 to 1630 Å.

(b) sapphire-xylene responding to U.V. radiation in the spectral region from 1420 to 1490 Å.

The combination of the responses of the two types of ion chambers on these vehicles provided the number density of molecular oxygen, $n(O_2)$, in the altitude range from about 90 to 160 Km.

The molecular oxygen densities computed by Ms Davis from the measured attenuation of the U.V. radiation, and courteously supplied to the author, were used in conjunction with the measured total densities, n_T, to calculate the number densities of N_2 and O, i.e., $n(N_2)$ and $n(O)$, respectively. This has been done by assuming that the percentage composition of the total oxygen, i.e., $n(O) + n(O_2)$, in the atmosphere does not change with height up to about 150 Km and it is the same as at sea level. At sea level the amount of oxygen pre-

sent in the air is 21% of the total density so that:

$$n(O) + n(O_2) = 0.21 n_T \qquad (3.39)$$

From the relation (3.39), $n(O)$ and $n(N_2)$ have been calculated and are presented in figures 3.15 and 3.16 for the Skylarks 1005 and 1207 data, respectively.

The total number densities used to calculate $n(O)$ and $n(N_2)$ had a degree of smoothness, $m = 5$, for both the X-ray and the E.U.V. data acquired during the downleg part of the flight. However, the $n(O_2)$ results determined from the ion chambers data of the 1207 flight, as supplied to the author, were highly structured. These were then smoothed by fitting a fourth order least square polynomial to the $n(O_2)$ profile and then used in this work. The smoothed $n(O_2)$ profile with other densities is shown in fig 3.16.

The profiles of $n(N_2)$ and $n(O)$ (fig 3.15 and 3.16) determined by the above discussed method do not satisfactorily agree with those of the mean CIRA (1972) data, especially at altitudes greater than about 120 Km. In fact, at these heights the calculated $n(N_2)$ values decrease with height less rapidly than the CIRA (1972) data while the opposite is true for $n(O)$. This deviation is due to the fact that $n(N_2)$ and $n(O)$ were calculated assuming that the percentage composition of total oxygen present in the atmosphere at these heights is the same as that at sea level. This assumption is not valid because it does not allow for the fact that above about 120 Km the atmospheric constituents are in a state of gravitational equilibrium in which the concentration of the light species is enhanced relative to the heavy constituents.

A second method has been used to determine $n(N_2)$, $n(O)$ and $n(O_2)$ from the measured n_T data. This consisted in solving simultaneously the following equation system:

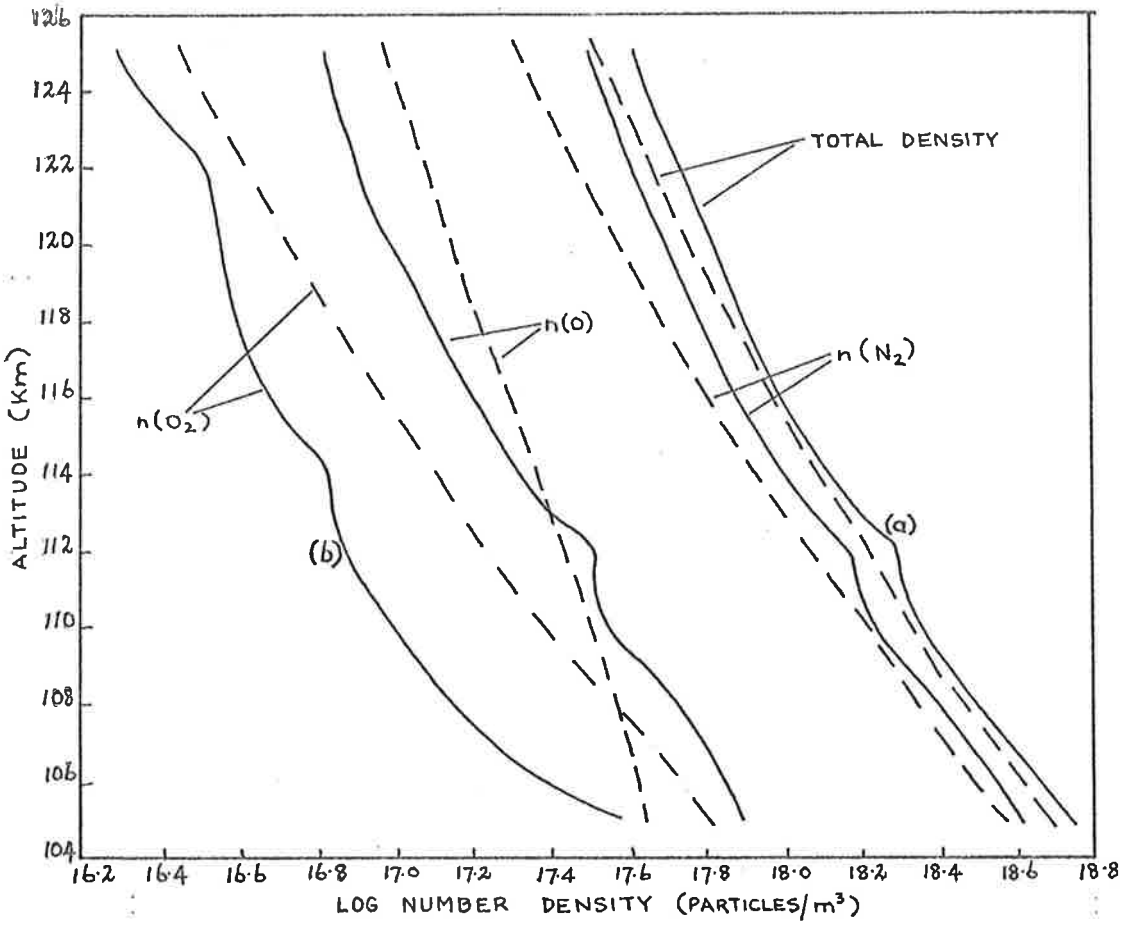

FIG 3·15: NUMBER DENSITY OF THE MAJOR ATMOSPHERIC CONSTITUENTS; (– – –) mean CIRA (1972) DENSITIES, (——) CALCULATED $n(O)$ AND $n(N_2)$.
(a) n_T FROM X-RAY DATA
(b) $n(O_2)$ FROM ION CHAMBER DATA.

FIG 3.16:

(1) Number density of N_2:

(a) determined from the measured $n(O_2)$ and n_T

(b) determined from the solution of equations (3.30)

(c) mean CIRA (1972)

(2) Number density of O_2:

(d) measured with Ion Chambers

(e) from solution of equations (3.30)

(f) mean CIRA (1972)

(3) Number density of O:

(g) determined from the measured $n(O_2)$ and n_T

(h) from solutions of equations (3.30)

(i) mean CIRA (1972)

(4) Total number density, n_T:

(j) determined from X-rays and E.U.V. detectors and for m = 5

(k) mean CIRA (1972)

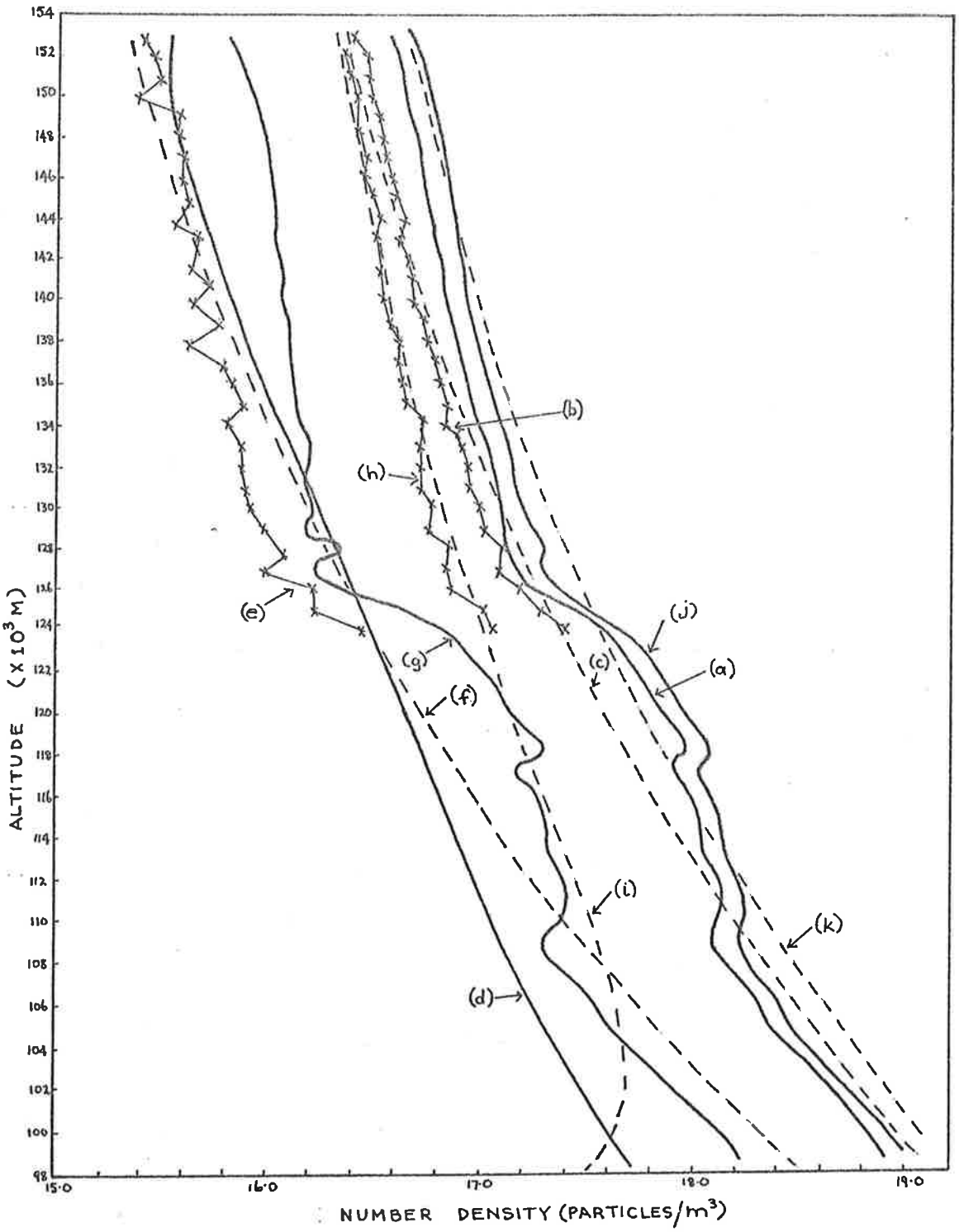
ALTITUDE (X10³M)
154
152
150
148
146
144
142
140
138
136
134
132
130
128
126
124
122
120
118
116
114
112
110
108
106
104
102
100
98
15·0
16·0
17·0
18·0
19·0
NUMBER DENSITY (PARTICLES/m³)
(a)
(b)
(c)
(d)
(e)
(f)
(g)
(h)
(i)
(j)
(k)

$$a_1.n(N_2) + b_1.n(O_2) + c_1.n(O) = \sigma_{eff1}.n_T$$
$$a_2.n(N_2) + b_2.n(O_2) + c_2.n(O) = \sigma_{eff2}.n_T \qquad (3.30)$$
$$a_3.n(N_2) + b_3.n(O_2) + c_3.n(O) = \sigma_{eff3}.n_T$$

where a_1, a_2 and a_3; b_1, b_2 and b_3 and c_1, c_2 and c_3 are the absorption coefficients for the gases N_2, O_2 and O, respectively, at three different wavelengths.

In solving the equation system (3.30), in order for the resulting densities $n(N_2)$, $n(O_2)$ and $n(O)$ to be meaningful, the absorption cross-sections for the gas species at the three wavelengths must be markedly different. Thus, this method can only be applied to the n_T determined from the E.U.V. data. The total densities used are those with a degree of smoothness m = 5 and for the downleg part of the flight of Skylark 1207. This is because the quality of the n_T data determined from the 850 Å radiation on the downleg part of the flight are superior to those of the upleg.

The absorption cross-sections used in this work are those presented in table 3.1 which are from the tabulated values of Stolarski and Johnson (1972). The effective cross-sections which appear in the equation system (3.30) are calculated with the aid of equation (3.27) using the absorption cross-sections of table 3.1 and the density data from the mean CIRA (1972) reference atmosphere. Once the equation system (3.30) has been solved, the resulting values of $n(N_2)$, $n(O_2)$ and $n(O)$ as a function of altitude are then used to recalculate the effective absorption cross-sections which in turn are used to solve the equation system (3.30) again. The iterative process is repeated until the values of $n(N_2)$, $n(O_2)$ and $n(O)$ become independent of the original densities values obtained from the mean CIRA (1972) and used to calculate the effective absorption cross-sections. The process converged to

Table 3.1

ABSORPTION CROSS-SECTIONS FOR THE

GAS SPECIES N_2, O_2 AND O

λ (Å)	$\sigma(N_2) \times 10^{-22} m^2$	$\sigma(O_2) \times 10^{-22} m^2$	$\sigma(O) \times 10^{-22} m^2$
850	7.5	9.3	1.8
770.4	15	18	3.9
703	19.7	28	7.3

the $n(N_2)$, $n(O)$ and $n(O_2)$ values presented in figure 3.16 after the third iterative cycle.

The $n(N_2)$ and $n(O)$ values calculated in this way agree satisfactorily with CIRA (1972) data. In the case of $n(O_2)$, however, the agreement is less satisfactory for altitudes less than about 140 Km. This is because at these heights the values of $n(O_2)$ are much smaller than those of $n(O)$ or $n(N_2)$ and when the equations (3.30) are solved any deviation of the measured n_T from the CIRA (1972) data is enhanced in $n(O_2)$.

The values of $n(N_2)$ and $n(O)$ have also been calculated by a third method in which the measured $n(O_2)$ and n_T are used. This method consisted in solving a system of two equations for the unknown $n(N_2)$ and $n(O)$ knowing $n(O_2)$ and n_T from the ion chambers and E.U.V. detector data, respectively. The resulting values of $n(N_2)$ and $n(O)$ were not significantly different from those determined by solving the equations (3.30) since at these heights $n(O_2)$ is about 1/10 of $n(N_2)$.

3.2.7 TEMPERATURE PROFILE OF THE NEUTRAL ATMOSPHERE

The temperature is one of the principal parameters required to describe the property of the upper atmosphere. There are two ways in which the temperature of the neutral atmosphere can be defined and determined:

(1) through the determination of the kinetic energy of the atmospheric constituents assuming that velocities of these particles have a Maxwellian distribution. The temperature defined in this way is referred to as the "kinetic temperature" and is usually determined from the density and composition measurements made by mass spectrometers with closed ion source (for further detail the reader is referred to section 4.4.4).

(2) from the density profile of one or more atmospheric constituents.

In this section only the method in which the temperature is derived from the density profile of one atmospheric constituent is described and used. The method is based on the fact that in the atmospheric region where the atmospheric species are in diffusive equilibrium (usually above about 100 to 120 Km), the density profile of the i^{th} constituent is given by:

$$n_i(z) = n_i(z_o).\frac{T(z_o)}{T(z)}.\exp\left(-\int_{z_o}^{z} \frac{1}{H_i}.dz\right) \qquad (3.31)$$

where

$$H_i = R.T(z)/m_i.g(z) \qquad (3.32)$$

called the "pressure scale height".

R = universal gas constant

$g(z)$ = acceleration due to gravity

m_i = molecular weight of the i^{th} constituent

and $T(z_o)$ and $n_i(z_o)$ are the temperature and density of the i^{th} constituent at the boundary height level z.

The parameter T(z) which appears in the equations (3.31) and (3.32) is referred to as the "scale height temperature". The gas species of the neutral atmosphere are in thermal equilibrium so that T(z) represents the temperature of the whole neutral atmosphere.

By integrating equation (3.31) on both sides from a boundary height level z_o to a level z, the temperature profile becomes:

$$T(z) = \frac{n_i(z_o).T(z_o)}{n_i(z)} - \frac{m_i}{R.n_i(z)} . \int_{z_o}^{z} n_i(z).g(z)dz \quad (3.33)$$

In equation (3.33) appears the parameter $T(z_o)$ which is not known "a priori" so that in the computation of T(z) a value from a reference atmosphere such as CIRA (1972) has to be used for $T(z_o)$. This should not present any major problem because if equation (3.33) is integrated downwards from a higher boundary level z_o to a lower level ($z_o > z$), the profile of T(z) rapidly converges becoming independent of the value assumed for $T(z_o)$.

Equation (3.33) has been used to calculate the temperature profile of the neutral atmosphere using the $n(N_2)$ data determined from the solution of the equation system (3.30) which are presented in fig 3.16. The temperature profile which has been calculated from the height interval of 124 to 154 Km is shown in fig 3.17 and reflects the wave-like structure of the density data. The temperature profile of the mean CIRA (1972) is also shown in this figure for comparison.

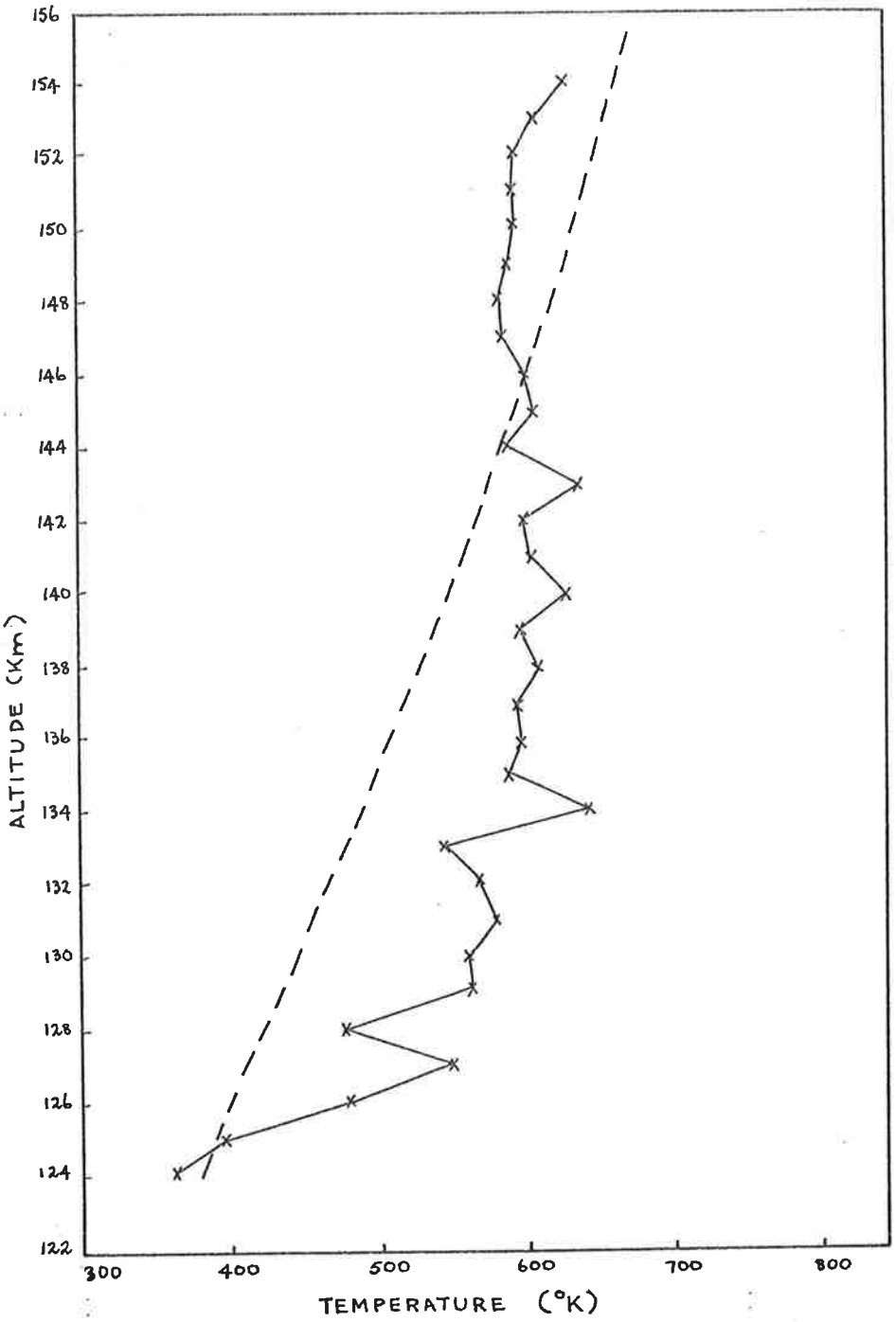

FIG 3·17: THE (×——×) INDICATES THE CALCULATED TEMPERATURE AS A FUNCTION OF ALTITUDE WHILE (– – –) INDICATES THE KINETIC TEMPERATURE OF THE MEAN CIRA (1972) REFERENCE ATMOSPHERE.

3.2.8 MODEL ATMOSPHERE DEPENDENCE OF THE MEASURED DENSITY DATA

In calculating the total number density, n_T, from the X-ray and E.U.V. data the composition of the atmosphere has to be known "a priori" so that $\overline{\sigma}_{eff}(h)$ can be determined (see section 3.2.2). This problem is usually solved by using the density data from a model atmosphere, such as the mean CIRA (1972), to calculate $\overline{\sigma}_{eff}(h)$. However, this means that the computed n_T data depend to some extent on the particular atmospheric model used. In this work it has been possible to recalculate $\overline{\sigma}_{eff}(h)$ and hence n_T using the values of $n(N_2)$, $n(O)$ and $n(O_2)$ determined by solving the equation system (3.30). The percentage deviations, R, of the new calculated total densities from the previous ones are from equation (3.2):

$$R = (1 - \overline{\sigma}_{eff}(\text{measured})/\overline{\sigma}_{eff}(\text{model}))\times 100 \qquad (3.34)$$

where $\overline{\sigma}_{eff}(\text{measured})$ and $\overline{\sigma}_{eff}(\text{model})$ are the absorption cross-sections computed using the calculated $n(N_2)$, $n(O)$ and $n(O_2)$ data and the densities from the mean CIRA (1972) reference atmosphere, respectively. The values of R are presented in fig 3.18. This figure shows that the maximum variation of the calculated n_T from the density data calculated with the aid of the CIRA (1972) data is 5.5%. Thus, the variation is not very large. But, more importantly, the new absorption cross-section increases the value of the total densities for altitudes less than about 140 Km and decreases them at higher altitudes and this has the effect of decreasing the amplitude of the density bulges by a few per cent.

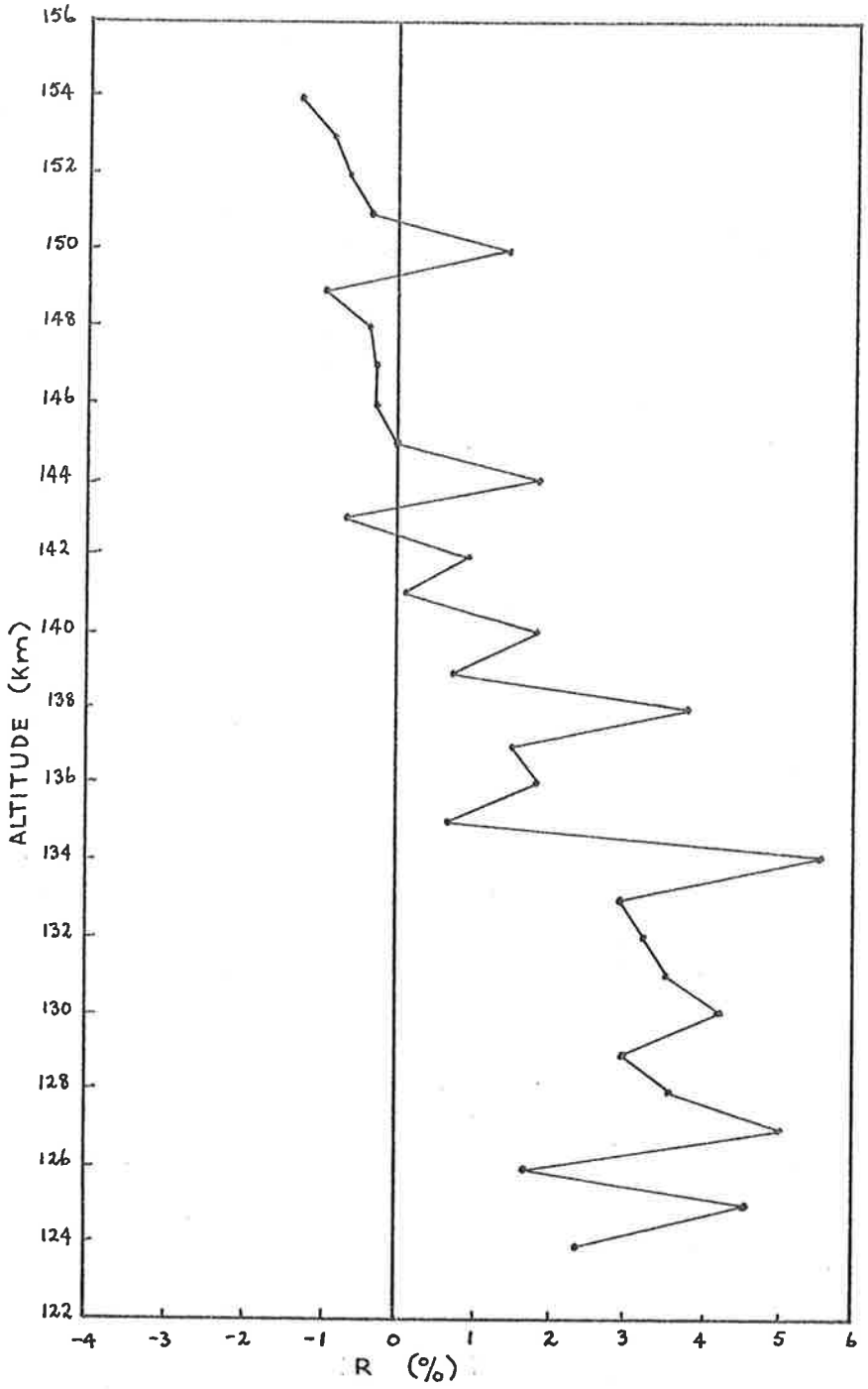

FIG 3·18 : EFFECT OF THE MODEL ATMOSPHERE DEPENDENCE ON THE CALCULATED DENSITIES.

3.2.9 ERRORS

In the analysis of the rocket data presented in this chapter it is difficult to estimate the errors since the calculations of the number densities depend strongly on the values of the absorption cross-sections used. However, the contribution of the statistical errors to the densities data has been estimated to vary from about 10 to 20% depending on the quality of the data. The errors are smaller for the E.U.V. data than those for the X-rays.

CHAPTER IV

MASS SPECTROMETER EXPERIMENT

4.1 SCIENTIFIC AIMS

The original aim of the mass spectrometer experiment was to carry out measurements of ionized and neutral particles of the atmosphere above 110 Km, thereby gaining experience in the complex field of rocket borne mass spectrometry and data reduction. Having this experience the next stage was to develop a cryogenic pump system to make measurements of the atmospheric constituents in the lower thermosphere and mesosphere, between 65 and 115 Km where most of the photochemistry takes place.

4.2 CHOICE OF A SUITABLE MASS SPECTROMETER

Since the early nineteen sixties a number of mass spectrometer experiments have been flown on rockets and satellites for the purpose of determining the composition and density of the terrestrial atmosphere. The mass spectrometers adapted for upper atmospheric research are mainly of the following types:

Bennett R.F. Spectrometer. An instrument which was flown by Brinton et al (1969) of the Naval Research Laboratory, and the Russians Istomin (1963), Danilov et al (1970), Zhood'ko and Klyueva (1970) and other workers.

Magnetic Mass Spectrometer. This has been flown mainly by the research group at the University of Minnesota as reported by Nier et al (1964), Hedin and Nier (1966), Hayden et al (1974) etc., and the Russian researchers.

Quadrupole Mass Spectrometer. This is the most common mass spectrometer employed in the probing of the earth's atmosphere, and it has been flown by Schaeffer and Nichols (1964), Ghosh et al (1968), and others, of the University of Michigan; Narcisi and Baily (1965), Narcisi et al (1971), and others, of the U.S. Air Force Research Laboratory; Mauersberger et al (1967), and others, of the University of Bonn and various other workers.

Monopole Spectrometer. This type of spectrometer has been flown mainly by the team at the University of Bonn, such as von Zahn and Gross (1969), Bitterberg et al (1970), Trinks and Von Zahn (1975) and others.

Omegatron. An instrument which has been employed on

more than 30 rocket flights; for example, Niemann and Kennedy (1966) of the University of Michigan, as well as others.

Of the mentioned spectrometers, only the quadrupole is a true mass/charge selector while the others are either momentum (magnetic analyzers) or velocity selectors (time of flight spectrometers). The quadrupole analyzer has several advantages over the other types, and these advantages are:

- no magnet is required and, as a result, it has no stray magnetic field which may interfere with the adjacent experiments.
- ease of operation.
- rugged, compact and light in weight.
- the performance of the instrument is relatively independent of the initial ion energy.
- low power requirements and the supporting electronics are relatively simple.
- has a high sensitivity and a linear voltage sweep gives rise to a linear mass spectrum.
- can be operated with good resolution at a higher pressure than most other mass spectrometers.
- fast mass scanning (up to 40000 AMU/sec).

Unfortunately, it has the disadvantage of having a poor peak stability if it is operated in a high resolution mode ($m/\Delta m > 500$), a disadvantage which in the case of atmospheric gas sampling does not present any real problem since the mass spectrum of the atmospheric gas is fairly simple and, as a consequence, the analyzer can be used with a low resolving power.

4.3.1 THEORY OF THE SPECTROMETER

The analyzer selected for in-flight composition analysis of the atmosphere is the quadrupole type, an instrument which, since its inception by Paul and Steinwedel (1953), because of its versatility, has evolved into a multipurpose mass spectrometer which has found widespread application in such fields as high vacuum technology, organic and inorganic chemistry, atomic and molecular physics, environmental studies and upper atmsopheric and space research, replacing in many cases the more conventional type magnetic mass spectrometer.

The mass spectrometer can be considered as consisting of a three component ensemble, as shown in fig. 4.1. The three components are: the ion source, the quadrupole apparatus and the detector. The neutral particles are ionized in the ion source and on passing through the quadrupole are filtered so that only ions of a certain mass/charge ratio will be transmitted and detected.

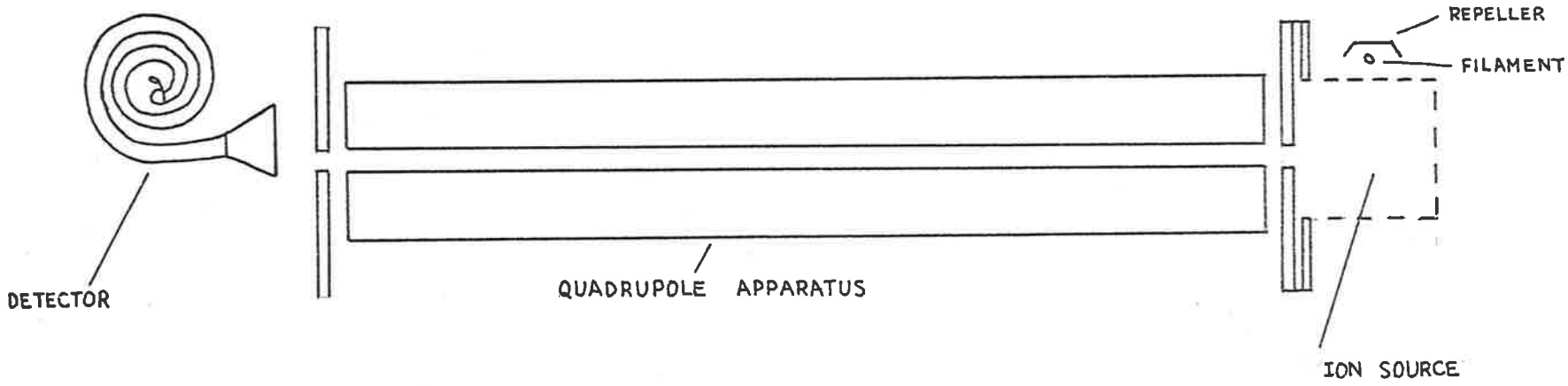

FIG. 4·1: SCHEMATIC CROSS-SECTIONAL VIEW OF THE MASS SPECTROMETER ENSEMBLE.

4.3.2 ELECTRODE CONFIGURATION

The theory of the quadrupole mass spectrometer was first discussed by Paul and Steinwedel (1953). This was followed by a description of an experimental mass filter in 1955 by Paul and Raether (1955). The analyzer is usually called a mass filter rather than a spectrometer because the selection of the ions comes about by trajectory stabilities of the ions in the quadrupole field instead of focusing properties.

The quadrupole theory of Paul and Steinwedel (1953) is based on an ideal device of which the electrodes are hyperbolic in structure of infinite length and positioned at 90^{o} apart as in figure 4.2a. In practice, though, the manufacture of hyperbolic electrodes is very difficult and time consuming so that they are usually approximated by those of simpler configuration such as circular rods (Dayton et al (1954)), plane (Schmidt (1972), Sakudo and Hayashi (1975)), and circular concave (Hayashi and Sakudo (1968)) electrodes as shown in figures 4.2b and 4.3.

Even though the Laplace equation for the field distribution for the above mentioned geometrical configurations of electrodes has been solved and the geometrical parameters have been calculated, to the knowledge of the author up to now, only the circular rod electrodes have been and are used in manufacturing the analyzers.

According to the calculations of Dayton et al (1954), the optimum radius R of the circular electrodes which approximate the hyperbolic configuration is:

$$R = 1.148 r_0$$

where $2r_0$ is the spacing between diametrically opposite electrodes (fig 4.2b), while Denison (1971) found that a better

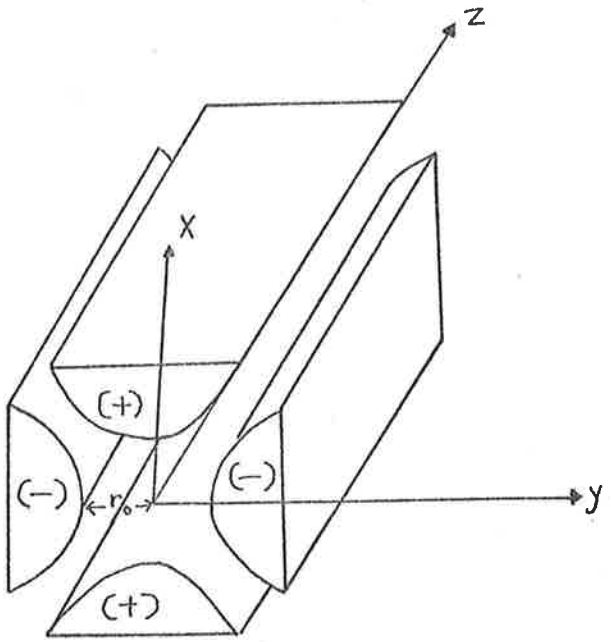

(a) HYPERBOLIC ELECTRODES

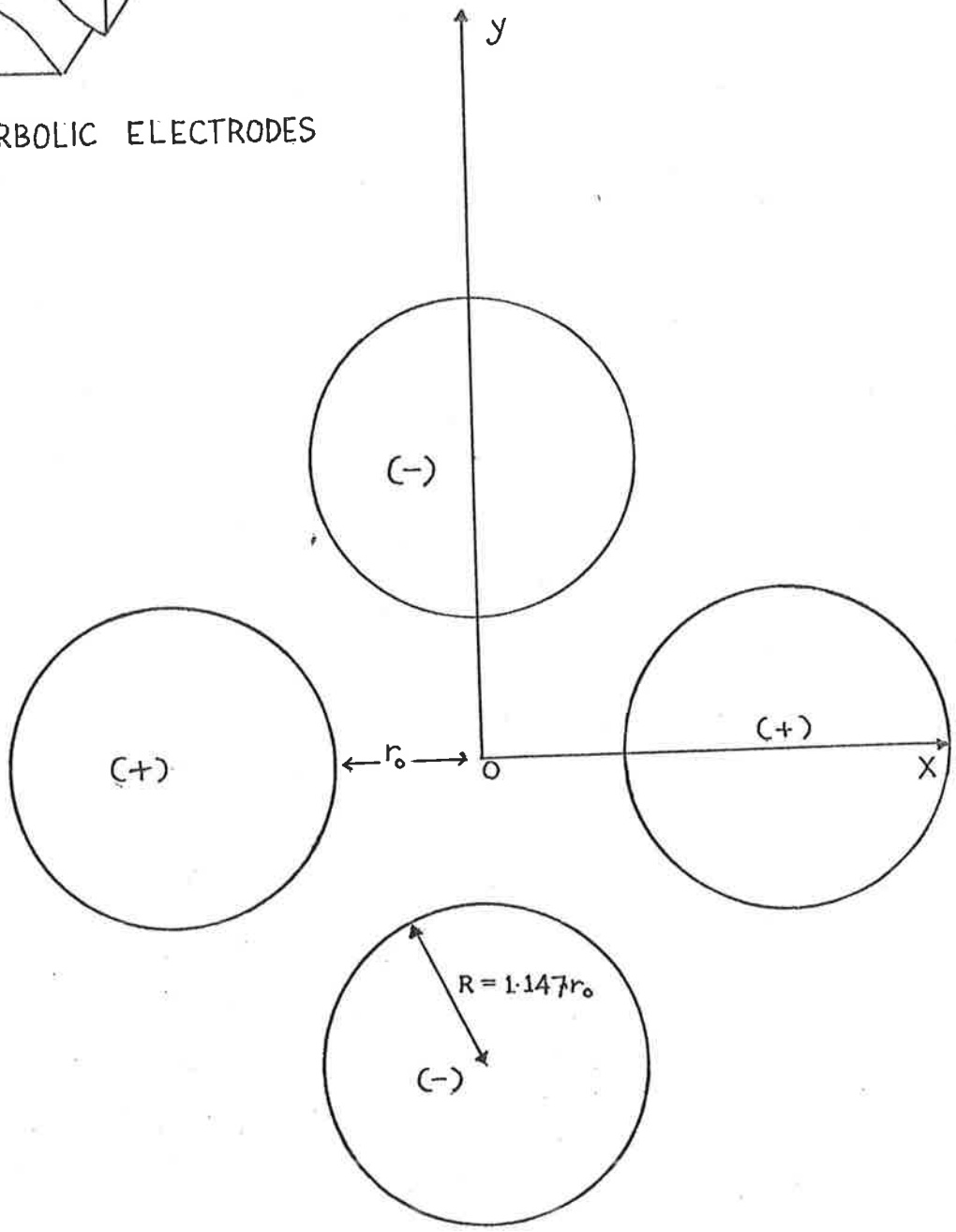

(b) CIRCULAR ELECTRODES

FIG. 4·2

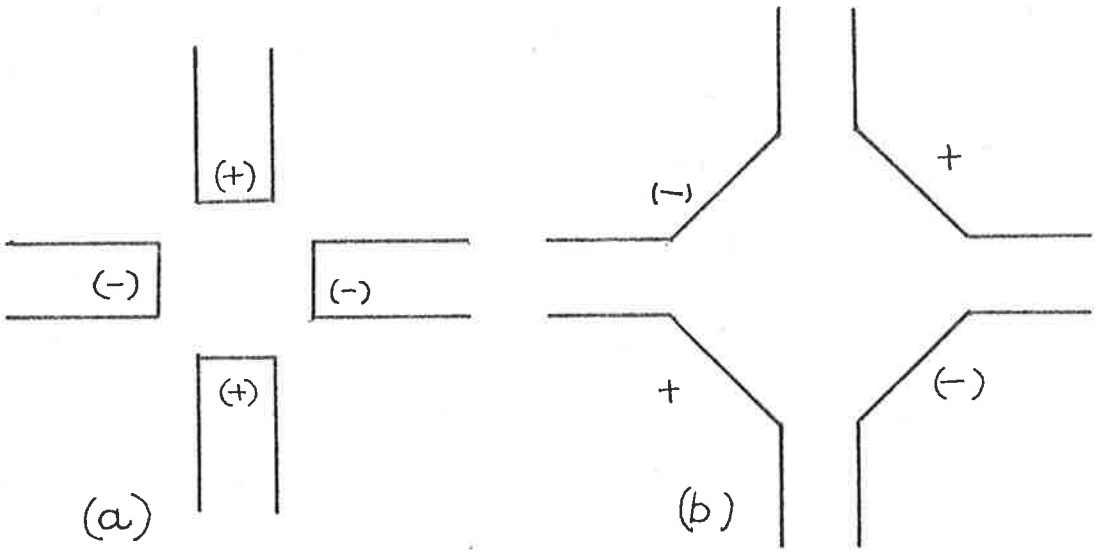

PLANE ELECTRODES (a) AND (b)
(SAKUDO AND HAYASHI (1975))

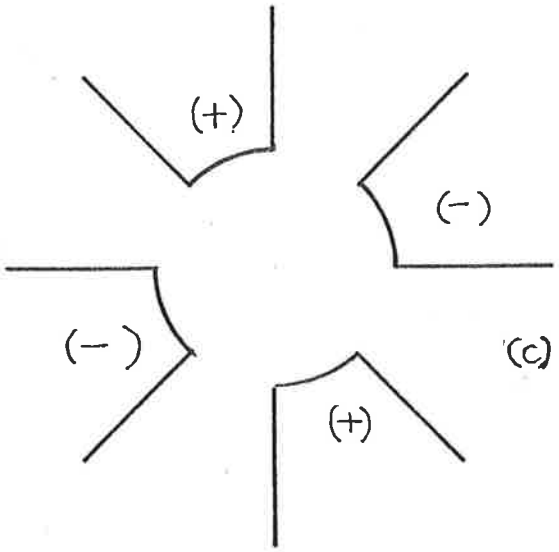

(c) CIRCULAR CONCAVE ELECTRODES
(HAYASHI AND SAKUDO (1968)

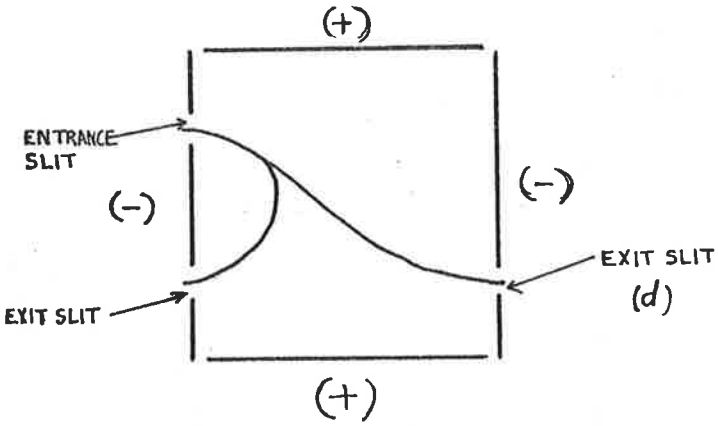

(d) PLANE ELECTRODES
(SCHIMDT (1972)).

FIG 4·3

value is:

$$R = 1.147r_o$$

He also found that by placing the device in a grounded cylindrical housing the quadrupole field in the analyzer is only slightly affected by the grounded vessel, and the effect is so small that in practice it can be neglected.

In using circular electrodes of optimum radius $R = 1.148r_o$ (Dayton (1954)) or $R = 1.147r_o$ (Denison (1971)), the ideal field is approximated only to a distance of about $0.8r_o$ from the centre of the field, and this has some degrading effect on the path stability of the ions, even though the effect again is very small (Denison (1971)).

4.3.3 EQUATION OF MOTION OF IONS IN THE QUADRUPOLE FIELD

For simplicity, the electrode structure of the mass spectrometer is assumed to be hyperbolic of infinite length so that the fringing fields can be neglected.

With the co-ordinate system of fig. 4.2a, the potential, ϕ, of the field at any point in the quadrupole can be expressed (Paul et al (1958)) by the equation:

$$\phi = \phi_o(t).(\alpha_x X^2 + \alpha_y Y^2 + \alpha_z Z^2) \qquad (4.1)$$

where $\phi_o(t)$ is the time-varying voltage waveform applied between adjacent electrodes.

If it is assumed that there is no space charge on the electrodes, then equation (4.1) must satisfy the Laplace equation:

$$\nabla^2\phi = 0 \qquad (4.2)$$

and by substituting equation (4.1) into equation (4.2), it follows that the constants α_x, α_y and α_z must satisfy the condition:

$$\alpha_x + \alpha_y + \alpha_z = 0 \qquad (4.3)$$

For the quadrupole analyzer the constants are chosen so that:

$$\alpha_x = -\alpha_y = 1/r_o^2 \text{ and } \alpha_z = 0 \qquad (4.4)$$

and the potential at any point in the analyzer becomes:

$$\phi = \phi_o(t).(X^2 - Y^2)/r_o^2 \qquad (4.5)$$

and the electric field along the three directions is:

$$\begin{aligned} E_x &= -\partial\phi/\partial X = -2\phi_o(t).X/r_o^2 \\ E_y &= -\partial\phi/\partial Y = 2\phi_o(t).Y/r_o^2 \\ E_z &= -\partial\phi/\partial Z = 0 \end{aligned} \qquad (4.6)$$

Under the influence of this field an ion of mass 'm' and charge 'e' on entering the analyzer will be subjected to the force:

$$\begin{aligned} F_x &= m\ddot{X} = eE_x = -2e\phi_o(t).X/r_o^2 \\ F_y &= m\ddot{Y} = eE_y = 2e\phi_o(t).Y/r_o^2 \\ F_z &= m\ddot{Z} = 0 \end{aligned} \qquad (4.7)$$

which can be simplified into;

$$\begin{aligned} &(a)\quad \ddot{X} + 2e.\phi_o(t).X/mr_o^2 = 0 \\ &(b)\quad \ddot{Y} - 2e.\phi_o(t).Y/mr_o^2 = 0 \\ &(c)\quad \ddot{Z} = 0 \end{aligned} \qquad (4.8)$$

The first two equations, 4.8 (a) and 4.8 (b), describe the equation of motion of the ion in the XY plane and it follows from them that the motion in each co-ordinate direction is independent of the motion in the other direction, i.e. each equation is dependent on a single co-ordinate either X or Y instead of both X and Y. This is not completely true in the case of an actual instrument because the electrodes are not hyperbolic but circular, and the components of the ion motion in the X and Y direction are not completely independent but are weakly coupled through the non-quadrupole field components (Denison (1971)).

Equation 4.8 (c) indicates that the ions move along the axis of the instrument with a constant velocity. This property gives the quadrupole analyzer an advantage over the other mass analyzers since the mass selection of the quadrupole spectrometer, with limits, is independent of the energy spread of the ions and of their initial velocities. In the above equations, the scalar potential $\phi_o(t)$ of the electric field can be any arbitrary periodic function of time, containing a DC component, either externally generated or inherent in the shape of the voltage waveform or both, applied to the electrodes (Richards et al (1974a)).

Until recently, all the quadrupole mass spectrometers were operated by applying a sinusoidal R.F. waveform, $V\cos\omega t$, and a DC component, U, to their electrodes so that the scalar potential assumes the form of :

$$\phi_o(t) = U + V\cos\omega t \qquad (4.9)$$

then Richards et al (1973 and 1974a) showed that the analyzer

could be operated by applying to its electrodes a rectangular waveform instead of the sinusoidal. This new mode of operation presents the advantage that no external DC component need be applied to the electrodes since the waveform itself already contains an intrinsic average value. In the case of the sinusoidal mode, as will be shown later, the ratio DC to AC, i.e. U/V must be kept constant to a tolerance of the order 1 in 10^5 otherwise the performance of the device is unsteady and varies over the mass range. When the instrument is used with a high resolution, this stringent tolerance on the ratio U/V may be difficult to fulfil, and as a consequence, the analyzer has a poor peak stability. This poor peak stability can be eliminated by applying to the electrodes a rectangular time-varying voltage waveform, but, unfortunately, this mode of operation has its own problem. The problem is in the building of the electronics to drive the device since high voltage (usually >100 volts) have to be switched at high frequencies (usually greater than 1 MHz).

For most applications the analyzer is not used with a high resolution so that the tolerance on the ratio U/V is not so stringent and it is more practical to operate the instrument in its original form (Paul and Steinwedel (1953), Paul and Raether (1955)), i.e. by applying a DC component and a sinusoidal time varying voltage waveform to its electrodes.

In this mode of operation, the equations of motion become:

$$\ddot{X} + 2e.(U + V\cos\omega t).X/mr_o^2 = 0$$
$$\ddot{Y} - 2e.(U + V\cos\omega t).Y/mr_o^2 = 0 \qquad (4.10)$$

which by making the substitution:

$$t = 2\theta \qquad (4.11)$$
$$a = a_x = -a_y = 8eU/m\omega^2 r_o^2$$
$$q = q_x = -q_y = 4eV/m\omega^2 r_o^2$$

they simplify into:

$$d^2X/d\theta^2 + (a + 2q\cos 2\theta).X = 0$$
$$d^2Y/d\theta^2 + (a + 2q\cos 2\theta).Y = 0 \qquad (4.12)$$

which are the Mathieu's equations in their canonical form (McLachlan (1947), Blanch (1965)). Since both equations are exactly of the same form, it is only necessary to consider the solution of one equation, say, the equation relative to the X co-ordinate.

Paul and Steinwedel (1953) in their study of the operation of the quadrupole mass spectrometer used an analytical solution of the Mathieu's equations to determine the ion's trajectories in the quadrupole field which is a laborious technique. With the advent of fast digital computers, more recently Dawson (1974), Richards et al (1974b), Richards and McLellan (1975) and various other authors have integrated numerically the differential equations of motion of the ions in the quadrupole field and computer plotted their trajectories, with different initial and boundary conditions.

A solution of the Mathieu's equation is of the form (McLachlan (1947)):

$$X = Ae^{\mu\theta}.\sum_{-\infty}^{+\infty} C_n.e^{in\theta} + Be^{-\mu\theta}.\sum_{-\infty}^{+\infty} C_n.e^{-in\theta} \qquad (4.13)$$

where A and B are integration constants and C_n and μ are constants which are functions of the variables 'a' and 'q'. The solutions are of two types:

(a) Stable Solution: in which X remains finite as $\theta \longrightarrow \infty$

(b) Unstable Solution: in this case $X \rightarrow \infty$ as $\theta \longrightarrow \infty$

Since θ is real, the nature of the solutions depends on the constant μ through the exponential factor $e^{-\mu\theta}$ or $e^{\mu\theta}$.

Four possibilities arise:

(1) If μ is real and non zero, the solution is unstable.

(2) If μ is a complex number, i.e. $\mu = \alpha + i\beta$ with $|\alpha| > 0$ and $|\beta| > 0$, the solution is unstable.

(3) If $\mu = iK$ is purely imaginary, with K an integer, the solution is stable but not periodic, i.e. it never repeats itself exactly at any interval.

(4) If $\mu = i\beta$ is purely imaginary, β satisfying the condition $0 < \beta < 1$, the solution is stable.

In the study of the operation of the quadrupole analyzer, the stable solution is the only one which is of interest, since it represents the trajectories of the ions reaching the detector placed at the other end of the field. The unstable solution gives rise to ion trajectories the transverse amplitudes of which increase with oscillations so that after a number of oscillatory motions, these ions reach the electrodes and are neutralized.

For stable solution, equation (4.13) can be put in the form:

$$X = A' \sum_{-\infty}^{\infty} {}_nC_n . \cos(n + \beta/2)\omega t + B' \sum_{-\infty}^{\infty} {}_nC_n . \sin(n + \beta/2)\omega t \qquad (4.14)$$

where A' and B' are constants of integration.

Since μ and hence the stability path of the ions depends on the parameters 'a' and 'q', it is possible to plot the regions in the a-q space which correspond to stable trajectories of the ions (fig 4.4). These stable regions have the property of being symmetrical, both about the a-axis and the q-axis, and hence if the AC and DC voltages are changed in sign it should have no effect on the trajectories of the ions.

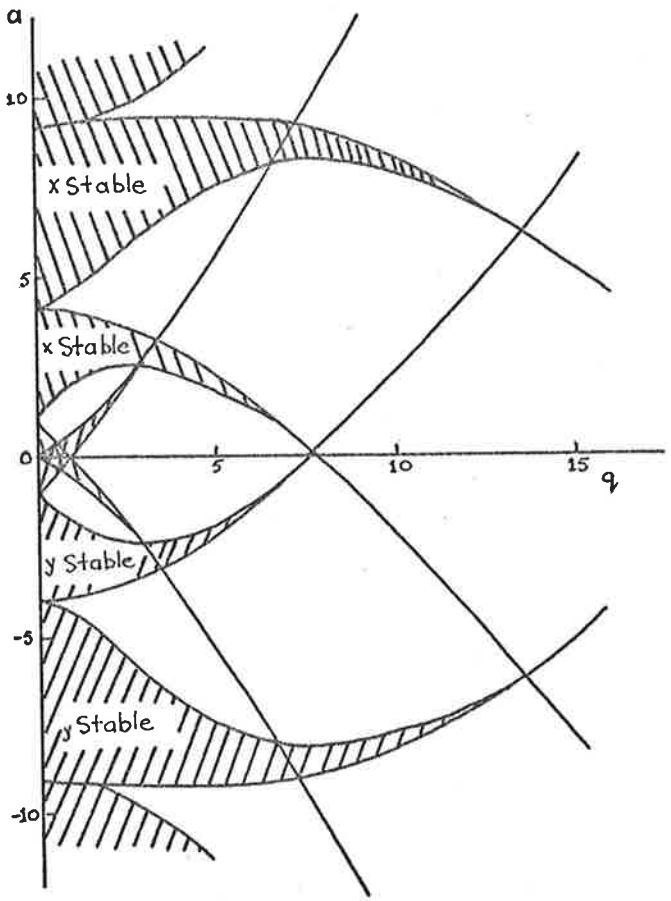

FIG. 4·4: THE STABILITY REGIONS FOR THE x AND y DIRECTIONS WHICH DIFFER BY THE FACTOR -1 ARE SUPER-IMPOSED (diagram from Dawson and Whetten (1969)).

Since an ion, to be transmitted by the analyzer, must have a stable path both in the X and in the Y directions, it is only feasible to use the stable region closest to the origin, which is shown enlarged in fig. 4.5. Fig. 4.4 shows the stability regions for the X and Y directions superimposed.

The value of β_x and β_y for the stability diagram of fig. 4.4 are different and as a result the trajectories of the ions along the respective X and Y axes are different. This difference is caused by the positive DC voltage component applied to the X electrodes with respect to the Y electrodes. The positive voltage on the X electrodes tend to make the ions stable in the X direction even in the absence of the AC component, i.e. q = 0, the equation of motion of the ion along the X direction, from the equation (4.12) becomes:

$$d^2X/d\theta^2 + aX = 0 \qquad (4.15)$$

which is the equation for simple harmonic motion. In the case of Y direction with no AC component the equation of motion becomes:

$$d^2Y/d\theta^2 - aY = 0 \qquad (4.16)$$

which has a solution of the form:

$$Y = e^{\pm\sqrt{a}\theta} \qquad (4.17)$$

The (positive) ions are attracted to the Y electrodes and their motion is *not* oscillatory. The application of the AC voltage component makes the motion of the ions oscillatory along both directions, but along the X direction has the effect of increasing the amplitude of the oscillations so that the ions become unstable, while along the Y direction it tends to counter-balance the defocusing effect of the DC component so that they become stable (Brubaker (1961)).

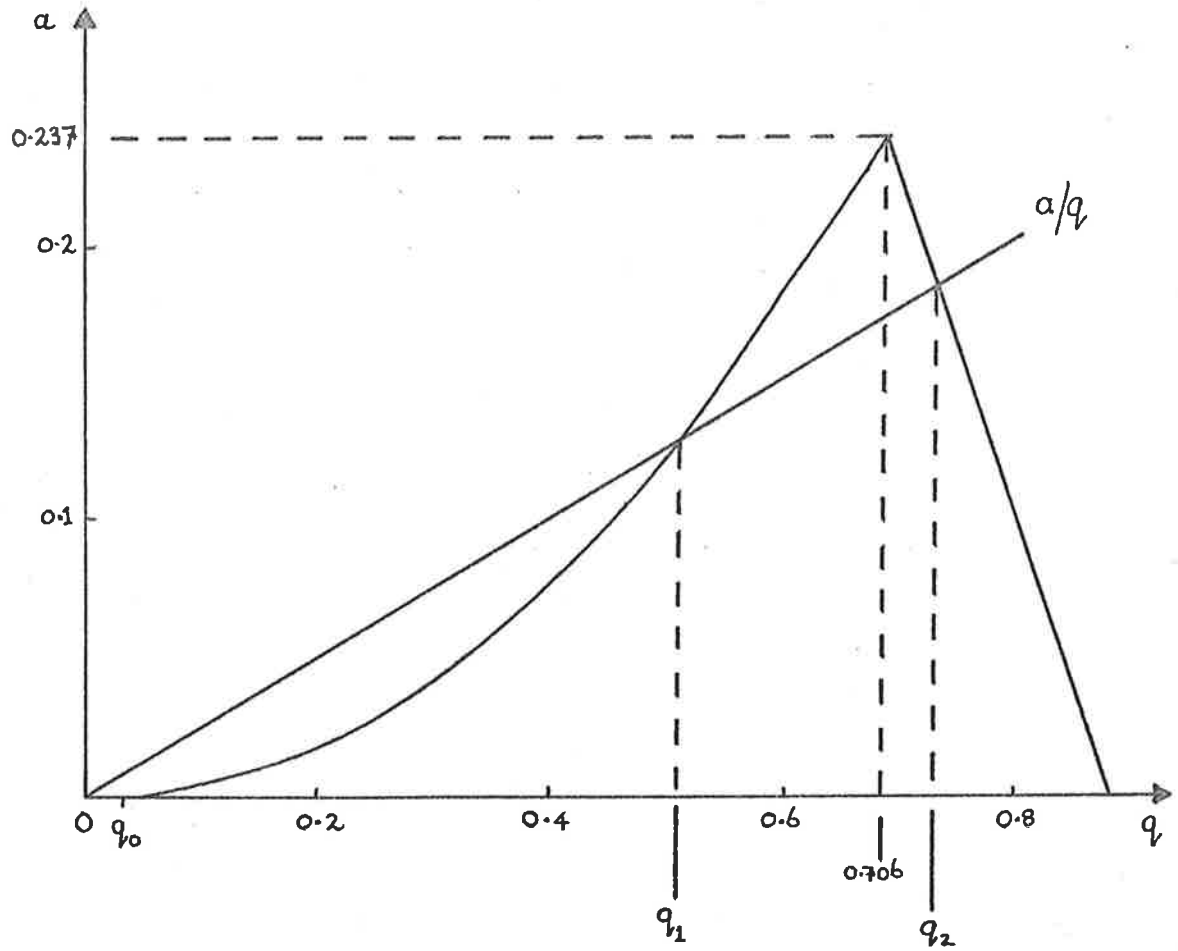

FIG. 4·5: ENLARGED STABILITY DIAGRAM FOR POSITIVE 'a' AND 'q' VALUES.

4.3.4 MASS SCAN

As already mentioned, an ion will have a stable path only if the values 'a' and 'q' fall in the stability diagram, and all the ions having the same values r_o, ω, U and V will have the same operating point in this a-q space. From equation (4.11), it follows that the ratio, $a/q = 2U/V$, does not depend on the ion's mass. This means that for the same ratio U/V, different mass/charge (m/e) values will have parameters 'a' and 'q' in the stability diagram which lie on a single straight line passing through the origin. This mass scan line is shown in figure 4.5. The slope of this line depends only on the ratio U/V. Thus, since 'a' and 'q' depend on the variables U, V and the frequency, ω, of the R.F. voltage, by keeping the ratio U/V constant mass scanning can be accomplished either by varying the magnitude of U and V such that their ratio is constant, or by varying the frequency. Usually it is electronically simpler to vary the magnitude of U and V instead of the frequency of the R.F.

The slope of the scan line can be chosen so that only an ion with a particular value of m/e, lying in the interval between q_1 and q_2 (fig 4.5), will be transmitted by the analyzer. All other ions with m/e greater than this value have unstable trajectories in the X direction and all those with m/e less than that particular value are unstable in the Y direction. From the above discussion, it follows then that the resolving power of the analyzer depends only on the ratio U/V (if the instrument is long enough) and it can be practically increased from zero to a theoretical limit value such that:

$$(U/V)_{limit} = 0.12$$

a value which corresponds to the intersection of the scan line with the apex of the stability triangle the limits of which from the solution of the Mathieu equation are:

$$q_{limit} = 0.70600$$
$$a_{limit} = 0.23699 \qquad (4.18)$$

The instrument will have zero resolution when the D.C. component is zero (U = 0) but not all the ions are transmitted by the analyzer. This is because the interception of the boundary curve of the stability diagram closest to the origin is not zero, but q_o, so that the instrument acts as a higher pass filter in which all the ions with ratio m/e above a certain m/e value (which is determined by the intersection of the boundary of the stability diagram with the q-axis) are transmitted.

4.3.5 MASS-VOLTAGE-REQUENCY RELATIONSHIP

From the equations:

$$a = 8eV/m\omega^2 r_o^2$$
$$q = 4eV/m\omega^2 r_o^2 \qquad (4.19)$$

and the limit value of 'a', 'q' at the apex of the stability diagram, it follows that:

$$V = 7.219 f^2 r_o^2 M$$
$$U = 1.212 f^2 r_o^2 M \qquad (4.20)$$

and $U/V \approx 1/6$

where f is in MHz, M in A.M.U., r_o in cm and U and V are in volts.

4.3.6 ENTRANCE APERTURE AND ANGLE OF ACCEPTANCE OF THE IONS

For 100% transmission, the diameter of the entrance aperture of the quadrupole spectrometer is:

$$D \approx r_o \cdot \sqrt{\Delta m/m} \qquad (4.21)$$

and again for 100% transmission the maximum angle of incidence of the ions to the axis of the analyzer (Paul et al (1958)) is:

$$\tan\psi_m = 1.4 \times 10^{-3} \times r_o^2/\ell^2 \qquad (4.22)$$

4.3.7 RESOLVING POWER AND ION VELOCITY

It was mentioned in section 4.3.4 that the resolving power of the quadrupole mass spectrometer depends on the value of the ratio of U/V. This is true only if the electrodes are of infinite length. In practice the length of the analyzer is not infinite but of a finite length ℓ. Thus, for mass separation to occur the ions must have sufficient number of oscillations inside the quadrupole field to ensure that the unstable ions are removed.

Paul et al (1958) found experimentally that the number of R.F. cycles required to remove the unstable ions for a resolution near 100 is;

$$n = 3.5\sqrt{m/\Delta m} \qquad (4.23)$$

where m is the mass of the ion and Δm is the mass peak width at half height and $m/\Delta m$ is the resolution of the instrument.

The above requirement sets an upper limit to the acceleration voltage of the analyzer which determines the axial velocity of the ions. According to Paul et al (1958), this accelerating voltage must satisfy the relation:

$$Vacc \ll 4.2 \times 10^2 \times f^2 \times \ell^2 \times \Delta m \qquad (4.24)$$

where f is the R.F. frequency in MHz, ℓ is the length of the electrodes in meters and Δm is in A.M.U.

4.3.8 PROFILE OF MASS SPECTRAL LINES AND FRINGING FIELDS EFFECTS

A quadrupole mass spectrometer having ions entering the field at different positions, with different angles of incidence and at different initial phases of the R.F. field, gives rise to an asymmetric spectral line profile of the mass peak. In fig. 4.6 there is shown a profile of nitrogen peak taken with a flight instrument, from which it can be seen that the peak is sharper on the high mass side of the line than on the low mass side. Paul et al (1958) thought that this asymmetry is due to the asymmetry in the stability diagram. In fact, they suggested that because of the asymmetric appearance of the stability diagram, when the transmission falls from 100% to below 100%, the profile of the spectral line changes from a trapezoidal (flat top) to a triangular peak, having a tail on the low mass side. Dawson (1974) in his detail study of the quadrupole analyzer by computer simulation found this not to be so. He found that the tailing effect on the low mass side is not due to the asymmetry in the stability diagram, but to the high energy ions which spend insufficient cycles in the field. His calculations also show that the mass peaks remain almost bell-shaped with only minor signs of asymmetry when the transmission falls below 100%.

Dawson (1974), in studying the effect of the initial R.F. phases and the fringing fields on the ions transmission and resolution, found that the ions entering at R.F. phases of 0, $\pi/2$ and π radians, have a higher transmission than those at $\pi/4$ and $\frac{3\pi}{4}$. But the reverse is true when the resolution is considered. It appears that ions entering the analyzer when the phases are 0 or π spend less time in the quadrupole

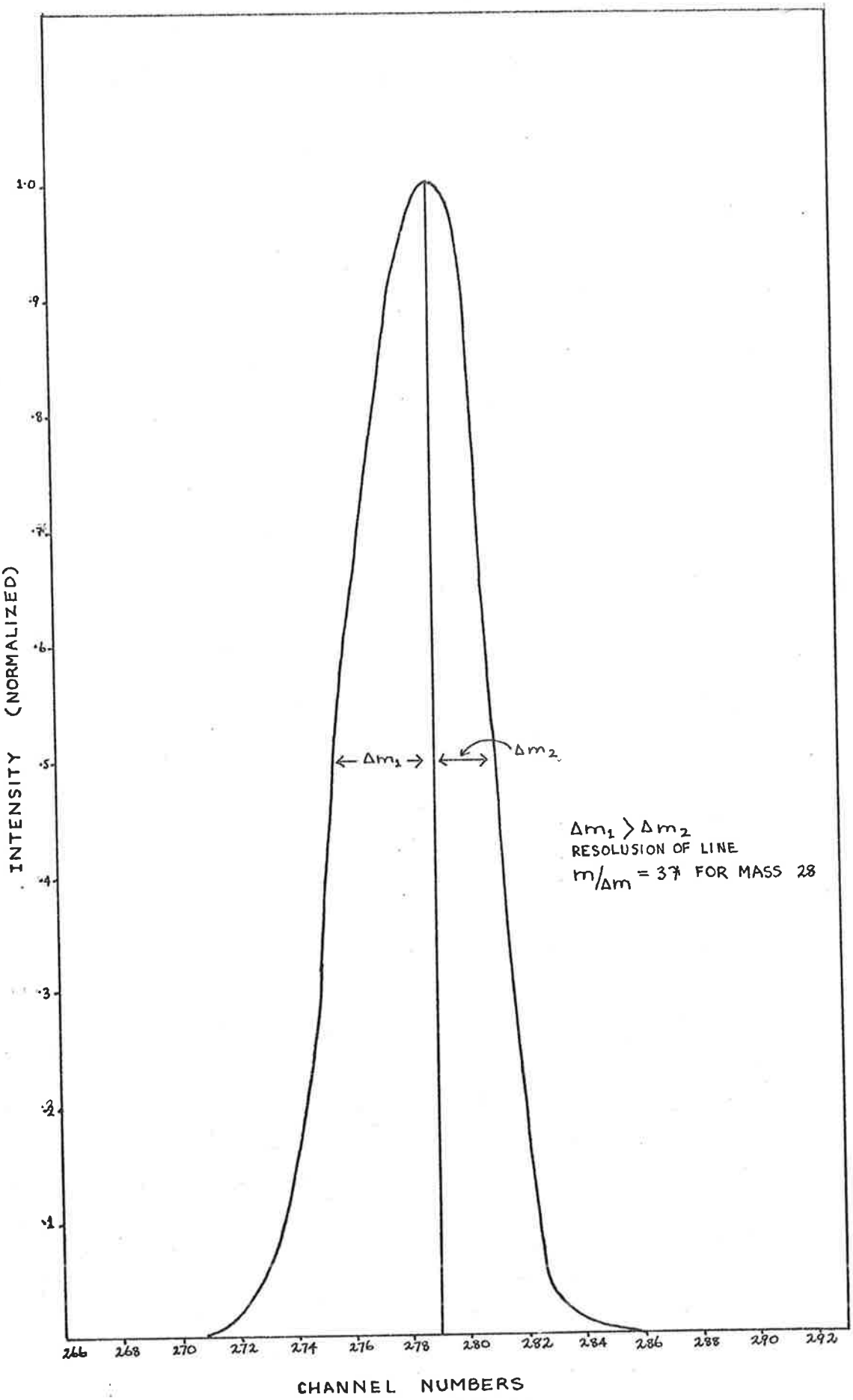

FIG. 4·6: MASS PROFILE OF N_2.

field than those entering at $\pi/4$ and $3\pi/4$ and, consequently, the tailing effect on the low mass side is more pronounced for the 0, $\pi/2$ or π phases.

This degradation in the resolution for the 0 or π phases seems to improve when fringing fields are considered. In fact, the works of Home et al (1972) and Dawson (1974) show that the fringing fields have a focusing action in a way as to make the trajectories similar for all initial phases of the R.F. field and to add filtering action to the main quadrupole field, thereby increasing the effective length of the quadrupole electrodes and, hence, the resolution.

As the aperture of the analyzer is reduced, the resolution and the transmission increase but when this aperture is restricted more than is necessary for 100% transmission then the resolution decreases, i.e., tailing on the low mass side of the spectral line increases, which seem to indicate that ions entering at the centre along the axis of the analyzer spend less time in the field. It appears that a "hollow" beam, where the ions density is smaller near the axis of the instrument, is preferable since it gives a better line profile (Dawson (1974)).

4.4.1 ION SOURCE

The use of mass spectrometers to make in situ measurements of the composition and density of the atmosphere presents problems which are not usually found in the laboratory analysis of a gas sample. Mass spectrometers employed in neutral gas require that the neutral particles are ionized and in general the ionization is accomplished by electron bombardment of the gas particles; the electrons being generated usually by a hot cathode filament.

The earth's atmosphere above about 70 Km is composed of gases of both molecular and atomic species and, ideally, in order to make accurate measurements of these particles' density, it is desirable that the gas sample entering the instrument does not interact with the instrument and that no reactions take place among the gas sample constituents. In practice, however, this is not possible since the atomic species, such as atomic oxygen and atomic hydrogen, have a high chemical activity which react strongly with the instrument's chamber walls, resulting in these gases being permanently adsorbed on the surfaces or recombined to form molecular species or both.

The presence of a hot filament in the ion source has a dramatic effect on the gas sample being analyzed. Various authors, such as Wagener and Marth (1957), Schlier (1958), Becker et al (1961) etc., have reported that for heated tungsten filaments in an atmosphere of oxygen, impurity gases (CO, CO_2, H_2O, atomic oxygen, etc.) are generated at the filaments surface, while Singleton (1966) found that the large amount of carbon monoxide produced in his system could not be explained by simply assuming that all the carbon monoxide is produced at the filament. He suggested that a certain amount

of carbon monoxide arises from the interaction of oxygen at the walls of the ion source, so that not only the filament but also the walls of the ion source are potential sites for carbon monoxide generation. Trinks (1973) has developed an ion source in which the electrons are generated by a U.V. excited photomultiplier, and found that the partial pressures of CO, and CO_2 produced on the walls of the ion source where lower by a factor of about 100 than those of a comparable hot filament source. His results tend to support the hypothesis that the CO and CO_2 gases are produced predominantly at the hot filament and only a small quantity at the surfaces of the ion source.

Another source of error introduced by the filament is that oxygen is pumped by heated tungsten or rhenium cathodes, thus reducing the amount of oxygen present in the gas sample. The reduction of oxygen goes into the formation of CO, CO_2, H_2O, atomic oxygen and vaporized tungsten oxide, WO_3, if a tungsten filament is used. The pumping speed of oxygen on tungsten filament has been reported by Schlier (1958) as 9 litres/sec.cm^2 at temperatures above 2000°K, while Gross (1970) has found a value of 7.6 $\pm$1.5 litres/sec.cm^2 for rhenium at a temperature of 2500°K and pressure of 2.6×10^{-7} torr. This means that for a rhenium filament of length 2 cm and diameter of 5×10^{-3} cm, approximately 0.3 c.c./sec. of oxygen is pumped away, at a pressure of 2.6×10^{-7} torr, a quantity which is negligible when considering the accuracy of the telemetred data from a rocket-borne mass spectrometer.

Tungsten, once it has been "fired", becomes very brittle, so that it is not generally employed in rocket-borne mass spectrometry; instead, rhenium, which is more ductile, is used.

The pumping speed and hence the surface reactions taking place at the surface of the filament are a function of its surface temperature, and the graph of fig 4.7, taken from the paper of Becker et al (1961), shows how the partial pressures of O_2, CO_2, CO and H_2O vary with the filament's temperature. The peaks at 1000°K for CO are due to CO desorption from the surface of the filament. The production of CO increases dramatically with temperature, and this is because at high temperatures (T>1650°K) atomic oxygen is produced which has a much higher chemical activity than molecular oxygen, and hence oxidizes the carbon atoms more readily.

The high chemical activity of atomic oxygen with the filament and walls of the ion source becomes very important when mass spectrometers are employed to determine its concentration and the concentration of minor constituents such as CO_2, CO, H_2O, etc. Nier et al (1964), during the laboratory calibration of their rocket-borne mass spectrometer, noticed that in oxygen-rich atmosphere, such as pure oxygen or dry air, chemical or catalytic reactions at or near the filament and the surrounding hot walls, produce whole families of background peaks of mass numbers 12, 14, 16, 18, 28, 44, etc., and brought to the attention of experimenters working in the field of rocket-borne mass spectrometry that the large amount of CO_2 measured in the atmosphere by means of mass spectrometers, which has a profile similar to atomic oxygen, is due to the oxidation of carbon containing impurities in or near the filament of the ion source and not of ambient origin. They found that the height of the mass peak, 44 A.M.U., was directly proportional to the amount of oxygen present in the ion source-mass spectrometer system.

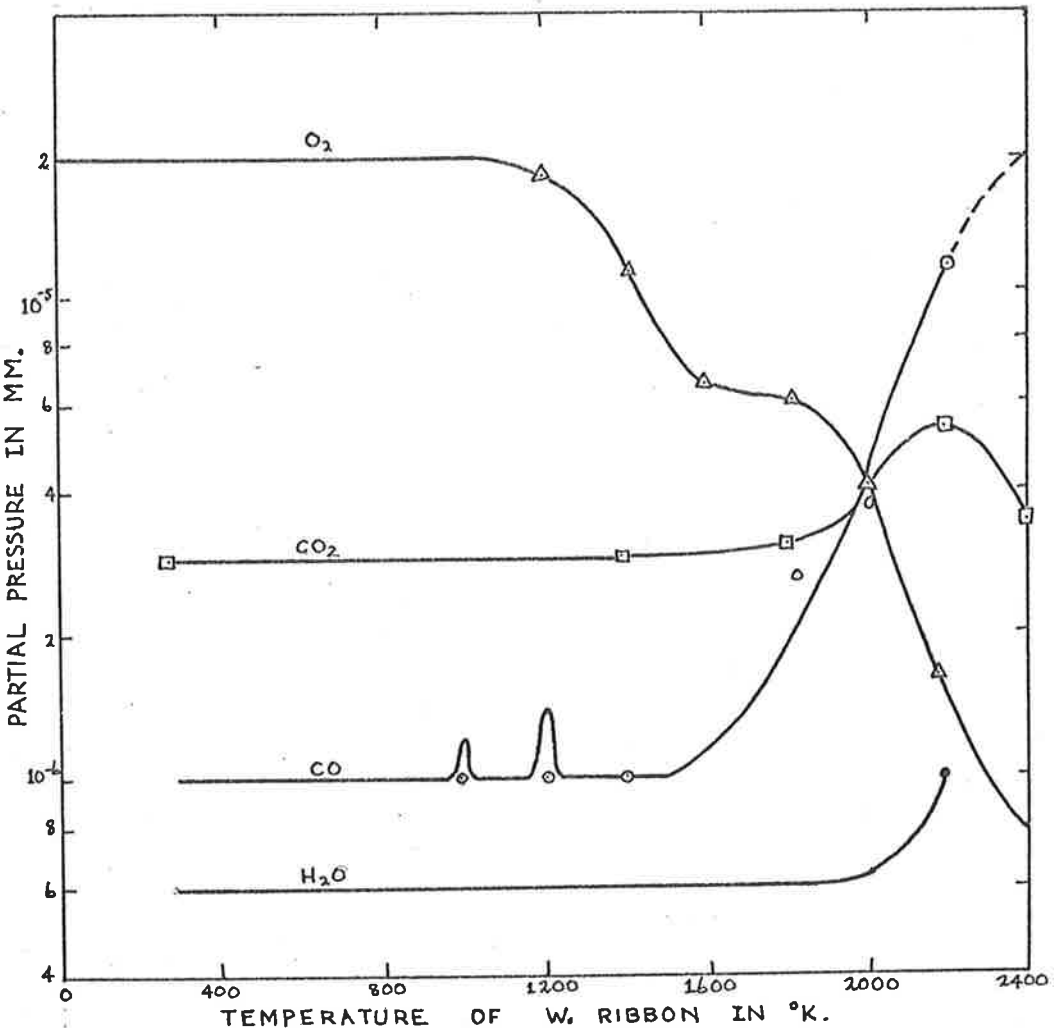

FIG. 4·7: VARIATION OF PARTIAL PRESSURES OF O_2, CO_2, CO AND H_2O AS A FUNCTION OF TEMPERATURE. (The graph is taken from the work of Becker et al (1961)).

4.4.2 THE ATOMIC OXYGEN PROBLEM

Through the years, since the advent of rocket-borne scientific instruments, the composition and density of the earth's atmospheric constituents have been determined by various methods such as satellite drag, E.U.V. extinction measurements, mass spectrometers, incoherent scatter, and from the diffusion spreading of chemiluminscent vapour clouds (see section 1.5.2). All these methods yield results which are reasonably consistent, as far as the non-reactive gases (N_2, Ar, He, etc) are concerned, but when measurements of the reactive, such as atomic oxygen, are made they give different results and, as a consequence, the concentration of the reactive species in the atmosphere is not well known.

In the case of atomic oxygen the determination of its absolute profile in the atmosphere seems to have evolved into a contest between the atmospheric research group of the University of Bonn (W. Germany) and that of the University of Minnesota (U.S.A.). In fact, in his survey of mass spectrometer measurements of the neutral atmosphere at 120 Km, von Zahn (1967) found that theoretical models give a value for the ratio of atomic to molecular oxygen, $n(O)/n(O_2)$, of approximately 4, whereas from mass spectrometer measurements this is only approximately one. Moe (1973), in re-examining the mass spectrometer density data and those derived from observations of drag force on satellites, presented a model in which $n(O)/n(O_2)$ is 1.6 at 120 Km. Von Zahn (1967) suggested that a considerable loss of atomic oxygen occurs in the ion source of mass spectrometers by both trapping at the walls and recombination to N_2O or CO_2 or both. He concluded that all atomic oxygen data taken with a mass spectrometer should be considered as a lower limit and could be in error by as

much as a factor of four. In another article von Zahn (1970) compared drag measurements at 150 Km with various density measurements and came to the conclusion that if it is assumed that the mass densities derived from drag data were high by 10%, whereas mass spectrometer measurements of atomic oxygen were low by a factor of 3 to 5, or even more, agreement could be obtained. The Minnesota $n(O)/n(O_2)$ values are even lower than these factors and lie in the range 0.4 to 0.7. Nier (1972) in defending the low values of atomic oxygen determined by mass spectrometers flown by his research group made a comparison between atmospheric densities determined from the low-altitude satellites OVI-15 and OVI-16, and those computed from mass spectrometer data and came to the conclusion that mass spectrometer data are lower by about a factor of 1.4 than those determined from satellite drag.

Since the low value of atomic oxygen measured with mass spectrometers is due to wall reactions of atomic oxygen with the ion source, the only way to measure the correct value of atomic oxygen is to suppress all chemical reactions from taking place at the ion source surfaces. To achieve this the German group (Offermann and Trinks (1971)) suggested the method of helium cooling the inner surfaces of the ion source whereby virtually all the particles impinging on the walls are frozen so that only particles coming directly from the atmosphere and suffering no collisions with the walls of the chamber will be ionized, and hence analyzed by the instrument.

Two rocket payloads each containing two mass spectrometers, one with a helium cooled ion source and the other with a conventional ion source, have been launched from Sardinia aboard Skylark rockets. The first payload

was launched on October 13th, 1970, and the second on February 7th, 1971. From these flights Offermann and von Zahn (1971), Offermann et al (1972) and Offermann and Grossmann (1973) reported a measured ratio of atomic to molecular oxygen ($n(O)/n(O_2)$) of 3.8 at 120 Km and of 13.6 at 150 Km, a value which is much higher than any values obtained in previous experiments with uncooled ion sources. Furthermore, only traces of mass 44 have been measured during these flights with the cooled ion source, the peak being two orders of magnitude lower than that of a comparable experiment with an uncooled ion source. Thus, they have been able to claim that for the first time true ambient CO_2 and atomic oxygen has been measured with mass spectrometers.

At the same time, the Minnesota group developed an ion source which, when used in a "flight-through" mode, the instrument detects only particles coming directly from the atmosphere, rejecting all the particles which have suffered a wall collision with the surface of the ion source (Hayden et al (1974)). Unfortunately, this type of ion source can only be used on satellites or high speed spacecraft since its mode of operation utilizes the velocity of the vehicle to distinguish between incoming ambient particles and ambient particles which have struck the instrument surfaces and become accommodated.

This ion source has been flown on the Atmosphere Explorer-C satellite and the measured densities of atomic and molecular oxygen have been published by Nier et al (1974). From their graphed data, the ratio of $n(O)/n(O_2)$ at 150 Km is approximately 3, which is still much lower than the value of 13.6 obtained by the Bonn group and the value of 8.2 from CIRA (1972) at this altitude.

Henderson (1974), using silver film sensors, measur-

ed the concentration of atomic oxygen at Wallops Island, and at the altitude of 120 Km obtained a density of atomic oxygen of approximately 5×10^{10} particles/cm^3, while CIRA (1972) gives a number density of 1.4×10^{11} particles/cm^3, and Offermann and Grossmann (1973) measured 1.01×10^{11} particles/cm^3 with their helium cooled ion source, a value which is approximately a factor of two higher than that of Henderson (1974). In his article, Henderson (1974) pointed out that his measured value of atomic oxygen density could be in error by as much as $\pm 50\%$.

Subsequent to the published data of the Bonn group on the ratio of $n(O)/n(O_2)$ at 120 Km, Lake and Nier (1973) set up a laboratory experiment to evaluate the loss of atomic oxygen in an ion source similar to that used on rocket-borne mass spectrometers. From their laboratory results, they concluded that in rocket flights using similar instruments the computed atomic oxygen densities, assuming no-loss conditions, may be low by a factor of 2.5, a factor which is again lower than the one suggested by von Zahn (1967, 1970) and then determined experimentally on two rocket flights with helium cooled ion source, but higher than the value put forward by Nier (1972) and Moe (1973).

No plausible expanation for the difference between the values of atomic oxygen densities determined by the Bonn and Minnesota groups has been put forward so far. At the present mass spectrometers cannot be directly calibrated for atomic oxygen in the laboratory because of complex problems in producing a beam of atomic oxygen of known concentration but, rather, the sensitivity of the instrument for atomic oxygen has to be determined indirectly, by computation, from that of molecular oxygen and methane. So it may well be that the discrepancy in the value of atomic oxygen measured by the

two groups is due to different methods of calibration of the analyzers. The Bonn group employs a dynamic gas flow system, while the Minnesota and other groups use a static method.

Another reason why mass spectrometers data of atomic oxygen obtained by different groups of experimenters could be different by a factor of 2 or 3 is that, as it will be explained in the next section, the atomic oxygen "conditions" the surface, i.e., the losses of atomic oxygen depend on the concentration of atomic oxygen and the time of exposure of the ion source surfaces to this concentration.

4.4.3 SURFACE INTERACTION PROCESSES

The loss coefficients of atomic oxygen at flux levels comparable to those in the upper atmosphere have been determined experimentally by Hacker et al (1961), Riley and Giese (1970), Wood (1971), Lake and Nier (1973), and Lake and Mauersberger (1974) for different metals such as aluminium, gold, silver, etc. Different authors for the same material have reported different values for the loss coefficients of atomic oxygen and the lack of agreement between the measurements is likely to be due to different surface conditions of the materials and the exposure time.

Lake and Mauersberger (1974) in a laboratory experiment in which they simulated mass spectrometer measurement of atomic oxygen in the upper atmosphere found that when a metal surface is exposed to atomic oxygen for the first time heavy losses of atomic oxygen occur until a monolayer of atomic oxygen is formed on the surface and then the losses remain almost constant. The major surface reaction is CO_2, which is formed in a reaction involving atomic oxygen from the beam and CO from the bombarded walls of the ion source (Lake and Nier (1973)). The production of CO_2 increases to a maximum and then falls off dramatically. This maximum production of CO_2 corresponds to the formation of the atomic oxygen monolayer and when the carbon on the surface is depleted the atomic oxygen converts to molecular oxygen.

Becker et al (1961) have shown that oxygen reacts preferentially with carbon at the surface of a hot filament and that there is a continuous replacement of the surface carbon by diffusion from the bulk which leads to a continuous generation of CO, CO_2 and, to a lesser extent, H_2O. They found that the diffusion rate of the carbon from the bulk is proportional to the concentration gradient and increases

exponentially as 1/T, where T is the temperature in degrees Kelvin. They also discovered that the filament could be made carbon free by glowing it at 2200°K in an oxygen atmosphere at a pressure near 10^{-6} torr for 10 to 60 hours.

Evidence that the carbon used by the atomic oxygen to form CO and CO_2 is diffused to the surface from within the material are to be found in the works of Offermann et al (1972), Hedin et al (1973) and Lake and Mauersberger (1974). Offermann et al (1972) noticed that even if special care is taken in preparing the instrument before flight so as to avoid any contamination by oil vapours no improvement of the ratio n(44)/n(28) inflight was obtained, while in a rocket flight by Mauersberger (1971) (from the paper of Lake and Nier (1973)), in which the ion source cover was removed near apogee, the atomic oxygen losses at 130 Km (apogee) were much higher than those at 110 Km. In another flight experiment in which a quadrupole mass spectrometer was flown on the Ogo 6 satellite, Hedin et al (1973) found that only after about 20 days in orbit the losses of atomic oxygen due to the reactions on the walls of the ion source to produce CO and CO_2 become insignificant and practically all of the oxygen recombined to form O_2. Lake and Mauersberger (1974), in their laboratory experiment, exposed the ion source to a beam of atomic oxygen and, after a certain time, turned the beam off and left the system pumping for 36 hours. They noticed that when the beam was turned on again the maximum production of CO_2 was much smaller and occurred earlier.

It follows then that materials which contain carbon are not suitable for ion sources. One of the most common materials, stainless steel, which is used extensively both in laboratory and flight experiments, is then a bad choice since it contains large quantities of carbon (0.08 to 0.2%, depend-

ing on the type of stainless steel (Handbook of Chemistry and Physics (1972)) and hydrogen. Some experimenters (Niemann et al (1973), Hedin et al (1973) and Trinks and von Zahn (1975)) have flown gold-plated stainless steel ion sources but, as Hedin et al (1973) have discovered, stainless steel acts as a reservoir for carbon which slowly diffuses to the surface through the bulk and gold layer.

Aluminium, because of its method of preparation, does not contain carbon or hydrogen impurities so that it is a better material for ion sources. Even the loss coefficient for atomic oxygen is lower than that of other materials. Lake and Mauersberger (1974) reported losses coefficients of 0.35 for gold and nichrome while for aluminium this is only 0.2. Unfortunately, aluminium in an atmosphere of atomic oxygen forms aluminium oxide which is an insulator, and the oxide surface may eventually charge up leading to a loss in the ion sensitivity due to stray electrostatic fields building up which may defocus the ion beam. A solution to this would be to gold-plate aluminium.

The atomic oxygen losses depend on a variety of parameters such as exposure time, ion source material and geometry, temperature and surface conditions (cleanliness) and, from the above discussion and those of the previous sections, it follows that the ion source is the most critical part of the mass spectrometer experiment, and it would be advantageous to eliminate the heated cathode filament and to generate the electron beam by other means, such as by the use of multipliers (Trinks (1973)), radio-active sources, field emission or photo-emission. Unfortunately, at the present stage of development, these are still too low in intensity or are too bulky for rocket and satellite experiments. Trinks (1973) has flown unsuccessfully his cold ion source on four

rockets so that at present it is impossible to assess how effective is this type of ion source when it comes to measure atmospheric atomic oxygen, CO, and CO_2 gases.

Further, wall reactions and recombination of the gas particles in the ionizing region of the ion source should be suppressed. This has been achieved by Offermann and Trinks (1971) in which they developed an ion source, the inner parts of which are cooled down to $8^{o}K$ by means of supercritical helium. Data on a modified version of the helium cooled ion source during supersonic rocket flights have been published by Offermann and Tatarczyk (1973) and Offermann and Scholz (1973). This modification is necessary so that neutral gas composition in the lower thermosphere and mesosphere (65 to 100 Km) can be measured.

4.4.4 TYPES OF ION SOURCES

During a rocket or satellite flight, the atmospheric particles enter the ion source of the mass spectrometer with velocities which are usually larger than the most probable thermal velocity of the ambient particles, and as a result the mass spectrometer would have to be calibrated in a wind tunnel to simulate the flight conditions. Unfortunately, accurate flight simulation of fast moving objects in the atmosphere such as rockets or satellites is very difficult to realize so that, instead, mass spectrometers are calibrated with diffuse gases at room temperature. The densities measured at the ion source during flight are, then, not the same as the ambient atmospheric densities, and it becomes necessary to determine a conversion factor which relates the densities in the ion source to the ambient densities. Depending on the type of ion source, this factor is a complicated function of the rocket velocity vector, the temperatures of the ion source and of the atmosphere, and gas-surface interactions at the ion source.

The ion sources flown on rockets or satellites are mainly of two types:

(a) Closed ion sources and

(b) Open ion sources.

Variations of these two types of ion sources are the:

(c) "Flight through" mode ion source of Hayden et al (1974).

(d) Helium cooled ion source of Offermann and Trinks (1971) and the

(e) Beam ion source of Melfi and Brock (1973).

Each type of the above mentioned ion sources have certain advantages and disadvantages when they are employed for atmos-

pheric composition and density measurements.

(a) The Closed Ion Source: The theory of the closed ion source is based on the following assumptions:

(1) That the pressure inside the ion source is low enough so that the mean free path is greater than the dimensions of the ion source enclosure. This means that the incoming particles must have a large number of collisions with the wall of the source so that full thermal accommodation to the ion source surface temperature takes place.

(2) The ion source is directly exposed to the atmosphere through an orifice the dimensions of which are very small compared to the inner area of the walls of the enclosure vessel of the ion source.

(3) At any altitude the average mass of the particles entering the ion source is equal to that of the particles leaving.

(4) The particles entering and those leaving the ion source possess Maxwellian velocity distributions.

The relationship between the densities of the particles in the ion source and the densities of the ambient particles is derived by equating the flux of the particles entering the orifice of the ion source to the flux of the particles leaving it.

In order to calculate the flux of the incoming particles a co-ordinate system OXYZ, fixed with respect to the ion source, but moving with a velocity vector $\underline{U}$ (rocket velocity) with respect to the atmosphere, is considered. The co-ordinate system (fig. 4.8) is such that the Z-axis passes through the centre of the ion source and the entrance orifice.

With this co-ordinate system and defining the following parameters:

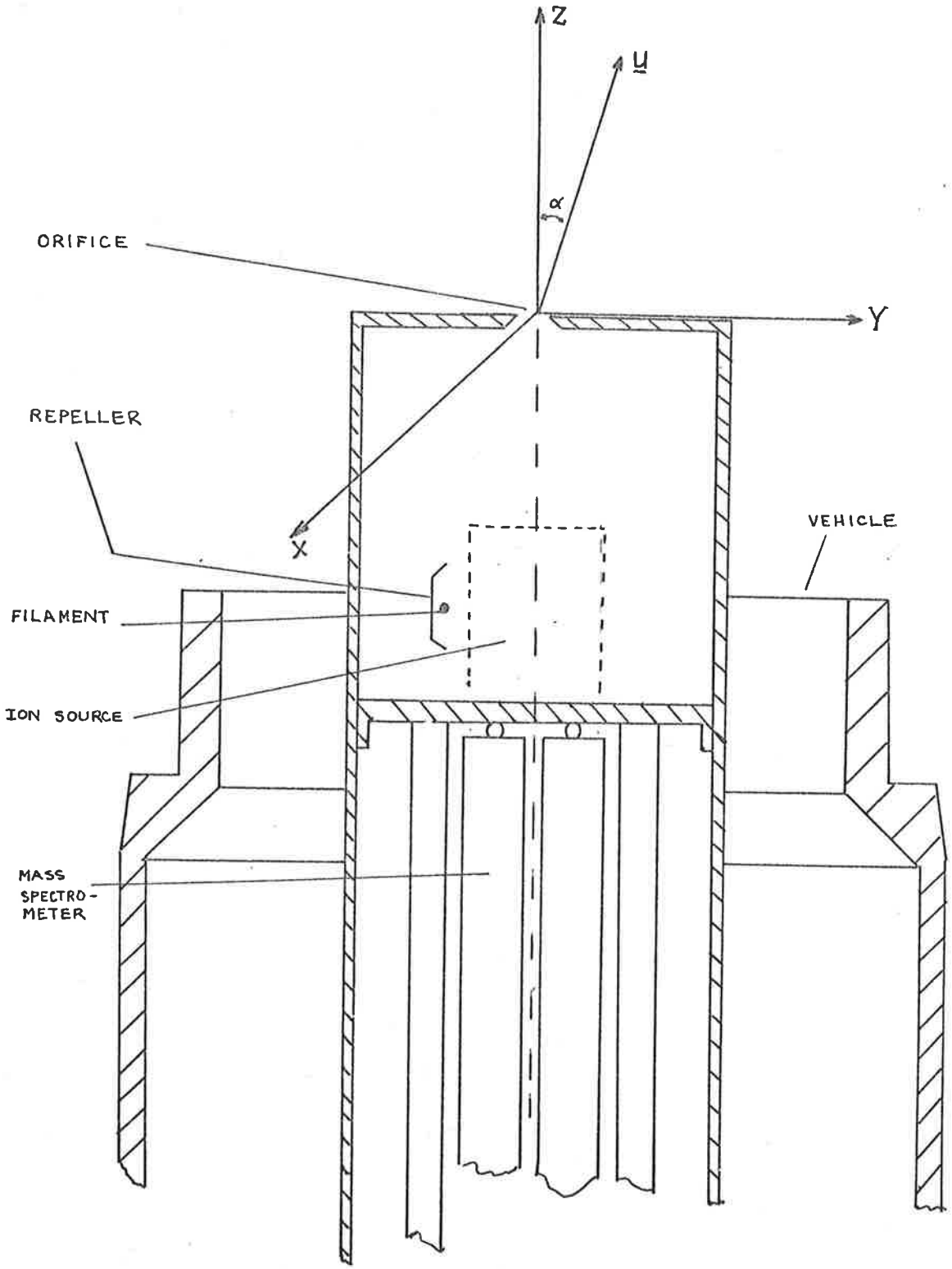

FIG 4·8: CROSS-SECTIONAL VIEW OF A CLOSED ION SOURCE

n_a = number density of the ambient particles

T_a = ambient temperature

m = mass of the particles

α = angle of attack (angle between the Z-axis and the velocity vector $\underline{U}$ of the rocket)

$$c_a = \sqrt{\frac{2KT_a}{m}} \qquad (4.25)$$

which is the most probable thermal velocity of the ambient particles.

$S = U/c_a$

$S_z = S.\cos\alpha$

T_{is} = temperature of the ion source

n_{is} = number density in the ion source

$$c_{is} = \sqrt{\frac{2KT_{is}}{m}} \qquad (4.26)$$

which is the most probable thermal velocity of particles, having been completely thermalized to the ion source's surface temperature.

The Maxwellian distribution of the incoming particles is:

$$f(V_x,V_y,V_z) = \left(\frac{m}{2\pi KT}\right)^{3/2}.\exp\left[-\frac{V_x^2 + V_y^2 + V_z^2}{c_a^2}\right] \qquad (4.27)$$

where V_x,V_y,V_z are the particles' velocity components along the X,Y,Z axes respectively.

By placing:

$$A = \left(\frac{m}{2\pi KT}\right)^{3/2} \qquad (4.28)$$

the distribution is simplified into:

$$f(V_x,V_y,V_z) = A.\exp\left[-\frac{V_x^2 + V_y^2 + V_z^2}{c_a^2}\right] \qquad (4.29)$$

With the co-ordinate system, which is fixed with respect to the surface of the ion surface, and moving with a

velocity $\underline{U}$, the gas is transformed to a drifting Maxwellian gas and the relative particle velocity is given by $\underline{U} + \underline{V}$. Then the flux of the incident particles on the entrance surface of the ion source is:

$$\phi_i = n_a \cdot \int_{-U_z}^{\infty} \int_{-\infty}^{\infty} \int_{-\infty}^{\infty} (U_z + V_z) \cdot f(V_x, V_y, V_z) dV_x dV_y dV_z \tag{4.30}$$

Integrating equation (4.30) with the aid of the error function:

$$\operatorname{erf}(x) = \frac{2}{\sqrt{\pi}} \int_0^x \exp(-t^2) dt \tag{4.31}$$

the incident flux of the particles becomes:

$$\phi_i = \frac{\pi}{2} \cdot A \cdot n_a \cdot c_a^4 \cdot F(S_z) \tag{4.32}$$

where:

$$F(S_z) = \sqrt{\pi} \cdot S_z \cdot (1 + \operatorname{erf}(S_z)) + \exp(-S_z^2) \tag{4.33}$$

Similarly, the outgoing flux is:

$$\phi_o = n_{is} \cdot \int_{-\infty}^{0} \int_{-\infty}^{\infty} \int_{-\infty}^{\infty} V_z' \cdot f(V_x', V_y', V_z') dV_x' dV_y' dV_z' \tag{4.34}$$

$$= \frac{\pi}{2} \cdot A' \cdot n_{is} \cdot c_{is}^4$$

where:

$$f(V_x', V_y', V_z') = A' \cdot \exp\left[- \frac{V_x'^2 + V_y'^2 + V_z'^2}{c_a^2} \right] \tag{4.35}$$

is the Maxwellian distribution of the outgoing particles, and:

$$A' = \left(\frac{m}{2\pi K T_{is}} \right)^{3/2} \tag{4.36}$$

Then, if :

$$\phi_i = \phi_o, \tag{4.37}$$

it follows that:

$$n_{is} = (A/A').(c_a/c_{is})^4.n_a.F(S_z) \tag{4.38}$$

and hence:

$$n_{is} = \sqrt{T_a/T_{is}}.n_a.F(S_z) \tag{4.39}$$

$$n_a = \sqrt{T_{is}/T_a}.n_{is}/F(S_z) \tag{4.40}$$

and the conversion factor for the "ram effect" is:

$$R(T_a,T_{is},S_z) = \sqrt{T_{is}/T_a}/F(S_z) \tag{4.41}$$

and

$$n_a = R.n_{is} \tag{4.42}$$

The closed ion sources have been flown on rockets and satellites by a number of experimenter groups such as Hedin and Nier (1966), Reber and Harpold (1967), Hedin et al (1973) and Trinks and von Zahn (1975).

This type of ion source is particularly suitable to measure densities of non-reactive gases such as N_2, He, Ar, etc., and the density of atomic oxygen above about 300 Km and total oxygen content below this altitude. In the case of oxygen measurement, it is generally assumed that all the atomic oxygen atoms recombine to molecular oxygen on the ion source walls, before they are ionized and detected. However, the mass spectrometer is not able to distinguish between ambient molecular oxygen and the molecular oxygen resulting from the recombination of atomic oxygen, but, rather, total oxygen content $n(O_2) + \frac{1}{2}n(O)$ is measured. For satellite measurements, this does not represent a problem, since the perigee of satellites is usually greater than about 300 Km, and from CIRA (1972), at 300 Km, the ratio of atomic to molecular oxygen is 172, so that ambient molecular oxygen represents only about 0.6% of the total oxygen content, a value which is very small.

The problem is mainly whether 100% recombination of atomic oxygen occurs or not. Hedin and Nier (1966) from their flight of two rocket-borne mass spectrometers with closed ion sources came to the conclusion that only about 15% of the atomic oxygen recombined into molecular oxygen. Reber and Harpold (1967), in an effort to obtain a high recombination coefficient for atomic oxygen, flew a closed ion source, the walls of which were coated with silver oxide. Even in this case the amount of recombination was still considerably lower than what they anticipated.

More recent evidence of 100% recombination has been given by Hedin et al (1973) and Trinks and von Zahn (1975).

The abnormal results of Hedin and Nier (1966) and of Reber and Harpold (1967) can be explained by the fact that their instruments were flown on rockets and usually rocket flights last less than ten minutes: a time scale which is not long enough for the atomic oxygen losses in the ion source to be reduced sufficiently for atomic oxygen to recombine totally into molecular form. In fact, Hedin et al (1973) found, from their instrument flown on Ogo 6 satellite, that it took 20 days of flight before 100% recombination was observed.

One advantage of using closed ion sources in measuring atomic oxygen above 300 Km is that since atomic oxygen is measured quantitatively as molecular oxygen it is not necessary to calibrate the instrument for atomic oxygen, a calibration which, at present, is practically impossible.

(b) Open Ion Source: In the case of the open ion source, in order to find a relation between the measured densities in the ion source and the ambient densities, the following possibilities have to be considered:

(1) particles that enter the ionizing region directly from the atmosphere without suffering

wall collisions with the source's inner surfaces.

(2) particles that on entering the ionizing region come in contact with the wall surfaces but do not thermally accommodate to the surface temperature.

(3) particles that on colliding with the walls of the ion source are only partially accommodated.

(4) particles that make multiple surface collisions before entering the ionizing region and are fully thermally accommodated.

(5) particles that are slowly emitted from the surface of the ion source (desorption).

(6) particles that chemically react with the ion source walls.

The formulation of the theory which takes into consideration all the above possibilities is at present practically impossible. This is because gas-surface interactions such as recombination, adsorption, desorption and chemical reaction which occur at the walls of the ion source are poorly known. Hedin et al (1964) have derived a function which relates the measured densities of the particles in the ion source to those of the ambient atmosphere for a simplified spherical model of the ion source. In the formulation of their theory they assumed that the atmospheric particles completely accommodate to the temperature of the walls of the ion source and that its geometry is such that it can be approximated by two spherical surfaces Σ_1 and Σ_2, as in fig 4.9. The spherical surface Σ_2 has an opening subtended by a cone with a half angle θ.

With these assumptions they calculated the density at the centre of the ion source enclosed by the surface as

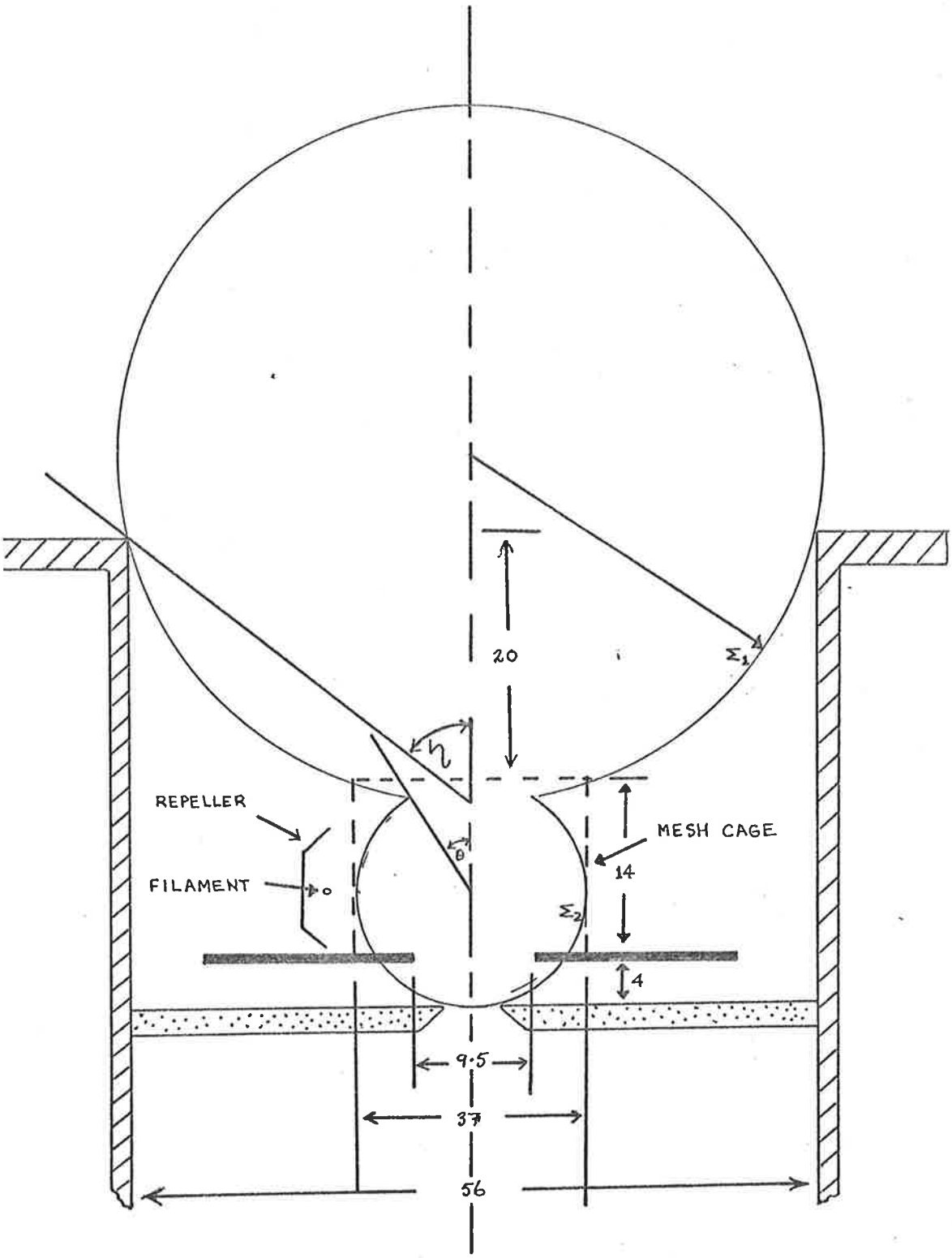

FIG. 4·9: SCHEMATIC VIEW OF THE CROSS-SECTION OF THE MASS SPECTROMETER ION SOURCE. WITH THIS GEOMETRY $\theta = 34°$ AND $\eta = 52°$. ALL DIMENSIONS ARE IN mm.

the sum of two terms: n_1 due to particles which have been reflected off surface Σ_2 after entering the inner enclosure either directly from the atmosphere or by reflection from surface Σ_1; and n_2 due to particles which reach the centre of Σ_2 directly from the atmosphere without any wall collision. They found that:

$$n_1 = n_a.\sqrt{T_a/T_{is}}.\left[F(S_z).\ K_1\sin^2\eta.\cos^2\eta/(1 - K_1.\cos^2\eta) + E(S_z,S_r,\eta)\right].\ K_2.\sin^2\frac{\theta}{2}.\cos^2\frac{\theta}{2}/(1 - K_2.\cos^2\frac{\theta}{2}) \tag{4.43}$$

and

$$n_2 = (n_a/2).\left[1 + \mathrm{erf}(S_z) - M_o^*.\exp(-S_z^2) - H^*(S_z,S_r,\theta)\right] \tag{4.44}$$

where

$$E(S_z,S_r,\eta) = F(S_z) - 2.M_o.\exp(-S_z^2) - H(S_z,S_r,\eta) \tag{4.45}$$

$$H(S_z,S_r,\eta) = 2.\exp(-S_z^2 - S_r^2).\sum_{m=1}^{\infty}(S_r^2)^m/(m!).\sum_{k=1}^{m}(\sin^2\eta)^k.M_k \tag{4.46}$$

$$M_o = \tfrac{1}{2}.\cos^2\eta.F(S_z.\cos\eta).\exp(S_z^2.\cos^2\eta) \tag{4.47}$$

$$M_1 = (3/2 + S_z^2.\cos^2\eta).M_o - \tfrac{1}{4}.\cos^2\eta \tag{4.48}$$

$$M_k = \left[(S_z^2.\cos^2\eta + \tfrac{1}{2}.(4k - 1).M_{k-1} - \tfrac{1}{2}.(2k - 1).M_{k-2}\right]/k \tag{4.49}$$

$$S_r = S.\sin\alpha \tag{4.50}$$

θ and η are defined as in fig 4.9.

$$H^*(S_z,S_r,\theta) = \exp(-S_z^2 - S_r^2).\sum_{m=1}^{\infty}(S_r^2)^m/(m!).\sum_{k=1}^{m}(\sin^2\theta)^k.M_k^* \tag{4.51}$$

$$M_o^* = (1 + \mathrm{erf}(S_z.\cos\theta)).\cos\theta.\exp(S_z^2.\cos^2\theta) \quad (4.52)$$

$$M_1^* = (\tfrac{1}{2} + S_z^2.\cos^2\theta).M_o^* + (S_z.\cos^2\theta)/\sqrt{\pi} \quad (4.53)$$

$$M_k^* = \left[(S_z^2.\cos^2\theta + \tfrac{1}{2}.(4k - 3)).M_{k-1}^* - \tfrac{1}{2}.(2k - 3).M_{k-2}^*\right]/k \quad (4.54)$$

and

K_1, K_2 = the probability of a particle being re-emitted after colliding with Σ_1, Σ_2, respectively.

In deriving equation (4.43) and (4.44), Hedin et al (1964) also assumed that the cosine law for diffuse reflection holds for the re-emission of the particles from the walls and that K_1 and K_2 are constants independent of time and of positions on the respective surfaces.

The weakness of this model is that it is practically impossible to know whether the hypotheses on which the model is based are fulfilled or not during a rocket flight. Furthermore, the name given to this type of ion source is misleading. This is because the measured density n_{is} is mainly determined by particles which have suffered wall collisions with the ion source, and hence the uncertainty in the absolute values of K_1 and K_2 give rise to erratic values of the ambient density n_a. In fact, if it is assumed that there is no absorption on the walls ($K_1 = K_2 = 1$) and that the instrument is used in the laboratory ($S_z = S_r = 0$), then:

$$n_1 = n_a.\sqrt{T_a/T_{is}}.\cos^2\frac{\theta}{2} \quad (4.55)$$

and,

$$n_2 = n_a.\sin^2\frac{\theta}{2}$$

With the geometry of fig 4.9, $\theta = 34^o$, and assuming

$T_a = T_{lab} = 20^oC$ and $T_{is} = 50^oC$, then

$$n_1 = 0.87n_a \text{ and}$$

$$n_2 = 0.09n_a \tag{4.56}$$

so that

$$n_1/n_{is} = 89\% \text{ and}$$

$$n_2/n_{is} = 11\% \tag{4.57}$$

From this it follows that only 11% of the particles come directly from the atmosphere, while 89% suffer wall collisions at the ion source.

The values of K_1 and K_2 depend on the gas-surface interactions occurring on the ion source walls and, since these phenomena are poorly understood, K_1 and K_2 are usually assumed to be one. For inert gases (He, N_2, Ar, etc) such a choice may be a reasonable one, although adsorption on the walls of the ion source still takes place. But when reactive gases such as atomic oxygen are considered the value, $K_1 = K_2 = 1$, is a very bad one and the resulting atomic oxygen densities are underestimated. Hedin et al (1964) found by applying a least square fit to their mass spectrometer data, that the values of K_1 and K_2 obtained in this way were very close to unity for mass 28, but much less than unity for mass 16. However, because of the uncertainty associated with the parameters K_1 and K_2, in their final analysis of the data, they assumed $K_1 = K_2 = 1$ for all masses. Niemann et al (1973) in a more detailed evaluation of the gas-surface interactions found from their mass spectrometer data a value of $K_1 = 0.56$ and $K_2 = 0.44$ for molecular nitrogen, a big contrast with the unity coefficients usually employed in most mass spectrometers' data analysis, while for molecular oxygen these values were $K_1 = 0.21$ and $K_2 = 0.79$.

Mauersberger et al (1967) calculated the ambient number density by assuming three different models for the ion source:

(a) Closed ion source model in which the gas comes to complete thermal equilibrium with the walls of the ion source.

(b) Open ion source with complete thermal accommodation.

(c) Open ion source with no accommodation.

The number densities computed using these models, even for molecular nitrogen, are dramatically different. For example, from their graphed values at 120 Km, the density of molecular nitrogen is $2x10^{11}$ particles/cm^3 for model (a), $3.2x10^{11}$ for model (b) and $7.5x10^{11}$ for model (c).

As already mentioned, a solution to the gas-surface interaction has been found by the experimenters at University of Bonn in which they helium-cooled the walls of the ion source, such that for all atmospheric gases of interest, except helium, the assumption that the values of $K_1 = K_2 = 0$ is valid, and the gas density in the ion source is virtually constituted of only directly incoming particles from the atmosphere. They have shown that reactive species such as atomic oxygen can be successfully measured if wall reactions are eliminated.

(c) Other Types of Ion Sources: Because of the high chemical activity of atomic oxygen and the uncertainty in the values of K_1 and K_2 for the less reactive gas such as molecular oxygen and nitrogen several attempts have been made to eliminate or reduce the gas-surface interactions at the walls of the ion source. The attempt made by the Bonn group has been very successful and has shown that reactive species can be correctly measured if wall reactions are suppressed.

Hayden et al (1974) have discussed in detail a Nier type ion source which makes use of the high velocity of the vehicle to discriminate against particles that suffer wall collision, while Melfi and Brock (1973), from the studies of the kinetic theory of a drifting Maxwellian gas and a near specular scattering law, devised an ion source the geometry of which is such that the gas-surface scattering and surface reactions are minimized. The ion source is made of two conical sections separated by a certain distance.

Unfortunately, this type of ion source has not yet been flown on rockets or spacecraft so that it is not possible to say whether it is able to measure accurately the densities of the reactive species in flight.

4.5.1 THE DETECTOR

The neutral atmospheric particles are ionized in open or closed ion sources and the ions, after passing through the mass spectrometer, are generally detected with a Faraday cup collector or with a suitable electron multiplier. The sensitivity of the quadrupole mass spectrometer is usually in the range 10^{-1} to 10^{-4} amperes /torr partial pressure of constituents and hence it could be used without an electron multiplier in the altitude range 110-200 Km. However, without the use of a mutiplier it is not possible to measure the minor atmospheric constituents such as argon, helium, CO_2, etc., and furthermore, the instrument has to be operated in a low resolution mode in order to maximize the transmission.

For altitudes above 200 Km the particle densities are low, and the use of an electron multiplier becomes essential. It may even become necessary to measure single ions, in which case high gain electron multipliers operating in a counting mode have to be used.

One of the so many problems encountered in employing mass spectrometers for atmospheric composition and density measurements is the dynamic range and the time response of the ion detector. The number densities of the principal atmospheric gases are presented in table 4.1. At 120 Km the density of the most abundant gas, molecular nitrogen, is 3.8×10^{17} molecules/m^3 while argon, the least abundant, at 250 Km is 1.5×10^{11} atoms/m^3. It follows then that if a mass spectrometer is used to measure the neutral densities in the altitude region 120-250 Km, the detector must have a dynamic range of at least six orders of magnitude ($\simeq 10^6$) and must have a time response such that it can follow a change in the

Table 4.1

CIRA (1972) NUMBER DENSITIES (PARTICLES/M^3) OF THE PRINCIPAL ATMOSPHERIC GASES.

Altitude (Km)	$n(N_2)$	$n(O_2)$	$n(O)$	$n(Ar)$	$n(He)$	$\frac{n(Ar)}{n(N_2)}$	$\frac{n(Ar)}{n(O)}$	$\frac{n(He)}{n(N_2)}$	$\frac{n(He)}{n(O)}$
120	3.8×10^{17}	5.4×10^{16}	1.4×10^{17}	1.5×10^{15}	3.45×10^{13}	3.9×10^{-4}	1.1×10^{-2}	9×10^{-5}	2.5×10^{-4}
150	2.7×10^{16}	2.9×10^{15}	2.4×10^{16}	4.6×10^{13}	1.7×10^{13}	1.7×10^{-3}	1.9×10^{-3}	6.4×10^{-4}	7.1×10^{-4}
200	2.6×10^{15}	2.1×10^{14}	5.5×10^{15}	1.8×10^{12}	1.1×10^{13}	7×10^{-4}	3.3×10^{-4}	4.1×10^{-3}	2.0×10^{-3}
250	4.3×10^{14}	2.7×10^{13}	1.9×10^{15}	1.5×10^{11}	8×10^{12}	3.4×10^{-4}	7.9×10^{-5}	1.8×10^{-2}	4.2×10^{-3}

intensity of the output ion current of a factor of about 10^4 in times of the order of milliseconds.

Various methods have been devised and employed in overcoming the problem of the wide dynamic range of the output signal of the analyzer. For instance, Mauersberger et al (1967) used a Faraday cup collector with two linear electrometers of different input resistors, while Bitterberg et al (1970), Trinks and von Zahn (1975), etc., have employed discrete dynodes electron multipliers and measured the amplified ion current with electrometers having logarithmic response. Spencer et al (1973) used an ion source in which the emission of the ionizing electron current was automatically adjusted so that the output signal from the electron multiplier was always on scale.

The discrete dynodes electron multipliers, even though in the past have been widely used in atmospheric research experiments, for many rocket and satellite applications, ~~they~~ are too big and cumbersome and they are being replaced with continuous channel electron multipliers (C.E.M.) commonly known as channeltrons. This is particularly true when digital rather than analog output is of interest.

4.5.2 THE CHANNEL ELECTRON MULTIPLIER

The inherent advantages of the continuous channel electron multipliers are: (a) low power consumption, (b) light weight, (c) physically small and simple to use, low background noise, high gain, rapid time response and rugged and respond to a wide variety of energetic radiation. The disadvantages are: a maximum counting rate of about 10^5 counts/sec. compared with about 10^7 counts/sec. of the discrete dynode electron multipliers, and degradation of gain with time (fatigue).

In its simplest form, the channel electron multiplier or channeltron is a straight glass capillary tube having dimensions such that the length to the inside diameter ratio is between 50 and 100. The internal diameter is usually between 0.7 and 2.2 mm. A layer of special semiconducting material, having secondary electron emission characteristics suitable for electron multiplication processes is deposited over the interior surface of the tube. The ohmic resistance of this semi-conducting layer is generally in the range 10^9 - $10^{10}\Omega$ for tubes with a film of metallic lead on the internal surface, and 10^{10} - $10^{11}\Omega$ for tubes of vanadium-phosphate glass.

When a potential difference is applied between the ends of the tube, an axial electric field is established along its length. Then, any electron ejected from the inside surface, either by means of photoelectric or secondary emission processes, will be accelerated along the tube and if it acquires sufficient energy ($>$ 50eV) on collision with the wall of the channel, generates secondary electrons. The resulting electron cloud is then further accelerated along the tube by the electric field until it strikes the wall again and generates more secondary electrons. The process is re-

peated many times and this avalanching mechanism produces a large number of electrons at the positive end of the tube. With a potential difference of 2.5 to 3.5 KV between the input and output ends of the channel, a saturated electron gain as high as 10^8 can be obtained, and its duration (full width at half height) is of the order of 10 nanoseconds. The saturation current is generally within a factor of 3 to 4 below the quiescent or standing current of the multiplier (Adams and Manley (1965)).

Straight channeltrons operated in this mode give rise to an output pulse with a rather long risetime of the order of 0.5 microsecond. This is much longer than the estimated transit time of the electron avalanche along the tube which is only a few tens of nanoseconds. This feature of the risetime output pulse is due to the ionization by the secondary electron cloud of the residual gas at the output end of the channel. Under the influence of the applied electric field, the ions then drift toward the more negative potential at the input end of the channel where they start a new electron cascade. The process is repeated and thus a sequence of "after pulses" may be observed which are revealed by the "staircase" appearance in the leading edge of the pulse (Yellin et al (1970), Evans (1965), etc.)

As a direct consequence of the ionization of the residual gas particles, the gain of the channeltron is sensitive to the changes in ambient pressure. In order to prevent the feedback of positive ions to the input end of the tube and thus eliminate the dependence of the gain on pressure, curved or spiral channeltrons are used. The gain is then independent of pressure for pressures less than 5×10^{-4} torr and the pulse is very narrow, of the order of 10 nanoseconds.

4.5.3 THE GAIN OF THE CHANNELTRON

The gain of a channeltron is a function of a number of parameters: the more important are the axial potential gradient, the shape and the dimensions of the tube, the secondary emission characteristics of the emissive layer and the presence of strong magnetic fields. For values of the gain below 10^7, the gain is an exponential and very steep function of the applied voltage. Above 10^7, saturation effects are observed which have been studied in some detail by a number of authors such as Evans (1965), Bryant and Johnstone (1965), Schmidt and Hendee (1966), Andresen and Page (1971) and Harris (1971), while Loubet and Barat (1973) have derived a theoretical expression for the gain of a C-shaped channeltron.

The channeltron is capable of producing two pulses of the same amplitude separated in time only by the pulse duration. However, since the wall resistance is generally 10^9 - $10^{11}\Omega$, the current available to be transformed into electron space current, and hence signal, is limited. If the pulse repetition rate is too high, at some point towards the output, the wall current is depleted enough to reduce the accelerating electric field, the energy gained by electrons between collisions along the tube, and therefore the secondary emission ratio, so that further gain is not achieved. A period exists similar to the Geiger and proportional counters during which the amplitude of the pulses is reduced dramatically. The period, or dead time, is connected with the RC relaxation time of the channel, during which surface charge is being redistributed, and it can be reduced by decreasing the ohmic resistance of the semi-conducting strip.

In fact, Mullard Pty Ltd (U.K.), at the author's

request, has made special types of channeltrons designated X812BL which have a resistance of $2 \times 10^8 \Omega$ and 1 cm slit instead of funnels. The counting rate of these channeltrons is of the order of 1 MHz and from preliminary results they do not seem to show significant fatigue effects. The channeltrons have been used as E.U.V. detectors on the Aerobee grazing incidence spectrometer.

Egidi et al (1969) have found that the asymptotic gain G_∞ of the lead glass channel electron multipliers is inversely proportional to the incident flux and derived the following empirical formula for it:

$$G_\infty = 1.3 \times 10^{10}/J \qquad (4.58)$$

where J is the incident flux in particles/second.

A typical pulse counting circuit for a channeltron is shown in fig. 4.10. In this circuit R_L is the load resistor and C_s is the sum of the input capacitor of the pulse amplifier and the stray capacitors. For a channeltron with a pulse amplifier circuit, which will be described in the next chapter, C_s has been measured to be 20pF. The amplitude of the output pulse is then given by:

$$V = \frac{\text{total charge}}{\text{capacitance}} = \frac{Q}{C_s} \qquad (4.59)$$

$$= \frac{1.6 \times 10^{-19} \times G_\infty}{C_s}$$

From equation (4.58) it follows that for counting rates of 10^5 and 10^3 pulses/sec., the values of the asymptotic gain are 10^5 and 10^7 respectively. Thus, for $G_\infty = 10^7$, V = 80mV and for $G_\infty = 10^5$, V = 0.8mV. This means that if the counting rate is too high, the mean height of the pulses may fall below the threshold of the amplifier and the counting rate will be low.

In the circuit of fig. 4.10, if the values of R_L

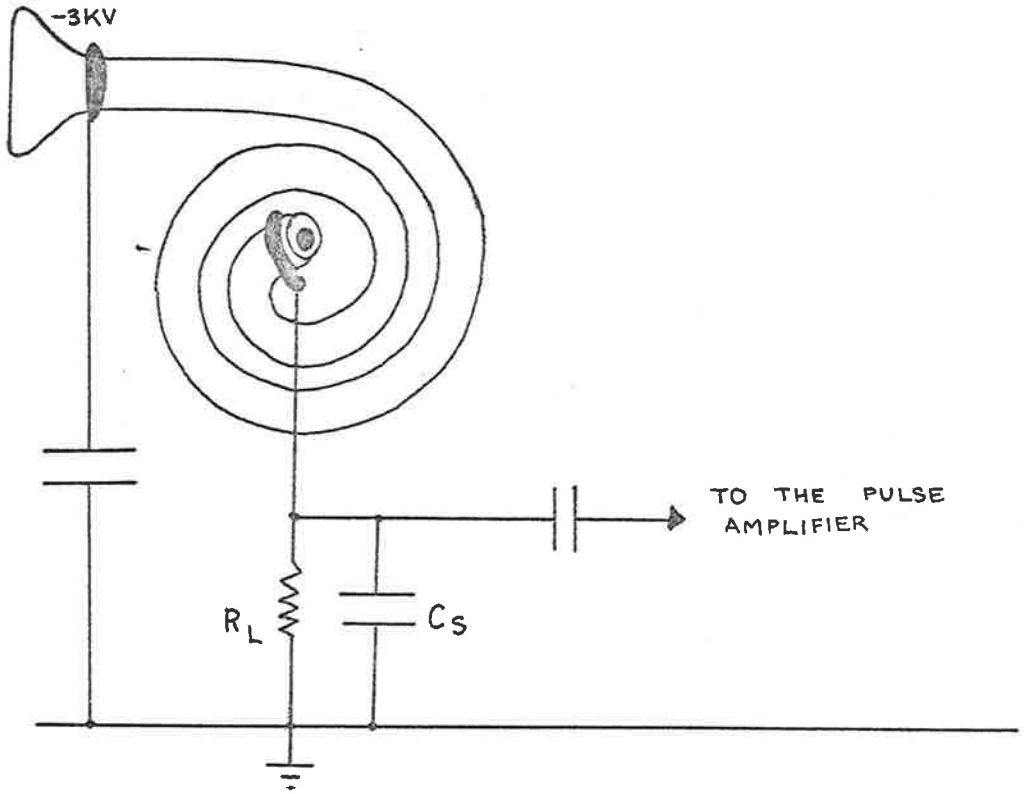

FIG. 4·10 SHOWS A TYPICAL PULSE COUNTING CIRCUIT FOR A CHANNELTRON.

is too big, then all the charge will be "dumped" on the capacitor C_s, and the pulse height is given by equation (4.59). However, if R_L is not very large and C_s is very small, then it is R_L which is responsible for the height of the pulses. The average current of each pulse is then:

$$I = 1.6 \times 10^{-19} \times G_\infty / t \qquad (4.60)$$

where t is the pulse width at half height in seconds. For a typical circuit t = 0.5 sec. and for $G_\infty = 10^7$, $I = 5 \times 10^{-6}$ amperes, so that the pulse height is:

$$V = IR = 5 \times 10^{-6} \times R_L \qquad (4.61)$$

and the maximum value of R_L is therefore 40 KΩ. Thus, if $R_L < 40$ K , the pulse height is given by equation (4.61) and if $R_L > 40$ K , it is given by equation (4.59).

To increase the counting rate, the load resistor, R_L in fig 4.10, can be replaced with a fast diode. The diode has a logarithmic current-voltage characteristics of the form:

$$I = I_o . (\exp(V/\eta V_T) - 1) \qquad (4.62)$$

where $V_T = T/11600$

T = temperature in degrees Kelvin

I_o = reverse saturation current

η = 1 for germanium diodes and 2 for silicon diodes.

If $V \gg V_T$, then it is possible to neglect the unity in (4.62) so that:

$$V = 2.3 \times \eta \times V_T \times \log I - \log I_o \qquad (4.63)$$

which can be put in the form:

$$V = a . \log I + b \qquad (4.64)$$

where a and b are constants which are functions only of the temperature.

By using the logarithmic characteristics of equation (4.64), it has been possible to increase the counting rate of the Mullard's B419BL channeltrons by a factor of three.

4.5.4 FATIGUE EFFECTS

Since their first applications in the various fields of research, the gain characteristics of channeltrons appeared to vary with the incident particle flux and time (fatigue). This problem is particularly important when the detectors are used on satellite or rocket-borne experiments where they are out of the control of the experimenter.

The mechanism of the gain fatigue has been poorly understood and it has been loosely attributed to the removal of surface contamination, since almost complete recovery is achieved if the detector is re-exposed to the atmosphere for a certain length of time. More recently, Prince and Cross (1971) suggested that in channeltrons an initial gain enhancement rather than a later gain fatigue occurs. Using the method of Auger electron spectroscopy, they found that on exposing the lead oxide glass to the atmosphere, the adsorbed oxygen concentration on the surface was 10 times the level of the stoichiometric value and came to the conclusion that it must be this high value of adsorbed oxygen concentration which is responsible for the initial gain enhancement. In their explanation of the electron emission enhancement mechanism, they assumed that on n-type semiconductors (such as lead glass) anionic absorption of oxygen occurs:

$$O_2 \text{ (gas)} + e^- \text{ (from n-type semiconductor)} \longrightarrow O^- \text{(adsorbed)}$$

and that during the secondary emission process, the anionic oxygen, O^-, donates an electron to the avalanching electron cloud and hence increasing the gain. As the surface oxygen is then depleted from the original level in high vacuum environments, the gain degrades, while at modest vacuum (between 10^{-4} and 10^{-6} torr) the multiplier performance should remain insensitive to time or variations in the operating pressure

since at these pressures there is enough oxygen present to maintain the excess surface oxygen concentration.

The theory of the gain fatigue presented by Prince and Cross (1971) is supported by the experimental findings of Egidi et al (1969) and Bennett and Thorpe (1970). In fact, Egidi et al (1969), using Bendix channeltrons at a pressure of 10^{-6} torr, found that the gain decreased with time, approaching an asymptotic value G_∞ given by equation (4.58), and, when the beam of the incident flux was turned off, the gain always recovered to its initial value. Whereas Bennett and Thorpe (1970), employing Mullard devices at a pressure of 10^{-8} torr, found that none of their multipliers showed any indication of the gain reaching an asymptotic value. They noticed that for a channeltron which was stored in a non-operating condition in a high vacuum chamber for 3000 hours the gain did not recover, while for another multiplier which was stored at a pressure of 10^{-6} torr it did recover.

Fig. 4.11 shows the fatigue effect of a B419BL Mullard channeltron in an atmosphere of argon at a pressure of 10^{-5} torr. This channeltron was used as an ion detector on the mass spectrometer payload L1003.

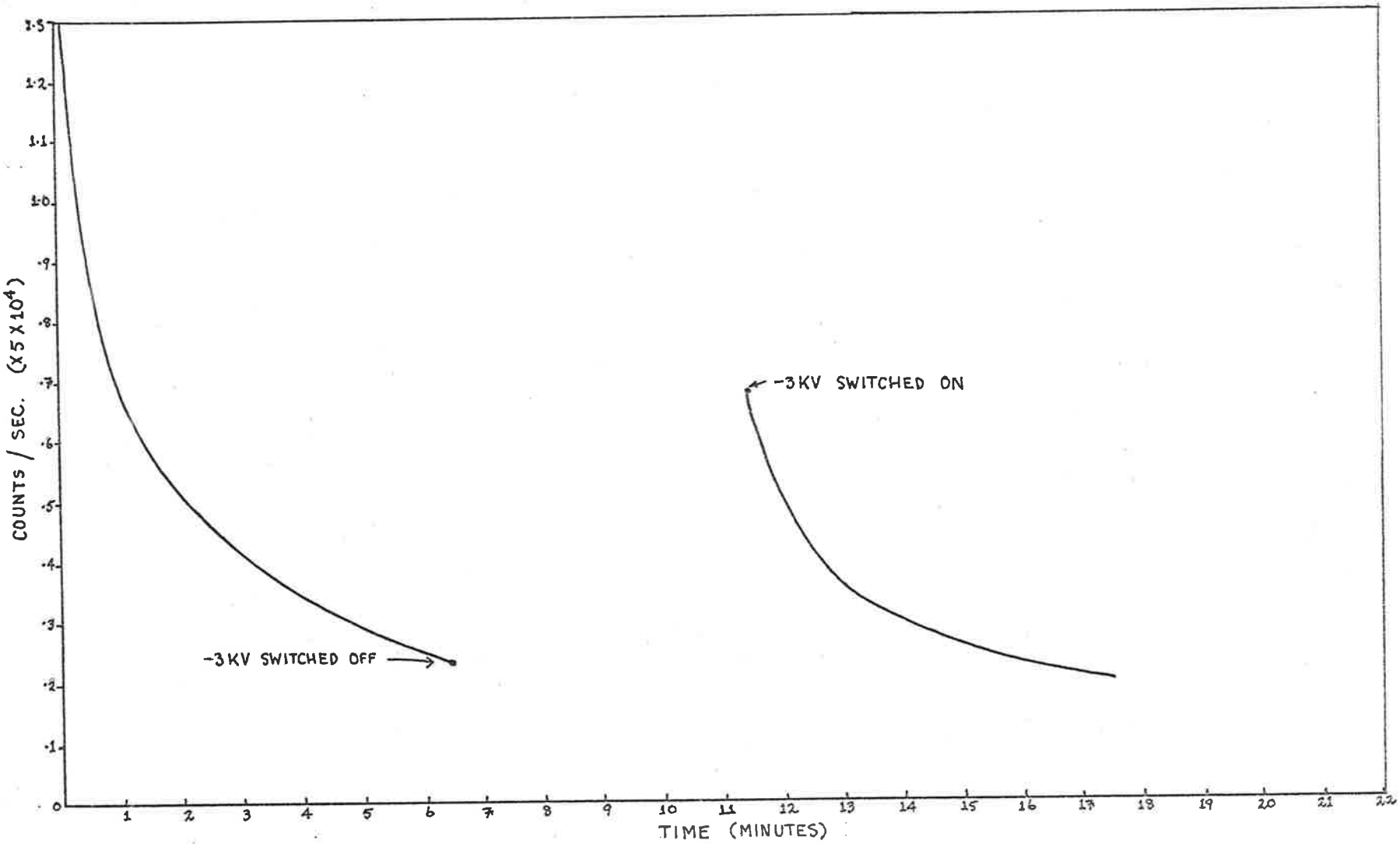

FIG. 4·11: THE FATIGUE EFFECT OF A B419BL MULLARD'S CHANNELTRON IN AN ATMOSPHERE OF ARGON AT A PRESSURE OF 10^{-5} TORR.

4.5.5 DETECTOR EFFICIENCY

The channel electron multipliers will respond to ions, β particles, X-rays, E.U.V. photons or any other sufficiently energetic radiation and, as a result, it is a very useful detector to be employed in a vast number of applications. However, the detection efficiency of the device is different for different forms and energies of excitation.

Various authors have measured the absolute or relative efficiency of the channeltrons for various forms of excitation and energies. Over most of the energy range the agreement of the results of different experimenters is very poor. This lack of agreement is mainly due to the experimental structure and techniques used which vary greatly from experiment to experiment. Another important fact is that the efficiency depends upon a number of parameters such as angle of incidence of the input radiation flux, gradient potential of the multiplier and geometry, and the presence of stray fields surrounding the entrance aperture of the multiplier.

For electrons the efficiency has been measured by Paschmann et al (1970), Egidi et al (1969), Evans (1965), Frank et al (1969), and others, and in general the detection efficiency increases reaching a maximum value of 85% at an energy of about 220 eV and then decreases quite rapidly for energies above this value.

The relative efficiency of the channeltrons for protons has been measured by Egidi et al (1969), for proton and argon ions by Fox et al (1970), for H^+, H_2^+, $^3He^+$, $^3He^{++}$, He^+, Ne^+ and Ar^+ ions by Burrows et al (1967), and for ions of mass 4 to 40 AMU by Potter and Mauersberger (1972). All the above measurements indicate that the efficiency increases with the energy of the ions reaching a maximum value of energy of about 5 KeV and then remaining approximately constant.

Burrows et al (1967) found empirically that excluding the diatomic H_2^+ ions the relative efficiency, ε_r, is proportional to the product of the velocity of the ions and the atomic number, A, to the power of 0.4:

$$\varepsilon_r \propto \text{velocity} \times A^{0.4} \qquad (4.65)$$

It follows, then, that for ions of different atomic number, having the same kinetic energy, the channeltrons are slightly more efficient in detecting the lighter ions than the heavier ones.

Lapson and Timothy (1976) have measured the detection efficiency of channeltrons with opaque MgF_2 photocathodes at wavelengths between 44 and 900 $\mathring{A}$, and found that over the wavelength region from 50 to 350 $\mathring{A}$ the efficiency to the E.U.V. quanta is a factor of two greater than those of uncoated multipliers, while Bordoni et al (1974) found that for X-rays in the energy range 8 - 100 KeV, the absolute efficiency ranges from 1.5×10^{-2} to 4×10^{-3}, respectively.

CHAPTER V

MASS SPECTROMETER PAYLOADS

5.1.1 TYPES OF ROCKET VEHICLES

As already mentioned in the previous chapter, the aim of the mass spectrometer experiments is to execute ion and neutral density measurements of the atmospheric constituents in the altitude region 110 - 250 Km. The gases of interest in this region have masses between 1 and 50 AMU and in order to achieve sufficient height resolution (< 2 Km) a quantity which depends on the speed of the rocket, and hence its apogee for a typical medium size rocket, the masses must be scanned about once per second. It is desirable to detect not only the abundant gases N_2, O_2 and atomic oxygen but also the minor atmospheric constituents such as CO_2, Ar, He and H_2 and, therefore, for a detector a multiplier is essential. The best choice is the channeltron, mainly because of its inherent small size and simplicity of use.

The altitude range (110 - 250 Km) is not arbitrarily chosen but, rather, the choice is related to the simplicity of the mass spectrometer experiments above an altitude of 100 Km and the types of rocket vehicles available. The region which would be of more interest is the region between about 65 and 100 Km, called the D-region. The experimental attraction for this region is that complex chemical and photochemical reactions take place here (see section 1.3.2) and there is a great need for more data on both the ion and neutral constituents which are essential for the elaboration of the photochemical models of the earth's atmosphere. However, there are mainly two problems which the experimenter has to face when he employs mass spectrometers in the D-region. The first problem

is that unless the rocket has a very low apogee ($<$110 Km) it usually moves in this region at supersonic speed and, as a consequence, for mass spectrometers which are at the uppermost part of the payloads and, hence, are looking into the direction of flight a shock wave develops in front of the entrance of the instruments which has the effect of making the interpretation of the measured data very difficult.

The second problem is that below an altitude of about 100 Km the mean free path of the molecules in the atmosphere is smaller than the dimensions of the mass spectrometers and, therefore, the pressure broadening of the mass peaks is so high that the peaks disappear completely into a high constant background. If it is then desired to utilize the mass spectrometer at altitudes below 100 Km, it is imperative to reduce the pressure inside the mass spectrometer housing so that the mean free path of the particles is at least equal to the dimension of the analyzer. A typical mass spectrometer with electrodes, say, 13.6 cm long, is unable to produce any mass spectrum if the pressure inside its enclosure vessel is higher than about 4×10^{-4} torr. Therefore, the mass spectrometers designed to be employed in the D-region carry with them usually an inbuilt cryogenic vacuum pump which is cooled either by liquid nitrogen or liquid helium. Another important matter to remember is that channeltrons cannot be operated at pressures higher than 5×10^{-4} torr.

For the proposed mass spectrometer experiment a rocket vehicle was required which had an ejectable nose cone and an apogee greater than 140 Km for a payload of at least 17 Kg weight. When the mass spectrometer experiment was planned the only suitable rocket available was the Lorikeet. The characteristics of this vehicle are that it has an initial acceleration of about 100 g, a maximum diameter of 130

mm and could take a payload (including nose cone, skin, aerials, etc) of a maximum length of 1300 mm and weight of 17 Kg to an altitude above 140 Km. The problem with this vehicle was that in order for it to be stable during flight with this type of payload it had to be equipped with large fins (178 mm x 178 mm) and it had to be spun about 10 rev./sec.

The dimensions of the mass spectrometer and electronics were such that the mass spectrometer experiment constituted the entire payload for the Lorikeet rocket. Two payloads, designated L1002 and L1003, were prepared using this type of vehicle and both carried a neutral mass spectrometer.

Another rocket which became available at a later stage was an Aerobee vehicle which, because of its size, carried both a neutral and an ion mass spectrometer. The analyzers were mounted on the top part of the payload with their axes parallel to the vehicle's axis and protruding into the nose cone which was ejected at about 90 Km.

5.1.2 THE QUADRUOLE MASS SPECTROMETER ASSEMBLY

The quadrupole mass spectrometer consisted of four cylindrical rods of diameter 9.44 mm which were mounted parallel to each other with their axes at 90^{o} apart on a circle of diameter 8.9 mm. This arrangement is shown in fig 4.2b. In order to mount the electrodes and insulate them electrically, four holes of diameter 2.25 mm were drilled in the two end flanges and in the end of the rods. The cylindrical electrodes were then located between the two flanges with 3 mm diameter ruby balls and the whole assembly was supported by four cylindrical spacers which were screwed into the end flanges. A view of the assembled mass spectrometer and ion source is shown in fig 5.1 and photograph 5.1.

Two sets of mass spectrometers were made. The first two quadrupoles which had electrodes 136 mm long were flown on the Lorikeet L1002 and L1003 rockets. In order to increase the resolving power of the analyzer, and hence to work at low frequency, the second set of analyzers had electrodes of length 200 mm. These instruments have been flown on the Aerobee. All the mass spectrometers were made of non-magnetic stainless steel.

Tests conducted at W.R.E. (Weapons Research Establishment, Salisbury) have shown that these mass spectrometers were very rugged. They withstood vibrations between 20 and 2000 Hz at 20g along the three axes and accelerations greater than 120g along the Z-axis.

The mass spectrometers had a field radius, r_o = 4.18 mm, and, therefore, the ratio R/r_o = 1.13 compared with the theoretical 1.147 (Denison (1971)). This discrepancy did not seem to be very important, since the mass spectrometers had a high transmission and a high resolving power.

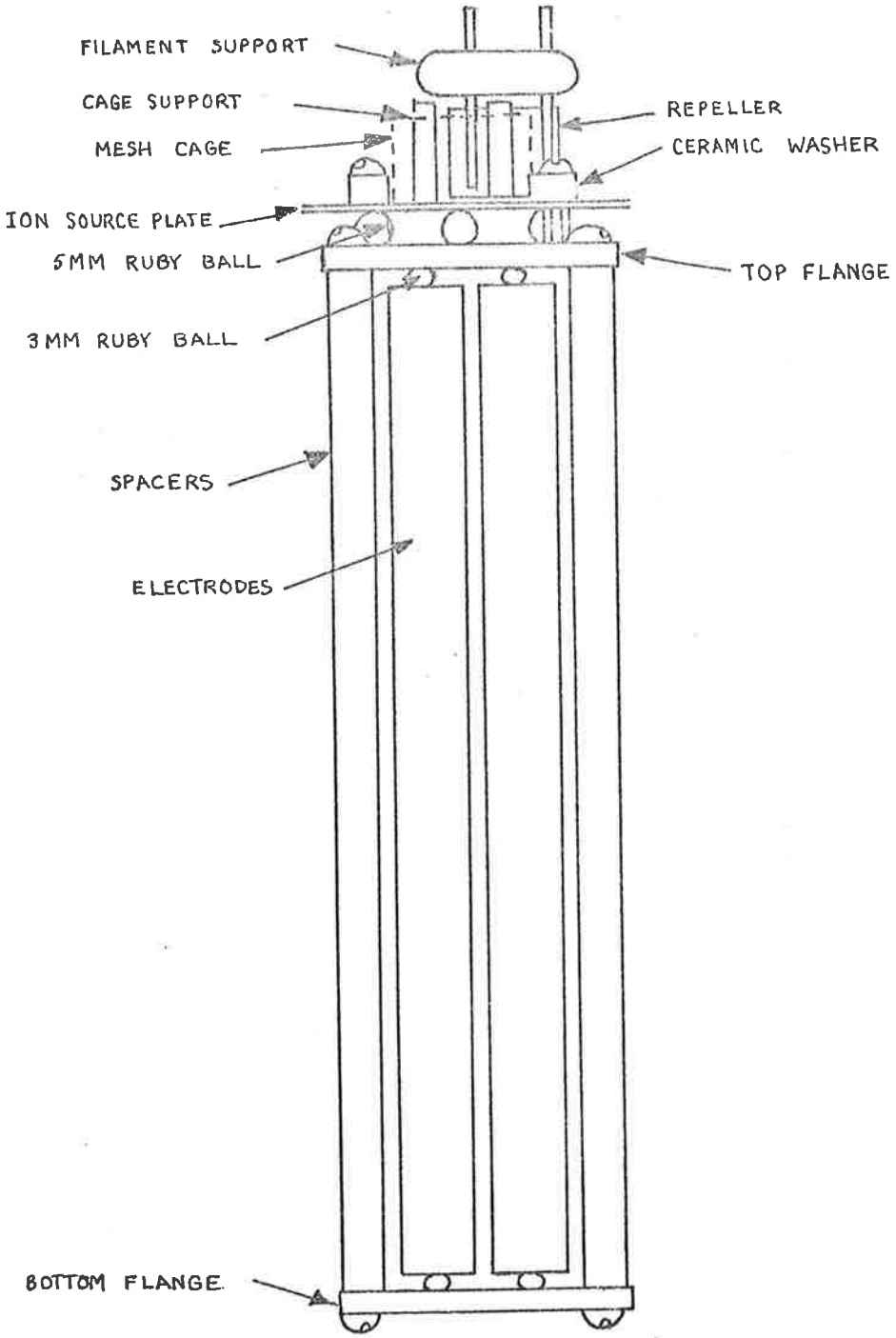

FIG. 5·1: SECTION VIEW OF A QUADRUPOLE MASS SPECTROMETER AND ALLIED ION SOURCE.

Photograph 5.1 Quadrupole mass spectrometer.

5.1.3 ION SOURCE

The ion source employed on each neutral mass spectrometer experiment, fig 4.9 and photograph 5.1, was of simple construction and could be defined as a quasi-opened ion source since $\theta = 34^{o}$ and $\eta = 52^{o}$. The filament used was of rhenium wire, of length 15 mm and diameter 25 μm. The energy of the ionizing electrons was variable between about 20 to 120 eV and that of the ions between 0 and 20 eV. The ions produced in the mesh cage were drawn toward the entrance aperture of the analyzer by the positive voltage (0 - 20 V) applied to the cage while those produced outside the cage were repelled by this positive voltage.

5.1.4 POSITION OF THE CHANNELTRON

The detectors used were Mullard type B419BL channeltrons which had a -3 KV applied to their funnels. The ions leaving the spectrometer were accelerated by the -3 KV and on striking the inside surface of the funnel caused electrons to be emitted which were then multiplied by a factor of about 10^7 by the avalanching process occurring inside the glass tube of the channeltron (see section 4.5.2).

The alignment of the channeltron entrance with the exit aperture of the mass spectrometer was found experimentally to be very critical. The best position was found to be that indicated in fig 5.2. If the channeltron was positioned exactly underneath the exit aperture of the analyzer it became very noisy, while if it was too "off-centred" the counting rate decreased rapidly. The reason for this behaviour is not clear, especially since it is very hard to imagine that ions with energies of only a few electron-volts are not drawn into the entrance of the channeltron when an accelerating voltage of -3 KV is applied to the funnel. The only plausible explanation is that since the inside surface of the channel and that of the funnel was coated with a thin semiconducting layer the voltage toward the channel decreased in magnitude and, hence, so did the field. Therefore, the field at the centre of the funnel was relatively weaker than that at the edge and if the funnel was too "off-centred" then most of the ions were drawn toward the edge instead of the centre of the funnel and, as a consequence, the emitted electrons moved away from the funnel toward a positive potential which, in this case, was the grounded plate above the funnel of the channeltron. It was then thought that by placing a fine mesh across the funnel this problem would have been solved, but, instead, the channeltron became noisy. The interesting part

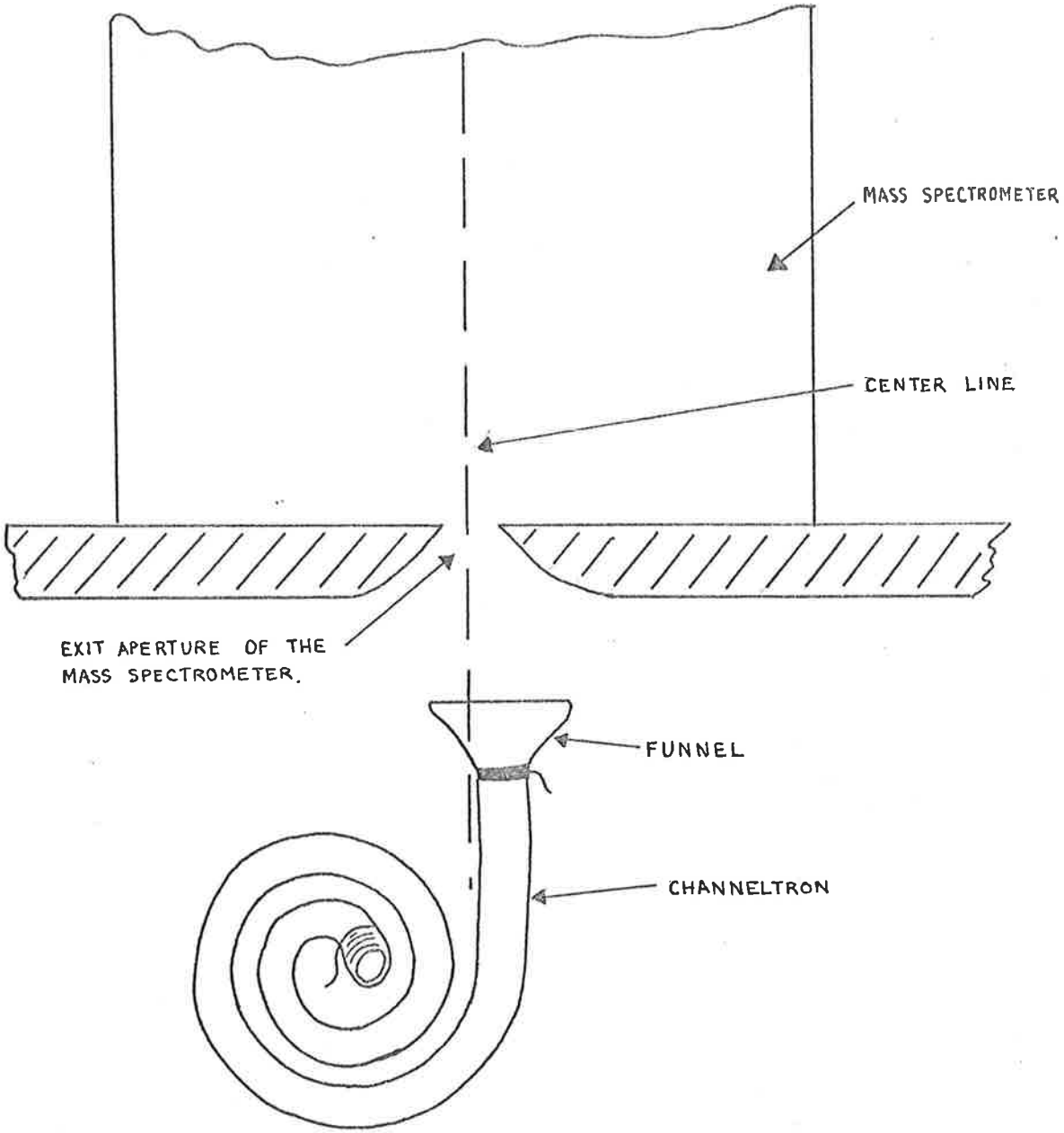

FIG. 5·2: MOUNTING POSITION FOR THE CHANNELTRON.

was that with the mesh across the funnel the resulting background of the mass spectrum was linear with pressure: the higher the pressure of the vacuum tank, the higher the background, and vice versa. It appears, then, that the channeltron could be used to accurately monitor pressure less than about 10^{-5} torr in vacuum systems.

The channeltron in the payloads was mounted in a tetrafluoroethylene (teflon) block, with a metal can over it to electrically shield the detector from the R.F. and other electrical noise which could have been present.

5.1.5 SPIN EFFECT

Of the three payloads already mentioned, the Aerobee was sun-stabilized while the Lorikeets L1002 and L1003 were spun at a rate of about 10 rev/sec. Thus, prior to launch of the Lorikeet vehicles it was important to evaluate the effect that the high spin rate would have on the transmission of the ions through the spectrometers.

The velocity of the ions is given by:

$$v_i = \sqrt{2qU/m_i} \tag{5.1}$$

where m_i is the mass of the ion, U their energy, and q their charge. If A is their mass number and V the accelerating potential of the ion source, then:

$$v_i = 1.388 \times 10^4 \sqrt{V/A} \tag{5.2}$$

For A = 28 (molecular nitrogen) and V = 1 eV:

$$v_i = 2.6 \times 10^3 \text{ m/sec.}$$

Thus, ions with this energy (1 eV) took only 52μ sec to transverse a distance of 136 mm, the length of the electrodes of the Lorikeet mass spectrometers. In this time the analyzer on each of these vehicles would have rotated by an angle of about 0.18 degrees and, hence, the high spinning rate of these vehicles should not have affected the measured mass spectra.

5.1.6 MASS SPECTROMETER HOUSING

The mass spectrometer housing consisted of two cylindrical sections of different diameters, photograph 5.2 and fig 5.3, as the analyzer and the detector enclosure. The whole container was machined from one piece of material to avoid any brazing of the joints and hence distortion of the cylindrical sections by heat. For the payloads L1002 and L1003, the housing was machined out of non-magnetic stainless steel, while for the Aerobee it was made of aluminium.

At the detector end the housing was sealed with the base plate on which the channeltron was mounted, and a gold seal was used for L1002 and L1003. The reason for the use of the gold seal is that initially it was planned to bake the whole assembly to a high temperature under vacuum, but unfortunately at a late stage it was discovered that teflon decomposes at temperatures higher than 360°C, and the channeltron cannot be subjected to temperatures higher than 150°C. Therefore, a viton O-ring would have been sufficient which, in actual fact, was used on the Aerobee mass spectrometers.

To the other side of the base plate was attached a pressurized box which contained the pulse amplifier, high voltages and the electronics to drive the analyzer. For electrical connections between the housing and the pressurized box, Ferranti ceramic to metal seals, type TDC-121-00, were used for the -3 KV and the output, while for the R.F. and DC voltages it was found that a 9 pin hermetically sealed Cannon connector, type DEH9P, was suitable.

At the other end of the enclosure, there was a cap which vacuum sealed with a viton O-ring the analyzer's housing. This cap was kept pressed against the top flange (fig 5.3) with a spring so that even when the outside pressure

Photograph 5.2: Quadrupole mass spectrometer and housing flown on the Aerobee vehicle.

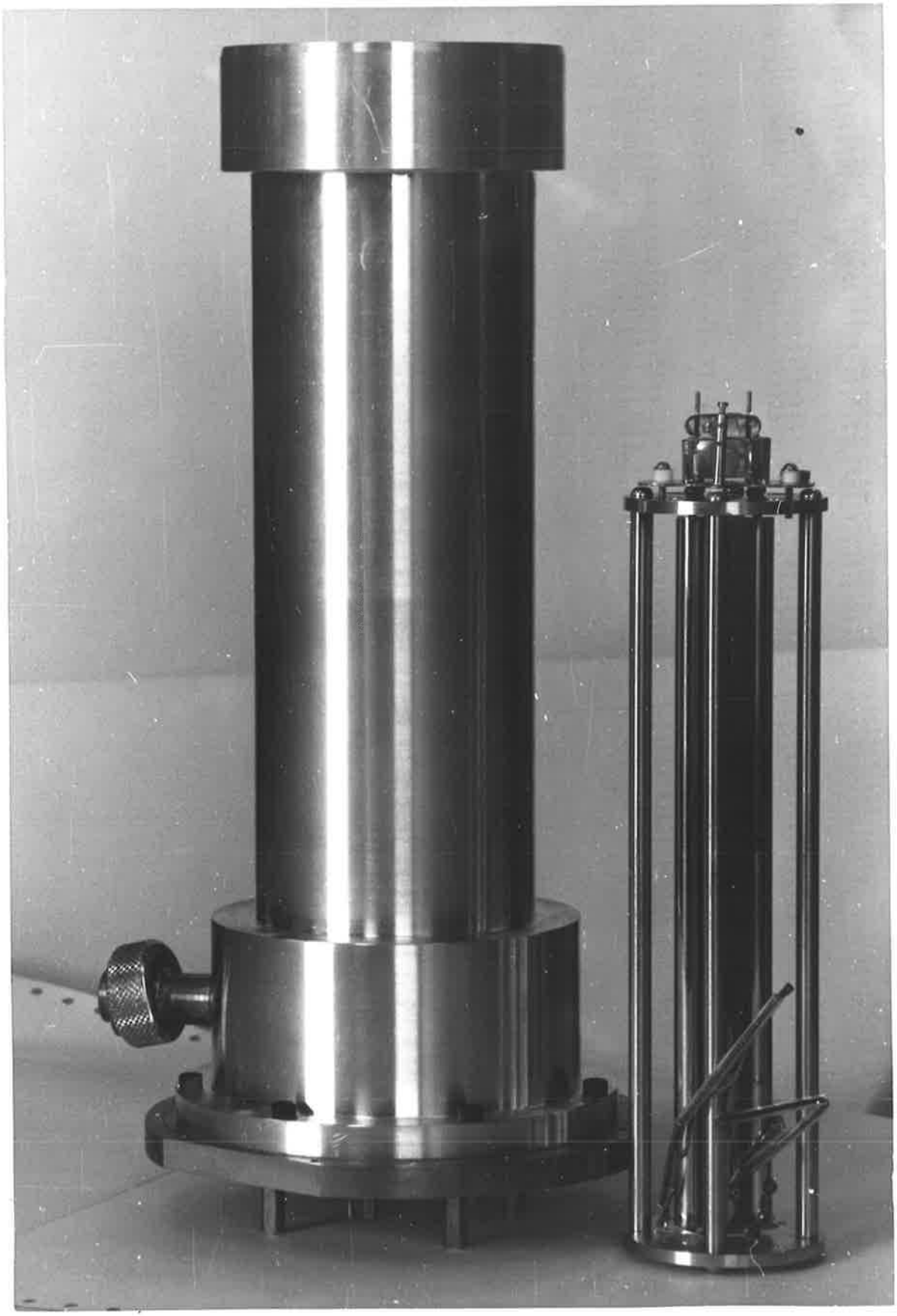

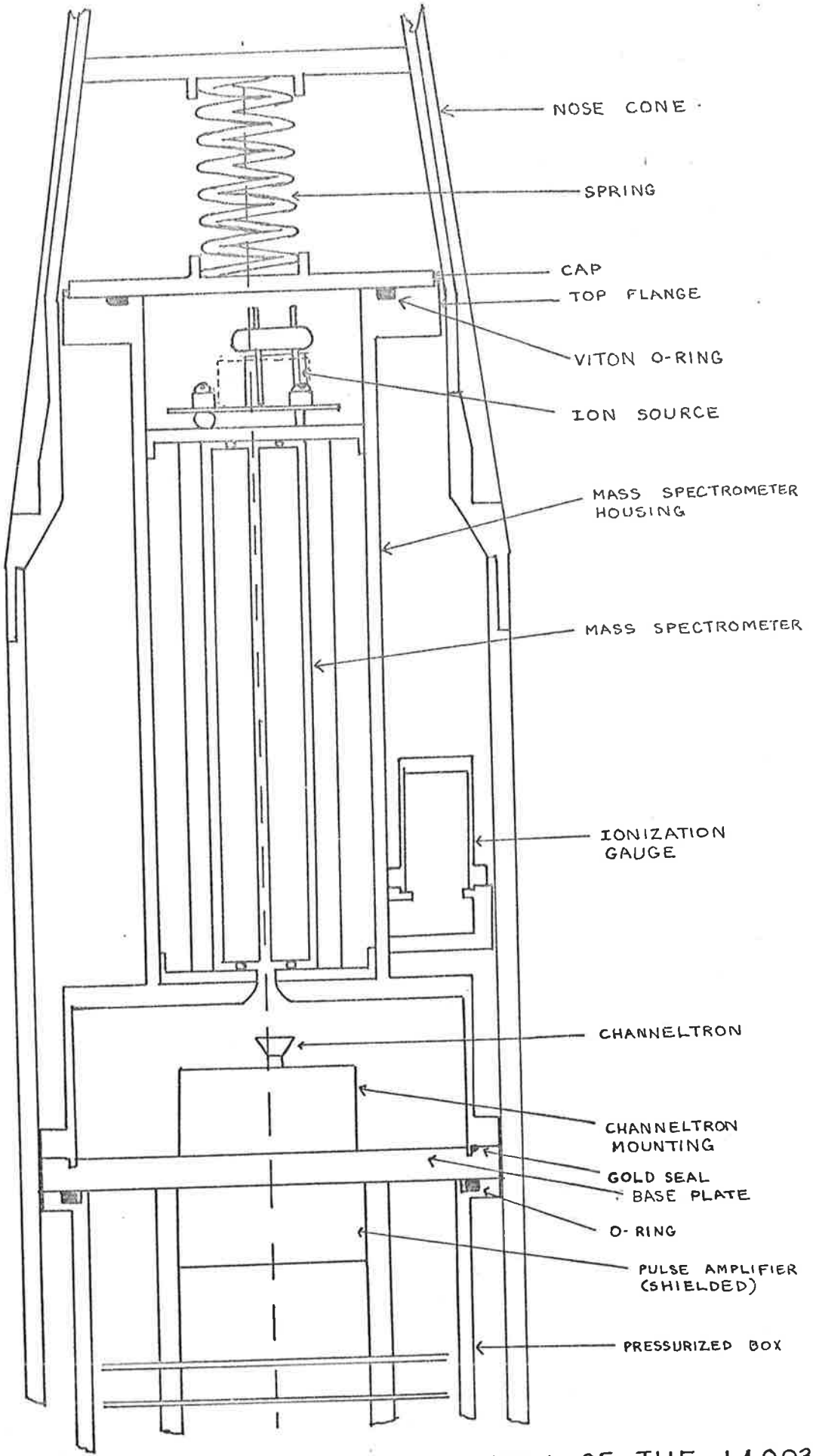

FIG 5.3: CROSS-SECTIONAL VIEW OF THE L1003 MASS SPECTROMETER PAYLOAD

was very low, a good vacuum could still be maintained inside. The cap and the spring were detached when the nose cone was ejected at an altitude of about 90 Km.

The mass spectrometer housing was pumped to a pressure better than 10^{-4} torr with an appendage pump, from the time the laboratory calibration was finished to about 20 minutes before launch. The appendage pump was a Varian Vac 2 ℓ/sec pump which was attached to the housing through a small Circle Seal vacuum tap model 9532T-4CC. The limited amount of space available for the instrument and the allied electronics on the payloads L1002 and L1003 meant that the mass spectrometer had to be pumped from outside the skin of the rocket and the pump had to be detached before launch. The use of the tap instead of the usual crimping method ensured that the vacuum inside the enclosure was conserved when the ion pump was detached. On the Aerobee there was sufficient space available for the pump to be permanently attached to the mass spectrometers but it was switched off before launch. There were several reasons for this. Tests had shown that under mechanical vibrations, and hence during the powered flight of the rocket, if the ion pump was on, it would outgas, and that even if the pump was electrically shielded using meshes some of the ions would always drift through the meshes reaching the funnel of the channeltron, whereby, if the detector was in operation, they would have been detected, giving rise to background noise. Another minor problem associated with the ion pump was that if the magnet of the pump was not properly shielded its strong magnetic field may have affected the trajectories of the ions in the analyzer and other adjacent experiments, especially experiments such as electron spectrometers. For this reason the magnet was taken off prior to launch of the Aerobee.

5.1.7 CLEANING PROCEDURES

All the mechanical parts related to the mass spectrometer, before they were assembled, were all placed in an ultrasonic bath of isopropyl alcohol and left in there for about an hour. After this the mass spectrometer instrument with the attached ion source, its housing, various plates, channeltron block, etc., were vapour degreased with isopropyl alcohol of analytical reagent purity. These parts were then mechanically assembled, electrically wired, and, before the channeltron was mounted, were vapour degreased again.

Isopropyl alcohol was chosen as a cleaning agent because it does not leave any deposit on the parts being cleaned.

5.2.1 ELECTRONIC CIRCUITS

A generalized block diagram of the electronics necessary to make the mass spectrometer payload functional during a rocket flight is given in fig 5.4. The operation of the mass spectrometer instrument requires that both R.F. and DC potentials of the type:

$$G(t) = f(t).(U + V.\cos\omega t) \qquad (5.3)$$

are generated and applied to its electrodes. In equation (5.3), U is the DC potential, V is the R.F. voltage (peak to peak) and f(t) is a ramp voltage, the amplitude of which modulates the R.F. and the DC potentials, thereby inducing mass scanning. It is essential that the ratio U/V which determines the resolving power of the analyzer is not only constant but this constant once set must remain of the same value during the laboratory calibration and the rocket flight, otherwise the resolution and hence transmission of the mass spectrometer changes and the resulting data are worthless. The ratio U/V is usually set for optimum resolution and transmission of the analyzer before the initiation of its calibration in the laboratory.

On the Lorikeets the high voltage (H.V.), R.F. and pulse amplifier were mounted in a pressurized box while other electronics associated with the functioning of the ion source, ionization gauge, magnetometer, or quadrant aspect sensors, telemetry, etc., were outside. The arrangement of the mass spectrometer's instrumentation and associated electronics is shown in fig 5.5 for the Lorikeet vehicles. On the Aerobee all the electronics were mounted inside the pressurized box and in the case of the neutral mass spectrometer these are shown in photograph 5.3.

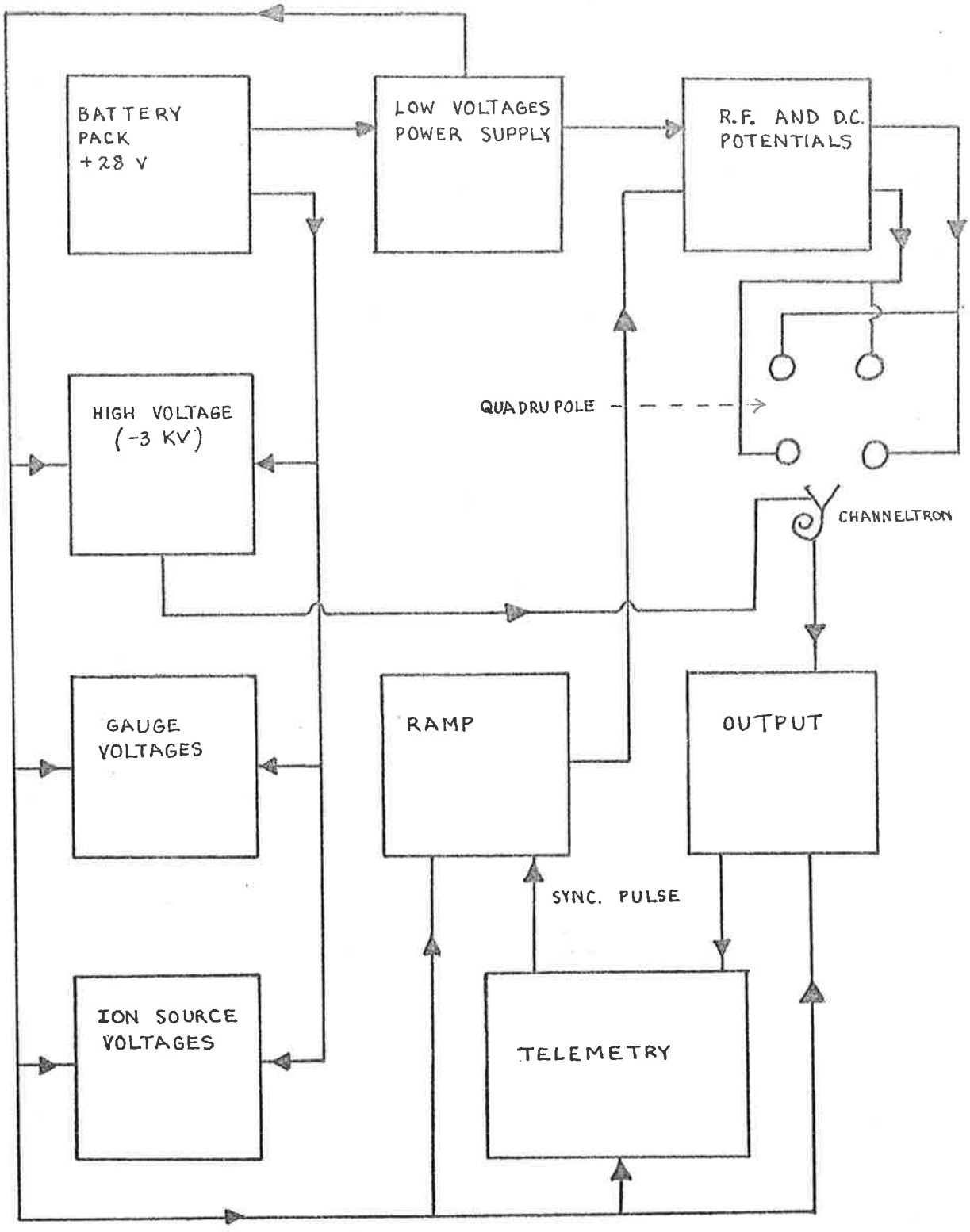

FIG. 5·4: BLOCK DIAGRAM OF THE ELECTRONICS OF THE LORIKEET MASS SPECTROMETER.

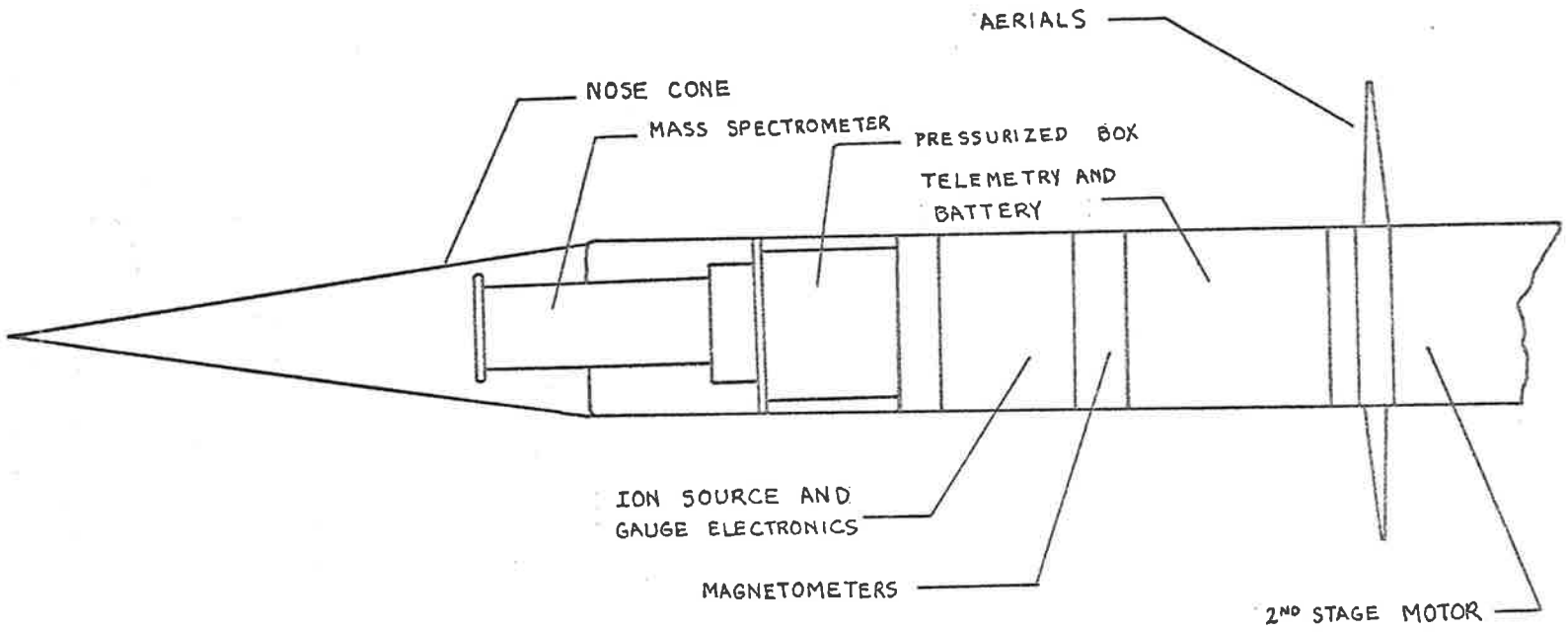

FIG. 5·5: SECTIONAL VIEW OF THE LORIKEET MASS SPECTROMETER VEHICLE.

Photograph 5.3: Flight electronic boards for the Aerobee's neutral mass spectrometer. The pulse amplifier is contained in the metal box while the R.F. and DC potentials for the quadrupole are on the board above the metal box. The next two boards contain the electronics for the ion source and the - 3 KV supply and are separated by a metal plate. The top board is the - 3 KV power supply.

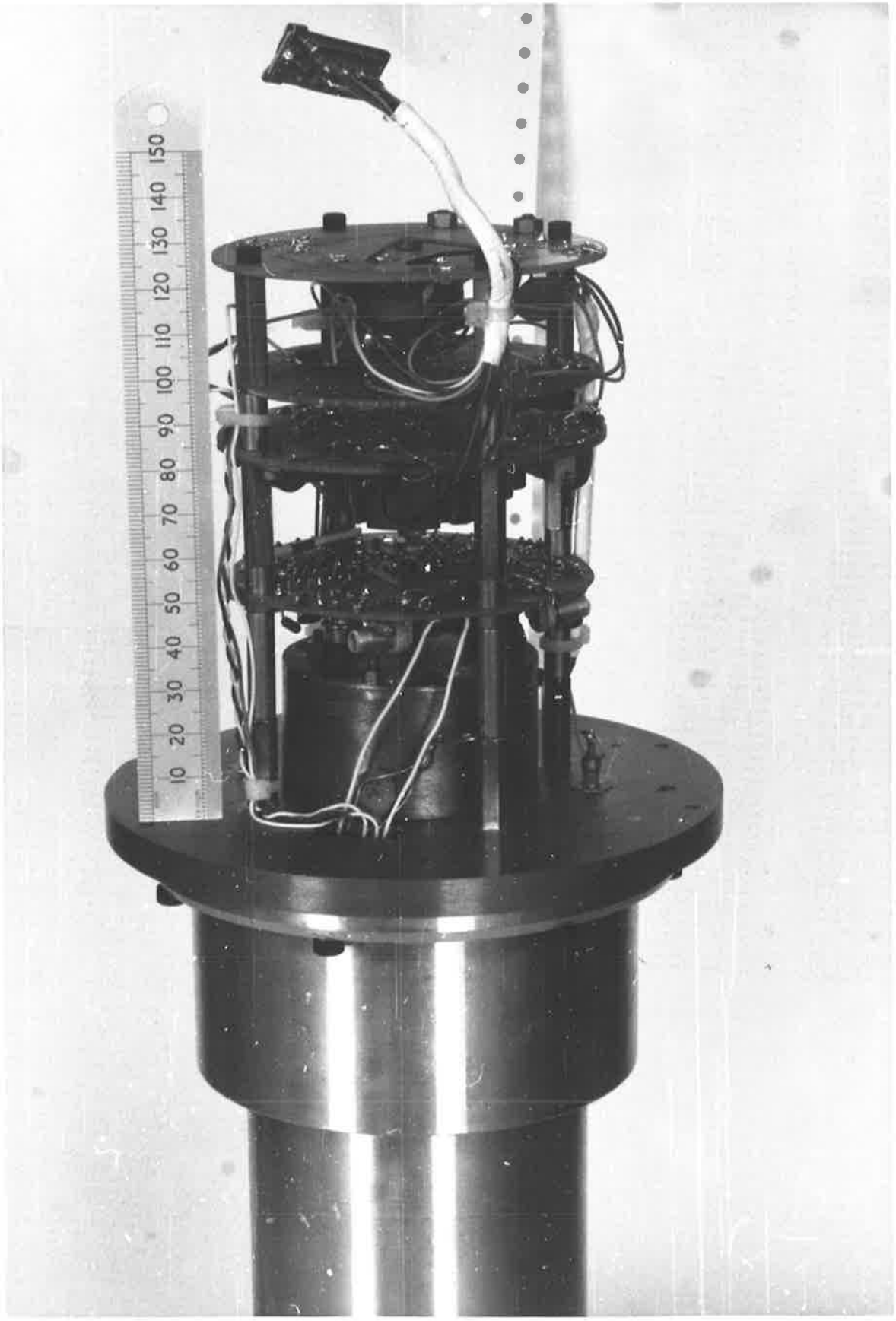
10 20 30 40 50 60 70 80 90 100 110 120 130 140 150

5.2.2 THE QUADRUPOLE ELECTRONIC CIRCUIT

For the programmed flights a very simple, rugged, compact, and low power crystal oscillator electronic circuit has been developed to drive the spectrometer. The circuit, Fig. 5.6, which is a combination of digital and analog electronics, generates a sinusoidal radio-frequency output that can be varied linearly over the range from 10 to 2000 volts (peak to peak) in response to a negative 0 - 10 volts input signal, which for the small flight analyzer (r_o = 4.0 mm and ℓ = 136 mm) and, at a frequency of 2.0 MHz, covers the mass/charge range from 1 to 100 A.M.U. The input signal can be swept either by a ramp or sawtooth voltage. The time constant of the DC potentials rectifying part of the circuit is less than 10 ms so that the sweeping frequency can be varied from about 100 Hz to DC.

The output stage is a high efficient-modified class B emitter modulator. This high efficiency minimizes the power requirement and eliminates the need to use heat sinks for transistors T_1, T_2, and T_3 of fig. 5.6. T_1 and T_2 are driven by square waves of opposite phase and the R.F. output is amplitude modulated by T_3. The square wave is obtained from a C.T.S. Knights self-contained crystal hybrid T.T.L. 2.0 MHz oscillator which comes in a TO-8 package. However, the circuit operates well at other frequencies provided that appropriate ferrite cores are used.

For the high voltage transformer, different types of core materials, shapes and sizes have been used, and it has been found that for radio-frequencies above 1 MHz, the Indiana General Q-3 ferrite toroid (dimension i.d. = 34.93 mm and o.d. = 60.33 mm) wound with 22 S.W.G. wire was the best. With this type of toroid, the tuned output has a high Q and consequently a low harmonic distortion. Any amplitude nonlineari-

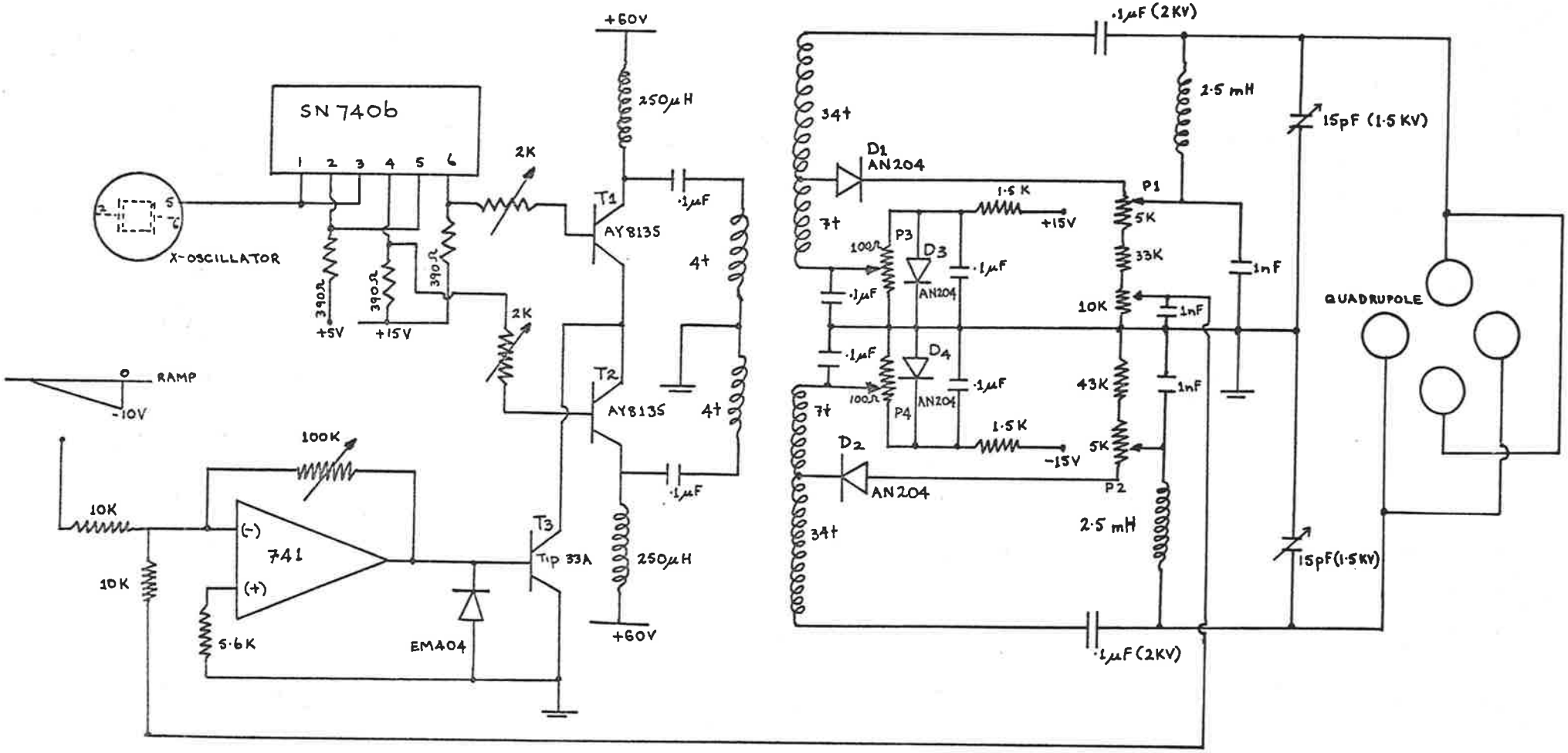

FIG 5·6: QUADRUPOLE DRIVE CIRCUIT.

ty is eliminated by the negative feedback from the rectified R.F. signal.

To ensure that the ratio DC/AC is stable, the DC potentials are derived directly from the R.F. by rectification using diodes D_1 and D_2 (fig. 5.6) and after filtering added to the R.F. signal through two R.F. chokes. At low voltages the forward transconductances of D_1 and D_2 are non linear and as a result the ratio DC/AC does not remain constant during a mass scan. To avoid this, the diodes are forward biased by a small DC current which can be adjusted for optimum resolution of the analyzer by adjusting the voltages across D_3 and D_4 (fig. 5.6). This ratio is also temperature dependent through the temperature dependence function of diodes D_1 and D_2. Even though the junction voltage of a diode only changes by about -2.5 mV/^{o}C, if during the running of the analyzer there is a large change of temperature, as it may occur during a rocket flight, the DC/AC ratio will change appreciably. In fact, if the analyzer is set to operate at a certain temperature T_o, and the temperature increases above T_o, then the resolution of the analyzer will become worse for lower masses and better for higher masses. It may happen that if the analyzer is operated at a high resolution, and there is a large temperature variation, the higher masses may even be partially or totally cut off. Vice versa, if the temperature decreases. This temperature dependence can be obviated by placing the diodes D_1, D_2, D_3, and D_4 in a miniature temperature controlled oven with the temperature set above the variable ambient temperature. For the flight analyzer the temperature is set at 65^{o}C and kept constant, within a half degree centigrade. Since the junction voltage drop of a diode is a negative function of temperature, the higher temperature (65^{o}C) has

also the advantage of decreasing the voltage drop across D_1 and D_2, therefore less bias is necessary across D_1 and D_2 to keep the ratio DC/AC constant. The circuit for the oven is shown in fig. 5.7.

The circuit of fig. 5.6 is simple and compact which makes it ideal for a rocket borne quadrupole mass spectrometer experiment. Unfortunately, with this circuit when it comes to set the value of the ratio DC/AC for optimum resolving power and transmission, two difficulties arise which make the setting procedures of this ratio tedious and lengthy. The difficulties are associated with the miniature oven which takes about 20 minutes before it stablizes itself to the set temperature, and the adjustment of the four potentiometers P_1, P_2, P_3 and P_4 (fig. 5.6) which determine the ratio DC/AC. The voltages which the four potentiometers regulate are interdependent, which means that if one potentiometer is adjusted, then all the others have to be reset, a procedure which is laborious. Fortunately, the resulting resolving power of the small mass spectrometer (ℓ = 136 mm) with this circuit was very high; in fact, a mass resolution better than $m/\Delta m \approx 200$ could be easily attained. Since for the purpose of atmospheric gas analysis a resolution equal to the mass being analyzed is sufficient, the instrument could be operated with a low R.F. frequency and the circuit of fig. 5.6 which has been flown on L1002 has been modified and improved for the L1003 and Aerobee mass spectrometers.

The improved version of the circuit of fig 5.6 is shown in fig. 5.8. The modification is mainly in the rectification of the DC from the R.F. For this purpose a peak detector which employs a fast integrated circuit chip, the

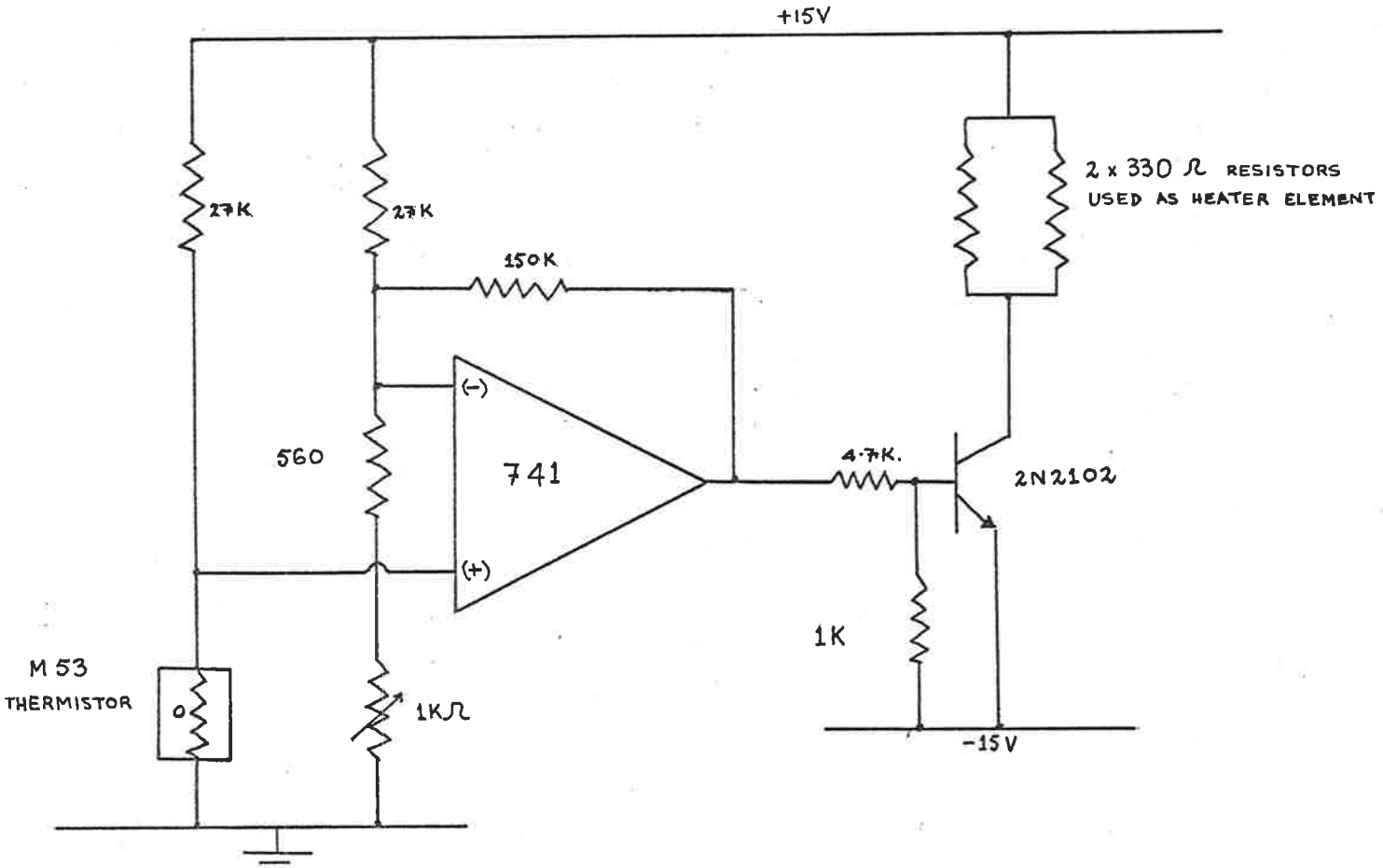

FIG. 5.7: CIRCUIT DIAGRAM FOR THE TEMPERATURE CONTROLLED OVEN.

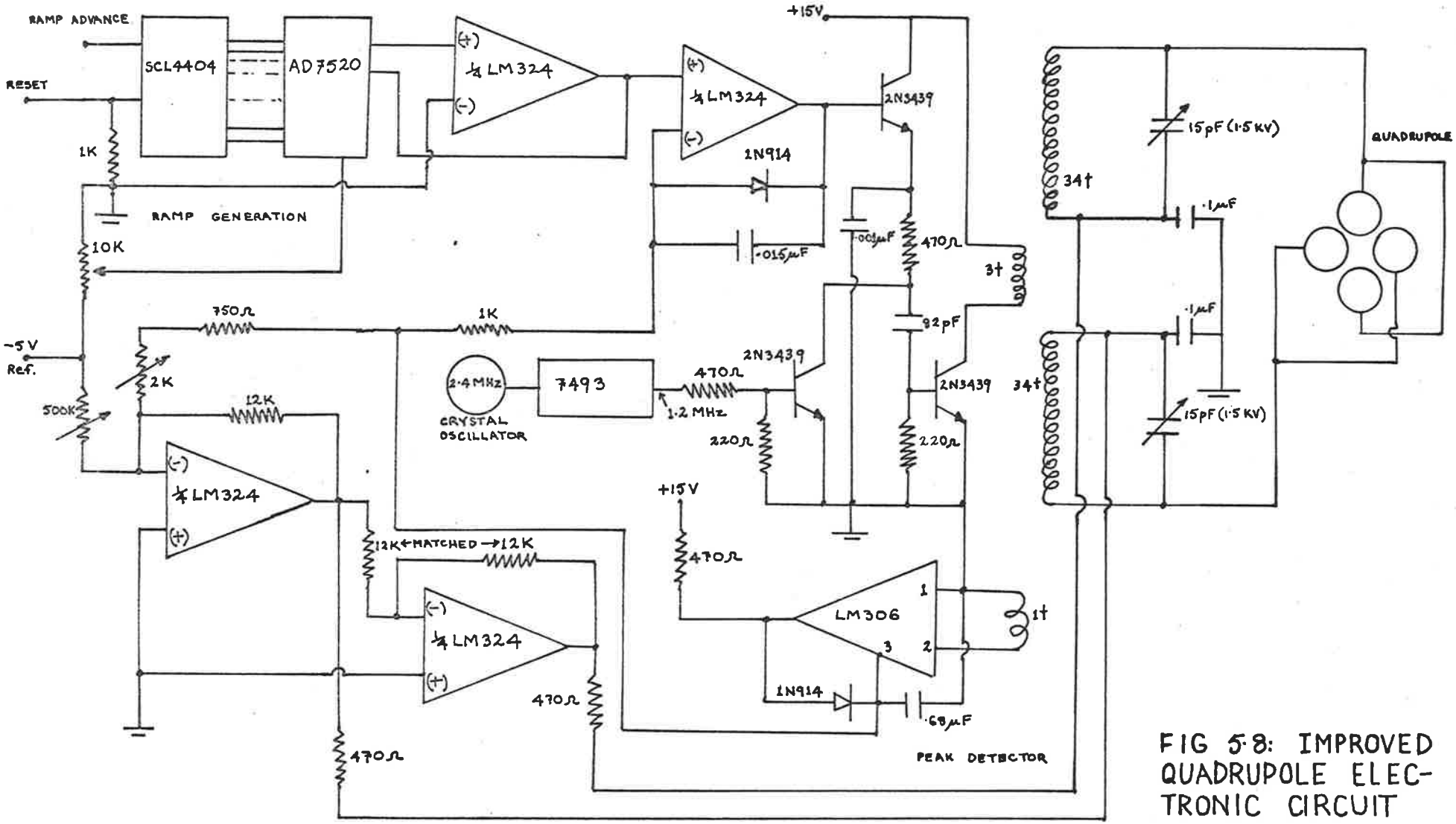

FIG 5.8: IMPROVED QUADRUPOLE ELECTRONIC CIRCUIT

LM306, has been used which works well at frequencies up to about 1.8 MHz. Above this frequency it loses linearity. With the use of this peak detector to generate the DC voltages the setting procedures for the ratio DC/AC are very simple as now all adjustments can be performed through the use of only one potentiometer and the use of the oven is no longer necessary.

With the lowering of the R.F. frequency from 2.0 MHz for L1002 to 1.2 MHz for L1003 and 1.0 MHz for the Aerobee mass spectrometers, it has been possible to use Q-2 ferrite toroids instead of the Q-3. The applied R.F. voltage is directly proportional to the square of the R.F. frequency (equation (4.20)), and, therefore, at low frequencies, low voltages are necessary to scan the same mass range. Thus, toroids of small dimensions can be used, since at these voltages they do not saturate. The advantage of this is that the resulting space required for the electronics on L1003 is much less than that required for L1002 and, as a consequence, on L1003 it has been possible to fly two axes magnetometers instead of the quadrant aspect sensors flown on L1002.

The toroids for the circuit of fig 5.8 are wound as in fig 5.9. The primary is made up of 3 turns while the two windings of the secondary have 34 turns each and the peak detector one turn. For the windings litz wire is used throughout. The L and C of the resulting toroid transformer is such that it requires further capacitance to tune the secondaries with the quadrupole and this extra capacitance is furnished through the two variable 1.5 KV printed circuit capacitors of 15pF which are made by Jackson Brothers (London).

With the foregoing mentioned circuits, the mass range for L1002 and the Aerobee mas spectrometers is from 1 to about 50 AMU while for L1003, because of low frequency

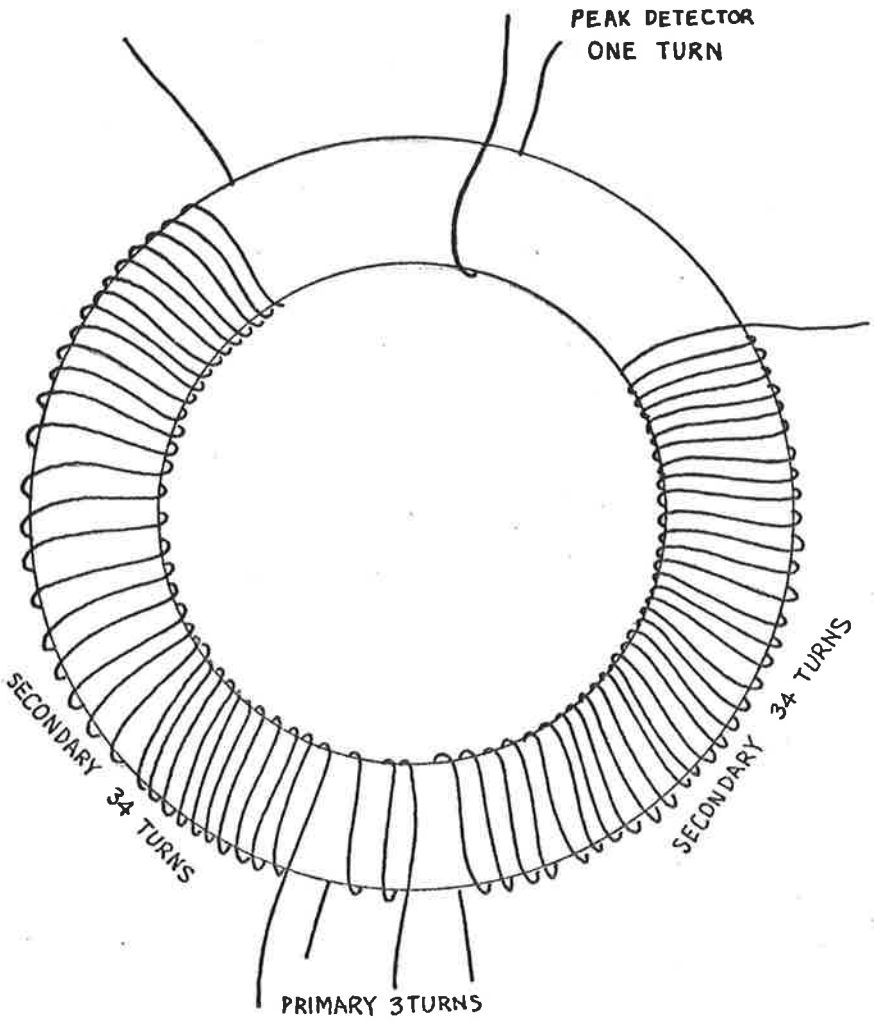

FIG. 5·9: TOROID TYPE Q-2 FERRITE OF INDIANA GENERAL OF DIMENSION I.D. = 34·9mm, O.D. = 60·3mm. DIRECTION OF WINDING IS AS SHOWN PRIMARY HAS 3 TURNS, WHILE THE TWO WINDINGS OF THE SECONDARY HAVE 34 TURNS EACH AND THE PEAK DETECTOR ONE TURN. THE TOROID IS WOUND WITH LITZ WIRE.

and the use of a mass spectrometer of short electrodes (136 mm) the mass range is from about 4 to about 50 A.M.U. In all cases the resolution is at least equal to the mass being analyzed.

5.2.3 RAMP GENERATION

For mass scan to be achieved it is necessary to amplitude modulate the R.F. with a ramp or sawtooth voltage. Another possible way of accomplishing mass scan is by frequency modulating the R.F., keeping constant the R.F. and DC voltages. With this method it is not practical to use a tuned circuit for the output stage of the R.F. drive circuit and, if a large mass range is required to be scanned, then the band width of the frequency modulation becomes very large. For these reasons, this method of mass scanning is not commonly used.

The method used for the rocket borne mass spectrometer experiments is amplitude modulation of the R.F. and the circuit for the ramp generation is shown in fig. 5.10 for L1002 payload while for L1003 is included in the circuit diagram of fig. 5.8.

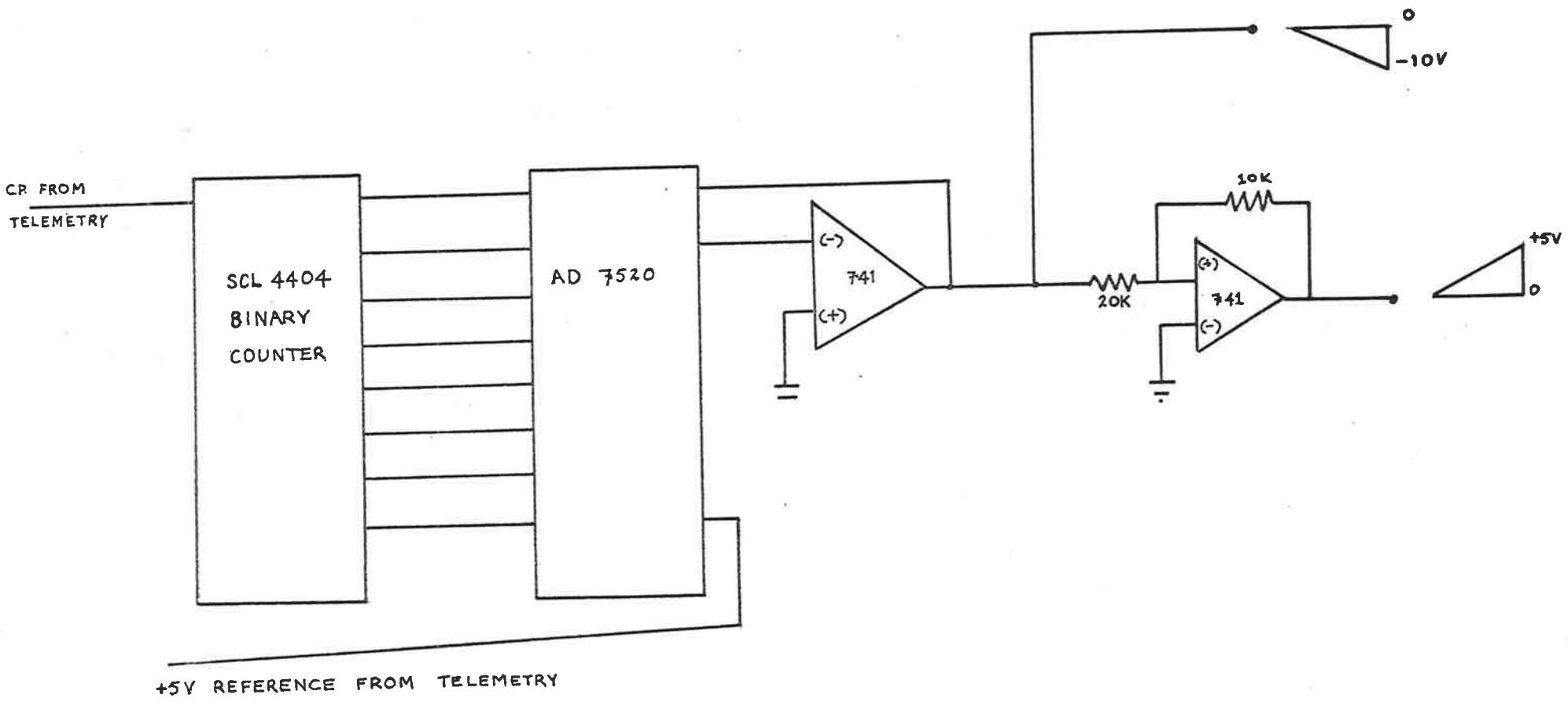

FIG. 5·10 RAMP GENERATION FOR THE R.F. AMPLITUDE MODULATION

5.2.4 PULSE AMPLIFIER

The detector (channeltron) is used in a pulse mode so as to exploit its dynamic range and to detect very weak signals. As already mentioned in chapter IV, it is capable of detecting pulses with a repetition rate greater than about 200 KHz for a few minutes and the risetime of its pulses is very small, the order of a fraction of a nanosecond. Thus, the pulse amplifier must have a bandwidth greater than about 200 KHz.

The pulse amplifier used to detect the mass spectra on the rocket borne mass spectrometer experiments is shown in fig. 5.11. It has a bandwidth of about 15 MHz and it is mounted in a metal box to electrically shield it from the R.F. and other electrical noise.

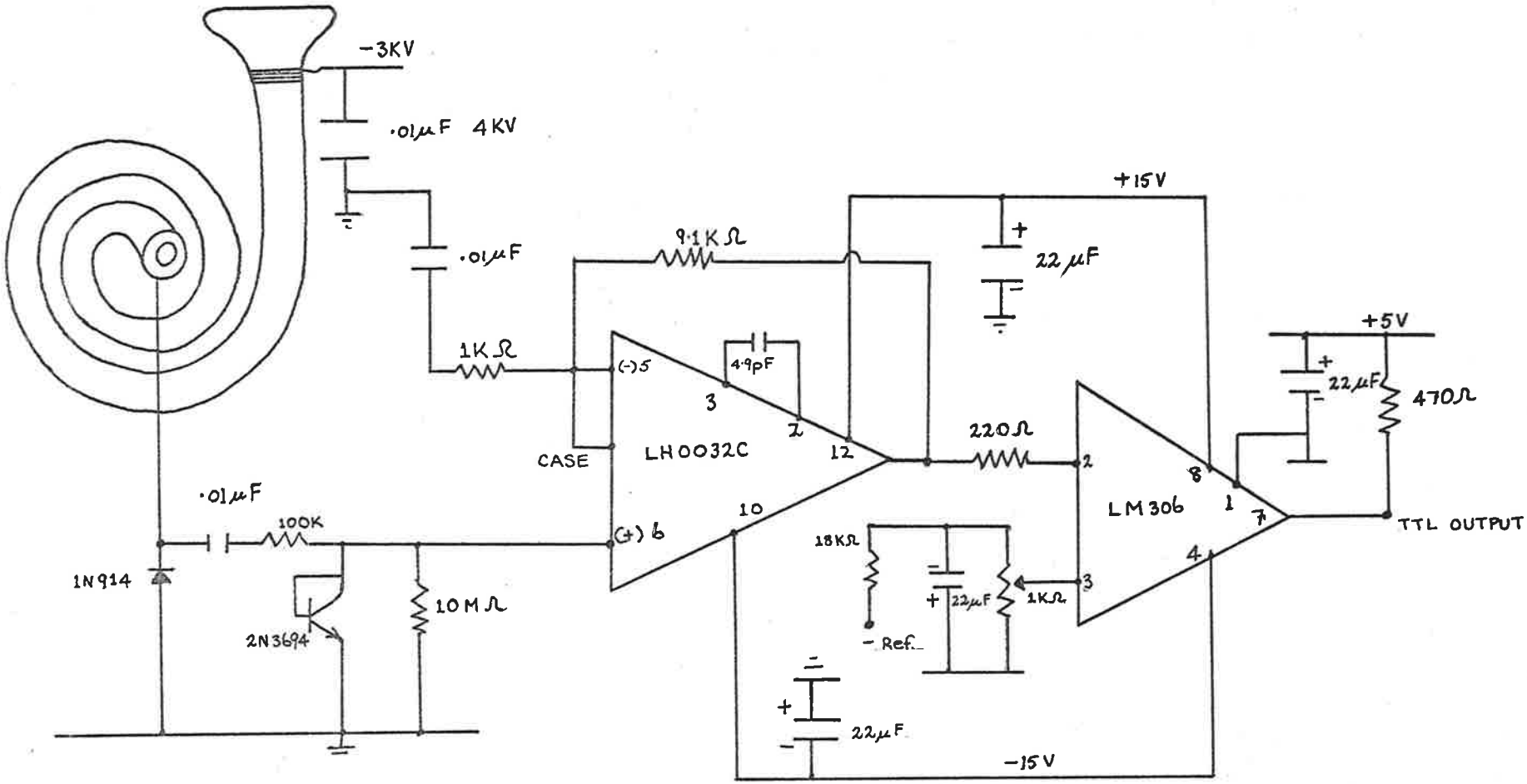

FIG. 5.11 PULSE AMPLIFIER

5.2.5 THE OUTPUT DIGITAL TO ANALOG BOARD

The TTL output signal from the pulse amplifier is divided by a factor of 2 and 8 using CMOS SCL4404 binary counters and the digital signal is converted into analog ramps with the aid of 8 bits CMOS digital to analog converters type AD7520. This conversion from digital to analog is necessary since the telemetry on the Lorikeet payloads is analog. The circuit for the D/A conversion is shown in fig. 5.12.

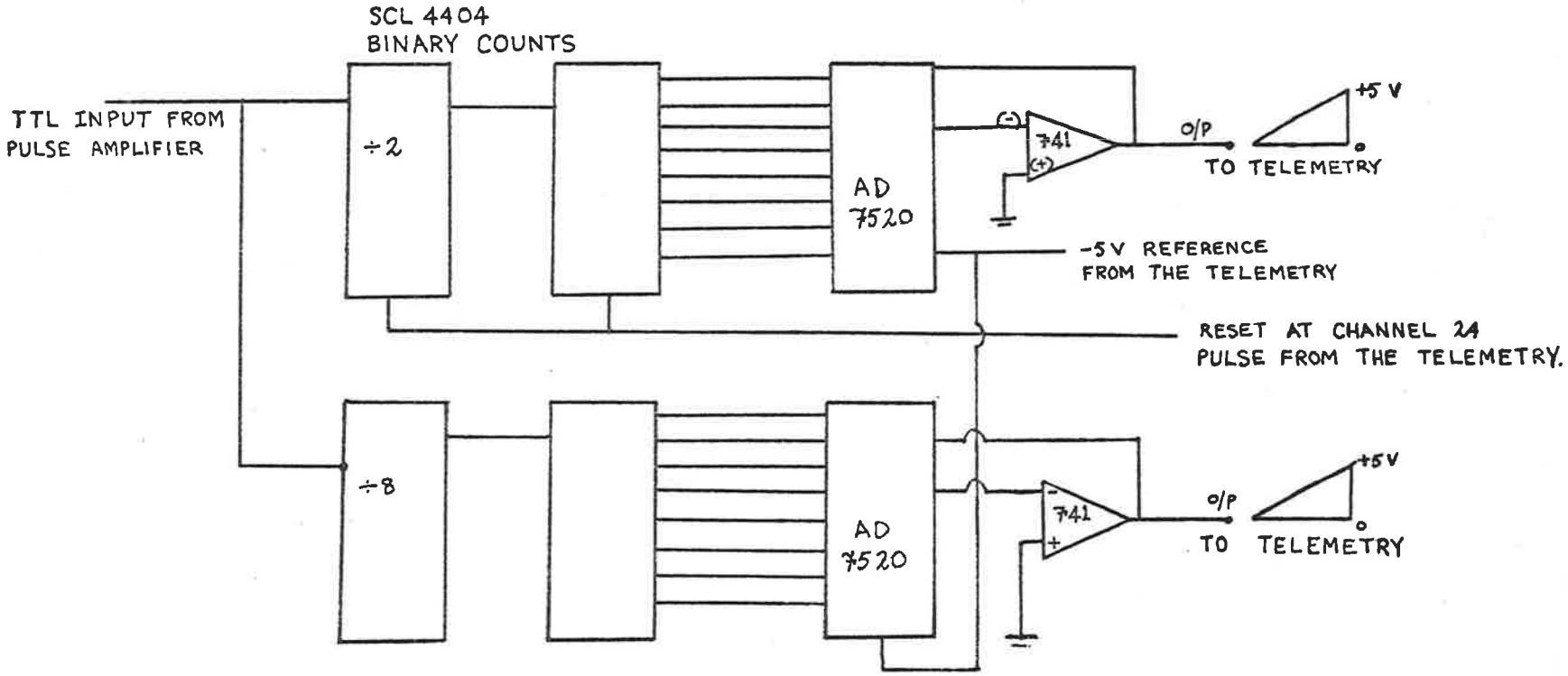

FIG. 5·12: OUTPUT DIGITAL TO ANALOG BOARD

5.2.6 HIGH VOLTAGES

The high voltages required by the mass spectrometer experiments both on the Lorikeets and the Aerobee vehicles were -3 KV for the channeltrons, -120 V for the ion sources and +120 V for the ionization gauges. The circuit for these supplies is shown in figure 5.13. The power supply is a regulated chopper which oscillates at about 50 KHz and the output voltages are floating and are derived from separate windings on the secondary of the transformer. The 3 KV is obtained by quadruplicating the 750 volts of this secondary winding. This is achieved with the use of the four capacitors and the four diodes type BYX10, while for the $\pm$ 120 voltages ordinary rectifying bridges are used.

The primary is centre tapped with 25 windings on each side of wire 22 S.W.G. while the two feedback windings have 2 turns each of 30 S.W.G. wire. The reference winding has 750 turns of 47 S.W.G. wire, and the $\pm$120 V windings have 120 turns of 30 S.W.G.each.

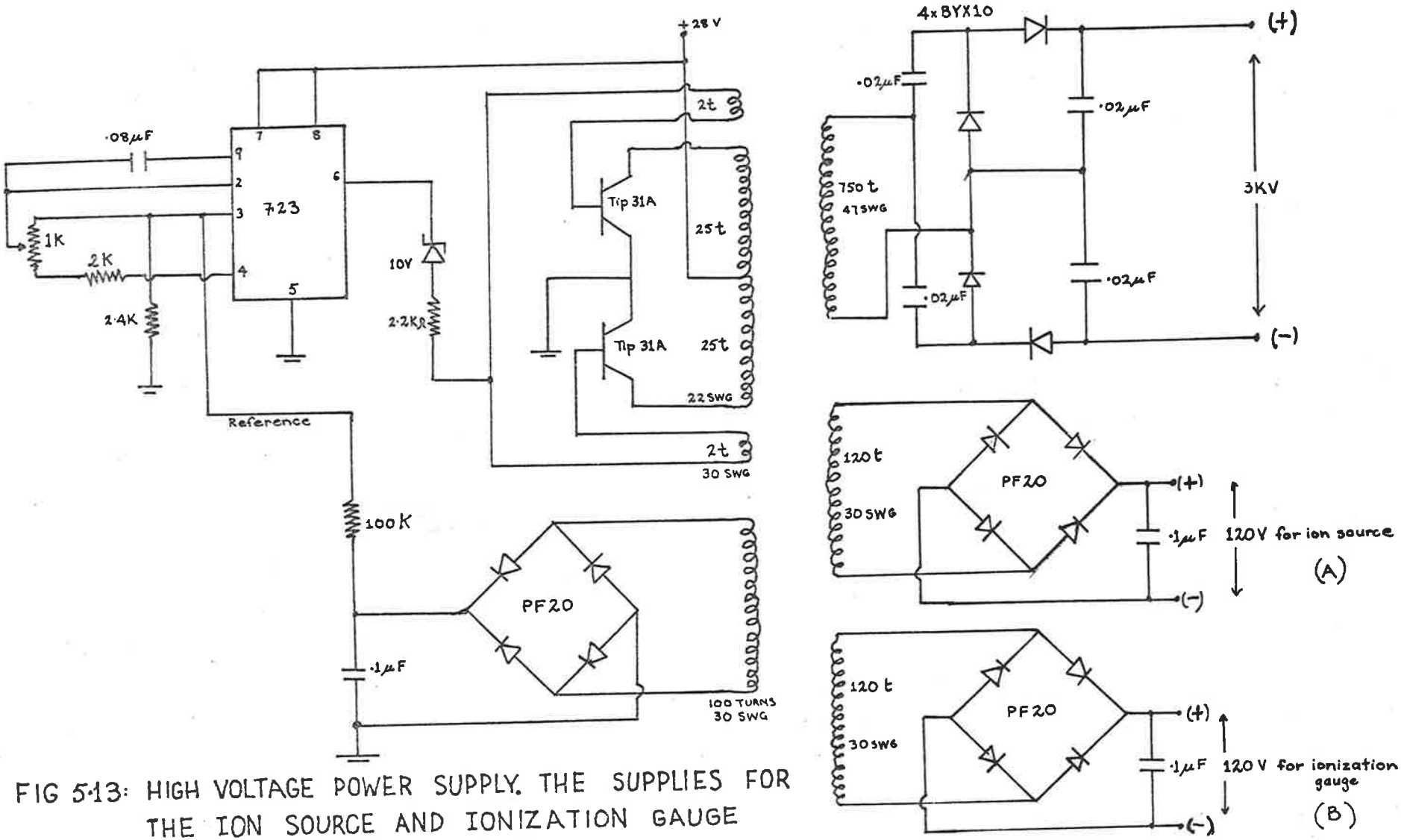

FIG 5·13: HIGH VOLTAGE POWER SUPPLY. THE SUPPLIES FOR THE ION SOURCE AND IONIZATION GAUGE ARE FLOATING.

5.2.7 ION SOURCE ELECTRONICS

The sensitivity of the mass spectrometer depends on the emission current of the filament which depends on its temperature. Hence, it is important that once the emission current is set to a certain value, it remains constant all the time. Therefore, the temperature of the filament must remain constant, and this is achieved with the use of the circuit of fig 5.14 whereby the emission current regulates itself to the set value by switching the filament on and off, at a frequency of about 5KHz. The regulation is better than 1%.

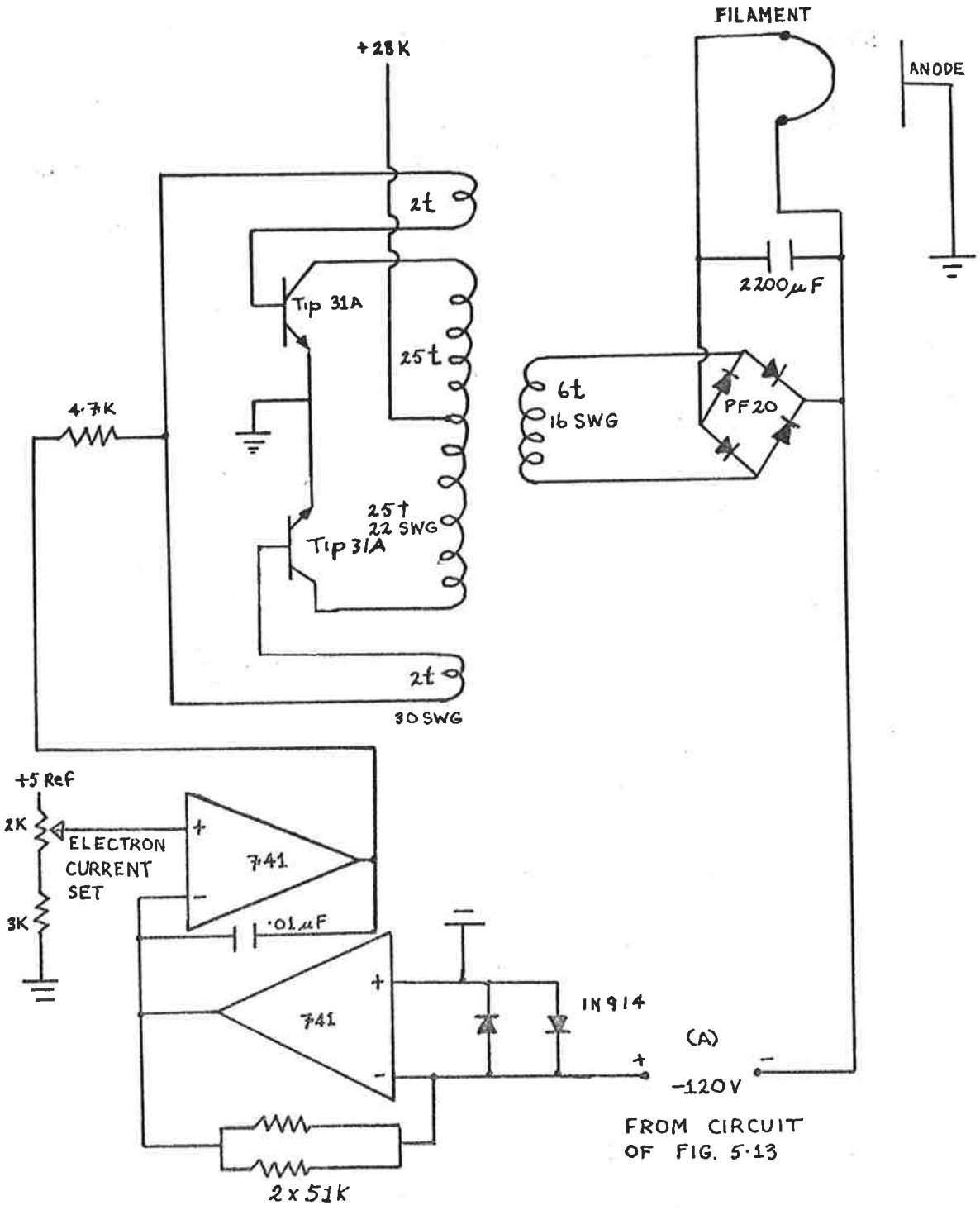

FIG. 5·14: ION SOURCE REGULATED POWER SUPPLY

5.2.8 IONIZATION GAUGE

The Lorikeet vehicles had an expected apogee of about 140 Km for the mass spectrometer experiments L1002 and L1003. No pump was flown on these flights and, as a consequence, the -3 KV could not be switched on at altitudes less than about 100 Km where atmospheric pressure is greater than about 10^{-4} torr. The mass spectrometers were pumped to a pressure better than 10^{-4} torr before launch, but about 20 minutes before launch the ion appendage pump was detached and during this time outgassing from the walls increased the pressure inside the vacuum housing of the instrument. The channeltron at pressures greater than 5×10^{-4} torr is very noisy and it takes a long time before it recovers again, a time which may be longer than the rocket flight. Therefore, the height range in which the measurements could be carried out was between 100 and 140 Km and if the rocket underperformed it would be even less. To make a maximum use of this altitude range, the payloads were fitted with an ionization gauge to safeguard against rocket underperformance.

The filament of the gauge was of rhenium wire so that it could be operated at pressures less than about 10^{-1} torr. The gauge was switched on soon after second stage burn and the high voltage was set to be switched on at an altitude of 100 Km if the reading of the gauge indicated that the pressure was better than 10^{-4} torr. If the indicated pressure was greater than 10^{-4} torr, then the high voltage would not be switched on and there was a time delay of 15 seconds during which the high voltage would come on if the pressure was satisfactory. After the 15 seconds, the high voltage would come on, irrespective of whether the pressure indicated by the gauge was less than 10^{-4} torr or not, so that the switch-

ing of the high voltage did not rely entirely on the functioning of the ionization gauge. This precaution was taken so that in the event of a malfunction of the gauge during the powered flight not all the flight would be lost.

The circuit for the ionization gauge's electronics and the high voltage switching mechanism is shown in fig 5.15.

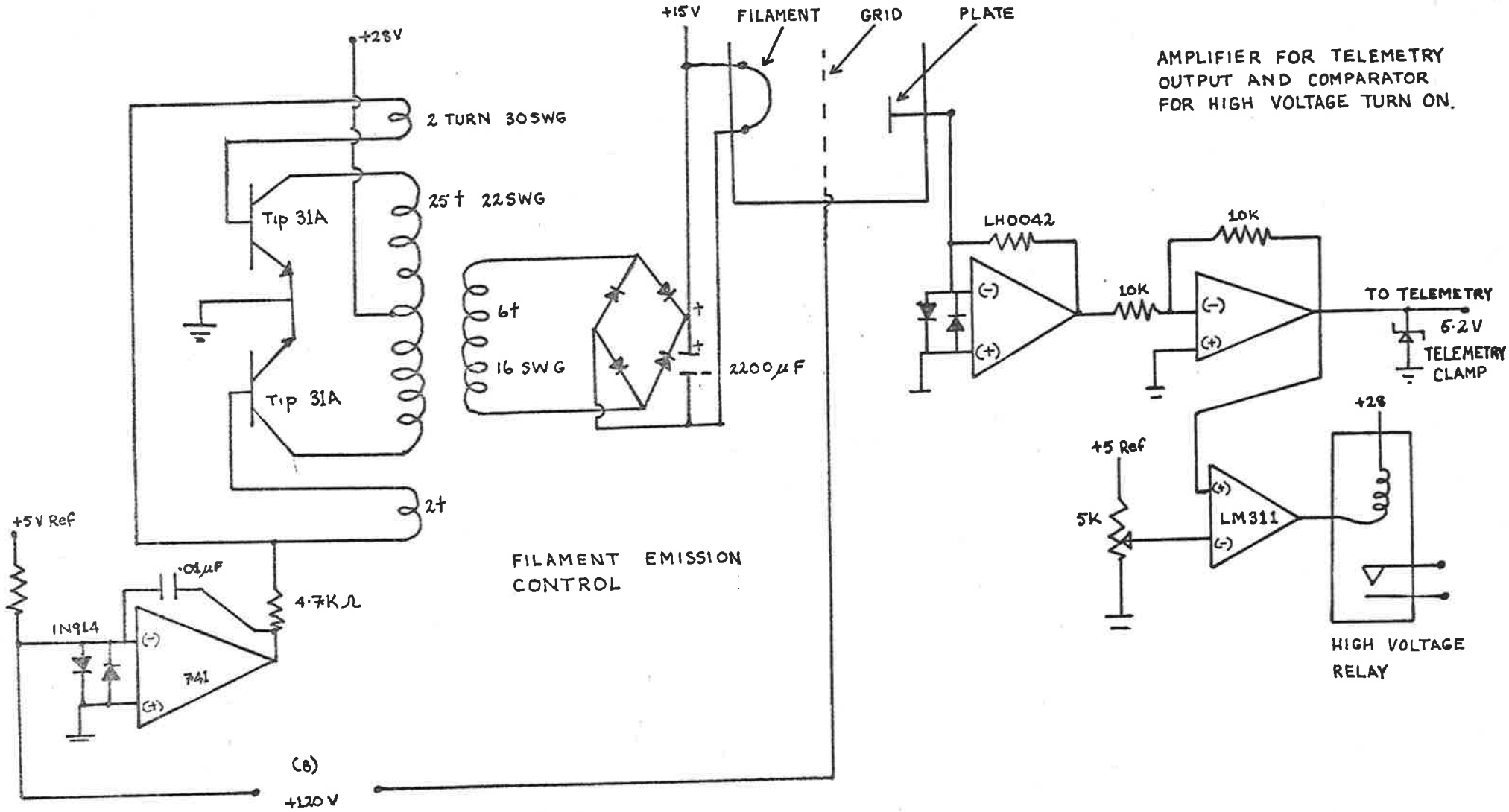

FIG. 5·15: IONIZATION GAUGE ELECTRONICS AND HIGH VOLTAGE SWITCHING SYSTEM.

5.2.9 ASPECT SENSORS

The ram effect which relates the number density of the atmospheric particles in the ion source to the ambient number density is a complex function of the angle of attack (equations (4.40), (4.43) and (4.44)), and, therefore, it is necessary to determine the aspect of the rocket during flight. The two most common ways that this can be achieved are:

(a) Optically, by flying aspect sensors which use the sun, the moon or the stars as light sources and, hence, reference positions.

(b) Magnetically, exploiting the direction of the earth's magnetic field lines with a magnetometer aboard the vehicles.

On the Lorikeet vehicle L1002 there was no space for a magnetometer so that two quadrant aspect sensors, one forward looking as in fig. 5.16 and the other side looking as in fig. 5.19, were flown. The quadrant aspect sensor is a position sensing device which uses four independent light sensitive areas in a two dimensional plane array. The type used is a Spot-2D made by United Detector Technology, Inc., and is sensitive to the spectral region from 300 to 1100 nm. With the cover mask as in fig. 5.16 and 5.19, its angle responses are shown in figs. 5.17, 5.18 and 5.20. The numbers on the graphs are the designated telemetry channels.

The electronic circuit for the aspect sensors is shown in fig. 5.21.

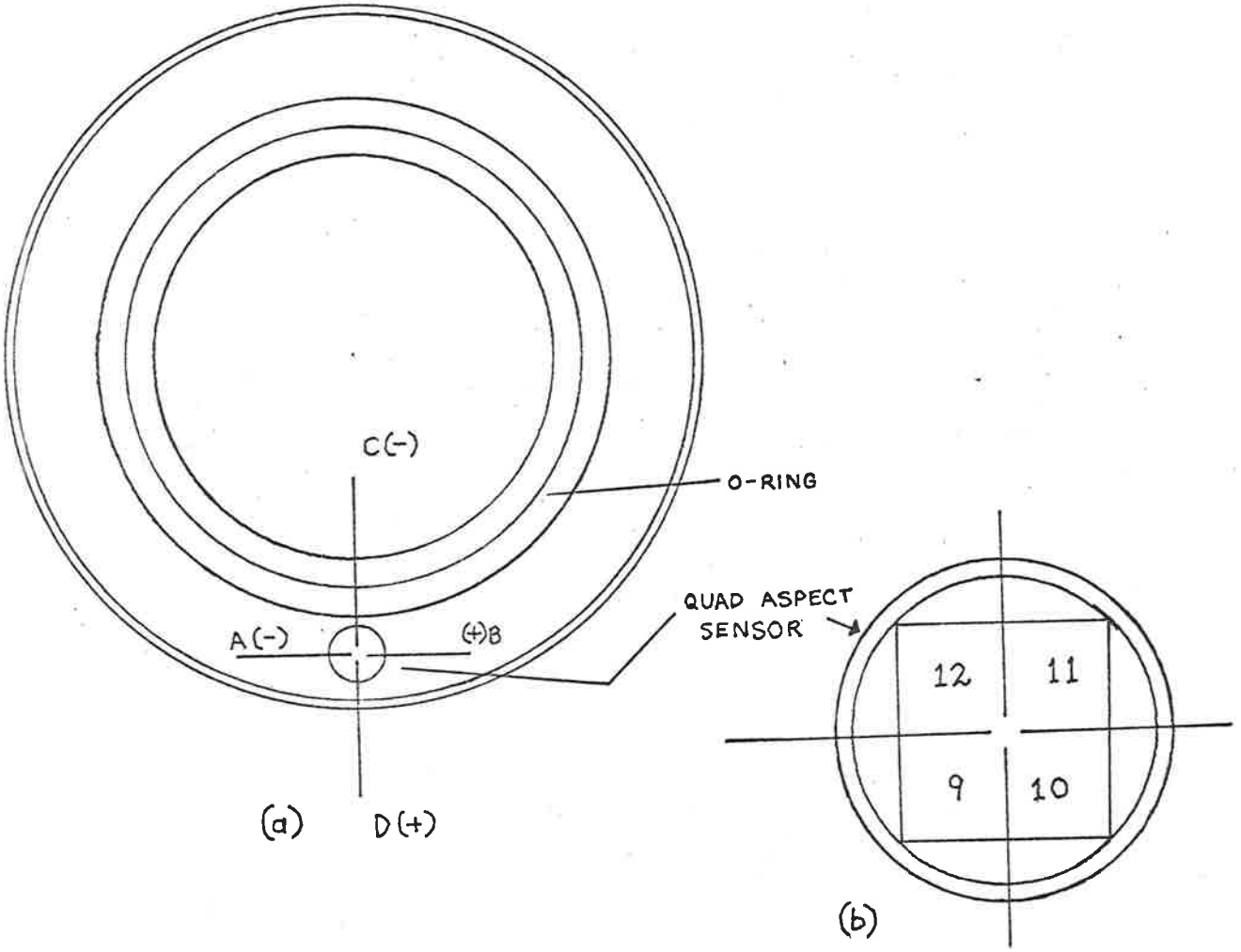

FIG 5·16 (a) POSITION OF THE FORWARD LOOKING QUAD ASPECT SENSOR ON THE L1002 VEHICLE.
(b) ENLARGED SURFACE OF THE SENSOR WITH THE DESIGNATED CHANNEL NUMBERS OF THE TELEMETRY.

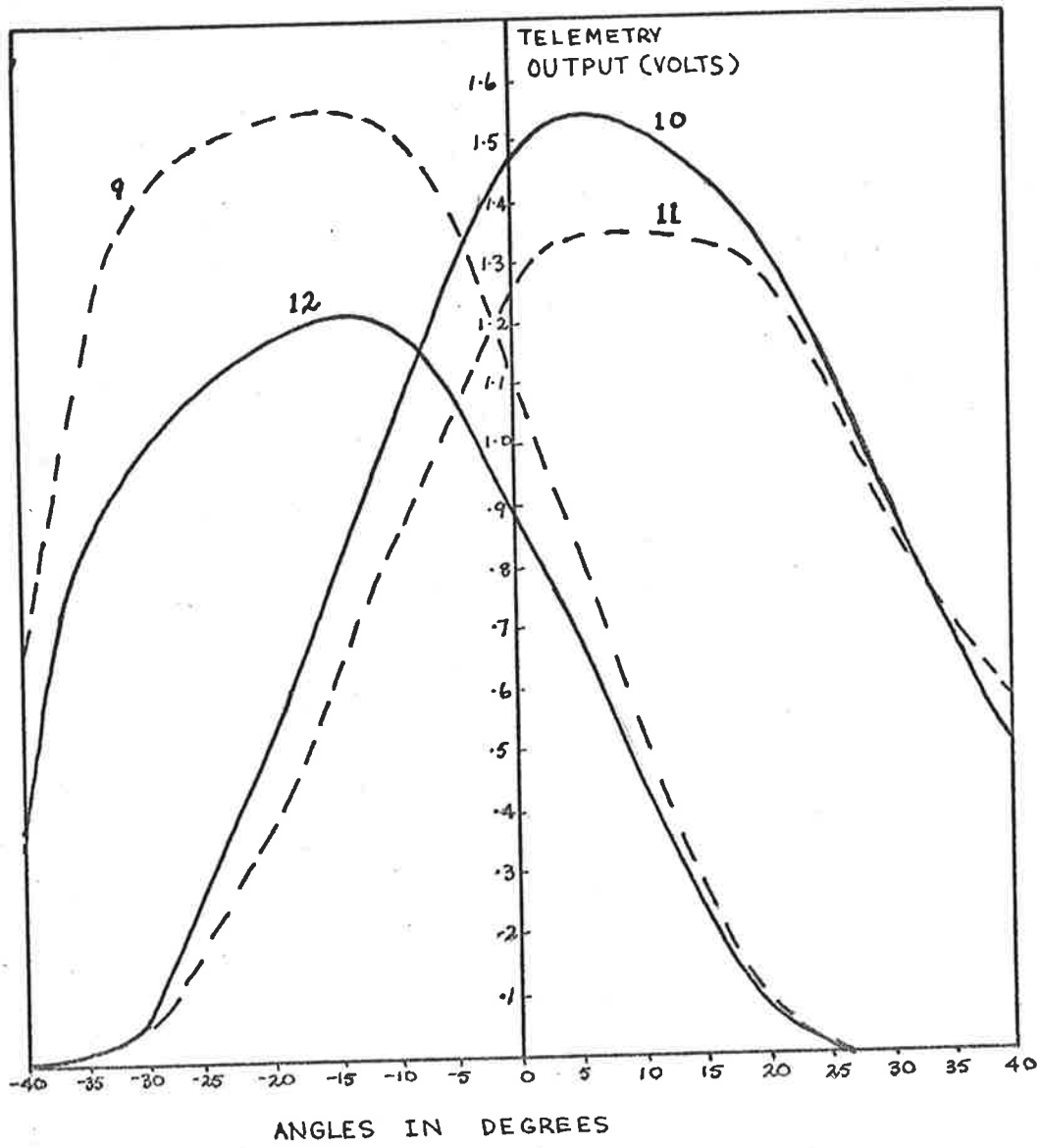

FIG. 5·17: ANGLE RESPONSE OF THE QUAD ASPECT SENSORS FROM A TO B. (FIG 5·16).

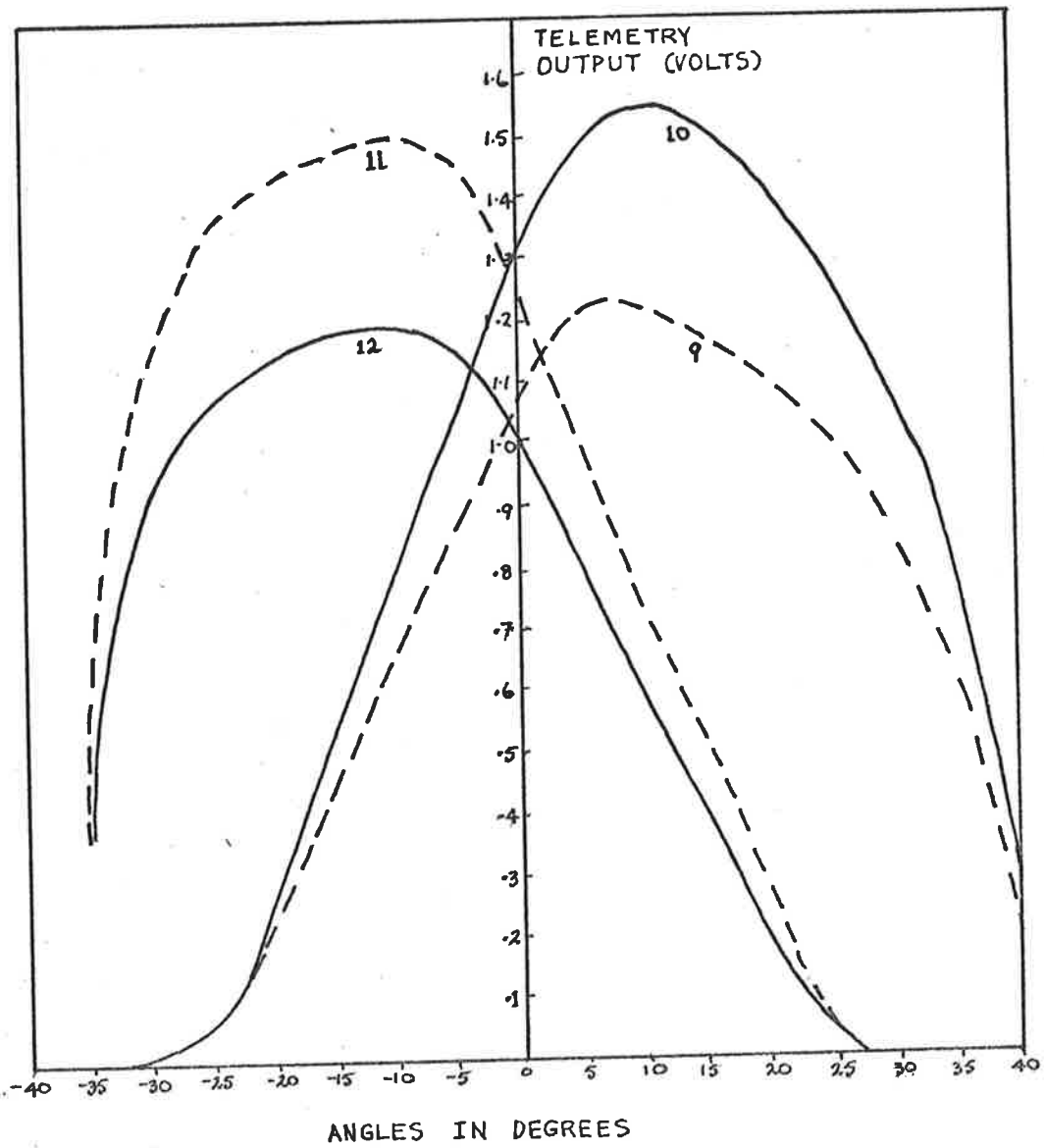

FIG. 5·18: ANGLE RESPONSE OF THE QUAD ASPECT SENSOR FROM C TO D (SEE FIG. 5·16). THE NUMBERS ON THE GRAPHS ARE THE TELEMETRY CHANNEL NUMBER OF THE QUADRANT OUTPUTS.

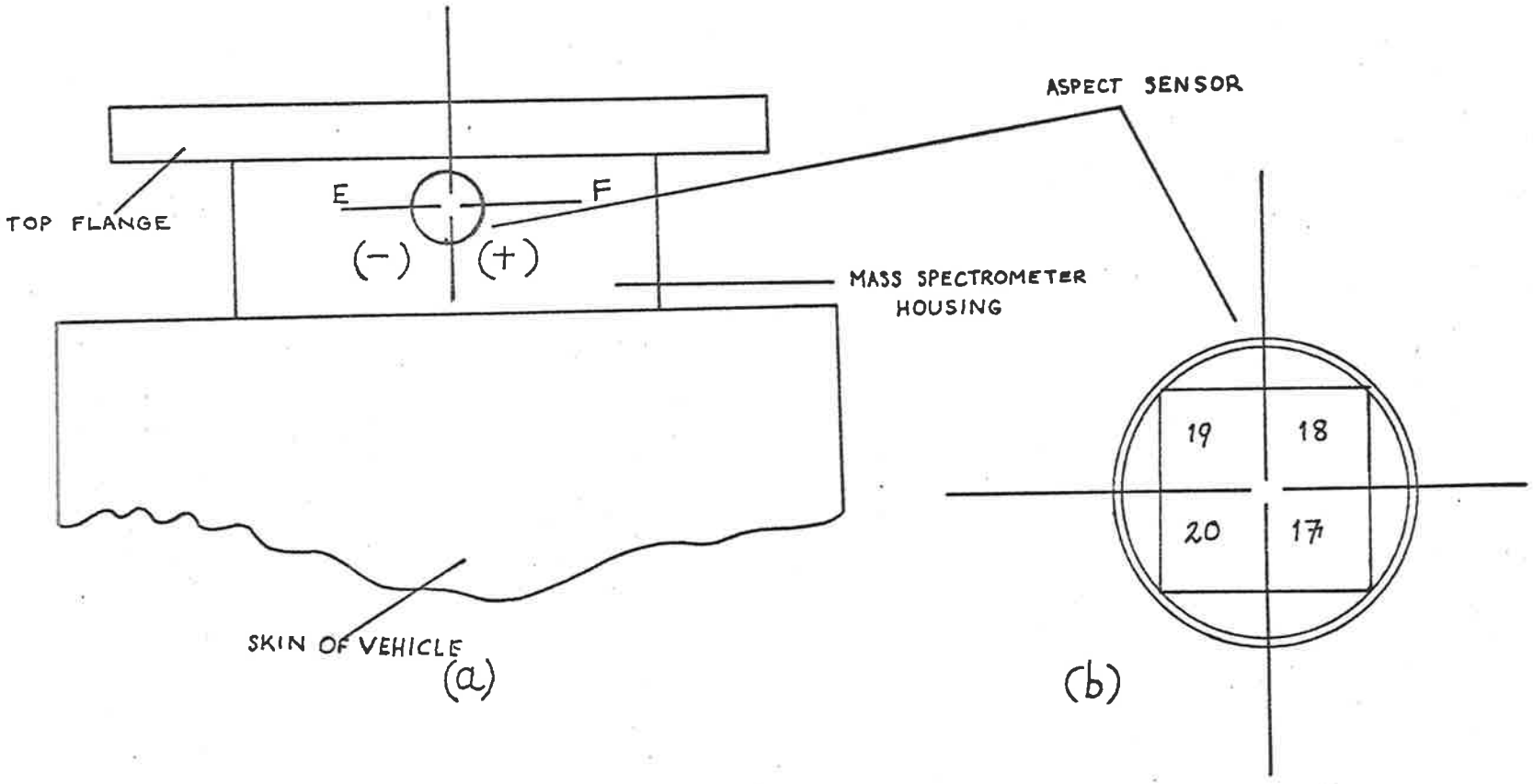

FIG. 5-19: (a) POSITION OF THE SIDE LOOKING ASPECT SENSOR ON L1002 VEHICLE.
(b) ENLARGED VIEW OF THE QUADRANTS OF THE ASPECT SENSOR WITH THE DESIGNATED TELEMETRY CHANNELS.

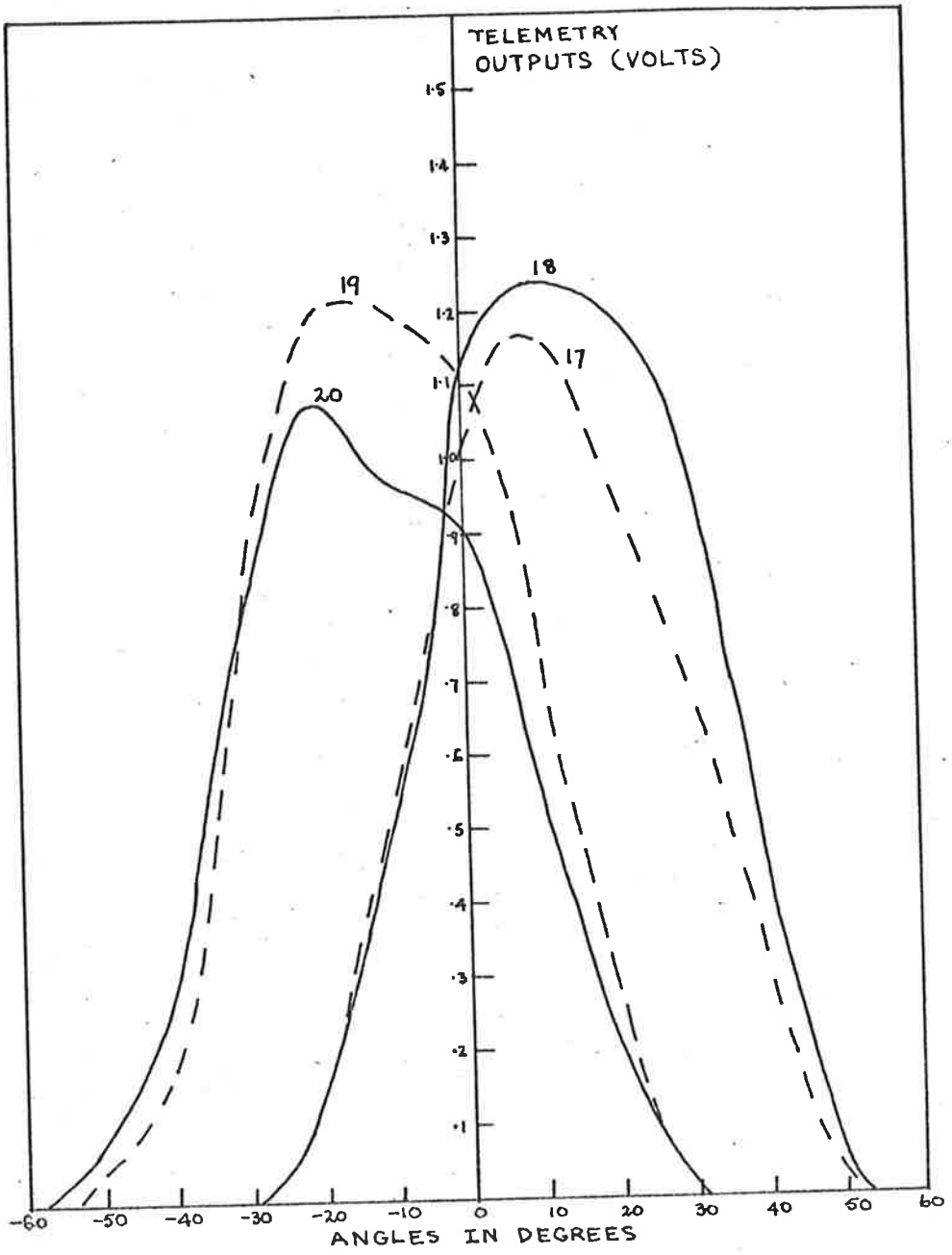

FIG 5·20: ANGLE RESPONSE OF THE SIDE LOOKING ASPECT SENSOR FROM E TO F. (FIG 5·19)

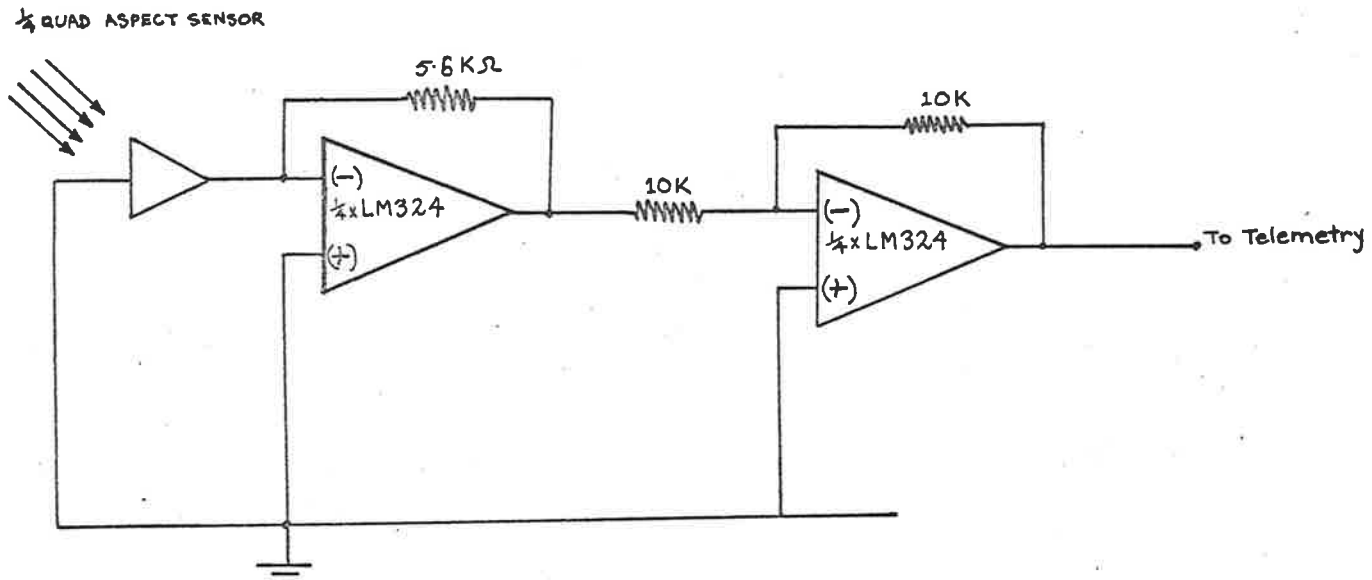

FIG 5·21: QUADRANT ASPECT AMPLIFIER. THERE ARE 8 AMPLIFIERS OF THIS TYPE.

5.2.10 MAGNETOMETERS

The second Lorikeet payload, L1003, carried a two axes magnetometer, model LFG-A13 made by Smith Industries, Ltd (Middlesex, U.K.) and a side looking solar aspect sensor so that its aspect could be determined unambiquously.

The circuit diagram of the magnetometer is shown in fig. 5.22 and it makes use of the unique property of the integrated circuit oscillator chip, 3038. This oscillator chip has outputs which give simultaneously sine, square and triangular waves in the characteristic phase relationship as shown in fig. 5.22. The sine wave is fed in series through a buffer amplifier to one of the windings of each magnetometer head, while the square wave with the use of a comparator and an exclusive OR gate is doubled in frequency and fed to the 532 multiplier. To achieve this frequency doubling, the threshold on the comparator is set so that the output square wave is 90^{o} out of phase with the square wave coming out of the output of the oscillator. The rest of the circuit is self explanatory.

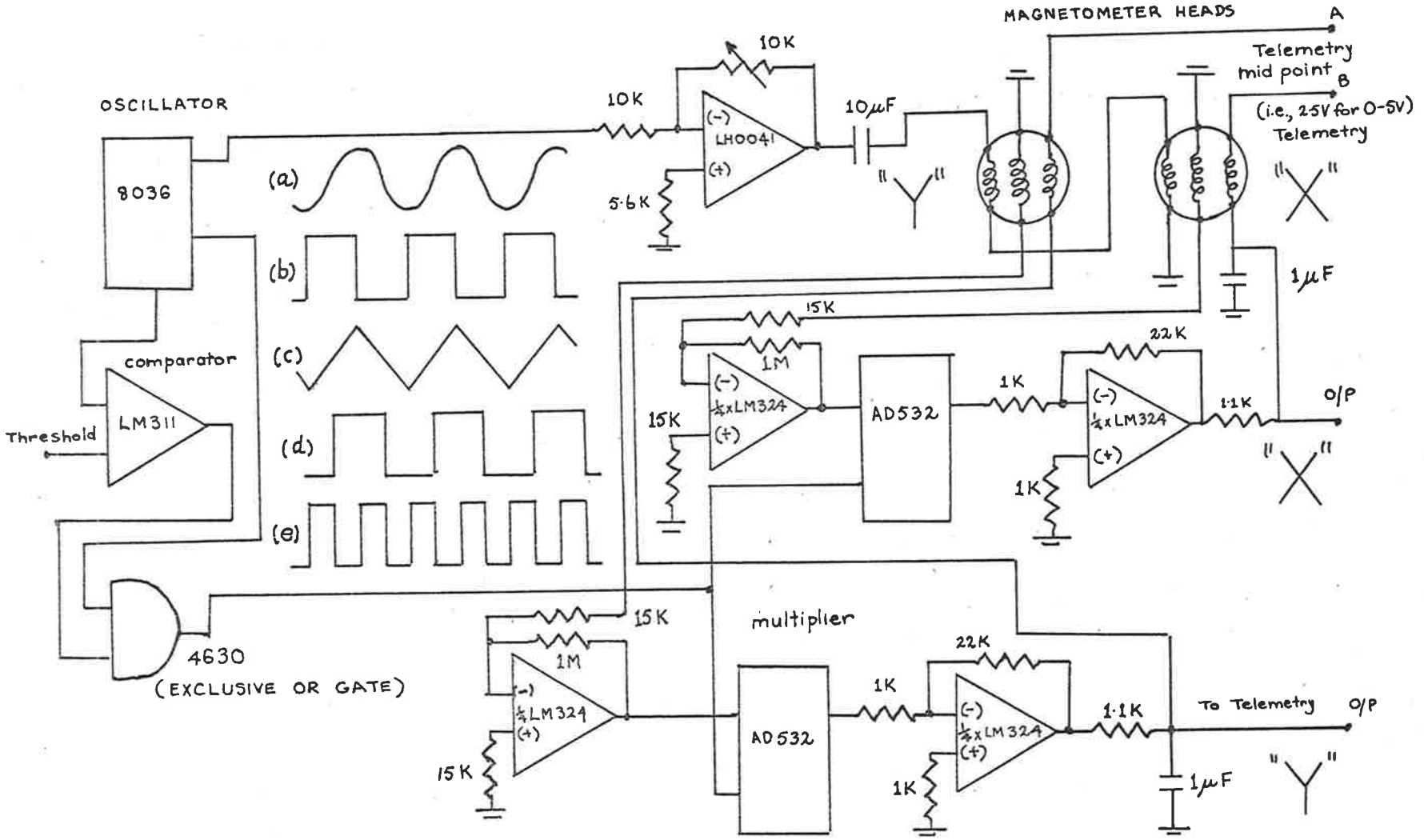

FIG 5·22: MAGNETOMETER ELECTRONIC CIRCUIT. Waveforms: (a), (b) and (c) outputs from oscillator, (d) output from comparator (e) output from exclusive or gate.

5.2.11 TELEMETRY

Both payloads, L1002 and L1003, had a 24 channel telemtry system. The telemetry accepted analog input signals having amplitudes in the range from 0 to +5 volts. These amplitudes then had to be converted to voltages in the range from -3 to +3 V to suit the sender. The sender is of the type TM5H made by E.M.I. and has a frequency of about 441 MHz. It operates on a +28 V supply and has an output power of 800 mW.

The complete telemetry circuit is shown in fig 5.23.

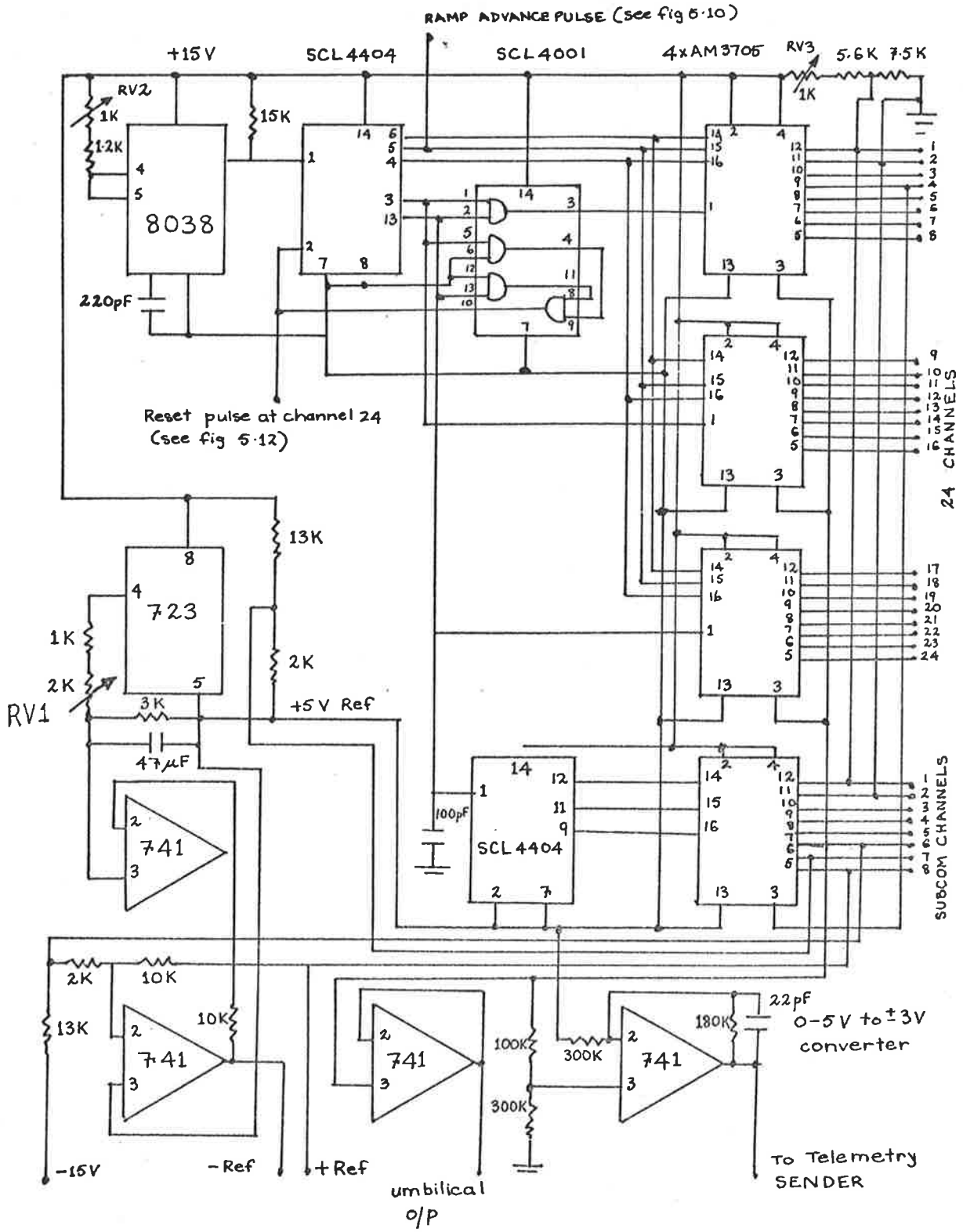

FIG 5·23: TELEMETRY CIRCUIT

Set RV2 for clock of 160 Hz

Set RV3 for sync. of 8·1 V

Set RV1 for +5·00 V Ref.

5.3.1 CALIBRATION OF NEUTRAL MASS SPECTROMETERS

The requirement for absolute in situ measurements of the atmospheric constituents by means of mass spectrometers makes it necessary to determine the absolute sensitivity of these instruments. Ideally to calibrate the spectrometers in the laboratory, they would need to be placed in a wind tunnel and simulate the flight conditions. The necessity for the flight simulation is in the fact that during a large portion of the ascent flight the atmospheric particles enter the ionizing region with relatively high velocities and as a result the number density in the ion source far exceeds that of the surrounding atmosphere. Unfortunately, flight simulations of rocket payloads are difficult to realize so that the analyzers are usually calibrated with diffuse gases at room temperature. Thus, the measured densities during flight have to be corrected for the "ram effect", an effect which makes the sensitivity of the analyzers dependent on the way the gas enters the ion source. It is much larger when the incoming gas particles form a nearly molecular beam (lower part of the rocket flight) than when they enter diffusively (apogee). Also, near apogee any outgassing from the ion source walls becomes important since it introduces errors in the measured densities.

For a quasi-opened ion source of the type shown in fig. 4.9, in the laboratory, the number density in the ion source $n_{s\ell}$ is related to the ambient number density $n_{a\ell}$ of the gas in the vacuum calibrating tank by equations (4.55), that is:

$$n_{s\ell} = n_{a\ell}(\sin^2\theta/2 + \sqrt{T_\ell/T_s}.\cos^2\theta/2) \qquad (5.4)$$

where T_ℓ and T_s are the temperatures of the ambient gas and ion source surfaces, respectively and θ is a geometrical parameter of the ion source. Then for a particular gas the

counting rate R_ℓ (counts/sec) from the output of the channeltron in the laboratory is:

$$R_\ell = S.n_{s\ell} \tag{5.5}$$

$$= S.n_{a\ell}.(\sin^2\frac{\theta}{2} + \sqrt{T_\ell/T_s}.\cos^2\frac{\theta}{2}) \tag{5.6}$$

where S is the sensitivity of the ion source-mas spectrometer-channeltron ensemble. This parameter, S, depends on the intensity of the ionizing electron current I^-, ionizing cross-section, σ, detection efficiency of the channeltron, ε, the transmission of the quadrupole, τ, energy of the ions, E, and the type of gas used through σ, ε and τ which are different for different gases. That is, for a particular gas:

$$S = S(I^-, \sigma, \varepsilon, \tau, E) \tag{5.7}$$

Equation (5.6) can then be written in the form:

$$R_\ell = S.G_o.n_{a\ell} \tag{5.8}$$

where:

$$G_o = \sin^2\frac{\theta}{2} + \sqrt{T_\ell/T_s}.\cos^2\frac{\theta}{2} \tag{5.9}$$

The factor $S.G_o$ is a function of a number of parameters which once the resolution of the analyzer is set are kept constant so that it can be determined in the laboratory from the slope of the straight line of the graph in which R_ℓ is plotted against $n_{a\ell}$. Then, during flight the counting rate, R_f, is:

$$R_f = S.G.n_a \tag{5.10}$$

where n_a is the ambient atmospheric particles' density and G, from equations (4.43) and (4.44) has the form:

$$G = \sqrt{T_a/T_{is}}.\left[F(S_z).K_1\sin^2\eta.\cos^2\eta/(1 - K_1.\cos^2\eta)\right.$$
$$\left. + E(S_z,S_r,\eta)\right].K_2.\sin^2\frac{\theta}{2}.\cos^2\frac{\theta}{2}/(1 - K_2.\cos^2\frac{\theta}{2})$$
$$+ \tfrac{1}{2}\left[1 + \mathrm{erf}(S_z) - M_o^*.\exp(-S_z^2) - H^*(S_z,S_r,\theta)\right] \tag{5.11}$$

where the different symbols have already been defined in section 4.4.4. Then, from equations (5.8) and (5.10), it follows that the measured number density during a rocket flight is:

$$n_a = R_f/S.G \qquad (5.11)$$

As already mentioned, the sensitivity factor S is derived from the calibration graphs while:

$$G = G(S_z, S_r, \theta, \eta, T_a, T_{is}, K_1, K_2) \qquad (5.12)$$

is computed from the geometrical parameters θ and η and temperature, T_{is}, of the ion source, vehicle velocity vectors, S_r, S_z, and the atmospheric ambient temperature, T_a, which is usually taken from a model atmosphere such as CIRA (1972). Also, assumptions have to be made as to the values to take for the accommodation coefficients, K_1 and K_2, for the various sampled gases.

The system employed for calibrating the mass spectrometers is shown in fig 5.24. A small volume V (c.c.) of a gas sample (e.g. O_2, H_2, Ar, He, CO_2) at a known pressure, P (torr), is admitted to a large vacuum tank of capacity 2.415×10^6 cubic centimetres. Knowing the temperature T (^oK) of the gas, the number density in the vacuum tank can be easily calculated from the Loschmidt's number which represents the number of particles in 1 c.c. of a gas at a temperature of 0^oC and normal atmospheric pressure. From this, the number of particles per c.c. in the tank is:

$$n = 5.63 \times 10^7 \times P \times V \times T \text{ particles/c.c.} \qquad (5.13)$$

where P, V, and T have already been defined. Thus, by knowing P, V, and T, it is possible to adequately calibrate the mass

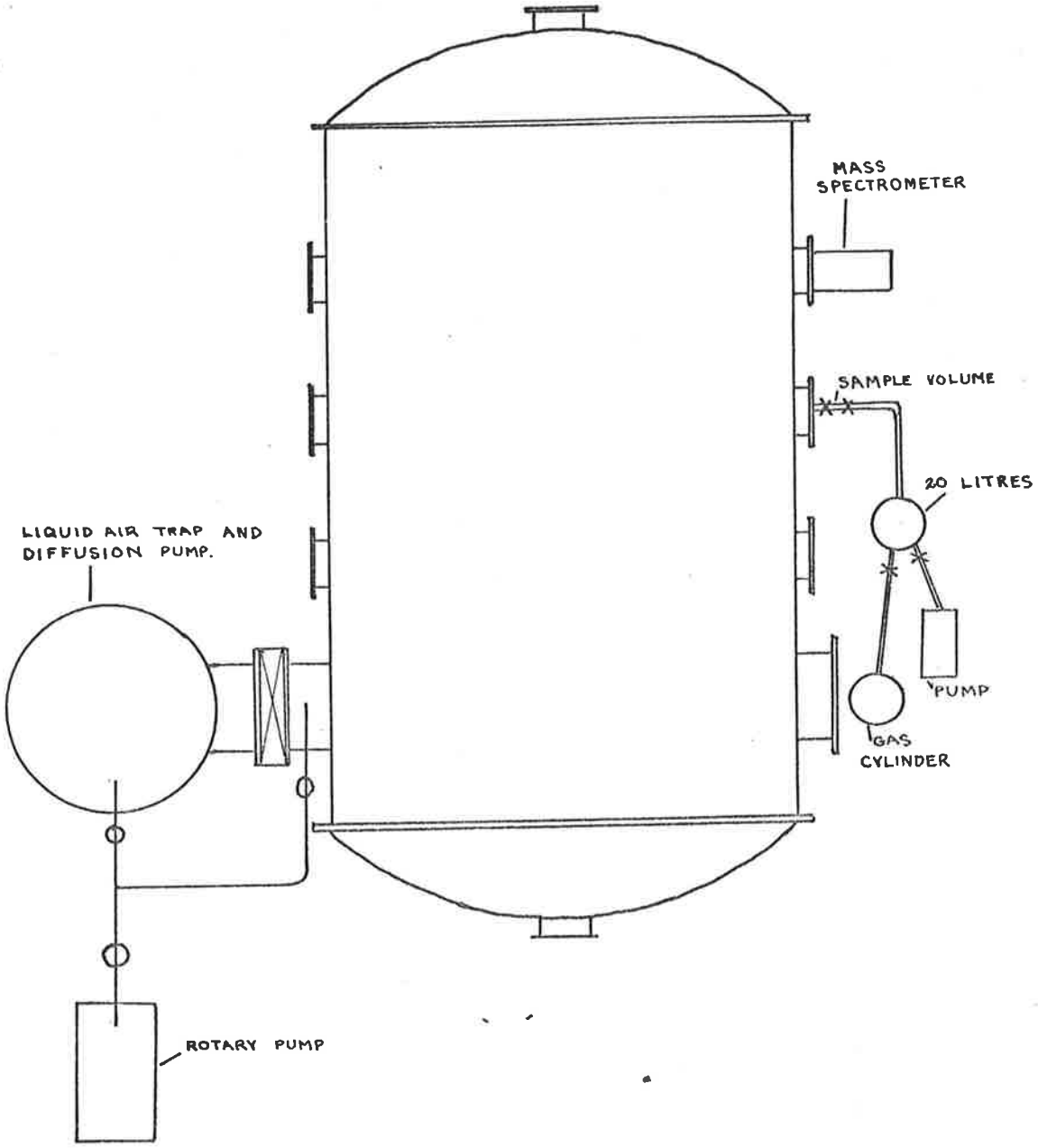

FIG 5·24: SCHEMATIC VIEW OF THE CALIBRATION SYSTEM FOR THE MASS SPECTROMETER

spectrometers absolutely.

During the calibration procedures of the analyzers, the temperature of the ion source's walls were kept (within a few degrees centigrade) equal to that of the laboratory's ambient. This could be done because the electron emission currents from the filaments were very low, only 8μA for the L1002 and L1003 payloads and 3.5μA for the Aerobee's analyzers, and the filaments were switched off after every mass scan. Furthermore, the ion source-mass spectrometer's housings were bolted on to the large vacuum tank which provided a large surface area and bulk material to dissipate and conduct heat away from the ion sources. Thus, in equation (5.8) G_o becomes equal to unity and the response of the mass spectrometers in the laboratory is independent of the ion source's geometry and temperature, provided T_s is kept equal to T_ℓ. Unfortunately, if the filament is kept switched on for a long period of time space charges built up in the ion sources so that the response of the mass spectrometers was not constant but increased slightly with time. This trend is the same for all gases and is shown in fig. 5.25 for the Aerobee's neutral mass spectrometer for molecular hydrogen. This space charge "build up" was due to the fact that the ion sources used were of simple geometry, and, by calibrating the analyzers at a certain fixed time after the filament had been switched on, the measured densities during flight can be corrected for the space charge effect. With the calibrating system used it was found that it was convenient to switch on the filament and allow 10 seconds to elapse before a mass scan was recorded (see fig. 5.25).

Plots of the reponses to different gases of the neutral mass spectrometers which constituted the payloads

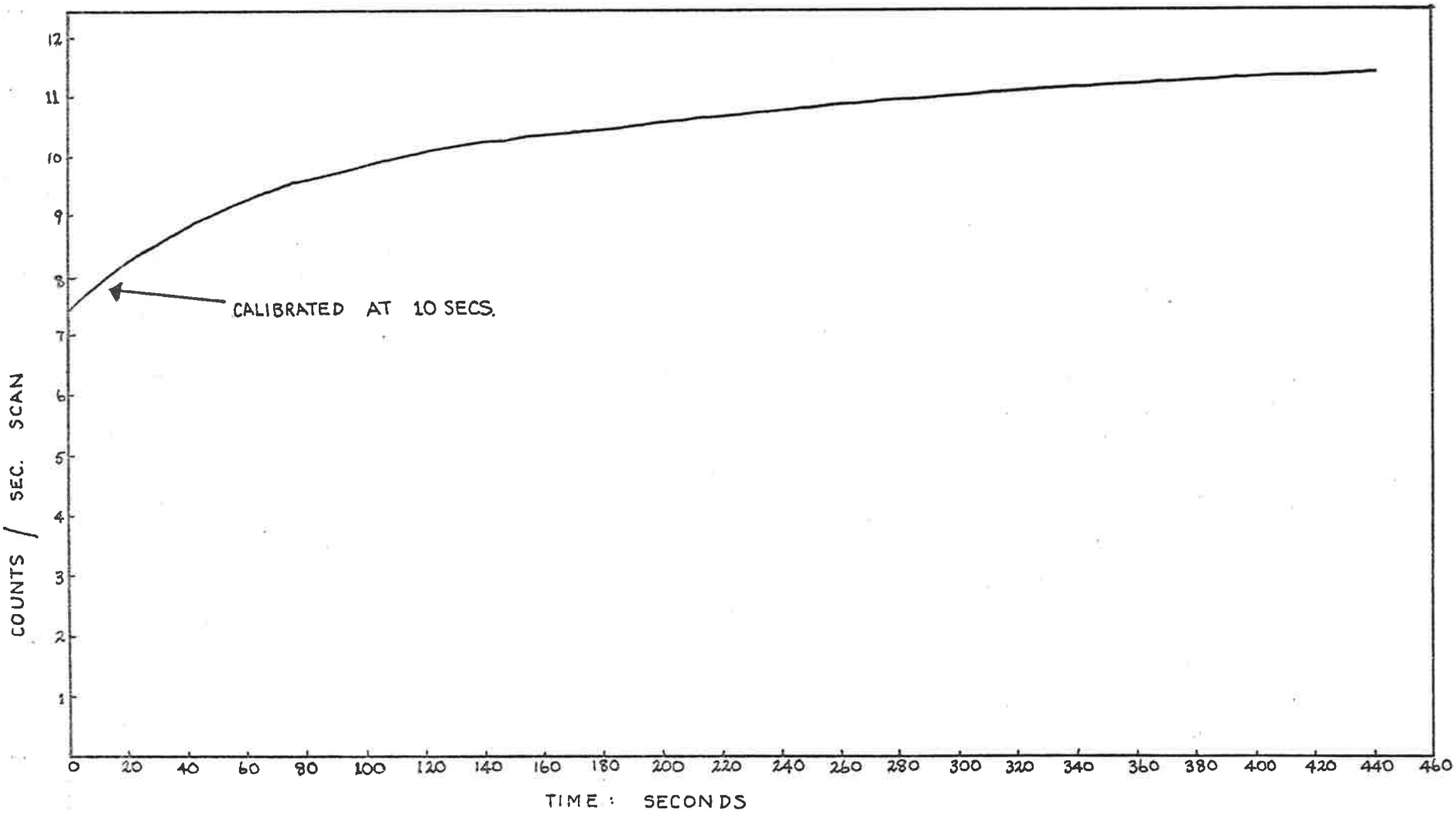

FIG. 5·25 TIME RESPONSE FOR THE AEROBEE'S NEUTRAL MASS SPECTROMETER FOR MOLECULAR HYDROGEN.

L1002, L1003 and that of the Aerobee are shown in figs. 5.26, 5.27, and 5.28 respectively and their values of the sensitivities are tabulated in table 5.1. The unit of sensitivity used is counts/number of particles per c.c. over one second mass scan period.

The sensitivities of the three mass spectrometers are different. The reason was that the first quadrupole, L1002, was operated at a radio-frequency of 2.0 MHz and hence had a high inherent mass resolution even though the length of its electrodes were only 136 mm, while the analyzer of L1003 was operated at a R.F. of 1.2 MHz and as a result in order to attain a resolving power at least equal to the mass being scanned, the ratio DC/AC had to be increased considerably which had the effect of decreasing the transmission and hence the overall sensitivity. The Aerobee's quadrupole had electrodes of length 200 mm and, as a consequence, the resulting resolving power was high even at the low radio frequency of 1.0 MHz. However, this low radio-frequency had the disadvantage that the AC voltage (peak to peak) on the adjacent electrodes of the analyzer required per unit mass was only 2.5 volts and a small R.F. feeding through the tuned tank circuit of the quadrupole degraded the ratio DC/AC and hence enhanced the transmission for hydrogen (fig. 5.28 and table 5.1). The sensitivities of the three neutral mass spectrometers were set such that the channeltrons used as the detectors did not saturate in flight in the altitude range 110-200 Km.

For data collection during calibration a multichannel storage device has been used and the accumulated counts have been corrected for the dead time of the storage device. For the gases oxygen and nitrogen the mass peaks have also

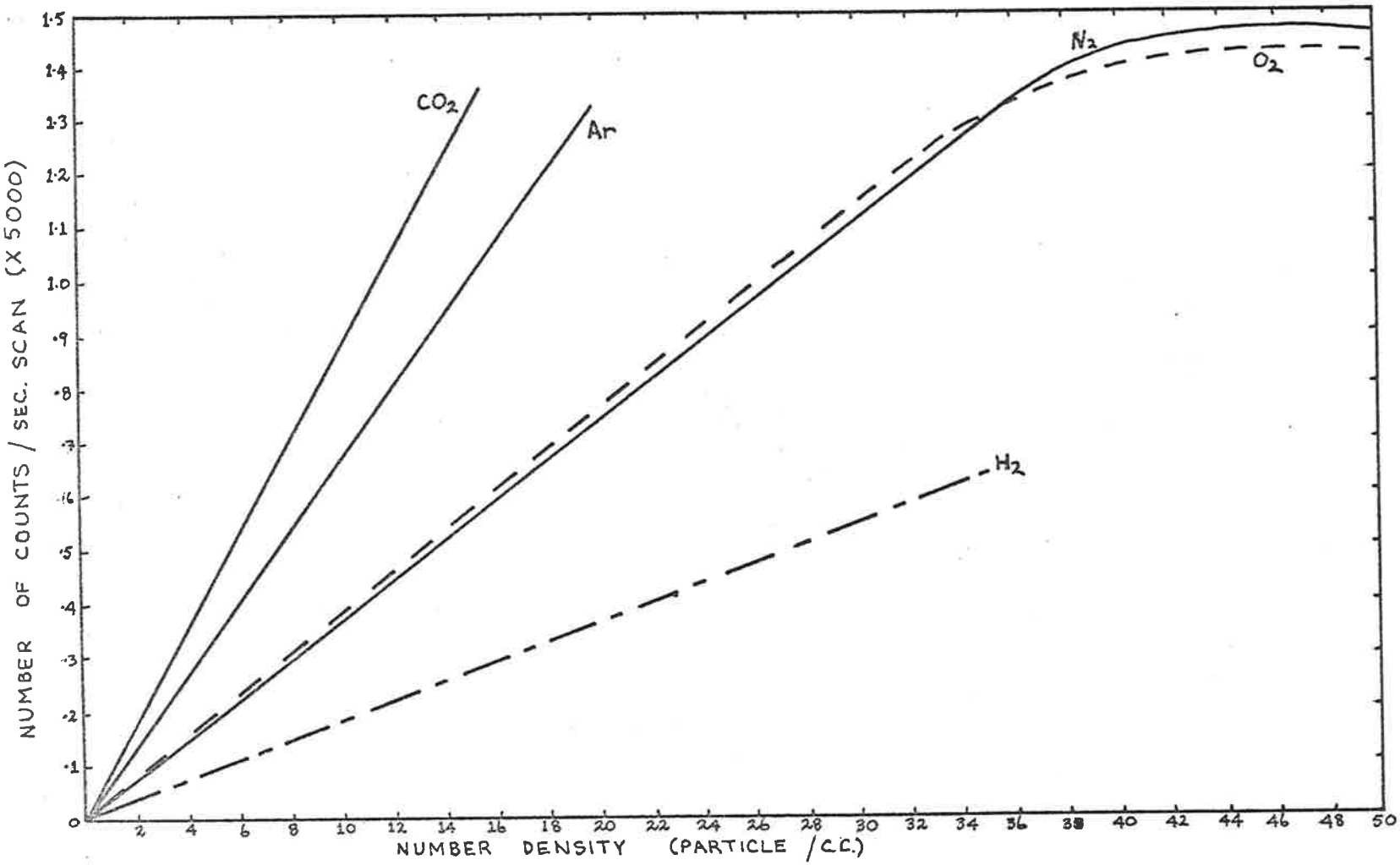

FIG. 5·26: RESPONSE OF THE MASS SPECTROMETER L1002 TO THE GASES O_2, N_2, Ar, CO_2 AND H_2.

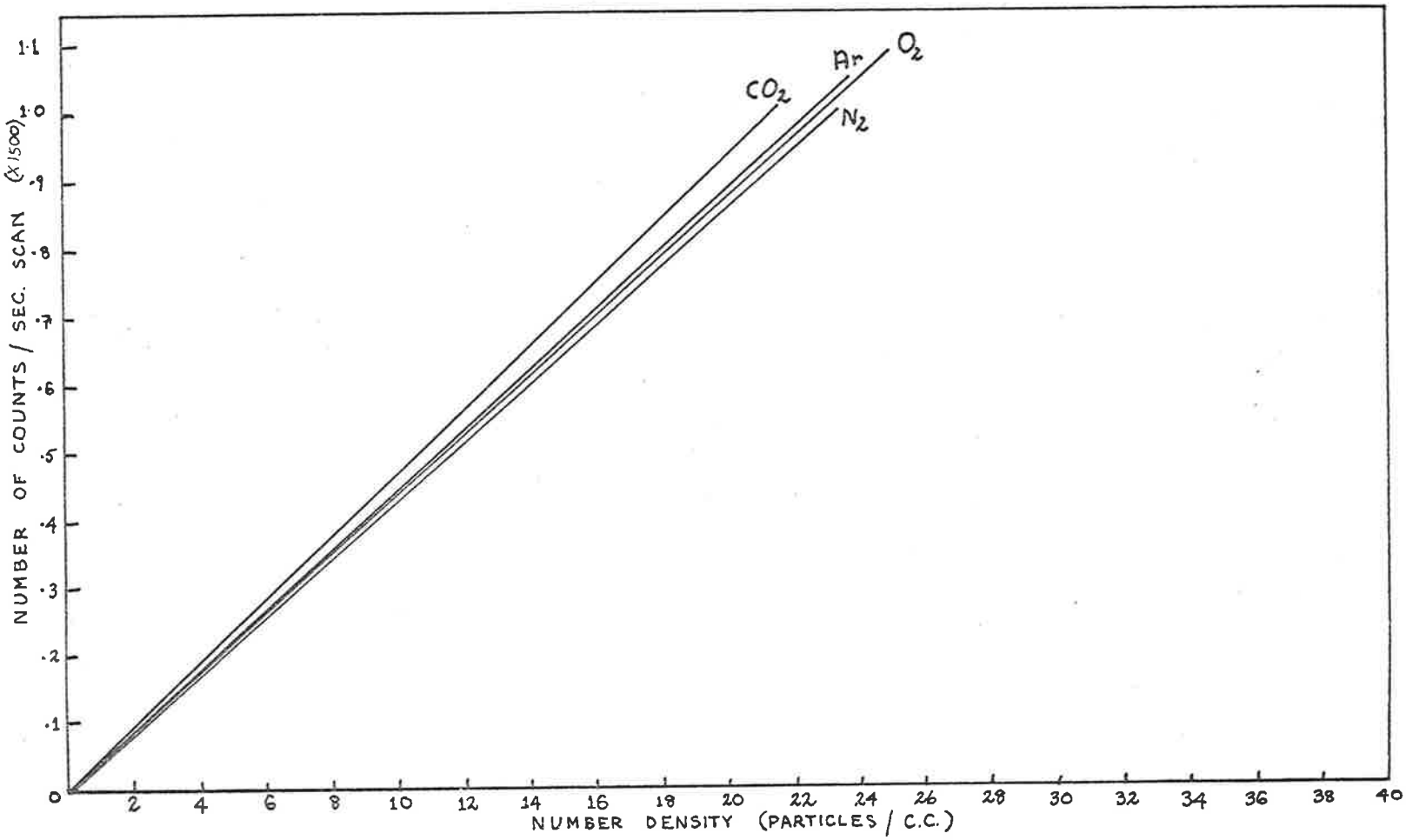

FIG 5·27: RESPONSE OF THE MASS SPECTROMETER L1003 TO VARIOUS GASES.

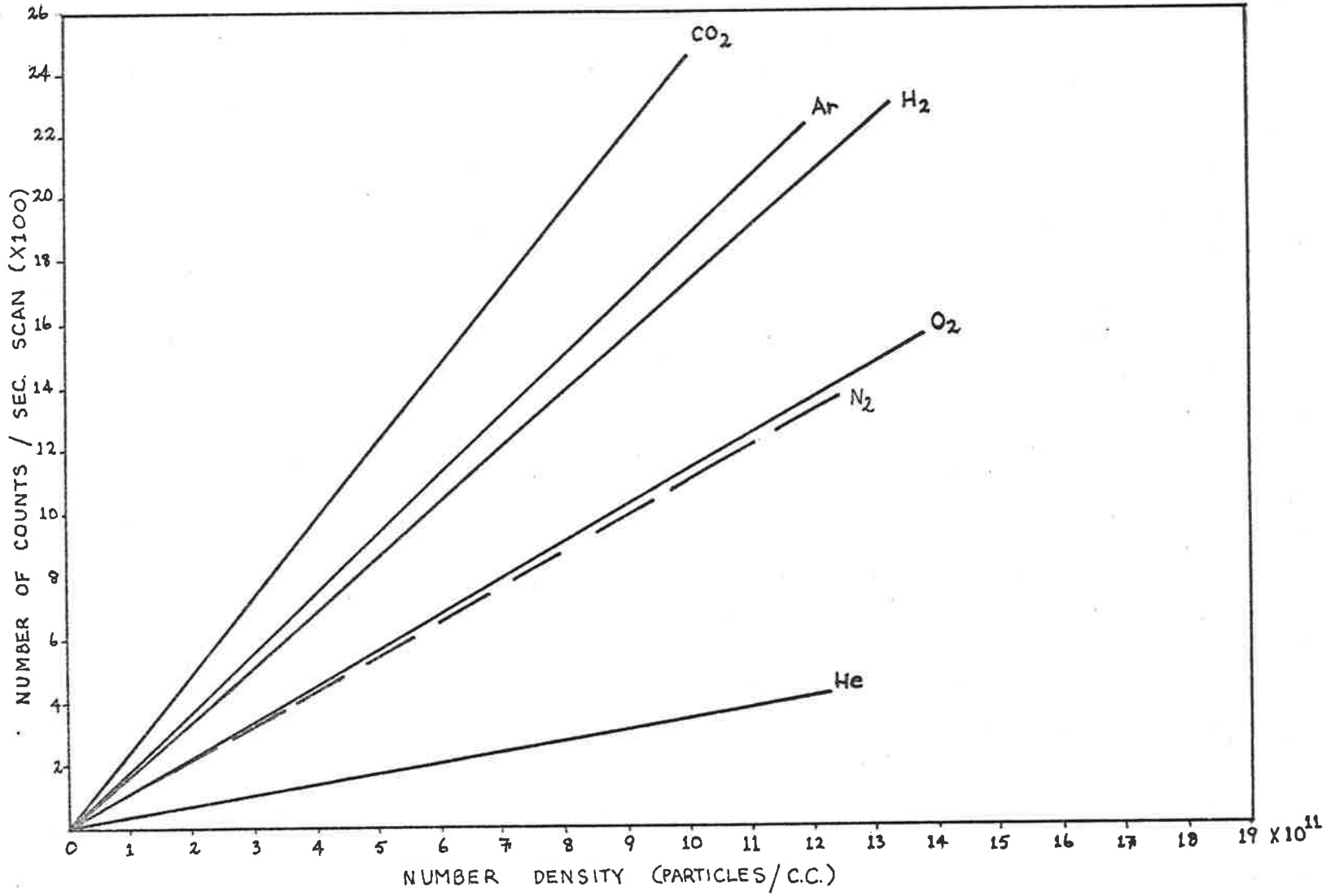

FIG. 5·28 RESPONSE OF THE AEROBEE'S NEUTRAL MASS SPECTROMETER TO VARIOUS GASES.

Table 5.1

SENSITIVITY S OF THE NEUTRAL MASS SPECTROMETERS L1002, L1003 AND AEROBEE FOR DIFFERENT GASES. THE UNIT FOR THE SENSITIVITY IS COUNTS/NUMBER OF PARTICLES PER C.C. IN ONE SECOND MASS SCAN.

gases	L1002	L1003	Aerobee
	$x10^{-10}$	$x10^{-10}$	$x10^{-10}$
$S(H_2)$	9.1	-	17.5
S(He)	-	-	3.5
$S(N_2)$	18.8	6.4	11.0
$S(O_2)$	19.1	6.6	11.4
S(Ar)	33.4	6.6	18.7
$S(CO_2)$	43.8	7.0	24.6

been corrected for the desorption of these gases from the surface of the vacuum tank so that the sensitivities lines of figs. 5.26, 5.27, and 5.28 represent the "true" sensitivities of the analyzers.

If the number density of the gases in the tank is too high, then saturation effect takes place. This is shown in fig. 5.26 for the L1002 quadrupole. Saturation starts occurring for values of number density of about 3.6×10^{12} particles/c.c. which corresponds to a pressure greater than 10^{-4} torr and hence an altitude in the atmosphere of less than 100 Km. For the analyzer of the L1003 payload the saturation effect occurs at much higher pressures since the sensitivity is less than that of L1002. The saturation effect is a combination of two processes: decrease of the gain of the channeltron with counting rate (section 4.5.3) and ion-neutral particles collisions in the quadrupole. In fact, at high pressures, because of the ion-neutral particles scattering, some of the unstable ions will reach the detector and the resolution deteriorates, while at the same time some of the ions, which at low pressure would have reached the collector, will be lost due to collisions and hence the transmission of the analyzer willbe low. But for a minor gas, having a partial pressure much less than the abundant gas, there still exists a linear relationship between ambient minor gas and its ions collected at the output of the quadrupole despite the presence of the major gas at high pressure (i.e. no saturation effect occurs for a gas having a partial pressure much less than the major gas).

A simple gas can generally produce several kinds of ions, which have a different mass/charge ratio. This effect is mainly caused by two different processes:

(1) molecular dissociation by electron impact or

other means and subsequent formation of two or more ions.

(2) double ionization (multiple ionizations are possible but much less frequent), thus ions with a mass/charge ratio half (or less) can appear on the mass spectrum.

As a result of processes (1) and (2), a single gas can yield several mass peaks, some of which may hide the presence of other traces of minor constituents; for example N_2 and CO have the same mass/charge ratio and the large amount of N_2 in the atmosphere makes it impossible to detect the presence of CO, unless special techniques are used such as the employment of a U.V. light source to ionize CO and not N_2.

The mass spectrum of the flight quadrupole on the payload L1003 is shown in fig. 5.29 while that of the neutral mass spectrometer of the Aerobee rocket is shown in fig. 5.30.

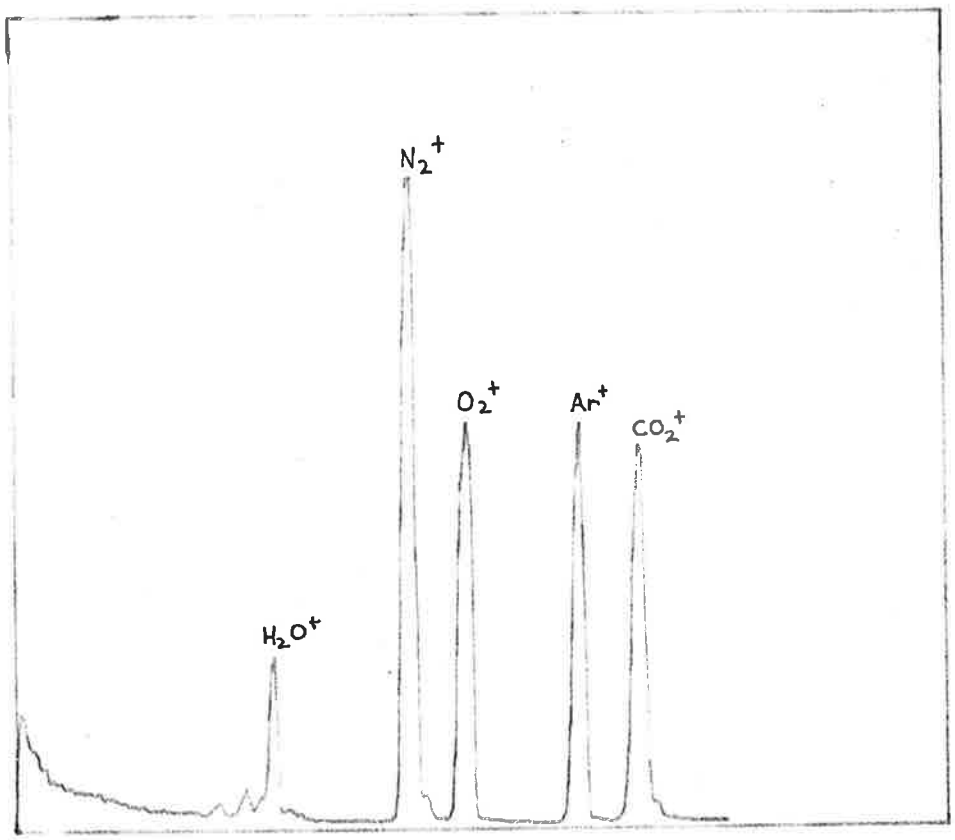

FIG 5·29: MASS SPECTRUM OF A MIXTURE OF N_2, O_2, Ar AND CO_2 GASES TAKEN WITH THE L1003 SPECTROMETER.

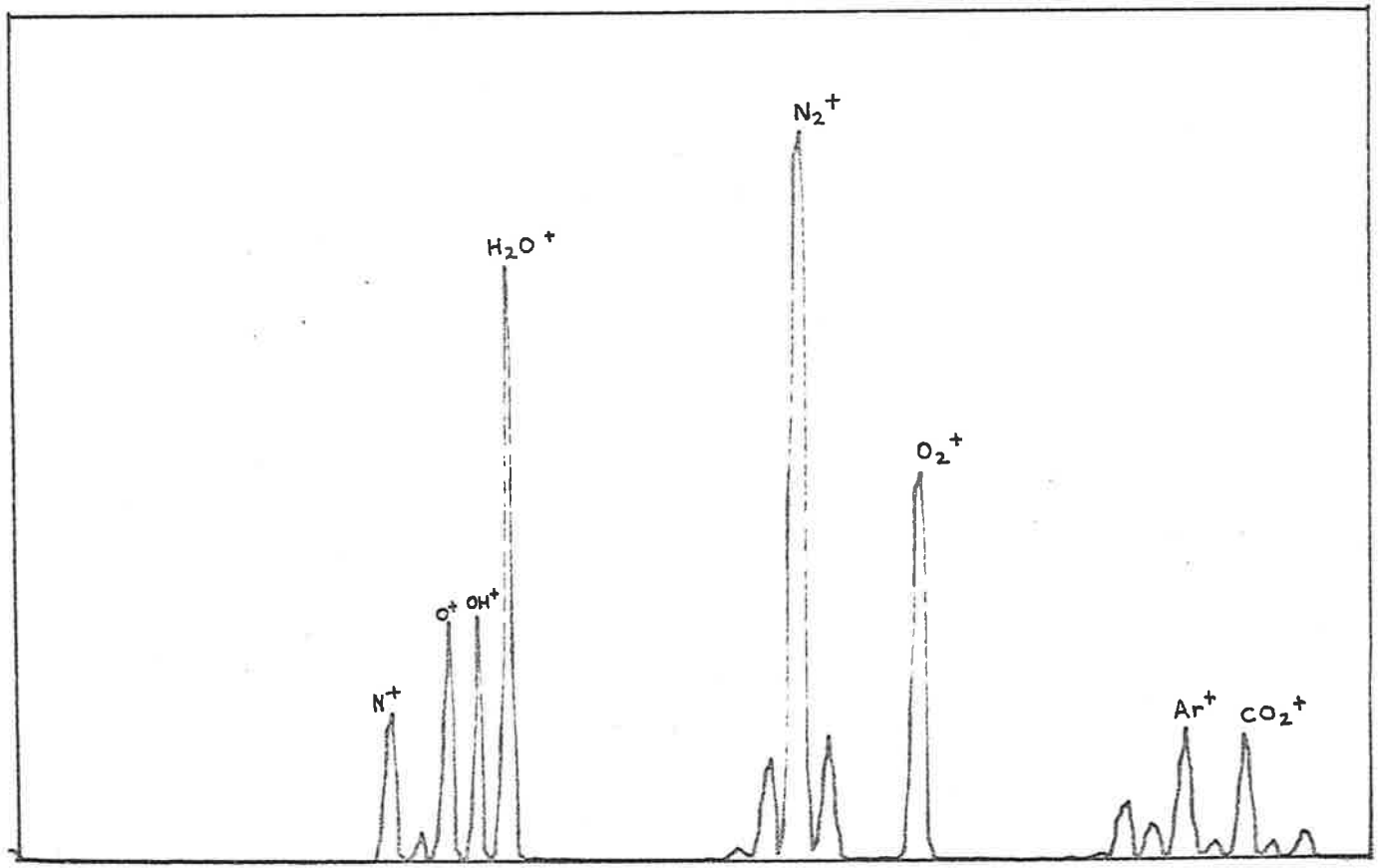

FIG 5·30: MASS SPECTRUM OF THE DESORPTED GASES OF THE VACUUM VESSEL TAKEN WITH THE NEUTRAL MASS SPECTROMETER FLOWN ON THE AEROBEE VEHICLE.

5.3.2 CALIBRATION OF NEUTRAL MASS SPECTROMETERS FOR ATOMIC OXYGEN

A direct calibration of the mass spectrometers for atomic oxygen in the laboratory is practically impossible and the difficulties lie mainly in the generation of a beam of atomic oxygen of a known concentration and in the fact that atomic oxygen reacts chemically with surfaces of the calibrating system. Atomic oxygen can be easily generated and there are mainly three ways in which this can be done:

(a) by the titration reaction

$$N + NO \longrightarrow N_2 + O \qquad (5.14)$$

(b) microwave discharge of molecular oxygen.

(c) thermal dissociation of molecular oxygen.

There are, however, three fundamental problems associated with the three methods of atomic oxygen generation. These are the formation of atomic oxygen in the excited states if method (b) is used, the formation of undesirable tungsten oxides, CO_2, CO, etc., at the filament's surface if (c) is used, and in the uncertainty of the atomic oxygen flux calibration.

Various attempts have been made to produce a beam of atomic oxygen in the laboratory for the purpose of calibrating mass spectrometers. For example, Narcisi et al (1962) used equation (5.14) to produce a beam of atomic oxygen while Niemann (1972) generated an atomic oxygen beam by thermal dissociation of molecular oxygen on the surface of a tungsten filament heated to 2800°K at a pressure of less than 10^{-4} torr. But as already mentioned, the main problem is in how to calibrate the generated beam.

Approximate calibration of the analyzers for atomic oxygen can be obtained from the molecular oxygen calibration. Knowing the ratio of ionization cross sections of atomic and molecular oxygen, which has been measured by Fite and Brack-

mann (1959), the number of O^+ ions formed at the ion source can be estimated, but it still leaves the determination of the mass discrimination factor, i.e. the transmission of the quadrupole and the detection efficiency of the detector for the O^+ ions. Some authors such as Trinks (1973) have determined the mass discrimination factor of the mass spectrometers by using methane, CH_4, which has the same mass number as atomic oxygen. Unfortunately, methane under electron bombardment breaks up into a large number of fragment ions such as CH_4^+, CH_3^+, C^+, and H^+ and some of these fragment peaks are very large. For example, the intensity of the peak of mass 15 is about 90% of that of mass 16, so that with the use of methane the discrimination factor can only be estimated but not accurately determined.

The calibration for atomic oxygen of the mass spectrometers on the L1002 and L1003 payloads have not been computed for a reason which will be given in section 5.4, while for the Aerobee vehicle the sensitivity is estimated as follows. The ratios DC/AC for both the neutral and ion mass spectrometers were set such that the resolving power for all masses of both instruments was the same and hence it is reasonable to assume that their transmission was also the same. Assuming this to be true, then from the values of the overall transmission of the ion mass spectrometer for the ions of atomic oxygen, $\tau(O^+)$, and those of molecular oxygen, $\tau(O_2^+)$, which are presented in table 5.2, the sensitivity of the neutral mass spectrometer for atomic oxygen is:

$$S(O) = \frac{\sigma(O)}{\sigma(O_2)} \cdot \frac{\tau(O^+)}{\tau(O_2^+)} \cdot S(O_2) \qquad (5.15)$$

where $S(O_2)$ is the sensitivity of the neutral mass spectrometer for molecular oxygen and $\sigma(O)$ and $\sigma(O_2)$ are the ionization

Table 5.2

THE OVERALL TRANSMISSION OF THE ION MASS SPECTROMETER FOR DIFFERENT IONS. THE UNIT USED IS NUMBER OF PARTICLES TRANSMITTED IN A SECOND MASS SCAN.

ions	Transmission $(\tau)x10^{-4}$
H^+	3.0
H_2^+	3.2
He^+	1.1
O^+	1.8
N_2^+	1.2
O_2^+	2.5
Ar^+	1.8
CO_2^+	3.0

cross sections for atomic and molecular oxygen, respectively, due to electron impact. From the measured values of Fite and Brackmann (1959) for $\sigma(O)$ and $\sigma(O_2)$ and the value of $S(O_2)$ which is given in section 5.3.1:

$$S(O) = 0.567 \times S(O_2) \qquad (5.16)$$

$$= 6.5 \times 10^{-10} \text{ counts/number of particles per c.c. in one second scan.}$$

a value which appeared to be reasonable.

5.3.3 CALIBRATION OF THE ION MASS SPECTROMETER.

The ion mass spectrometer was similar to the neutral one in all respects except for the ion source which had been replaced by a mesh disc of 3.2 cm diameter and a collecting plate in front of the quadrupole's entrance orifice. A schematic view of the front section of the ion mass spectrometer and the laboratory's ion source used to ionize the neutral gas is shown in fig. 5.31.

The task of calibrating the ion mass spectrometer was found to be much easier than that of the neutral ones. In fact, it was sufficient to "flood" the vacuum tank with the required gas and to measure the total ion current on the collecting plate with a high impedance amplifier, the electronic circuit of which is shown in fig. 5.32, instead of the total density of the particles in the tank. Thus, if V_p is the voltage produced by the ions current across a high value resistor, R, of the amplifier of fig. 5.32, the number of ions per second passing through the entrance orifice of the quadrupole is:

$$N_i = \tau_m \cdot (A_q'/A_p) \cdot (V_p/qR) \qquad (5.17)$$

where A_q is the area of the entrance aperture of the quadrupole which is 0.126 cm^2, A_p the effective area of the collecting plate (11.2 cm^2), q, the ion's charge, and τ_m, the transmission of the mesh across the aperture of the collecting plate which is 89%. Since $R = 9.97 \times 10^9 \Omega$, then:

$$N_i = 6.26 \times 10^6 \times V_p \text{ ions/sec.} \qquad (5.18)$$

If R_ℓ is the number of counts per second scan from the output of the detector, then the best fit of the plot of R_ℓ against N_i will determine the overall transmission (i.e. that of the mass spectrometer and of the detector), τ, of the particular ion specie of interest, i.e.:

$$R_\ell = \tau N_i \qquad (5.19)$$

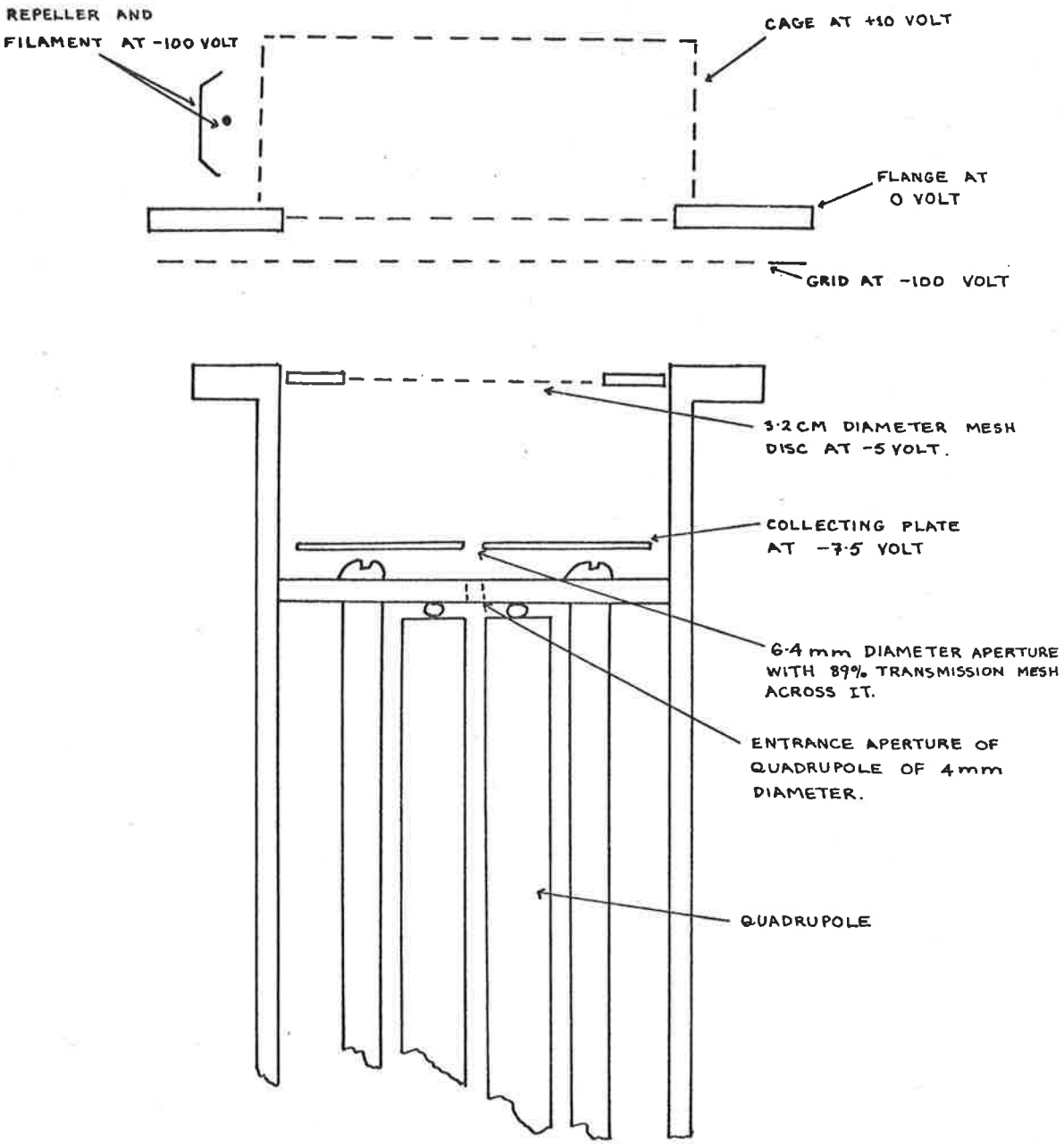

FIG 5·31: SCHEMATIC VIEW OF THE FRONT SECTION OF THE AEROBEE'S ION MASS SPECTROMETER AND ION SOURCE USED TO CALIBRATE THE ANALYZER.

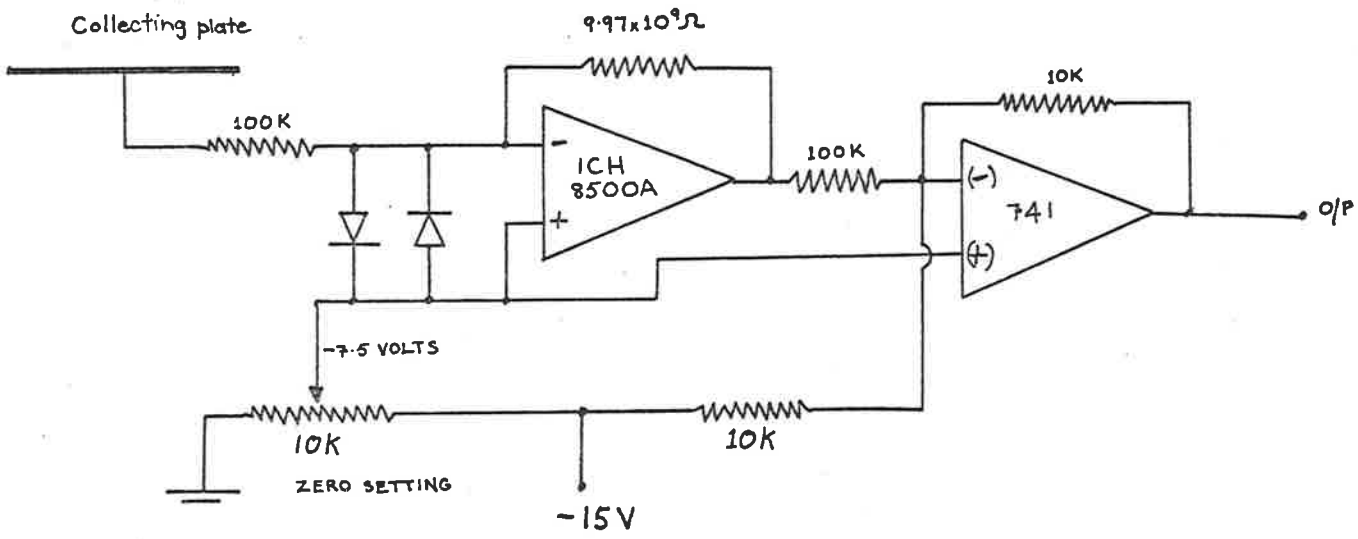

FIG 5·32: CIRCUIT DIAGRAM OF THE HIGH IMPEDANCE AMPLIFIER USED TO MEASURE THE TOTAL ION CURRENT OF THE ION MASS SPECTROMETER.

The overall transmission for different ion masses is tabulated in table 5.2.

The Aerobee's payload also contained an ion energy spectrometer which as a "back up" to the ion current measured at the collecting plate provided an in-flight calibration of the instrument for atomic oxygen ions. Thus, when the Aerobee's data from the mass spectrometers and ion's energy spectrometer become available, the overall transmission, $\tau(O^+)$, and hence sensitivity, $S(O)$, of the two analyzers for atomic oxygen will be revised.

5.4 CONCLUSION

The first rocket borne mass spectrometer experiment, L1002, was scheduled to be launched in early November, 1975, but due to a combination of technical problems with the vehicle, it was not until the 10th of August, 1976, that it was finally launched. This payload had been at Woomera three times, calibrated three times, on the launcher five times and each time, except for the fifth, had to be withdrawn. Unfortunately, when it was finally launched, the flight was a failure. The nose cone which was timed to come off at an altitude of about 90 Km ejected 30 seconds late which even though the gauge indicated a bad pressure, after about 15 seconds delay, the reading of the gauge was over-ruled and the high voltage and the filament come on. The high voltage coroned and the filament broke when the nose cone ejected.

Payload L1003 was launched on the 11th of August, 1976. On this occassion the nose cone come off too early, 25 seconds after launch which corresponded to an altitude of about 30 Km, and the heat generated by the shock wave in front of the ion source melted the glass supports of the filament. A remnant of this vehicle is shown in photograph 5.4.

The Aerobee vehicle was successfully launched on the 22nd of February, 1977, at 6^h36^m C.S.T. (Australian Central Standard Time) and, from the examination of the flight records, it appears that all instruments functioned satisfactorily.

The mass spectrometer program in the Department of Physics, University of Adelaide, started with the development of the quadrupole instruments and allied electronics for the rocket flights L1002, L1003 and the Aerobee. When the program started it was hoped that it would have continued for many years in the future, since the University of Adelaide was the only University in Australia which was actively involved with

Photograph 5.4: Remnant of the L1003 mass spectrometer.

rocket research of the atmosphere. Unfortunately, the rocket program has terminated with the launching of the Aerobee vehicle and, following this, the mass spectrometer program will continue but in a different field. The analyzers will be employed for environmental studies of such pollutants as hydrocarbons, NO_x and halogens on the ground and in the tropospheric and stratospheric regions of the atmosphere.

CHAPTER VI

ELECTRON ENERGY ANALYZERS AND THE MEASURED PHOTOELECTRON SPECTRA

6.1.1 INTRODUCTION

In this chapter will be described the types of electrostatic energy analyzers which have been flown successfully on Skylark 1207 and the Aerobee 13.123IS vehicles. The analyzers or spectrometers are of two types;

(a) relatively high resolving power instruments which give differential energy spectra of the charged particles.

(b) analyzers with relatively low energy resolution and which measure the integral energy spectra of the charged particles.

On the Skylark vehicle a small differential electrostatic analyzer (DESA) has been flown while the Aerobee rocket, as part of the payload, contained a high energy resolution DESA and electron and ion retarding potential analyzers, abbreviated as ERPA and IRPA, respectively, which provided low energy resolution spectra of the ionospheric electrons and ions.

The purpose of these experiments is to procure information on the intensity and energy distribution of the photoelectrons and superthermal electrons. In addition, the ERPA flown on the Aerobee vehicle provides information on the very low energy electrons and the vehicle's potential during flight, while the IRPA provides inflight calibration of the ion mass spectrometer and temperature of the ionized atmospheric constituents. However, only the electron energy spectra data of the Skylark's flight will be presented at the end of the current chapter.

6.1.2 THE DIFFERENTIAL ELECTROSTATIC ANALYZERS

Since Hughes and Rojansky (1929) showed that a radial inverse first-power electrostatic field can be used to analyze the energy of charged particles, electrostatic electron spectrometers have been extensively studied and used.

The four most common types of analyzers are:

(1) The Parallel-Plate Analyzer. This is the simplest analyzer both to construct and to treat theoretically. It consists of two parallel-plates (fig 6.1a) held at different potentials and focusing of the charged particles takes place for a deflecting angle $\phi = 45^{o}$.

(2) The Spherical Analyzer. It ocnsists of two semi-spherical plates separated by a distance $\Delta R = R_2 - R_1$, where R_2 and R_1 are, respectively, the radii of the outer and inner plate of the instrument (fig 6.1b). It has two dimensional focusing properties, the focusing angle of which is $\phi = 180^{o}$.

(3) Co-axial Cylindrical Analyzer. This instrument is comprised of two co-axial cylinders of radii R_1 and R_2 (fig 6.1c). Focusing takes place in two dimensions and the focusing angle is $\phi = 42^{o}18.5'$.

(4) The Cylindrical Analyzer. The analyzer is basically composed of two cylindrical plates of radii R_1 and R_2 (fig 6.2a) and focusing takes place in one dimension for a deflecting angle of $\phi = 127^{o}17'$.

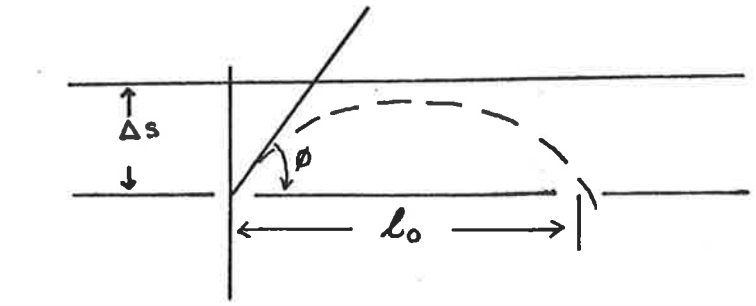

(a)

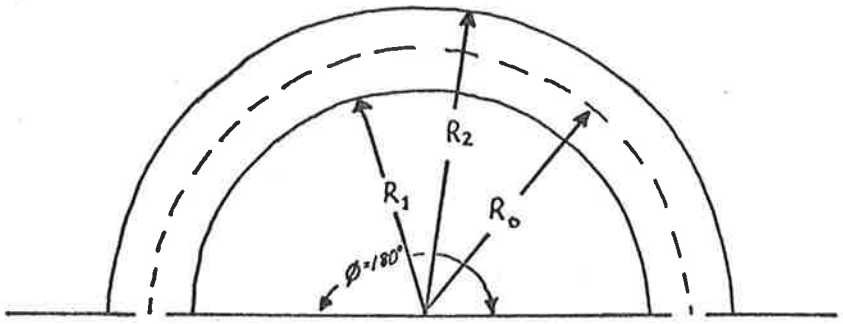

(b)

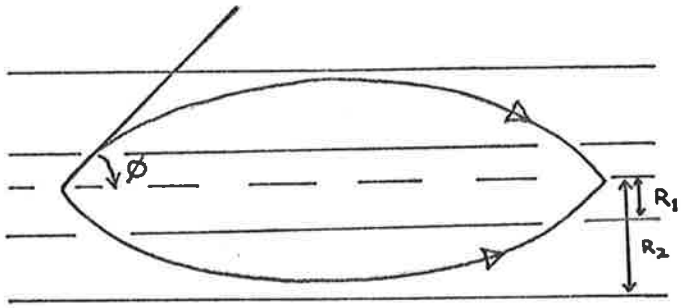

(c)

FIG 6·1: SCHEMATIC DIAGRAMS OF:
(a) PARALLEL PLATE ANALYZER
(b) SPHERICAL ANALYZER
and (c) CO-AXIAL ANALYZER

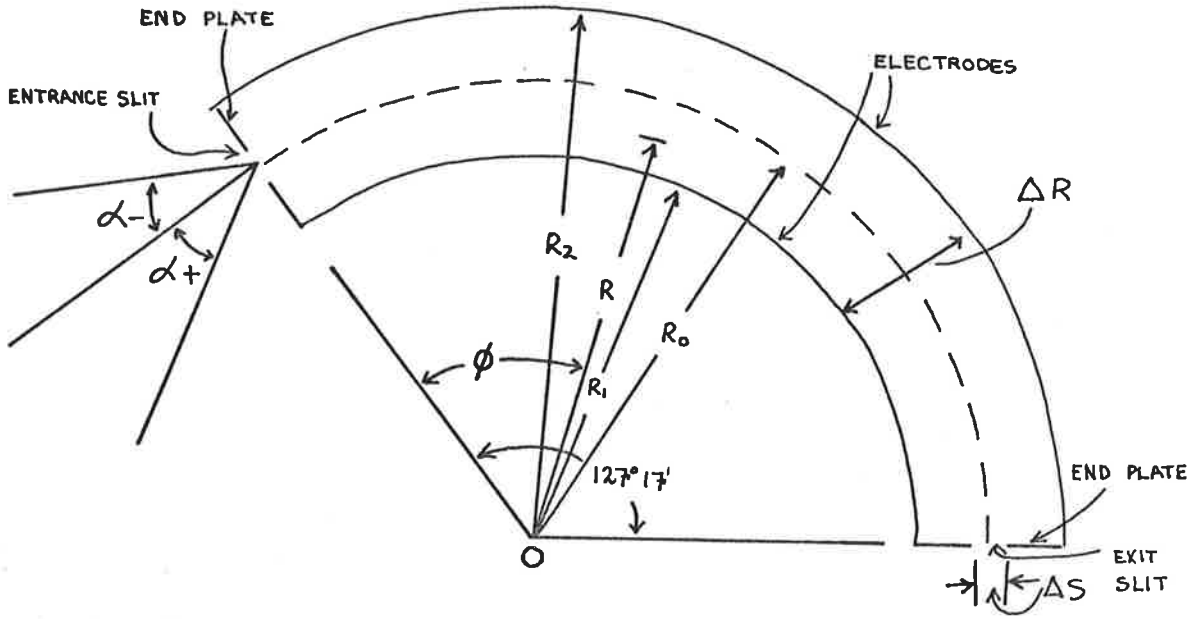

FIG 6·2a : SCHEMATIC DIAGRAM OF THE CYLINDRICAL ANALYZER.

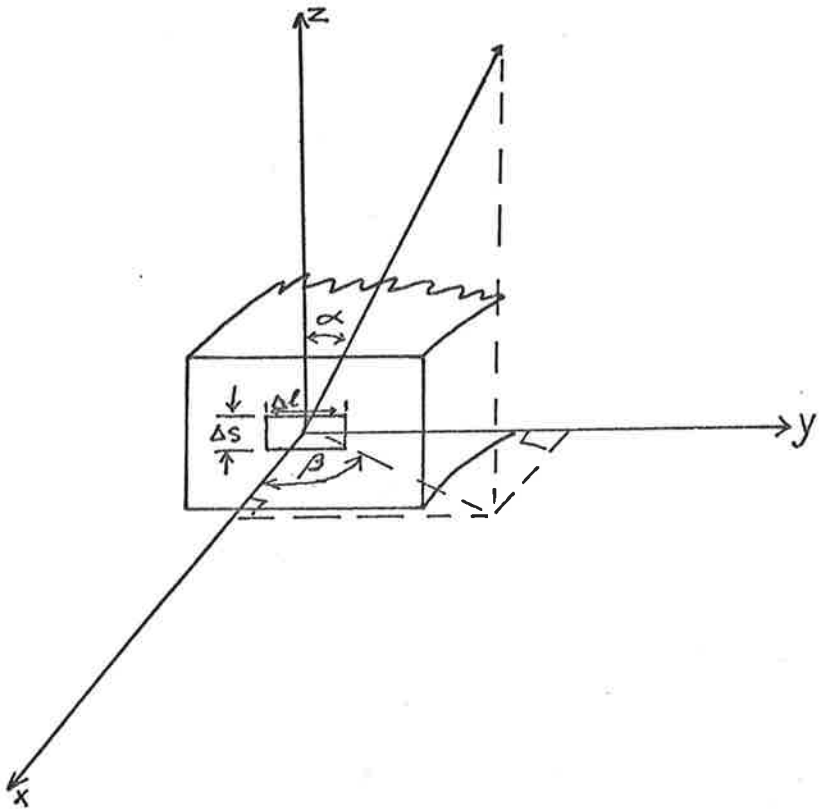

FIG 6·2b: SCHEMATIC DRAWING ILLUSTRATING THE APERTURE ANGLE α AND β.

6.1.3 COMPARISON BETWEEN THE FOUR TYPES OF ANALYZERS

The aim of the electrostatic analyzer experiments on the Skylark 1207 and Aerobee 13.123IS rockets is to measure the differential energy spectrum of the photoelectrons in the upper atmosphere from a height of 110 to 200 Km. The choice, then, of which electrostatic analyzer to fly depends on which of them satisfy certain important criteria, in addition to size, weight and power consumption limitations. These features are:

(1) simple in mechanical construction and rugged enough to withstand the acceleration and vibrations occurring during the powered part of the flight.

(2) good energy resolution.

(3) high sensitivity.

The parallel plate electrostatic analyzer, even though it is very simple to construct, is cumbersome to use because the charged particles must enter the instrument at an angle of 45^{o} with respect to the axis of the instrument (fig 6.1a) in order for them to be focused (Harrower (1955)).

The spherical and co-axial cylindrical analyzers both focus the charged particles in two dimensions. However, with comparable resolution the co-axial analyzer has a much larger azimuthal acceptance angle than the spherical analyzer and, hence, a much higher sensitivity. In fact, Hafner et al (1968), from a comparison of performance between the spherical and co-axial cylindrical analyzers, concluded that the co-axial analyzer is superior to the spherical instrument, although they pointed out that when the construction of the instrument is considered there are inherent difficulties in designing the electron lenses necessary for the analyzer in order to have this large acceptance angle.

The choice, then, of which analyzer to employ on the rocket payloads lies mainly between the spherical and cylindrical analyzers. The properties of both of these analyzers are characterized by:

(1) the ratio of the elctrode separation, ΔR, to the mean radius, R_o, i.e., $\Delta R/R_o$.

(2) the slit width, ΔS.

(3) the semi-acceptance angles α and β, respectively, in the radial and axial planes (fig 6.2).

In choosing the type of analyzer for the rocket experiments the first thing to consider is whether it can be made using the tools and machineries already available. Cylindrical electrodes are much easier to machine and to mount than the spherical ones. Furthermore, the focal points of the spherical analyzer are 180^o apart while those of the cylindrical instrument are only $127^o17'$ apart, so that for comparable instruments the cylindrical analyzer can be made smaller.

However, the spherical analyzer has the advantage of having a higher sensitivity than the cylindrical type, which results from the fact that while the dependence of the energy acceptance of the charged particles on the angle α is practically the same for the two analyzers, the dependence on the angle β is not. In the case of the spherical analyzer, the charged particles describe semi-circular arcs regardless of the angle β, i.e., the spherical analyzer accepts all charged particles of a certain energy independently of the angle β. The cylindrical analyzer, instead, accepts only those charged particles with angles of incidence lying in the range $\pm \beta_{max}$, and, hence, having velocity components less than $V_o \cos\beta_{max}$ perpendicular to the entrance aperture of the instrument, where V_o is the velocity of the particles, the value of which corresponds to the voltage applied between the electrodes.

This property of the cylindrical analyzer need not be a complete disadvantage because it is able to detect the direction of the motion of the particles as well as their energy, while the spherical analyzer is only capable of detecting the direction of motion of the particles in one direction.

From the above considerations it has, then, been decided that the type of instruments to fly on the Skylark 1207 and Aerobee 13.123IS rockets are the cylindrical analyzers.

6.1.4 THE CYLINDRICAL ELECTROSTATIC ANALYZER

The theory of the cylindrical electrostatic analyzer was first developed by Hughes and Rojansky (1929) when they showed that a radial inverse first power electric field can be used to focus electron beams every $127^{o}17'$. Hughes and McMillen (1929) built such an instrument and showed that it could be used as an energy analyzer. Marmet and Kerwin (1960) improved it by adding secondary electron suppression grids while Froitzheim et al (1975) used corrugated electrodes to reduce the background counts. More recently Rudd (1972) has derived an expression for the transmission of the analyzer while Rogers and Horton (1943) have extended the theory of the cylindrical analyzer to include relativistic effects.

Basically, the instrument consists of two concentric 127^{o} cylindrical plate sectors with plates at each end housing the entrance and exits slits (fig 6.2a). An inverse first power radial electrostatic field is set up by applying a potential difference between the cylindrical electrodes giving rise to the following potential function, P(R):

$$P(R) = V_1 + \frac{(\Delta V . \ell n(R/R_1))}{\ell n(R_2/R_1)} \qquad (6.1)$$

where $\Delta V = V_2 - V_1$ and R_1 and R_2 are the radii of curvature of the inner and out electrodes, respectively, V_1 is the voltage applied to the inner electrode and V_2 the voltage applied to the outer electrode while R is the radial co-ordinate with the origin at the centre of the curvature of the cylinders (fig 6.2a). Under the influence of such a field, the charged particles moving perpendicular to the field lines will have circular trajectories if their kinetic energy, E, satisfy the equation:

$$E = \frac{\Delta V}{2 \ell n (R_2/R_1)} \qquad (6.2)$$

The differential equation describing the trajectories of the charged particles in polar co-ordinates R and ϕ is given by:

$$\frac{d^2U}{d\phi^2} + U = \frac{E_o}{U.E.\cos^2\alpha} \qquad (6.3)$$

where $U = R_o/R$ and E_o is the kinetic energy of particles entering the analyzer perpendicular to the radial field, i.e., $E = E_o$ when $\alpha = \beta = 0$. A first order solution given by Hughes and Rojansky (1929) is :

$$U = \frac{E_o}{E\cos^2\alpha}.(1 - \cos(\sqrt{2}.\phi)) + \cos(\sqrt{2}.\phi) - \frac{\tan\alpha.\sin(\sqrt{2}.\phi)}{\sqrt{2}} \qquad (6.4)$$

and the position of best re-focusing is:

$$\phi_f = 127^o 17' \qquad (6.5)$$

The resolving power (full width at half maximum), R_p, correct to second order in α is:

$$\begin{aligned} R_p &= \Delta E/E \\ &= \Delta S/R_o + 4\alpha^2/3 \end{aligned} \qquad (6.6)$$

where ΔS is the slit width.

If the effect of the angle β is included, then according to Rudd (1972) the resolving power becomes:

$$R_p = \Delta S/R_o + \alpha^2/3 + \beta^2/4 \qquad (6.7)$$

where the angles α and β have already been defined (fig 6.2b).

6.1.5 ENERGY DISTRIBUTION OF THE CYLINDRICAL ANALYZER

Roy and Carette (1971) have shown that the profiles of the energy distribution of the cylindrical, spherical and co-axial cylinder analyzers, depend on the ratio, G., of the space of separation between the electrodes, ΔR, to the mean radius, R_o, of the instrument, i.e., $G = \Delta R/R_o$ (fig 6.2a). For a small value of G, which corresponds to a small angular aperture since the angular aperture is proportional to the electrode separation, ΔR, the energy distribution of the cylindrical analyzer has an almost symmetrical shape, but with increasing values of G the distribution becomes asymmetric and a tail appears on the high energy side. The energy distribution is fairly symmetric up to a value of $G = 0.2$, but for G greater than 0.2 the high energy tail appears.

The reason for the high energy tail is that for small values of G the angular aperture is smaller and the charged particles with positive and negative angles of incidence are transmitted equally but with increasing G, and hence angles of incidence, the transmission of the particles with positive angles of incidence ceases before that due to the negative angles. This means that the charged particles injected toward the inner electrode can be transmitted with a larger angle of incidence than those injected toward the outer electrode and, hence, with a higher energy. Thus, it follows that the asymmetry in the shape of the energy distribution is caused by the α^2 angular dispersion resulting from a large value of G.

The origin of the asymmetry in the energy distribution is explained in detail by Bryce et al (1973). These authors calculated the potential distribution of a cylindrical analyzer having a radial field distorted by the entrance

and exit aperture conducting plates positioned at a deflect-angle ϕ = 0 and ϕ = 127°17' respectively. They found that if the end plates are at zero potential and if voltages of equal magnitude but opposite in sign, +V and -V, are applied between the inner and outer electrodes the field lines near the end plates have very little radial component except at the exact electrical center which occurs, in this case, where $R = R_o$. Thus, except at the electrical center, the deflection of the charged particles in the radial direction is weakened and the particles drift toward the outer electrode of the analyzer. Furthermore, the field distortion decreases with the separation between the electrodes.

The asymmetry in the energy distribution can be reduced by considering only positive or negative acceptance angles (Roy and Carette (1970)). However, the deflecting angle, for which the profile of the energy distribution is best (highest resolution) is again a function of the parameter G and the smaller G is the closer the deflecting angle of best resolution, ϕ_r, approaches the focusing angle ϕ_f (i.e., 127°17') of the instrument. Moreover, for positive acceptance angles ϕ_r is less than ϕ_f, while for negative acceptance angles ϕ_r is greater than ϕ_f (Roy and Carette (1970)). One disadvantage in using only positive or negative acceptance angles is that the transmission of the analyzer is approximately reduced by a factor of two.

6.1.6 OPTIMIZING THE CHARACTERISTICS OF THE ANALYZER

The cylindrical analyzer can be improved in a number of ways. For example, by:

(1) Background Suppression. The background counts of the analyzer are due to reflected and secondary electrons from the inner and outer electrodes of the instrument. This background can be reduced in different ways, for example, by:

(a) using grids as Marmet and Kerwin (1960).

(b) coating the electrodes with soot which captures the reflected and secondary electrons.

(c) corrugating the electrodes as Froitzheim et al (1975) have done.

(2) Optimizing the Transmission. Rudd (1972) has shown that for an analyzer with a narrow resolution function the output current becomes optimum if the angular aberration terms in equation (6.7) are equal and each is one-fourth the slit term, i.e.,

$$4\alpha^2/3 = \beta^2 = \Delta S/R_o \qquad (6.8)$$

which defines the maximum acceptance angles, i.e.

$$\alpha_{max.} = \pm\sqrt{\tfrac{3}{4}.\Delta S/R_o} \qquad (6.9)$$

$$\beta_{max.} = \pm\sqrt{\Delta S/R_o} \qquad (6.10)$$

So that by choosing the acceptance angles α and β less than $\alpha_{max.}$ and $\beta_{max.}$, respectively, the transmission of the analyzer is optimum.

(3) Optimizing the Energy Resolution. To reduce the high energy tail and to make the energy distribution symmetric (Roy and Carette (1971)) and to improve the transmission (Bryce et al

(1973)) the exit slit has to be displaced both radially at a distance $R = R_o - S$, where the parameter S indicates a small displacement along the radial direction, and angularly since charged particles in a field distorted by the end plates come to focus at a deflecting angle $\phi < 127^{\circ}17'$. However, this method of improving the instrument requires complicated computer calculations in solving the differential equation of the charged particles moving in a radial distorted field, especially since the sign of S cannot be readily predicted.

As already mentioned, another way to reduce the high energy tail is to use the analyzer with only positive or negative aperture angles (Roy and Carette (1970)). But, this has the effect of reducing the transmission of the analyzer by a factor of about two. If the reduction in sensitivity of the instrument can be tolerated, then, the method of using only positive or negative angular apertures can be used to improve the resolving power of the analyzer. However, the same result can be achieved by using the analyzer with a small G value without having to modify the entrance and exit slits and going through complex and tedious calculations to find the deflecting angle of best resolution, ϕ_r, for that particular geometry of the analyzer. It must be remembered that the sensitivity of the analyzer is proportional to the parameter G (Roy and Carette (1971)) and,

hence, if G_- is reduced by a factor of two, then, the sensitivity is also reduced by a factor of two.

(4) Vertical Focusing. Leventhal and North (1971) have found that if a voltage is applied to the top and bottom plates which support the cylindrical electrodes of the analyzer, vertical focusing of charged particles occurs. This vertical focusing has the effect of increasing the transmission and the increase is quite substantial. In fact, Leventhal and North (1971) found that the transmission increased by a factor of five from having the plates grounded to applying a small voltage, V_z, to them. However, the necessary voltage required to achieve vertical focusing depends on the voltage difference, $\Delta V = V_2 - V_1$, applied across the cylindrical electordes and on the ratio V_2/V_1. Thus, for optimum transmission of the analyzer V_z has to be determined experimentally.

(5) Finite Length of the Slits. To reduce the field distortion due to the finite ratio of the analyzer's height, H, to the slit length, L, i.e. H/L, this ratio must be as large as possible.

(6) Fringing Field Shielding. Herzog (1940) and Wollnick (1967) have derived approximate solutions for fringing fields in the case of a parallel plate condenser, while Wollnick and Ewald (1965) have shown that if the analyzer is placed inside the dihedral segments, as in fig 6.3, the calculations performed for a parallel plate condenser can also be used for a cylin-

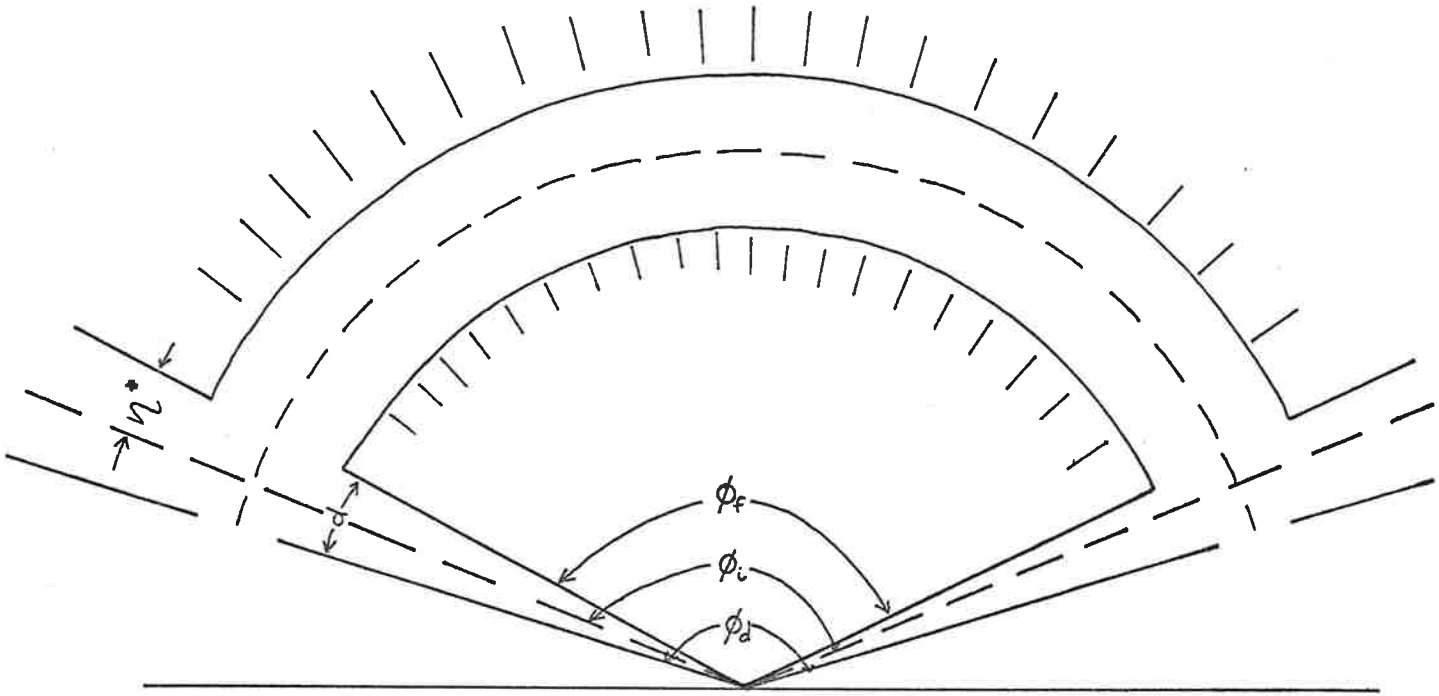

FIG 6·3: ARRANGEMENT PROPOSED BY WOLLNIK AND EWALD (1965) FOR THE SHIELDING OF THE FRINGING FIELD IN TOROIDAL-TYPE SPECTROMETERS. THE RADIAL DOTTED LINES REPRESENT THE IDEAL FIELD BOUNDARY.

drical, spherical or toroidal condenser to a very good approximation. From the geometry of fig 6.3, the deflection angle, ϕ_i, of the ideal field becomes:

$$\phi_i = \phi_f + 2\eta^* \qquad (6.11)$$

and the dihedral angle is given by:

$$\phi_d = \phi_f + 2d \qquad (6.12)$$

where the angles η^* and d as defined in fig 6.3 have been calculated by Herzog (1940) as a function of the electrode separation, ΔR, and slit width, ΔS, and reproduced by Wollnick (1967). Thus, by using the geometry of fig 6.3 the fringing effects due to the end plates can be minimized.

(7) Space Charge. If a channel electron multiplier is used as a detector, then, the space charge effect need not be considered since to avoid saturation of the multiplier the counting rate must be kept smaller (less than 10^5 counts per sec.).

6.2.1 THE FLIGHT ANALYZERS

The rocket borne energy analyzer experiments were designed to provide information on the intensity and energy distribution of the fast electrons in the lower thermosphere. During the course of this work, three rocket vehicles became available to the author which were suitable for this type of experiment. These vehicles were Skylark 1207, Super-Chief II NB21.252 and Aerobee 13.123IS. Furthermore, the electron spectrometers had to be designed and built to fit in the limited space provided for them on the payload of these vehicles.

The Super-Chief vehicle was launched on July 23, 1974, at 23^h08^m local time from Wallops Island (U.S.A.), but due to vehicle failure the flight was abortive. The Skylark and Aerobee rockets, as already mentioned in section 1.1.2, were launched both from Woomera and both were morning flights. The purpose of the spectrometer on the Aerobee vehicle was to provide information on the low energy electrons during the formation of the diurnal structure of the E and F_1 regions while the Skylark's spectrometer provided information on the fast electrons when these regions were already formed.

The electron energy spectrometer on the Aerobee vehicle was much larger in physical size than that on the Skylark which, as a consequence, had much better characteristics.

6.2.2 MECHANICAL CONSTRUCTION OF THE CYLINDRICAL ANALYZERS

Mechanically, the cylindrical electrostatic analyzer is composed of the following components:

(a) two cylindrical electrodes (fig 6.2)

(b) two insulating plates supporting the electrodes

(c) two end plates housing the entrance and exit slits

(d) a collimator to limit the maximum value of the angles α and β (fig 6.2) in accordance with equations (6.9) and (6.10).

All the flight analyzers were made of aluminium and those spectrometers flown on the vehicles Skylark and Super-Chief, because of their small dimensions, R_o being only 50 mm, the electrodes were machined directly from a 152 mm diameter cylindrical rod of aluminium. However, in the case of the Aerobee's spectrometer, because of the size of the electrodes, R_o = 127.5 mm, aluminium plates of 12 mm thick had to be used. These plates were cut to the cylindrical shape, welded, and annealled. After this, the two rolled cylindrical tubes were machined and cut to the specified electrodes.

The insulating plates for all spectrometers were made of teflon (P.T.F.E.) with grooves cut to accommodate the two electrodes of the analyzer (photograph 6.1).

The end plates housing the entrance and exit slits were also made of teflon. However, in the case of the Aerobee's analyzer, it was found in a late stage of development of the instrument that the best material to use for the end plates and the two slits is the fibre glass of a single sided printed circuit board with the copper conducting layer on the outside. The copper layer is, then, earthed so that the printed circuit material, in addition to providing electrical insulation between the electrodes and overall rigidity to the analyzer,

Photograph 6.1: View of a fully assembled cylindrical analyzer flown on the Aerobee vehicle.

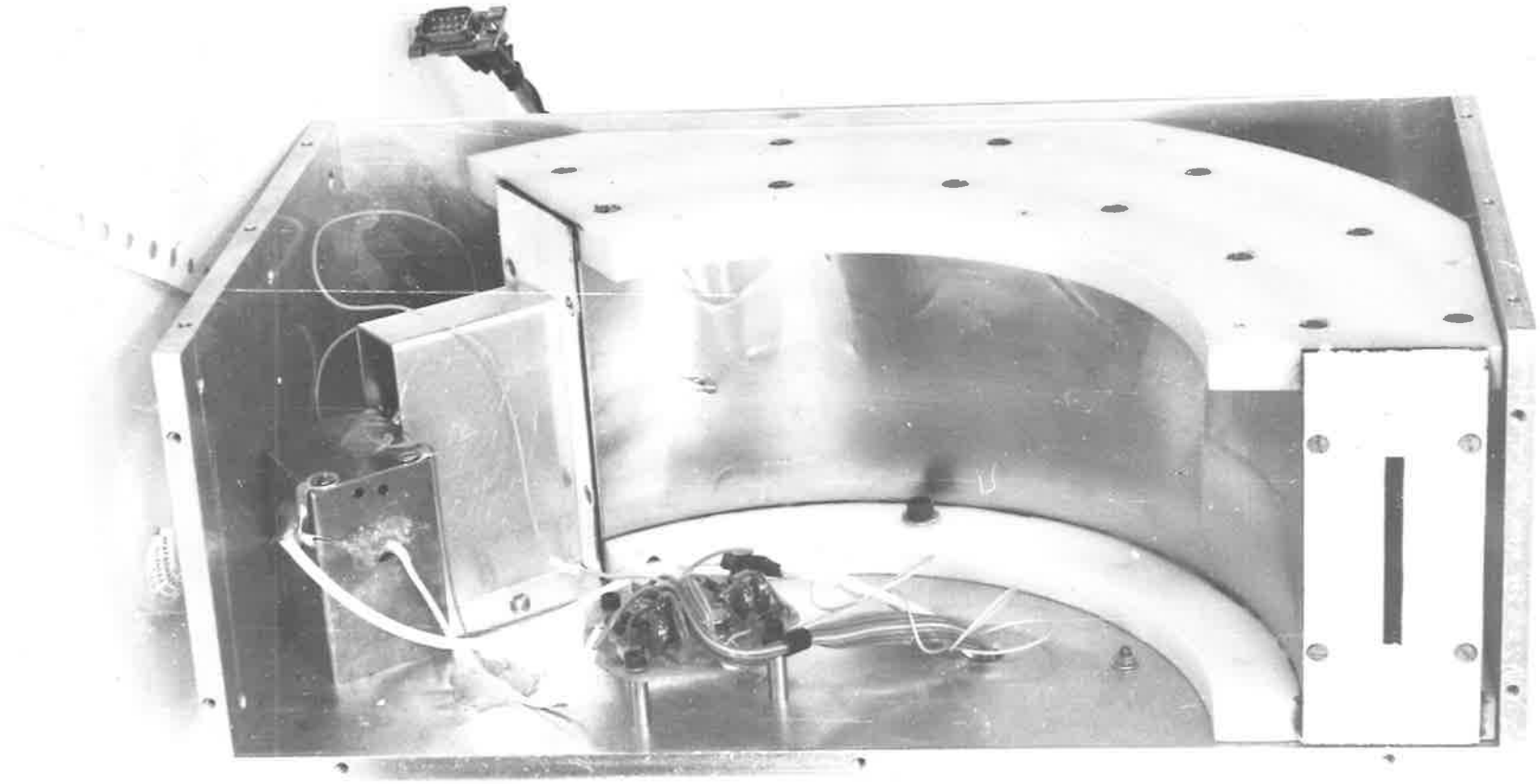

acts as an electrical shield, which is important, especially, at the exit slit where the detector, a channeltron, had 200 volts applied to its funnel. Thus, the teflon end plates of the Aerobee's analyzer which is shown in photograph 6.1 have been replaced with those made from printed circuit board material.

The slits of the Skylark's analyzers were made from razor blades' edges while those of the Aerobee's spectrometer were cut in the printed circuit end plates with the milling machine.

The collimators for all the spectrometers were made of aluminium, but, while for the Skylark's instrument were simply rectangular holes of 4 mm x 3 mm, in the case of the Aerobee's analyzer, because of the inherent high resolving power of this instrument, the collimator was slightly more sophisticated. In fact, the collimator was made of 13 square holes of 3 mm x 3 mm, having a depth of 40 mm (photograph 6.2).

Photograph 6.2: View of the collimator of the cylindrical analyzer flown on the Aerobee vehicle.

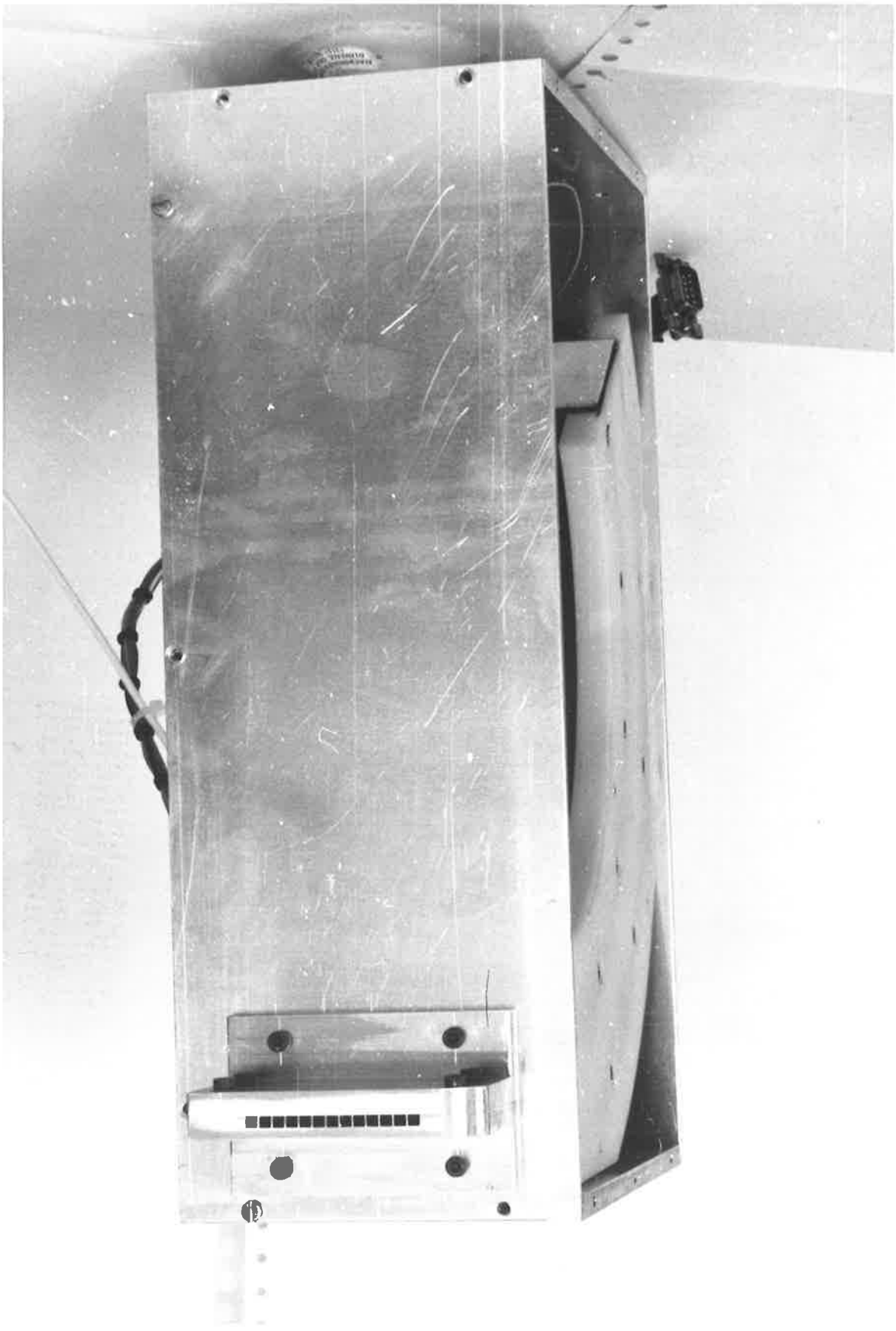

6.2.3 FEATURES OF THE FLIGHT CYLINDRICAL ANALYZERS

The characteristics of the designed flight electron spectrometers are as follow:

(1) Physical dimensions of electrodes. The Skylark's analyzer had the inner and outer electrodes of radius R_1 and R_2, respectively:

$$R_1 = 45 \text{ mm}$$
$$R_2 = 55 \text{ mm} \qquad (6.13)$$

while for the spectrometer of the Aerobee's payload:

$$R_1 = 115 \text{ mm}$$
$$R_2 = 140 \text{ mm} \qquad (6.14)$$

so that the analyzers of both vehicles had a G factor (section 6.1.5) of about 0.2 and thus the energy distribution function of the spectrometers were fairly symmetrical.

(2) Dimensions of Slits. Both the entrance and exit slits of the Aerobee's instrument were 2 mm wide and 45 mm long while those of the Skylark's analyzer were 3 mm wide and 4 mm long.

(3) Dimensions of Collimators. The Skylark's analyzer was fitted with a colimator having a depth of 30 mm and the entrance aperture of the same dimension as the slits so that it defined the maximum values for the angles α and β as follow:

$$\alpha_{max.} = \pm 5.5^\circ$$
$$\beta_{max.} = \pm 7.6^\circ \qquad (6.15)$$

However, from the geometry of the combination analyzer-collimator in which the exit slit was also taken into account resulted that $\beta_{max.}$ for the analyzer was $\pm 3^\circ$. Unfortunately, a

similar response of the instruments as a function of the angle α cannot be determined from the geometry of the analyzer-collimator arrangement but has to be determined experimentally.

In the case of the Aerobee's spectrometer, the collimator was made of 13 square holes of 3 mm x 3 mm and of depth of 40 mm. However, the distance between the entrance aperture of the collimator and the entrance slit was 45 mm so that the combination slit-collimator defined an $\alpha_{max} = \pm 3.2^{o}$ and $\beta_{max} = \pm 4.3^{o}$.

(4) Collecting Area. The collecting area for Skylark's instrument was 12 mm^2 while for that of the Aerobee payload it was 117 mm^2.

(5) Energy Resolution. In accordance with equation (6.7) and using the above determined values for the angles α and β the energy resolution, R_p, for the Skylark and Aerobee analyzers was, respectively, 6.4% and 1.81%.

(6) Fringing Fields. One of the biggest problems which experimenters working with electron spectrometers have to face is how to minimize the distortion of the radial field caused not only by the fact that the electrodes are not of infinite length and height, but, also by the presence of the end and supporting plates and slits. A method to reduce the fringing field, and hence improve the overall characteristics of the instrument, has already been discussed in section 6.1.5. However, the author has found that by coating the end and supporting insulating plates with a thin layer of semi-

conducting material, a continuous electrical conduction inside the analyzers is produced and the fringing fields can be practically eliminated. The only field distortion which cannot be eliminated in this case is that caused by the apertures of the entrance and exit slits which for most applications of the spectrometers are very small.

It has been found that the best way to deposit a film of semiconducting material on the teflon plates is be spraying on them a thin coat of SPARVAR ultra flat black paint, number S-11. This paint has the property that when it dries it behaves like a semiconductor material, the electrical resistance of which depends on the thickness of the coat. In fact, by using this paint, the overall resistance between the electrodes of the Skylark's spectrometer was of the order of 500 KΩ while that of the Aerobee's analyzer was about 100KΩ.

(7) Background Counting. The electrodes of the analyzers were coated with a fuliginous substance so as to capture any stray electron which impinged on them. It was found that the most efficient electron capture substance was the "fluffy" coating of carbon produced by the acetylene flame. A similar coat was also deposited in the collimators.

(8) Earth's Magnetic Field. To reduce the earth's magnetic field inside the spectrometers and hence to avoid any defocusing effect that this magnetic field may have on the trajectories of

the low energy electrons, the instruments were completely enclosed in a Co-Netic magnetic shield.

6.2.4 RAMP VOLTAGES OF THE ANALYZERS.

If the voltages, V_1, and, V_2, are applied, respectively, to the inner and outer cylindrical electrodes of the spectrometers, then, the field potential between the electrodes is given by equation (6.1). Under the influence of such an electrostatic field only charged particles having a kinetic energy, E, given by equation (6.2) will be transmitted by the analyzer, i.e.;

$$E = \Delta V/(2\ln(R_2/R_1)) \tag{6.16}$$

where $\Delta V = |V_2 - V_1|$

For a given geometry of a spectrometer the factor:

$$C = 1/(2\ln(R_2/R_1)) \tag{6.17}$$

is constant so that E is proportional to ΔV, i.e.;

$$E = C\Delta V \tag{6.18}$$

However, if the field potential given by equation (6.1) is not zero at the aperture of the entrance slit, the charged particles on entering the analyzer will be accelerated or decelerated by this field and the value of the constant C is no longer that defined in equation (6.17), but, depends on the ratio V_2/V_1, due to the change of kinetic energy of the charged particles at the entrance slit. However, it must be remembered that the particles leaving the analyzer are subjected to equal and opposite fields to those entering the instrument so that they emerge at the exit slit with the original kinetic energy. Thus, if the ratio V_2/V_1 is kept constant the kinetic energy of the charged particles can be scanned by varying ΔV, i.e.;

$$E = S\Delta V \tag{6.19}$$

where S is the sensitivity of the spectrometer.

For the flight spectrometers the voltages applied to the electrodes were of the form:

$$V_n = V_i.e^{k(n-1)} \tag{6.20}$$

where the parameter n indicates the number of voltages increments ΔV from the initial voltage $(V_{i2} - V_{i1})$ applied between electrodes such that the corresponding energy increment, ΔE, which is the energy band pass of the instrument, satisfy the relation:

$$\Delta E = R_p . E \tag{6.21}$$

where R_p is the resolving power of the instrument. Ideally, the voltages applied to the electrodes should be of the form;

$$V_n = V_i(1 + R_p)^{n-1} \tag{6.22}$$

and since the voltage, V_n, in the equations (6.20) and (6.22) is the same, the value of the constant k can be determined, i.e.,

$$k = \ln(1 + R_p) \tag{6.23}$$

In the case of the Skylark's spectrometer the voltages applied to the electrodes of the analyzer were asymmetric. In fact, the outer electrode of the analyzer was grounded while a positive voltage of the form given in equation (6.20) was applied to the inner electrode. The electronic circuit for the generation of this exponential ramp is shown in figure 6.4. However, in the case of the Aerobee's analyzer the voltages V_1 and V_2 were symmetrical with respect to ground. In fact, two exponential ramps of exactly the same amplitude but opposite in sign were generated as in figure 6.5 and applied to the electrodes.

The amplitude of the ramp voltages were set such that the Skylark's analyzer measured energy spectra of photoelectrons from 1 to 400 eV and the Aerobee's instrument from 1 to 100 eV and the ramps had a period of 8 and 3.2 seconds, respectively.

The energy scale calibration of the exponential ramp voltages for the Aerobee's spectrometer is shown in fig 6.6. The ramps were set such that V_i = 0.2 volts, n = 256 steps and V_{256} = 20 volts

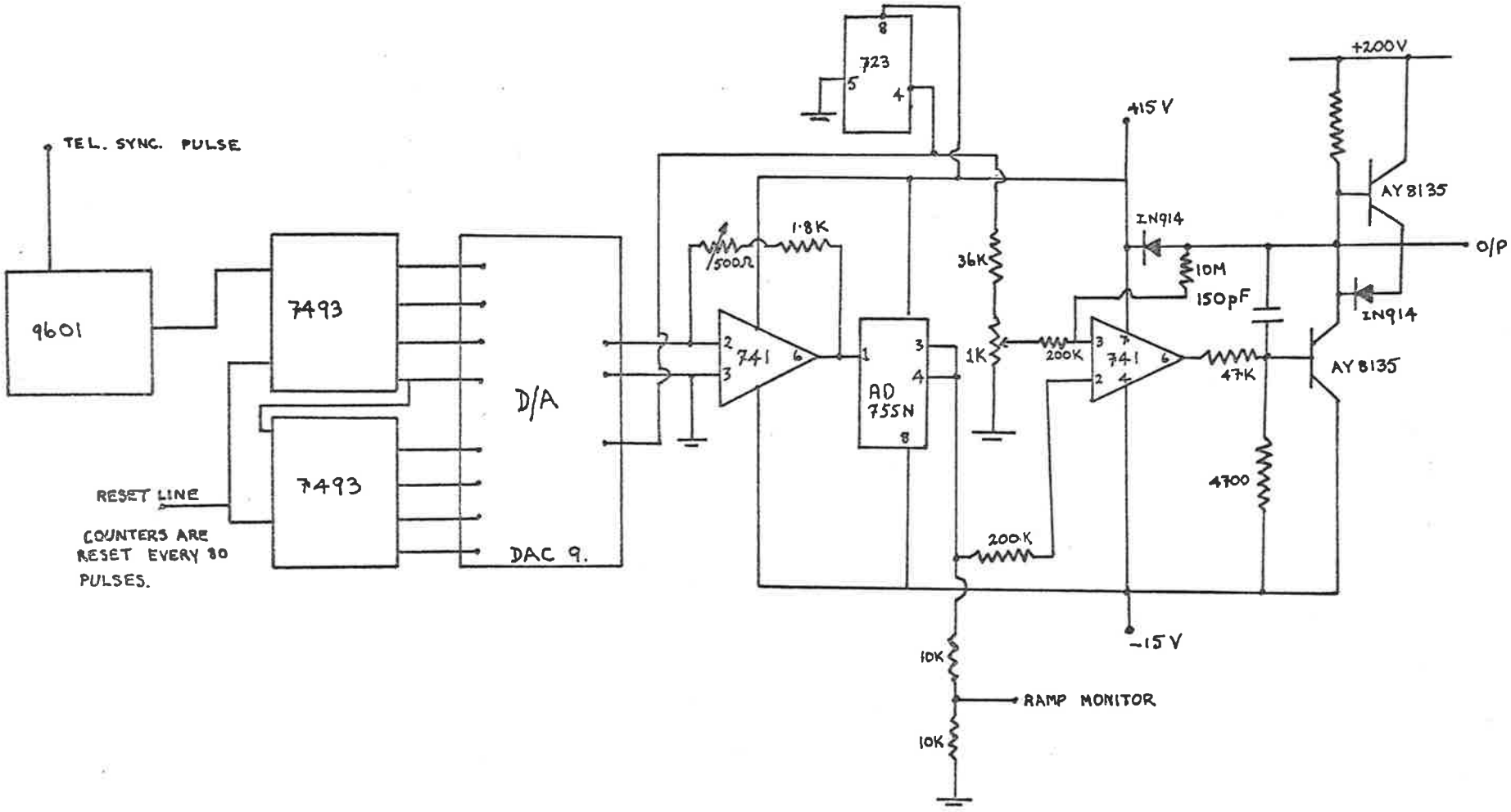

FIG 6·4: SKYLARK ANALYZER RAMP GENERATION

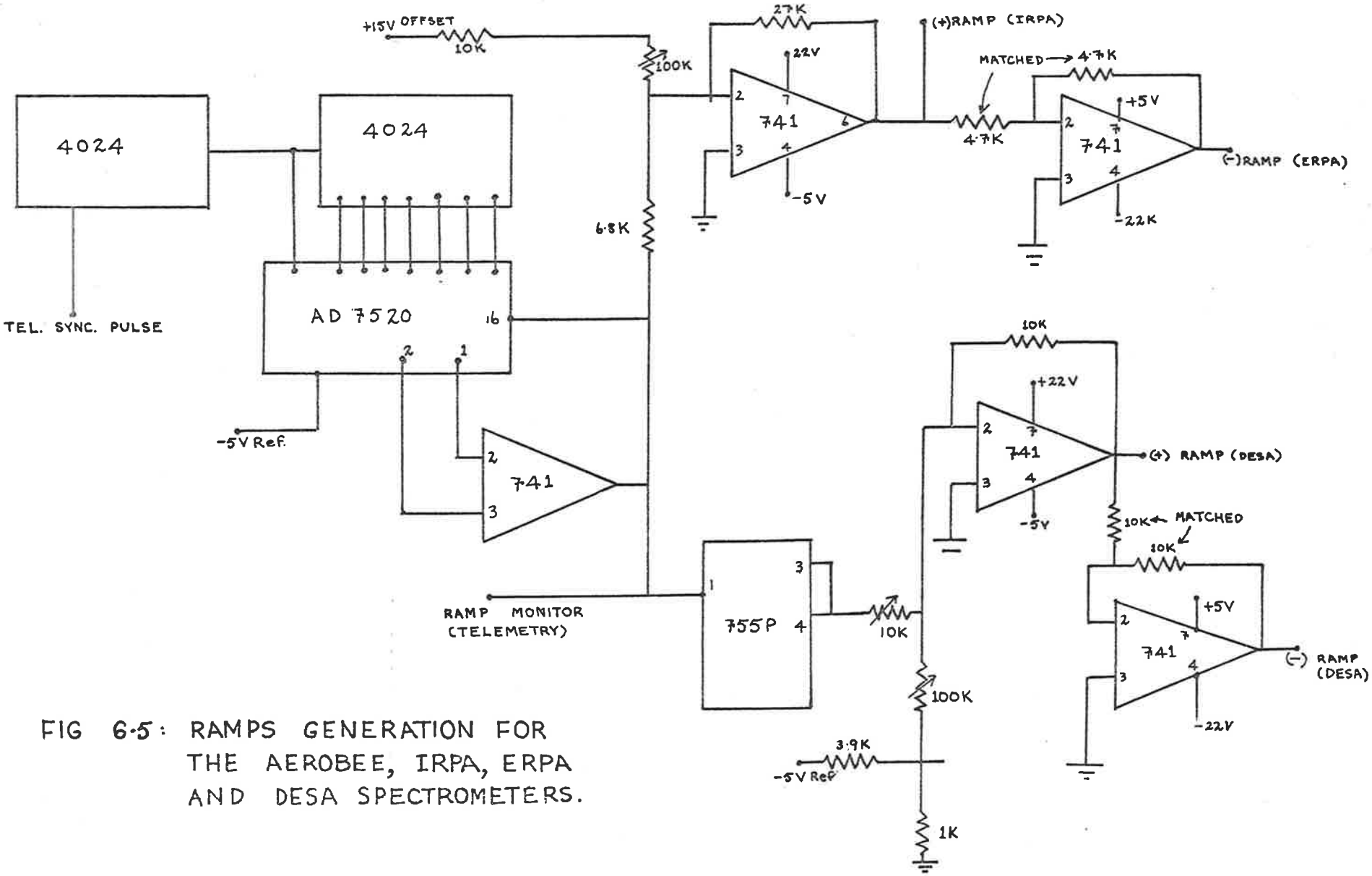

FIG 6-5: RAMPS GENERATION FOR THE AEROBEE, IRPA, ERPA AND DESA SPECTROMETERS.

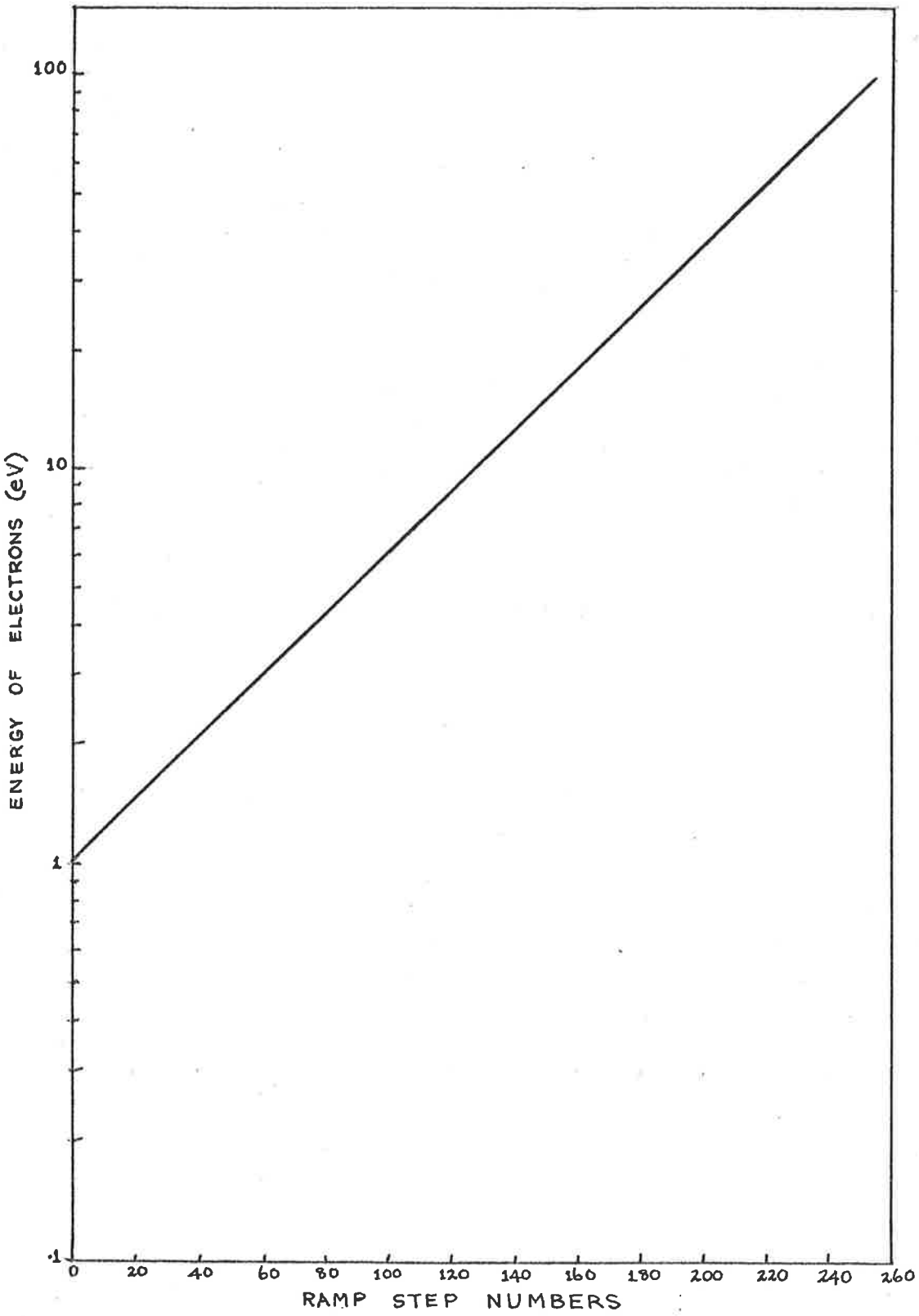

FIG 6·6: RAMP CALIBRATION FOR THE AEROBEE ANALYZER.

6.2.5 CALIBRATION OF THE ANALYZERS

During the rocket flights the spectrometers measure the number of electrons per unit time, N, as a function of the energy of the electrons and, of course, of height. Subequent to the flight, however, it is necessary to relate the measured counts per unit time to the flux of the ionospheric electrons. If this flux at the energy E is indicated by a function f(E), then:

$$f(E) = \frac{N}{E.\mathcal{E}.A.\Omega.R_p} \text{ electrons/cm}^2\text{.sec.eV. sterad.} \quad (6.24)$$

where E is the energy of the electrons in eV determined by using equation (6.19), A is the area of the entrance aperture in cm^2, Ω the solid angle of the instrument for which the electrons are accepted, R_p is the resolving power of the instrument as defined in section 6.1.4 and $\mathcal{E}$ is the overall efficiency of the spectrometer.

Thus, the laboratory calibration of the instrument consists of determining the following parameters:

(a) Sensitivity, S. Using equation (6.19) the sensitivity of the spectrometers can easily be determined experimentally. For the Skylark's analyzer the sensitivity was found to be 2.0 while for the Aerobee's spectrometer it was 2.6.

(b) Resolving power, R_p. The resolving power of the spectrometers of the Skylark and Aerobee payloads as determined experimentally were 6.5% and 1.82%, respectively, compared with the theoretical values of 6.4% and 1.81% (Section 6.2.3(5)). The experimental values of the resolving power of the two instruments are very close to the theoretical values and this is due to the fact that the fringing fields in the

analyzers have been reduced by coating the insulating and end plates with a thin layer of conducting material (see section 6.2.3 (6)).

(c) Area of the entrance aperture, A. As already mentioned in section 6.2.3 (4), the collecting area for the Skylark's analyzer was 0.12 cm^2 while for that of the Aerobee's was 1.17 cm^2.

(d) Overall efficiency, $\mathcal{E}$. The efficiency of the analyzers has been determined experimentally by measuring per unit time with the channeltron and as a function of energy the number of electrons leaving and entering the instruments, respectively, through the exit and entrance slits. The ratio of these two quantities will give the transmission of the analyzer. Unfortunately, this method does not give the overall efficiency of the combination analyzer-channeltron.

The channeltrons used as electron detectors in the spectrometers had about 200 volts applied to their funnels. Moreover, the Skylark's analyzer was set to measure electron energies from about a few eV to 400 eV while that of the Aerobee's payload from a few eV to 100 eV. Thus, it was necessary to know the efficiency of the channeltrons in the energy range 200 to 600eV for the Skylark's instrument and from 200 to 300 eV for the Aerobee's spectrometer. However, there are experimental difficulties in measuring the efficiency of channeltrons because it is required to produce a beam

of less than about 10^5 electrons per second from a hot filament which must not only be kept constant with time but its intensity must be known. It was then thought that it is best to use the efficiencies of channeltrons which have been reported in the literature and measured by different authors. For this work the values of the measured efficiencies were taken from the compilation of Bennani et al (1973). From this compilation it was found that the average efficiency of the channeltron in the energy range 200 to 600 eV is $(79 \pm 14)\%$.

The efficiency of the analyzers appeared to be independent of the energy of the electrons and were $(19.4 \pm 2.9)\%$, and $(14.1 \pm 2.4)\%$, respectively, for the analyzers which were flown on the Skylark and Aerobee vehicles and, thus, the overall efficiency for the two spectrometers were, respectively, $(15.3 \pm 5.0)\%$, and $(11.1 \pm 3.9)\%$.

(e) Solid angle, Ω. The solid angle of the Skylark's analyzer was determined at different energies by using a collimated beam of electrons of about 0.5 mm in diameter. The angular response of this instrument is shown in fig 6.7 for angles α and β and for electrons of 28 eV. From this figure it is seen that the response of the analyzer for the angle, α, is asymmetric and this is due to the fact that the transmission of the particles with positive α of incidence ceases before that due to negative α

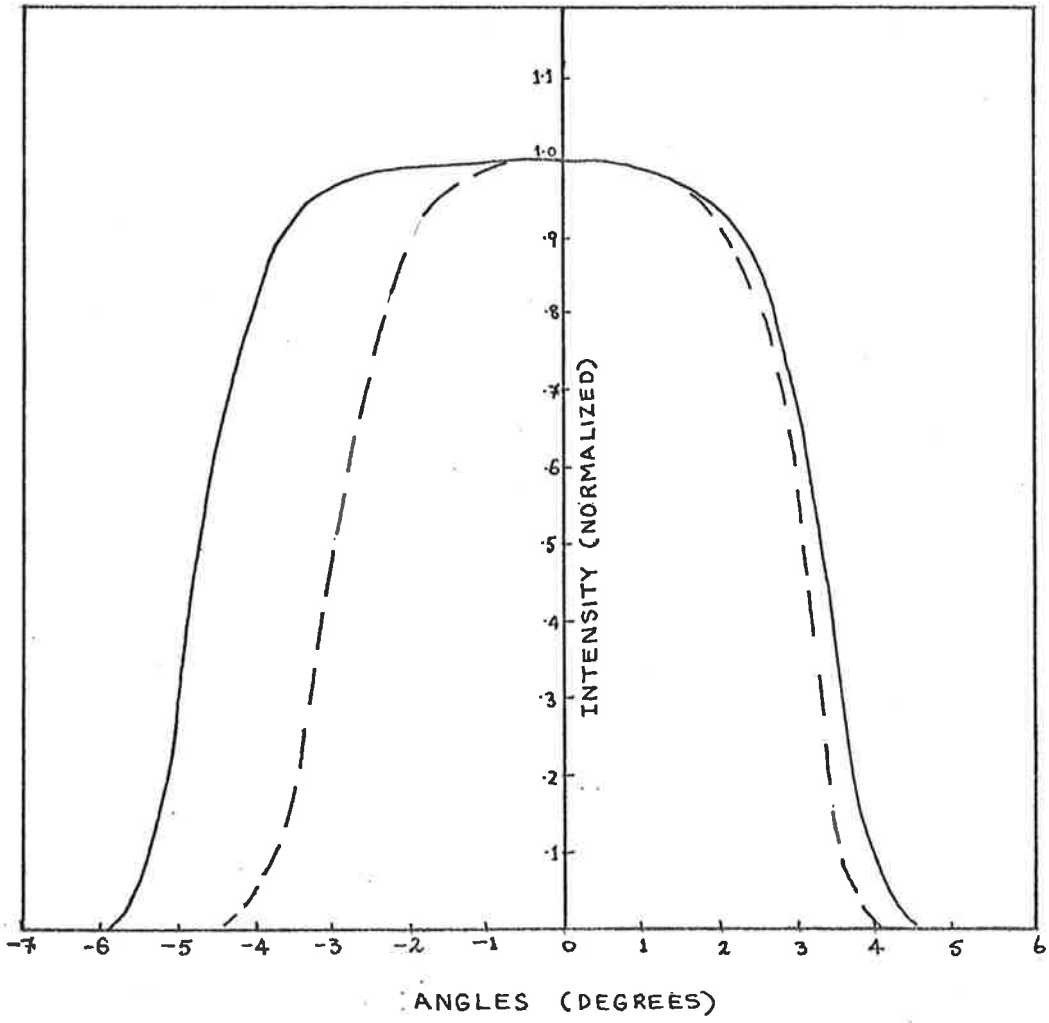

FIG 6·7: ANGLE RESPONSES OF THE SKYLARK'S ANALYZER FOR THE ANGLE β (— — —) AND α (——).

(see section 6.1.5). The determined angles α and β, at full width half maximum, are 8^{o} and 6^{o}, respectively, while the solid angle is:

$$\Omega = 1.5 \times 10^{-2} \text{ steradians} \qquad (6.25)$$

For the Aerobee's instrument these angles are:

$$\alpha = \pm 3^{o}$$

$$\beta = \pm 4^{o} \qquad (6.26)$$

$$\Omega = 1.5 \times 10^{-2} \text{ steradians}$$

However, in this case the angles α and β have not been determined experimentally but are the geometrical calculated angles. These angles are small enough to assume that they are the actual acceptance angles of the Aerobee's analyzer.

6.3.1 THE RETARDING POTENTIAL ANALYZERS

Two retarding potential analyzers have been flown on the Aerobee vehicle. As already mentioned in section 6.1.1, the purpose of this experiment was to measure the density and the low resolution energy spectrum of the thermal and quasi-thermal electrons and the density and energy spectrum of the ions. The data from the electron analyzer should provide information on the electron temperature and the potential of the vehicle with respect to the ambient plasma during the flight while the data from the ion analyzer should provide the ion temperature and inflight calibration of the ion mass spectrometer. In this work the analyzers will be known with the acronym of ERPA and IRPA, respectively, for the electron and ion spectrometers.

The analyzers are similar in mechanical construction and are shown in fig 6.8. They consist of a collimator, five grids G_1, G_2, G_3, G_4 and G_5 made of stainless steel mesh each having a transmission of 87% and a collector which collects the ion or electron current. Grids G_1, G_2 and G_4 are maintained at the same potential as the vehicle while a ramp and a suppressor voltage of the correct sign are applied to G_3 and G_5, respectively. The suppressor has the function of preventing the collection of the ionospheric electrons by the ion spectrometer or the ion by the electron analyzer. All the surfaces were made of the same type of material so that contact potentials need not be considered. The collimators have the function of limiting the angle of acceptance of the instruments to a small value and this is important since the resolving power of the analyzers is given by:

$$R_p = \tan^2\theta \qquad (6.27)$$

where θ is the angle of acceptance of the collimators. For the flight instruments $\theta = 14.7^\circ$ and hence $R_p = 7\%$.

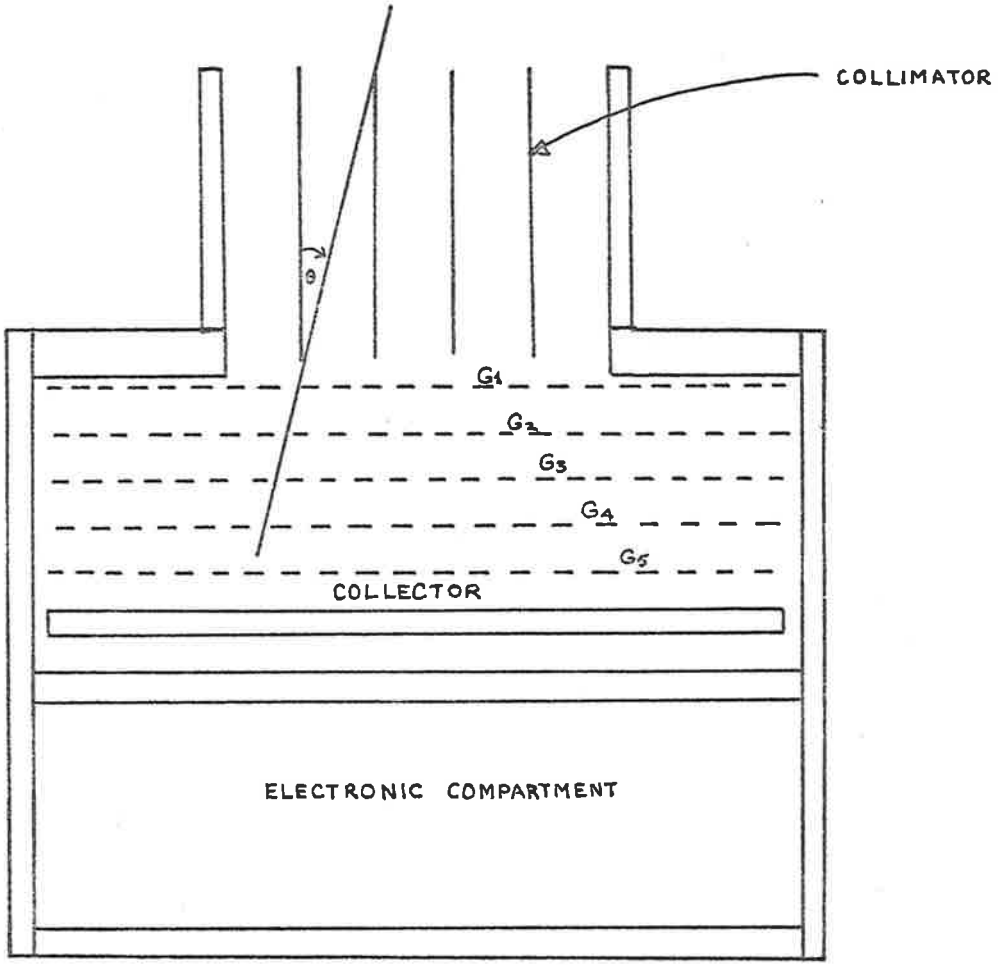

FIG 6·8 SECTIONAL VIEW OF THE ELECTRON AND ION RETARDING POTENTIAL ANALYZERS FLOWN ON THE AEROBEE VEHICLE.

The inside part of the collimators and the collecting plates were coated with a fuliginous substance. The purpose of this was to capture any electron or ion impinging on the inside surfaces of the collimators and to increase the collecting efficiency of the collecting plates.

Two linear ramps with a period of 3.2 seconds and generated by the electronic circuit of fig 6.5 were applied to the grids G_3. The ramp with voltage varying linearly from 2.08 to -18.1 volts was applied to the grid G_3 of ERPA while for IRPA the ramp voltage varied from -2.09 to +18.1 volts. The suppressor voltages were +15 and -15, respectively, for ERPA and IRPA.

The calibration of these instruments involved mainly the determination of the absolute transmission as a function of the energy of the charged particles in the energy range of interest. A schematic view of the arrangement of the apparatus used to calibrate IRPA is shown in fig 6.9b. The transmission of the instrument is determined by measuring the current of the transmitted ions collected by the collector of the analyzer and the incident ion current by sliding the Faraday cup in front of the ion source. The energy of the ions is varied by varying the voltage on the mesh cage.

To calibrate the ERPA the electron gun shown in fig 6.9a is used in front of the electron analyzer. For ERPA the transmission as a function of energy of electrons is shown in fig 6.10. The transmission increases with energy reaching the theoretical transmission of 50% for energy of 18 eV.

In the case of IRPA there were difficulties in calibrating the instrument absolutely. The difficulties were mainly due to the fact that the electron gun used to produce the required ions, being turned on for a few seconds, resulted in low energy electrons "flooding" the vacuum vessel contain-

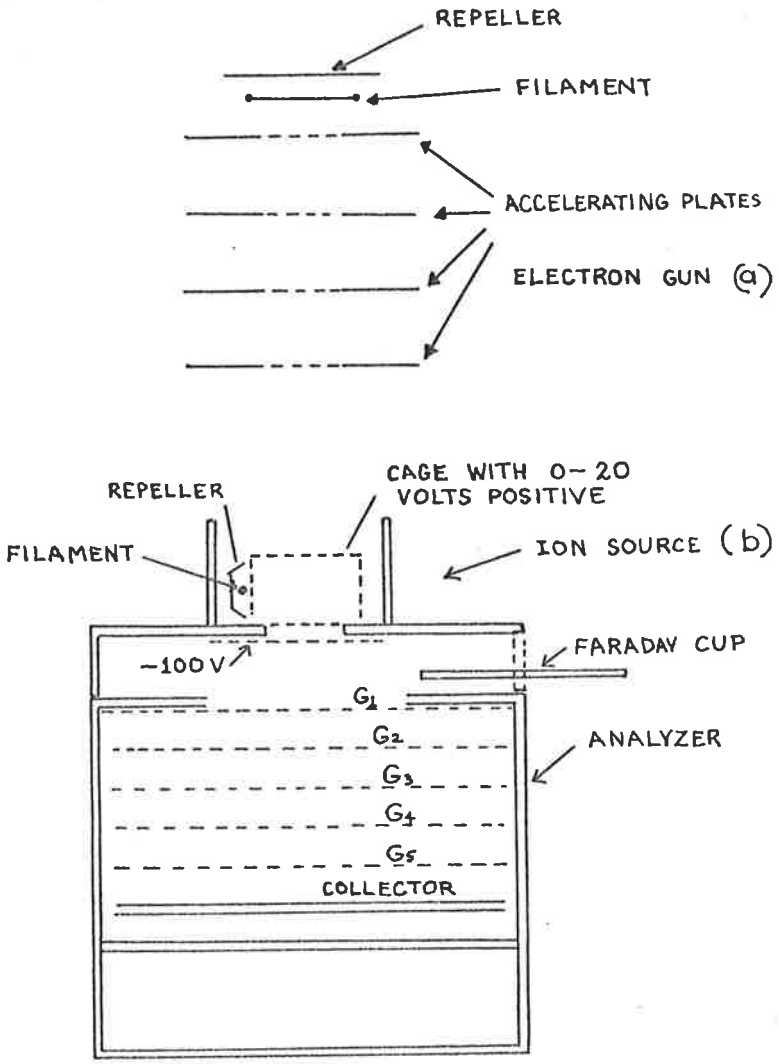

FIG 6·9: SCHEMATIC VIEW OF THE ARRANGEMENT OF THE RETARDING POTENTIAL ANALYZER AND:

(a) ELECTRON GUN USED TO CALIBRATE ERPA.

(b) ION SOURCE USED TO CALIBRATE IRPA.

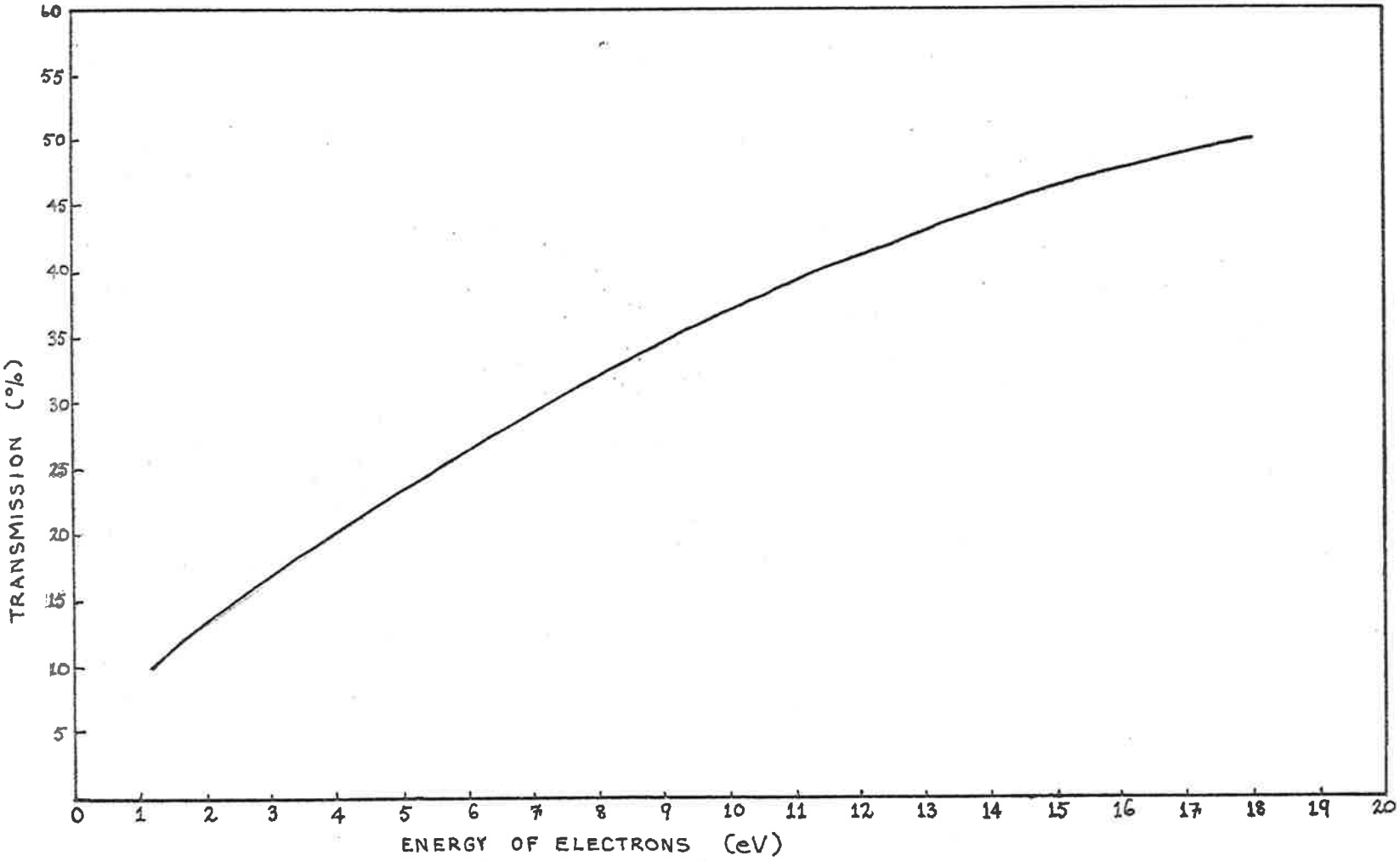

FIG 6·10: TRANSMISSION AS A FUNCTION OF ELECTRON ENERGY OF ERPA.

ing the analyzer. These low energy electrons were capable of penetrating the instrument not only through the entrance aperture of the analyzer where they would be discriminated, but also through the minute openings such as joints of the instrument's housing. In the case of ERPA and the cylindrical analyzers (DESAs) the problem was solved by sealing off all the joints of the housing of the instruments with masking tape so that these electrons could only enter the analyzers through the entrance apertures and which were subsequently discriminated by the ramp voltages. However, when it came to measure the absolute transmission of IRPA, the Faraday cup used to measure the incident ion current collected not only the ions but also these low energy electrons which resulted in the transmission being overestimated. Because of the work load of the author, having to calibrate a diverse number of instruments in a short period of time before the launch of the vehicle, it was not possible at that stage to devise a better system to calibrate the ion analyzer. The instrument was calibrated at the high ion energy of 18 eV, the transmission of which was 49%. It is expected that the transmission function is not very different from that of ERPA. However, the flown IRPA has been recovered and it is in a good condition so that it can be calibrated.

6.4.1 THE MEASURED ENERGY SPECTRA OF PHOTOELECTRONS

In this section are presented the differential energy spectra of the ionospheric photoelectrons measured with the Skylark's cylindrical analyzer. The spectra presented are those measured during the downleg part of the flight since the quality of the data on the downleg are superior to those of the upleg. The reason behind this is that, due to space limitation, it was not possible to design and build the instrument so that it could be evacuated before the launch of the vehicle. As a consequence, during flight it took longer than expected for the instrument to evacuate through the provided evacuating porthole to the ambient atmospheric pressure and for the channeltron to stabilize.

The ramp voltage applied between the electrodes of the analyzer was such that the energy spectra of the photoelectrons was measured between 1 and 400 eV in a time interval of 8 seconds. The scanning period had the effect that at about an altitude of 110 Km a single energy spectra was obtained in a 7 Km height interval while at about 142 Km altitude in a 4 Km interval and at the apogee (about 178 Km) in less than a 1 Km interval. In this work two sets of energy spectra of the ionospheric electrons are presented. The spectra of the first set are shown in figures 6.11, 6.12 and 6.13 and are of single scans at mid-spectrum altitudes of 110, 142 and 178 Km. The second set of scan which are shown in figures 6.14, 6.15 and 6.16 represent all the scans on the downleg part of the flight and are grouped into five spectra each representing the average of five consecutive scans.

The general shape of the spectra shown in the above mentioned figures remain unchanged with height but the level of the electron fluxes increase with altitude. Furthermore, the electron fluxes as a function of energy, f(E), can be,to

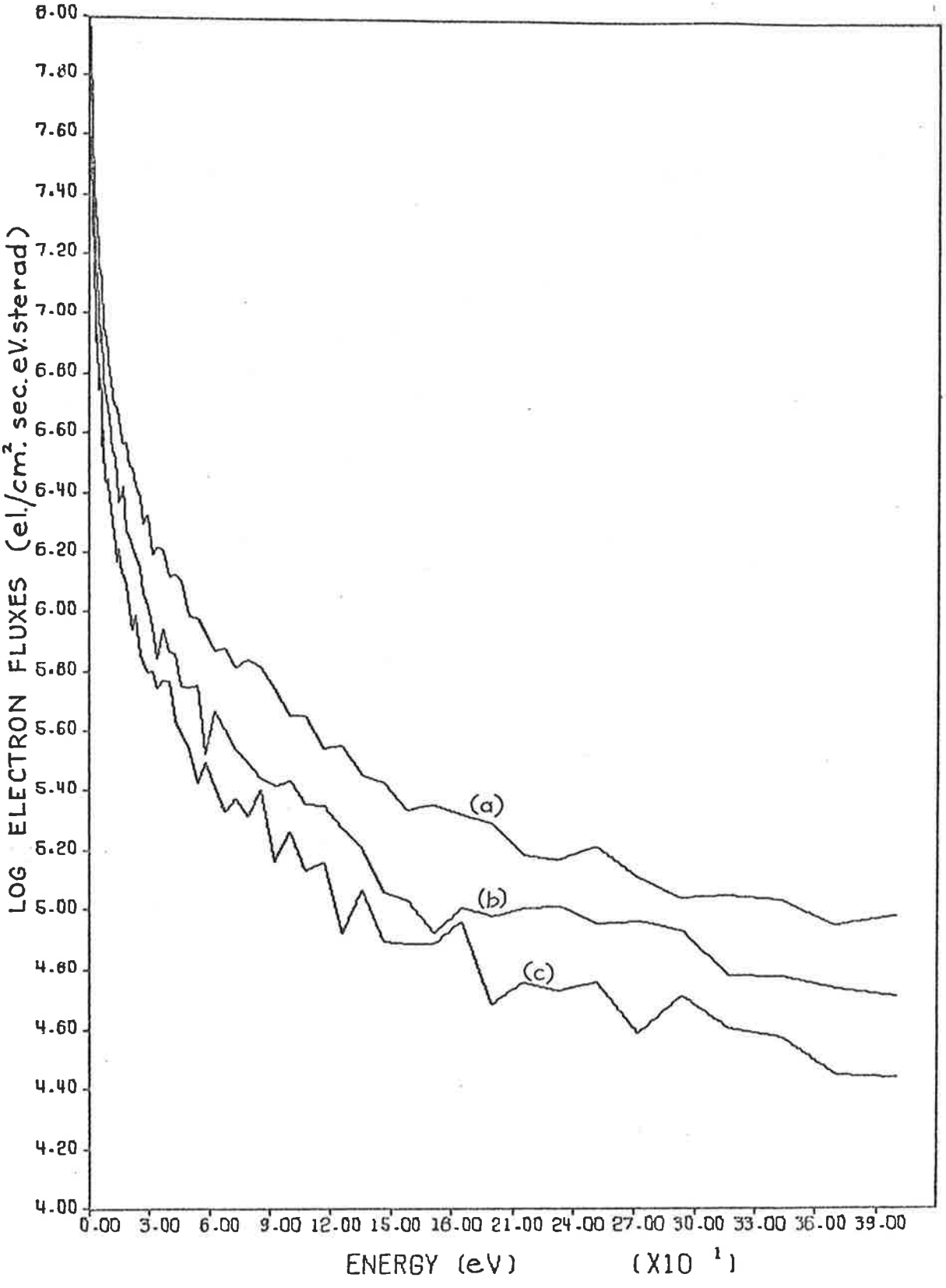

FIG 6·11 : SINGLE SCAN PHOTOELECTRON ENERGY SPECTRA AT MID-SPECTRUM ALTITUDE OF:
(a) 178 Km
(b) 142 Km
(c) 110 Km
ON A LINEAR ENERGY SCALE.

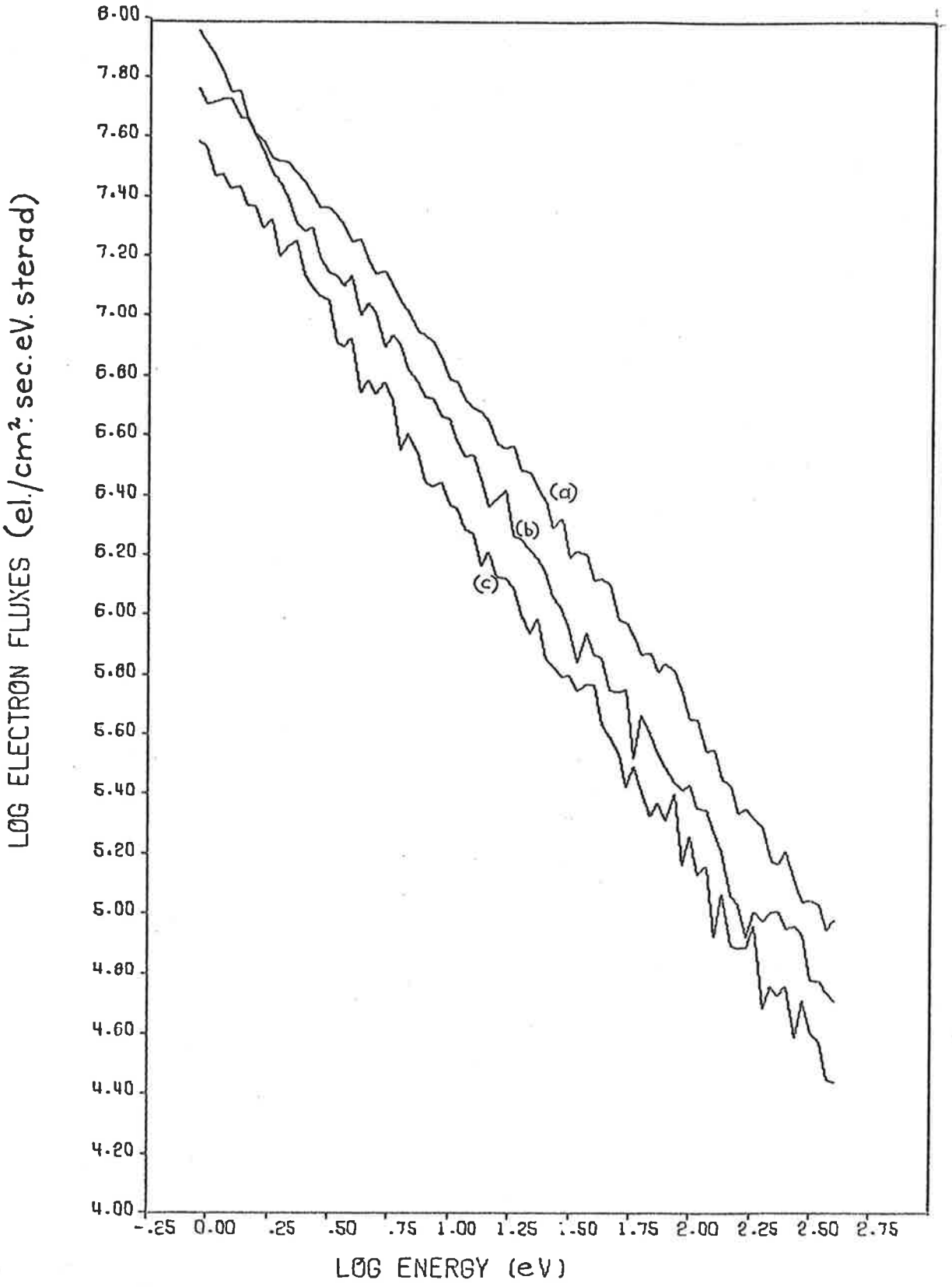

FIG 6·12 : SINGLE SCAN PHOTOELECTRON ENERGY SPECTRA AT MID-SPECTRUM ALTITUDE OF:
(a) 178 Km
(b) 142 Km
(c) 110 Km
ON A LOG ENERGY SCALE.

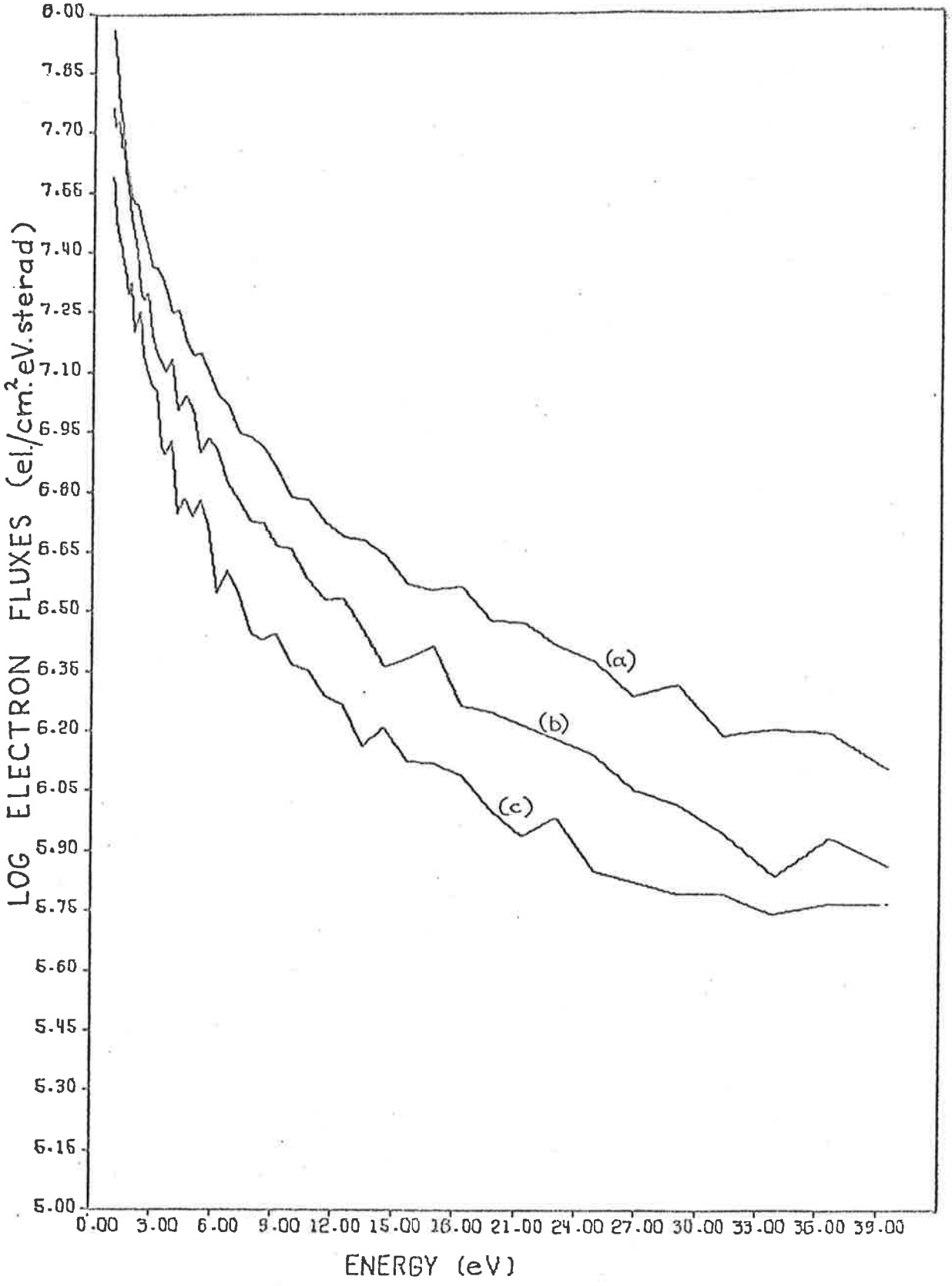

FIG 6·13: SINGLE SCAN PHOTOELECTRON ENERGY SPECTRA AT MID-SPECTRUM ALTITUDE OF:
(a) 178 Km
(b) 142 Km
(c) 110 Km
ON A LINEAR ENERGY SCALE

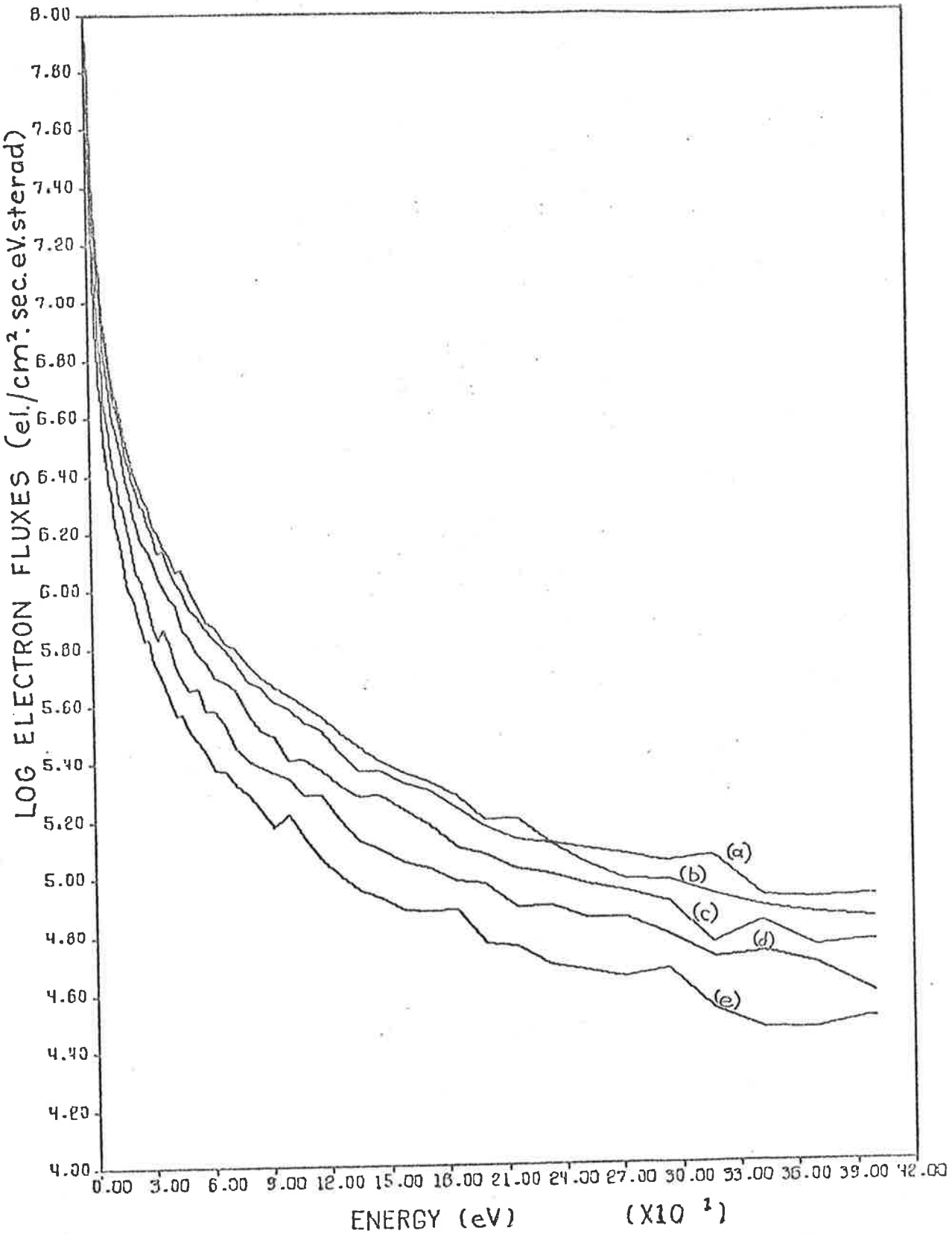

FIG 6·14: AVERAGED PHOTOELECTRON ENERGY SPECTRA IN ALTITUDE RANGE: (a) 177 - 172 Km
(b) 172 - 162 Km
(c) 162 - 145 Km
(d) 145 - 122 Km.
(e) 122 - 91 Km
ON A LINEAR ENERGY SCALE.

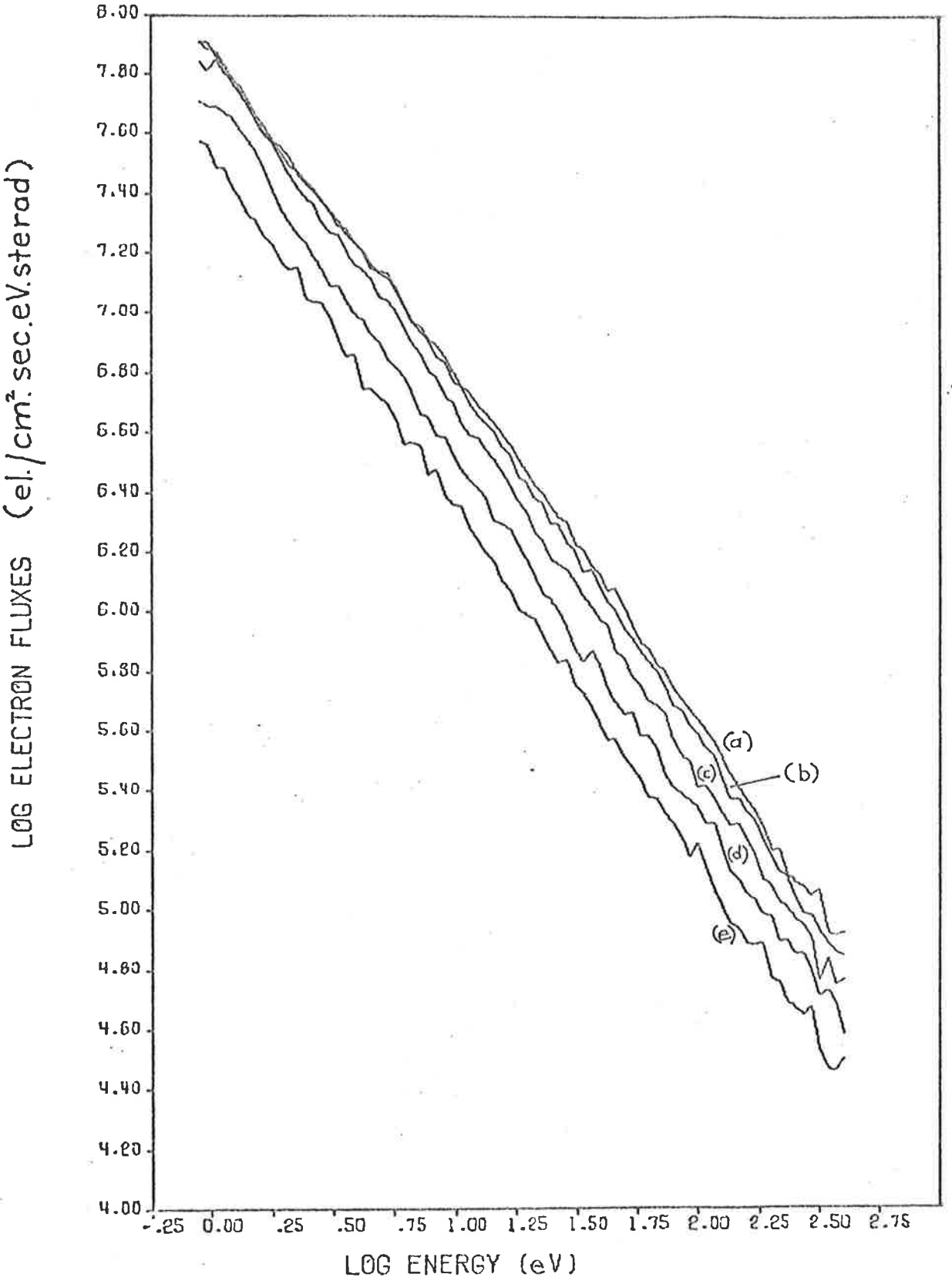

FIG 6·15 : AVERAGED PHOTOELECTRON ENERGY SPECTRA IN ALTITUDE RANGE: (a) 177 - 172 Km
(b) 172 - 162 Km
(c) 162 - 145 Km
(d) 145 - 122 Km
(e) 122 - 91 Km
ON A LOG ENERGY SCALE.

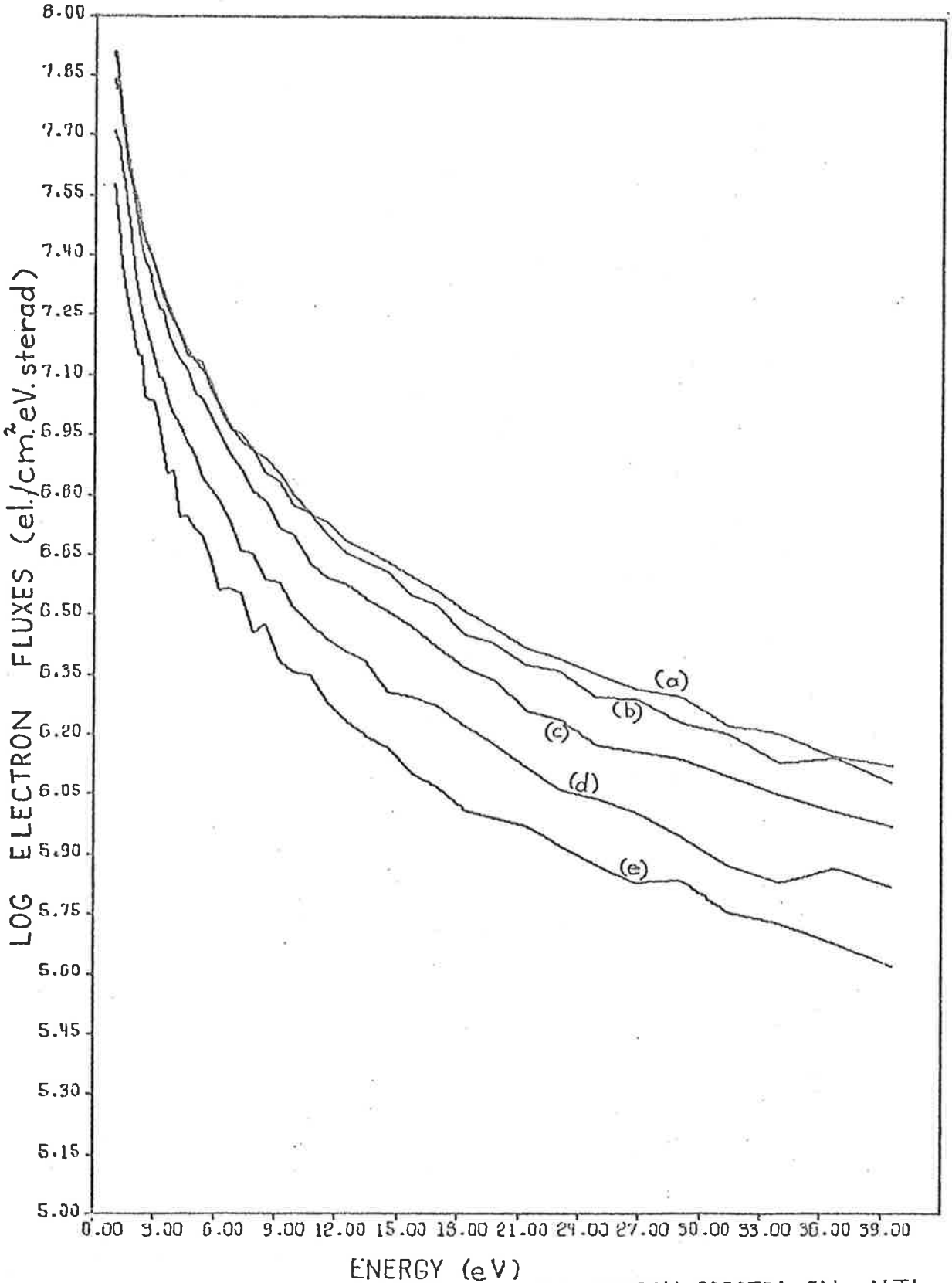

FIG 6·16: AVERAGED PHOTOELECTRON ENERGY SPECTRA IN ALTITUDE RANGE: (a) 177 - 172 Km
(b) 172 - 162 Km
(c) 162 - 145 Km
(d) 145 - 122 Km
(e) 122 - 91 Km
ON A LINEAR ENERGY SCALE.

a good approximation, represented by a simple power-law dependence on the energy. In fact, the electron fluxes for the spectra shown in fig 6.14 can be represented by:

$$F(E) = 3.43 \times 10^{7} \times E^{-1.19} \text{ electrons/cm}^2\text{sec.eV.sterad.} \quad (6.28)$$

for the altitude range 122 - 91 Km and by:

$$F(E) = 8.14 \times 10^{7} \times E^{-1.14} \text{ electrons.cm}^2\text{sec. eV. sterad} \quad (6.29)$$

for the altitude range 177 - 172 Km.

In the energy spectra of the photoelectrons measured with the Skylark's analyzer only a small amount of structure appears to be present and mainly for the single scan spectra (figures 6.11, 6.12 and 6.13). The lack of structure in the measured data in comparison with the calculated energy distribution of the photoelectrons (see section 1.3.5 for the bibliography) is mainly due to instrumental effects. In fact, the resolving power of the analyzer was only 6.5%. Moreover, the voltage across the electrodes of the analyzer was incremented in steps of 8% instead of the 6.5% so that the data points on the energy scale do not overlap since they are spaced wider than the instrumental energy half width (6.5%) and, therefore, a significant amount of structure is lost between adjacent points. There is, however, some structure and the broad features in the theoretical spectra are present in the measured spectra. For example, in fig 6.13 the spectrum at 110 Km altitude shows two distinct peaks, one at 23 and the other at 14.5 eV, while for the spectrum at 142 Km there is a peak at 16.9 eV and for the spectrum at 178 Km there are again two peaks, one at 18.3 and the other at 29 eV. According to theory, in the energy range 20 - 30 eV, the energy distribution function should have three peaks for the primary photoelectrons. The peaks should be positioned on the energy scale

at 22.2, 23.9 and 27.2 eV and are due to the primary photoelectrons produced by the HeII (304 $\mathring{A}$) solar radiation ionizing the atomic oxygen atoms to form O^+ ions in the ^2P, ^2D and ^4S states, respectively. To the knowledge of the author, to date, these three lines have not been resolved as three distinct separate lines by any rocket or satellite borne analyzer. Even the high resolving power (2.5%) analyzer flown on the Atmosphere Explorer-C satellite has not been able to resolve the three peaks (Doering et al (1975) and Victor et al (1976)).

Referring back to the spectra of fig 6.13, if it is assumed that the peak at 23 eV of the spectrum at 110 Km should be positioned on the energy scale at 24 eV, then it follows that the rocket vehicle acquired a potential of -1 volt at 110 Km, +1.5 volts at 142 Km and +2.8 volts at apogee. This change in vehicle's potential as it travelled through the ionosphere is the main cause of the loss of structure in the averaged spectra which are shown in figures 6.14, 6.15 and 6.16.

Since the earlier nineteen seventies there have been several measurements of the energy distribution of the ionospheric photoelectrons made by both rocket and satellite analyzers. For the purpose of comparing the author's results with the theoretical and measured spectra by other authors, values of fluxes of photoelectrons for the energies 10, 20, 30, 50 and 80 eV and altitudes less than about 200 Km are listed in tables 6.1 and 6.2. The different authors' values of the fluxes are obtained from the graphed spectra reported in the literature. From the values of the electron fluxes listed in tables 6.1 and 6.2 it can be seen that the present flux levels for the energy range less than about 60 eV compare reasonably well with those determined experimentally or theoretically by other authors. However, a rigorous comparison

Table 6.1

Authors	Present Results			Knudsen and Sharp (1972)	Mukai and Hirao (1973)		Hays and Sharp (1973)	Doering et al (1975)
Solar zenith angle	50^{o}			47^{o}	43^{o}		90^{o}	60^{o}
altitude (Km)	177 - 172	162 - 145	122 - 91	180	200	120	202	159
Energy (eV)	F(E)	F(E)	F(E)	F(E)	F(E)	F(E)	F(E)	F(E)
10	6.3×10^{6}	5×10^{6}	2.3×10^{6}	1.7×10^{7}	2×10^{7}	9×10^{6}	2×10^{7}	3.2×10^{6}
20	2.9×10^{6}	2.2×10^{6}	9.9×10^{5}	3.4×10^{6}	3×10^{6}		4.2×10^{6}	9×10^{5}
30	1.9×10^{6}	1.3×10^{6}	6.7×10^{5}	1.4×10^{6}	2×10^{6}			7×10^{5}
50	1×10^{6}	6.9×10^{5}	3.2×10^{5}	4×10^{5}				2×10^{5}
80	5.5×10^{5}	3.7×10^{5}	1.9×10^{5}					3×10^{4}

F(E) = electron flux in electron/eV cm^{2} sec. sterad.

Table 6.2

Authors	Victor et al (1976)		Mantas and Bohill (1975)		Doering et al (1970)		
Solar zenith angles	not specified		0		60^{o}		
altitude (Km)	measured 252 - 209	calculated 232	calculated 139	calculated 179	140	160	180
Energy (eV)	F(E)	F(E)	F(E)	F(E)	F(E)	F(E)	F(E)
10	2.2×10^{6}	1.5×10^{7}	2×10^{6}	$\sim 1 \times 10^{7}$	4.6×10^{5}	1.5×10^{6}	2.6×10^{6}
20	1.8×10^{6}	2×10^{6}	$\sim 7 \times 10^{5}$	$\sim 2.5 \times 10^{6}$	1.7×10^{5}	7×10^{5}	8×10^{5}
30	$\sim 1 \times 10^{6}$	$\sim 1 \times 10^{6}$	$\sim 3 \times 10^{5}$	$\sim 9 \times 10^{5}$			
50	2×10^{5}	$\times 10^{5}$	$\sim 1.2 \times 10^{5}$	$\sim 2.7 \times 10^{5}$			

F(E) = electron flux in electron/eV cm^{2} sec. sterad.

between electron fluxes determined by different authors is not possible for two reasons:

(1) the reported measurements have been made at different geographical latitude and for different solar zenith angles and solar conditions, and,

(2) the absolute values of the electron fluxes are subjected to large errors due to problems associated in calibrating the instruments absolutely.

Doering et al (1970) have indicated that the absolute values of their measured electron fluxes could be in error by a factor of 1.5, while Knudsen and Sharp (1972) estimated that their flux levels could be in error by a factor of 2. Furthermore, Doering et al (1975) have been able to determine the efficiency of the analyzer which has been flown on the Atmosphere Explorer-C satellite with an accuracy of only $\pm$20%. In comparison, the overall efficiency of the author's analyzer has been determined to be no better than $\pm$30% accuracy. Moreover, the measured data are subjected to statistical errors which in the case of the present results vary from 3% to 4% from the lower to higher energies for a single scan spectrum obtained at the apogee to an error from 4% to 7%, respectively, for a spectrum obtained at 110 Km altitude. Thus, the single scan energy spectra are subjected to a total error which varies from 33 to 37% while the averaged spectra are only slightly more accurate since they represent averaged spectra over five consecutive scans. Hence, comparison between measured electron energy spectra can be made only in a broad sense and mainly for the general shape of the spectra.

As already stated, the present results compare favourably with those of other experimenters for less than

about 60 eV. However, for energies greater than about 60 eV the present electron fluxes are much larger than theory predicts for quiet solar condition. According to theory, the fluxes of ionospheric electrons for energy greater than 60 eV and for quiet solar condition should decrease quite rapidly because of the decrease of the solar fluxes at short wavelengths (less than about 200 $\mathring{A}$). This effect has been observed by Doering et al (1975) and Victor et al (1976). However, the present measurements were made when the solar disk was highly disturbed. In fact, the geomagnetic planetary three-hour-range index (K_p) was 5^-. Thus, the author's larger electron fluxes at higher energies must be attributed mainly to the enhanced solar emission of radiation in the E.U.V. and X-ray spectral regions. Only a small contribution to these electron fluxes can be due to scattered photons entering the instrument through the pumping porthole and entrance aperture. The analyzer was positioned on the vehicle so that the entrance aperture and pumping porthole were at right angle to the direction of the sun and hence no direct sunlight could enter the instrument. Also, there were grids with large negative voltages in front of the porthole so that again no stray electrons could enter the analyzer except through the entrance aperture. It is expected that this background noise due to stray scattered photons is small; however, there is no way in which its magnitude can be estimated so that it cannot be subtracted from the presented electron fluxes. Furthermore, to the knowledge of the author, no measurements of the ionospheric electron fluxes for energies greater than 60 eV have been reported in the literature, except those reported by Doering et al (1975) and Victor et al (1976) and the latter authors do not state the solar condition under which the measurements were made. Thus, a comparison between these fulxes and present re-

sults for energies greater than about 60 eV cannot be made.

EPILOGUE

In its interaction with solar and galactic radiation the earth's upper atmosphere gives rise to a multitude of physical, chemical and optical phenomena which no single parameter can describe. As a consequence, during the course of this work the author has tried and succeeded in developing and flying, on a number of rocket vehicles, different types of instruments in order to measure simultaneously more than one atmospheric parameter. Unfortunately, the number of successful flights have been few and, as a result, the amount of data presented in this thesis is scanty. However, the bulk of the data which has been acquired by the instruments flown on the Aerobee vehicle, although still to be processed, show that the preliminary results from the flight records, as illustrated in Appendix B, are promising.

Even though successful flights have been few, the practical knowledge gained by the author in designing, calibrating and flying of various types of instruments has culminated in flying all these instruments on a single vehicle, the Aerobee. These, with the instruments prepared by other members of the Space Research Group of the University of Adelaide has, perhaps, made the Aerobee payload one of the most complete instrumented aeronomic payloads ever to be launched from Woomera Rocket Range, South Australia.

Other members of the Space Research group working on the Aerobee were Dr R. C. Schaeffer who has flown

(1) a 1/8 meter U.V. spectrometer which measured solar radiation as a function of altitude in the spectral region from 1380 to 1750 Å.

(2) a multichannel photometer which measured the red, 6300 Å, and green, 5577 Å, atomic oxygen airglow lines, those of the O-O band of the

first negative system of N_2^+, 3914 Å, and the second positive band of N_2, 3371 Å.

(3) a pin diode responding to the 0-0 atmospheric O_2 band to determine the O_3 high altitude profile.

Ms L. A. Davis who has flown ion chambers sensitive to solar radiation in the spectral regions 1150 - 1350 Å, 1050 - 1350 Å and 1420 - 1490 Å to determine the concentration of molecular oxygen and Ms J. Lean who has prepared a grazing incidence spectrometer which measured the absorption of solar radiation in the wavelength region 200 - 1100 Å as a function of altitude.

APPENDIX A

COMPUTATION OF THE FIRING TIME OF ROCKET VEHICLES

For rocket borne experiments it is often necessary to launch the vehicle at a time when celestial bodies such as the sun, moon and stars are in a particular position in the sky. It then becomes essential to calculate the time at which the vehicles have to be fired in order for these bodies to be at a certain height above the horizon. The computation is done for the sun and it is as follows.

If, h, is the height of the sun above the horizon, then its zenith angle, z, is 90-h and from spherical trigonometry its Hour's Angle, H, can be determined, i.e.:

$$\cos z = \sin\varphi \sin\delta + \cos\varphi \cos\delta \cos H \qquad (A.1)$$

where φ = latitude of launcher and

δ = declination of the sun.

The Hour's Angle (H.A.) of the sun determined from the expression of (A.1) is either in the first or in the fourth quadrant. The siderial time, t_s, is then:

$$t_s = \alpha + H \qquad (A.2)$$

where α is the Right Ascension (R.A.) of the sun and if H_E is the Hour's Angle of the Equinox, then the local Hour's Angle is:

$$H_L = H_E - \psi \qquad (A.3)$$

where ψ is the longitude of the launcher. The firing time t_f is:

$$t_f = t_s - H_L \qquad (A.4)$$

$$= \alpha + H - H_E + \psi \text{ in Universal Time (U.T.).}$$

For Australian Central Standard Time (C.S.T.):

$$t_f = \alpha + H - H_E + \psi - 9^h30^m \qquad (A.5)$$

For Woomera, $\varphi = -30^\circ 35'$ and $\psi = 136^\circ 31'$E.

APPENDIX B

ILLUSTRATION OF THE AEROBEE'S DATA

The Aerobee vehicle, launched at 6^h36^m (C.S.T.) on February 22nd, 1977, carried a set of co-ordinated experiments prepared by the Space Research Group of the University of Adelaide, which measured simultaneously a number of atmospheric parameters. These experiments were specifically designed and the time of launch of the vehicle was arranged at a time such that the measured data permitted a detailed study and formulation of the formation of the diurnal ionospheric E and F_1 regions.

All the author's experiments on this vehicle appear to have functioned satisfactorily and the telemetred results show promise, although at this stage it is too premature to speculate on the quality of the data. The graphical representation of the "quick-look" record of the telemetred data for small sections of the flight is shown in figures B.1, B.2, B.3 and B.4. Figure B.1 shows the integral mass spectrum of the neutral mass spectrometer at heights of about (a) 113 Km and (b) 123 Km for the upleg part of the flight while figure B.2 shows the ion mass spectrum at the heights of about (a) 166 Km, and (b) 149 Km for the downleg part of flight. From figure B.1 it can be seen that N_2 is the major constituent while the measurements of the ion mass spectrometer (fig B.2) indicate that in the ionospheric region between about 140 to 170 Km NO^+ is the dominant ion followed by O^+ and O_2^+. This trend in which NO^+ dominates over O^+ and O_2^+ in the morning ionosphere at these heights is corroborated by the ion mass spectrometer observations of the night-time mid-latitude ionosphere (Johnson (1972)).

The data from the electrostatic analyzers are shown in figures B.3 and B.4 for the altitudes of about 177 and 118

Km, respectively, for the downleg part of the flight. In these figures (a) represents the logarithm output of the ion retarding potential analyzer (IRPA) and (b) represents the integral energy spectrum of the cylindrical analyzer.

The reader is reminded that the Aerobee vehicle carried a PCM telemetry system (section 2.1.20) so that the output from these instruments, except for IRPA and ERPA are in a digital format. However, for display purpose the signals have been converted to the analog format.

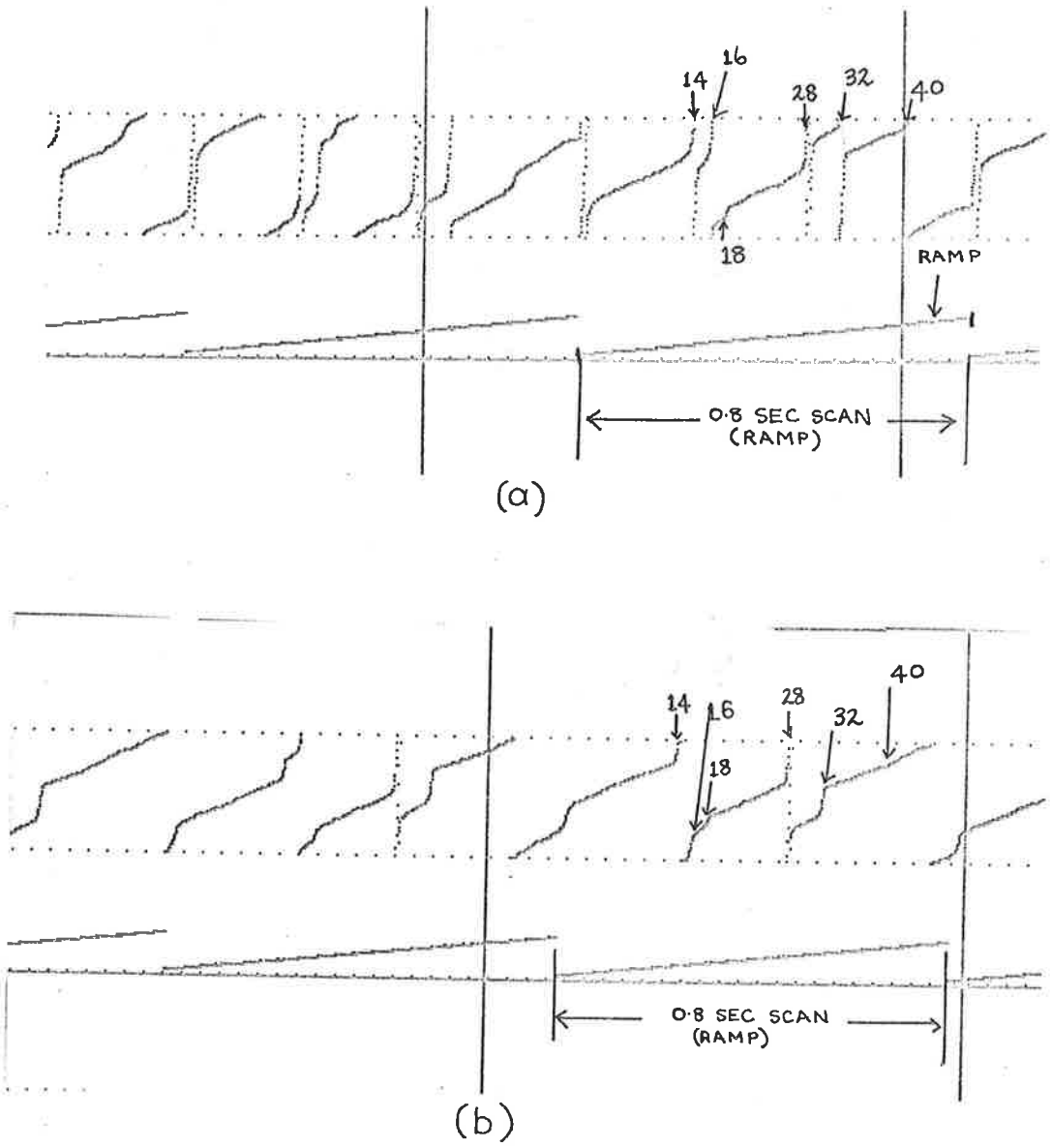

FIG B.1: "QUICK-LOOK" RECORD OF THE NEUTRAL MASS SPECTROMETER GIVING THE INTEGRAL MASS SPECTRA OF THE ATMOSPHERIC CONSTITUENTS TAKEN ON THE UPLEG PART OF THE FLIGHT AT ALTITUDES OF ABOUT:

(a) 113 KM

(b) 123 KM

THE MASS OF THE CONSTITUENTS ARE AS INDICATED.

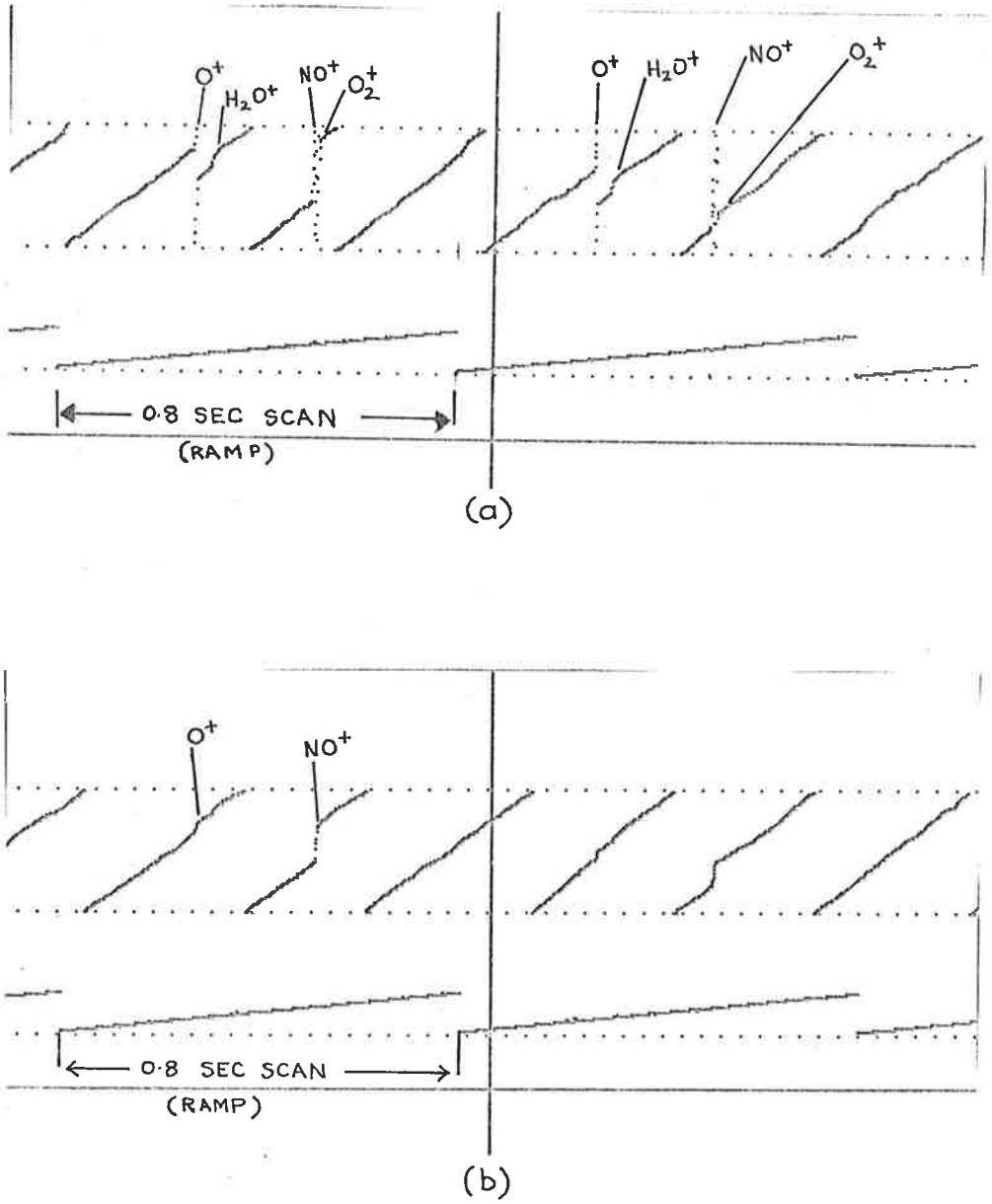

FIG B.2: "QUICK-LOOK" RECORD OF THE ION MASS SPECTROMETER GIVING THE INTEGRAL MASS SPECTRA OF THE ATMOSPHERE ION SPECIES TAKEN ON THE DOWNLEG PART OF THE FLIGHT AT ALTITUDES OF ABOUT:

(a) 166 KM

(b) 149 KM

THE IDENTIFIED ION CONSTITUENTS AS INDICATED.

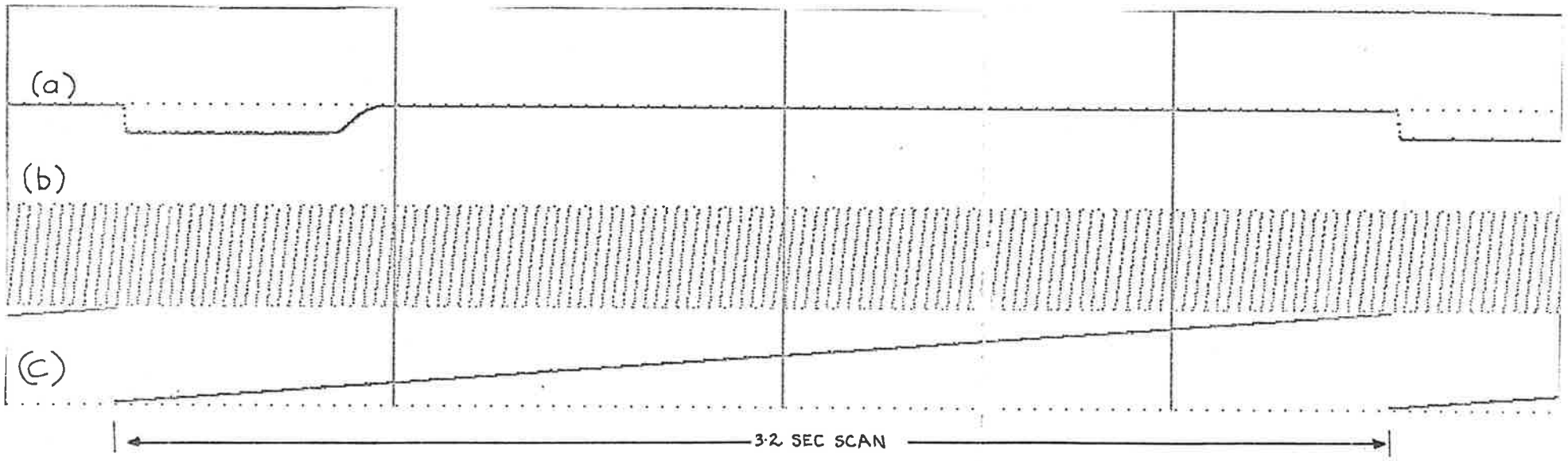

FIG B.3: "QUICK-LOOK" RECORD OF THE OUTPUT FROM:

(a) ION RETARDING POTENTIAL ANALYZER (IRPA)

(b) CYLINDRICAL ANALYZER (DESA)

(c) LINEAR RAMP (MONITOR)

AT THE APOGEE OF THE FLIGHT (177 KM)

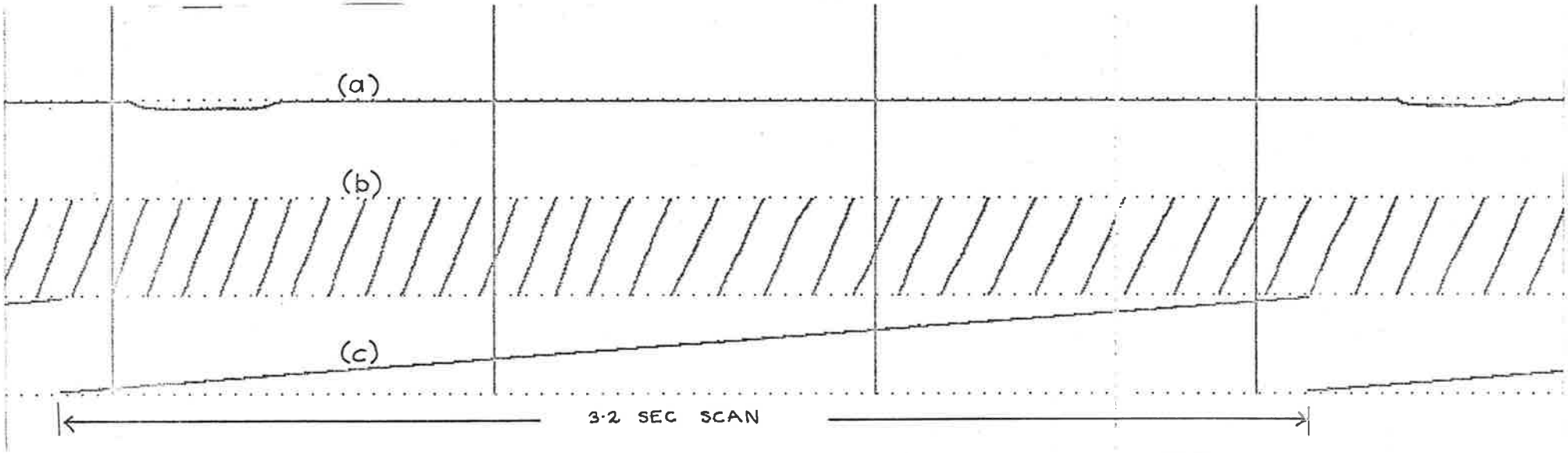

FIG B.4: "QUICK-LOOK" RECORD OF THE OUTPUT FROM:

(a) ION RETARDING POTENTIAL ANALYZER (IRPA)

(b) CYLINDRICAL ANALYZER (DESA)

(c) LINEAR RAMP (MONITOR)

AT AN ALTITUDE OF ABOUT 118 KM (DOWNLEG)

BIBLIOGRAPHY

ACKERMAN, M., SIMON, P., VON ZAHN, U., AND LAUX, U., 1974.
J. Geophys. Res., 79, 4757.

ADAMS, J., AND MANLEY, B.W., 1965.
Electronic Eng., 37, 180.

AIKIN, A.C., GOLDBERG, R.A., AND AZCARRAGA, A., 1974.
Space Res., 14, 283.

ALCAYDE, D., BAUER, P., JAECK, C., AND FALIN, J.L., 1972.
J. Geophys. Res., 77, 2368.

ALCAYDE, D., BAUER, P., AND FONTANARI, J., 1974.
J. Geophys. Res., 79, 629.

ANANTHAKRISHNAN, S., AND RAMANATHAN, K.R., 1969.
Nature, 223, 488.

ANDRESEN, R.D., AND PAGE, D.E., 1971.
Rev. Sci. Instrum., 42, 371.

APPLETON, E.V., AND BARNETT, M.A.F., 1925.
Proc. Roy. Soc., A109, 621.

ARNOLD, F., KISSEL, J., KRANKOWSKY, D., WIEDER, H., AND ZAHRINGER, J., 1971.
J. Atmos. Terr. Phys. 33, 1169.

ASHIHARA, O., AND TAKAYANAGI, K., 1974.
Planet. Space Sci., 22, 1201.

AXFORD, W.I., 1963.

J. Geophys. Res., 68, 769.

AXFORD, W.I., 1967.

Space Res., 7, 126.

BANKS, P.M., 1966.

Planet. Space Sci., 14, 1085.

BANKS, P.M., 1969.

Proc. of I.E.E.E., 57, 258.

BANKS, P.M., AND KOCKARTS, G., 1973.

'Aeronomy', Part A and B: Academic Press, N.Y.

BANKS, P.M., SCHUNK, R.W., AND RAITT, W.J., 1974.

Geophys. Res. Letters, 1, 239.

BARTH, C.A., 1964.

J. Geophys. Res., 69, 3301.

BARTH, C.A., 1966.

Ann. Geophys., 22, 198.

BECKER, J.A., BECKER, E.J., AND BRANDES, R.G., 1961.

J. Appl. Phys., 32, 411.

BELROSE, J.S., 1965.

'Physics of the Earth's Upper Atmosphere': ed. C.O. Hines, I. Paghis, T.R. Hartz and J.A. Fejer: Prentice-Hall, N.J.

BENNANI, A.L., PEBAY, J., AND NGUYEN, B., 1973.

J. Phys. E: Sci. Instrum., 6, 1077.

BENNETT, F.D.G., AND THORPE, D.G., 1970.
J. Phys., E: Sci instrum., 3, 241.

BERGER, M.J., AND SELTZER, S.M., 1964.
Nasa SP-3012.

BIONDI, M.A., 1969.
Can. J. Chem., 47, 1711.

BISI, A., AND ZAPPA, L., 1955.
Nuovo Cimento, 5, 988.

BITTERBERG, W., BRUTCHAUSEN, K., OFFERMANN, D., AND VON ZAHN, U., 1970.
J. Geophys. Res., 75, 5528.

BLANCH, G., 1965.
'Handbook of Mathematical Functions': ed. M. Abramowitz and I.A. Stegun: Dover Publications, Inc., New York.

BORDONI, F., MARTINELLI, M., PAGANINI FIROATTI, M., AND RICCI PIERMATEI, S., 1974.
Nuclear Instrum. and Methods, 116, 193.

BOTHE, G.P., 1974.
J. Atmos. Terr. Phys., 36, 1537.

BOURNE, I.A., AND HEWITT, L.W., 1968.
J. Atmos. Terr. Phys., 30, 1381.

BREIT, G., AND TUVE, M.A., 1926.
Phy. Rev., 28, 554.

BRINTON, H.C., PICKETT, R.A., AND TAYLOR, H.A., 1969.
J. Geophys. Res., 74, 4064.

BRUBAKER, W.M., 1961.
Colloq. Spectrosc. Intern., 9th, Lyon, France, June (1961).

BRYANT, D.A., AND JOHNSTONE, A.D., 1965.
Rev. Sci. Instrum., 36, 1662.

BRYCE, P., DALGLISH, R.L., AND KELLY, J.C., 1973.
Can. J. Phys., 51, 574.

BURKHALTER, P.G., BROWN, J.D., AND MYKLEBUST, R.L., 1966.
Rev. Sci. Instrum., 37, 1267.

BURROUS, C.A., LIEBER, A.J., AND ZAVIANTSEFF, V.T., 1967.
Rev. Sci. Instrum., 38, 1477.

BYRNE, J., 1962.
Proc. Roy. Soc. Edimb., A, 66, 33.

CAMPBELL, J.L., AND LEDINGHAM, K.W.D., 1966.
British J. of Applied Physics, 17, 769.

CARVER, J.H., MITCHELL, P., MURRAY, E.L., AND HUNT, B.C., 1964.
J. Geophys. Res., 69, 3755.

CARVER, J.H., AND MITCHELL, P., 1967.
Nuclear Instrum. and Methods, 52, 130.

CARVER, J.H., EDWARDS, P.J., GOUGH, P.L., GREGORY, A.G., ROFE, B., AND JOHNSON, S.G., 1969.
J. Atmos. Terr. Phys., 31, 563.

CARVER, J.H., HORTON, B.H., ILYAS, M., AND LEWIS, B.R., 1977a.
"Molecular Oxygen Densities and the Atmospheric Absorption of Solar Lyman-α Radiation".
J. Geophys. Res., (in press).

CARVER, J.H., DAVIS, L.A., HORTON, B.H., AND ILYAS, M., 1977b.
"Ultraviolet Extinction Measurements of Molecular Oxygen Density".
To be submitted to J. Geophys. Res.

CHAMPION, K.S.W., 1969.
Space Res., 9, 459.

CHANDRA, S., AND SINHA, A.K., 1973.
Planet Space Sci., 21, 593.

CHARLES, M.W., AND COOKE, B.A., 1968.
Nuclear Instrum. and Methods, 61, 31.

CHIMONAS, G., AND AXFORD, I.W., 1968.
J. Geophys. Res., 73, 111.

CICERONE, R.J., AND BOWHILL, S.A., 1971.
J. Geophys. Res., 76, 8299.

CICERONE, R.J., SWARTZ, W.E., STOLARSKI, R.S., NAGY, A.F., AND NISBET, J.S., 1973.
J. Geophys. Res., 78, 6709.

COCKROFT, A.L., AND CURRAN, S.C., 1951.
Rev. Sci. Instrum., 22, 37.

COLEGROVE, F.D., JOHNSON, F.S., AND HANSON, W.B., 1966.
J. Geophys. Res., 71, 2227.

COSPAR International Reference Atmosphere (CIRA).
North-Holland Publsihing Co., (Amsterdam) 1961,
1965, and
Akademie-Verlag (Berlin) 1972.

CURRAN, S.C., ANGUS, J., AND COCKROFT, A.L., 1949.
Phil. Mag., 40, 929.

CURRAN, S.C., AND CRAGGS, J.D., 1949.
'Counting Tubes, Theory and Applications':
Butterworths Scientific Publications.

DALGARNO, A., McELROY, M.B., AND MOFFETT, R.J., 1963.
Planet Space Sci., 11, 463.

DALGARNO, A., AND DEGGES, T.C., 1968.
Planet Space Sci., 16, 125.

DANILOV, A.D., 1970.
Space Res., 10, 725.

DANILOV, A.D., ISTOMIN, V.G., SEMENOV, V.K., 1970.
Space Res., 10, 742.

DANILOV, A.D., 1972a.
Space Res., 12, 1299.

DANILOV, A.D., 1972b.
Space Res., 12, 891.

DAWSON, P.H., AND WHETTEN, N.R., 1969.
Advances in Electronics and Electron Physics,
27, 60.

DAWSON, P.H., 1974.

Int. J. Mass Spectrom. Ion Phys., 14, 317.

DAYTON, I.E., SHOEMAKER, F.C., AND MOZLEY, R.F., 1954.

Rev. Sci. Instrum., 25, 485.

DEN BOGGENDE, A.F.J., BRINKMAN, A.C., AND DE GRAAFF, W., 1969.

J. Phys. E: J. Sci. Instrum., 2, 701.

DENISON, D.R., 1971.

J. Vac. Sci. Technol., 8, 266.

DeVRIES, L.L., 1972.

Space Res., 12, 867.

DICKINSON, R.E., LAGOS, C.P., AND NEWELL, R.E., 1968.

J. Geophys. Res., 73, 4299.

DICKINSON, P.H.G., BOLDEN, R.C., AND YOUNG, R.A., 1974.

Nature, 252, 289.

DOERING, J.P., FASTIE, W.G., AND FELDMAN, P.D., 1970.

J. Geophys. Res., 75, 4787.

DOERING, J.P., PETERSON, W.K., BOSTROM, C.O., AND ARMSTRONG, J.C., 1975.

J. Geophys. Res., 80, 3934.

DONAHUE, T.M., 1972.

Radio Sci., 7, 73.

DONAHUE, T.M., GUENTHER, B., AND THOMAS, R.J., 1973.

J. Geophys. Res., 78, 6662.

DUNKIN, D.B., FEHSENFELD, F.C., SCHMELTEKOFF, A.L., AND FERGUSON, E.E., 1968.

J. Chem. Phys., 49, 1365.

EDWARDS, P.J., BURTH, G.J., AND KNOX, F., 1969.
Nature, 222, 1052.

EGIDI, A., MARCONERO, R., PIZZELLA, G., AND SPERLI, F., 1969.
Rev. Sci. Instrum., 40, 88.

EVANS, D.S., 1965.
Rev. Sci. Instrum., 36, 375.

FAIRE, A.C., MURPHY, E.A., AND THIELE, O.W., 1970.
Space Res., 10, 188.

FAIRE, A.C., MURPHY, E.A., AND OLSEN, R.O., 1973.
Space Res., 14, 97.

FANO, U., 1947.
Phys. Rev., 72, 26.

FEHSENFELD, F.C., SCHMELTEKOFF, A.L., SCHIEFF, H.I., AND FERGUSON, E.E., 1967.
Planet. Space Sci., 15, 373.

FEHSENFELD, F.C., FERGUSON, E.E., AND BOHME, D.K., 1969.
Planet. Space Sci., 17, 1759.

FEHSENFELD, F.C., DUNKIN, D.B., AND FERGUSON, E.E., 1970.
Planet. Space Sci., 18, 1267.

FELSKE, D., MARTINI, L., STARK, B., AND TAUBENHEIM, J., 1972.
Space Res., 12, 651.

FERGASON, L., 1966.
Rev. Sci. Instrum., 37, 964.

FERGUSON, E.E., AND FEHSENFELD, F.C., 1962.
J. Geophys. Res., 73, 6215.

FERGUSON, E.E., AND FEHSENFELD, F.C., 1969.
J. Geophys. Res., 74, 5743.

FERGUSON, E.E., 1972.
Radio Sci., 7, 397.

FINK, R.W., JOPSON, R.C., MARK, H., AND SWIFT, C.D., 1966.
Rev. Mod. Phys., 38, 513.

FITE, W.L., AND BRACKMANN, R.T., 1959.
Phys. Rev., 113, 815.

FOX, J.N., FITZWILSON, R.L., AND THOMAS, E.W., 1970.
J. Phys. E: Sci. Instrum., 3, 36.

FRANCEY, R.J., 1970.
J. Geophys. Res., 75, 4849.

FRANK, L.A., HENDERSON, N.K., AND SWISHER, R.L., 1969.
Rev. Sci. Instrum., 40, 685.

FRIEDMAN, M.P., 1970.
Smithsonian Astrophys. Obs. Spec. Rep. No 316.

FROITZHEIM, H., IBACH, H., AND LEHWALD, H., 1975.
Rev. Sci. Instrum., 46, 1325.

GHOSH, S.N., HINTON, B.B., JONES, L.M., LEITE, R.J., MASON, C.J., SCHAEFER, E.J., AND WALTERS, M., 1968.
J. Geophys. Res., 73, 4425.

GOLD, R., AND BENNETT, E.F., 1966.
Phys. Rev., 149, 201.

GOLDBERG, R.A., AND AIKIN, A.C., 1971.
J. Geophys. Res., 76, 8352.

GOLSHAN, N., AND SECHRIST, C.F., 1975.
Radio Sci., 10, 305.

GOOD, R.E., AND GOLOMB, D., 1973.
Space Res., 13, 249.

GROSS, J., 1970.
Z. Naturforsch, A, 25, 900.

HACKER, D.S., MARSHALL, S.A., AND STEINBERG, M., 1961.
J. Chem. Phys., 35, 1788.

HAFNER, H., SIMPSON, J.A., AND KUYATT, C.E., 1968.
Rev. Sci. Instrum., 39, 33.

HALL, L.A., SCHWEIZER, W., AND HINTEREGGER, H.E., 1965.
J. Geophys. Res., 70, 105.

HAMLIN, D.A., AND MYERS, B.F., 1974.
Planet. Space Sci., 22, 1343.

'Handbook of Chemistry and Physics', 1972.
52nd Edition, (Chemical Rubber Co., Cleveland, Ohio, U.S.A.)

HANNA, G.C., KIRKWOOD, D.H.W., AND PONTECORVO, B., 1949.
Phys. Rev., 75, 985.

HANSON, W.B., 1963.
Space Res., 3, 282.

HARPER, R.M., WARD, R.H., AND WHITEHEAD, J.D., 1975.
Radio Sci., 10, 357.

HARRIS, I., AND PRIESTER, W., 1962.
J. Atmos. Sci., 19, 286.

HARRIS, I., AND PRIESTER, W., 1965.
J. Atmos. Sci., 22, 3.

HARRIS, L.A., 1971.
Rev. Sci. Instrum., 42, 987.

HARRIS, R.D., AND TOHMATSU, T., 1972.
Proceedings of the Conference on Theoretical Ionospheric Models, June 14 - 16, 1971. The Pennsylvanian State University, Report No 401.

HARROWER, G.A., 1955.
Rev. Sci. Instrum., 26, 850.

HAYASHI, T., AND SAKUDO, N., 1968.
Rev. Sci. Instrum., 39, 958.

HAYDEN, J.L., NIER, A.O., FRENCH, J.B., REID, N.M., AND DUCKETT, R.J., 1974.
Int. J. Mass. Spectrom. Ion. Phys., 15, 37.

HAYS, P.B., AND ROBLE, R.G., 1973.
Planet. Space Sci., 21, 339.

HAYS, P.B., AND SHARP, W.E., 1973.
J. Geophys. Res., 78, 1153.

HEDIN, A.E., AVERY, C.P., AND TSCHETTER, C.D., 1964.
J. Geophys. Res., 69, 4637.

HEDIN, A.E., AND NIER, A.O., 1966.

J. Geophys. Res., 71, 4121.

HEDIN, A.E., HINTON, B.B., AND SCHMITT, G.A., 1973.

J. Geophys. Res., 78, 4651.

HENDERSON, W.R., 1974.

J. Geophys. Res., 79, 3819.

HENDRICKS, R.W., 1972.

Nuclear Instrum. and Methods, 102, 309.

HENKE, B.L., AND ELGIN, R.L., 1970.

Advances in X-ray Analysis, 13, 639.

HEOGY, W.R., FOURNIER, J.P., AND FONTHEIM, E.G., 1965.

J. Geophys. Res., 70, 5464.

HERZOG, R.F., 1940.

Phys. Z., 41, 18.

HINTEREGGER, H.E., HALL, L.A., AND SCHMITKE, G., 1965.

Space Res., 5, 1175.

HINTEREGGER, H.E., 1970.

Ann. Geophys., 26, 547.

HOLME, A.E., THATCHER, W.J., AND LECK, J.H., 1972.

Vacuum, 8, 327.

HOLMES, J.C., JOHNSON, C.Y., AND YOUNG, J.M., 1965.

Space Res., 5, 756.

HORTON, B.H., 1977.

Australian Physicist, 14, 122.

HUDSON, R.D., 1971.

Rev. Geophys. and Space Phys., 9, 305.

HUGHES, A.L.L., AND McMILLEN, J.H., 1929.

Phys. Rev., 34, 291.

HUGHES, A.L.L., AND ROJANSKY, V., 1929.

Phys. Rev., 34, 284.

HUNT, B.G., 1971.

J. Atmos. Terr. Phys., 33, 929.

HUNT, B.G., 1973.

J. Atmos. Terr. Phys., 35, 1755.

ISTOMIN, V.G., 1963.

Space Res., 3, 209.

JACCHIA, L.G., SLOWEY, J.W., AND VERNIANI, F., 1967.

J. Geophys. Res., 72, 1423.

JACCHIA, L.G., 1971.

Smithsonian Astro Phys. Obs. Special Report 332.

JACCHIA, L.G., SLOWEY, J.W., AND VON ZAHN, U., 1976.

A paper presented at COSPAR Meeting in Philadelphia, Pennsylvania, U.S.A., on June 15 - 19 (1976).

JOHANNESSEN, A., AND KRANKOWSKY, D., 1974.

J. Atmos. Terr. Phys., 36, 1233.

JOHNSON, C.Y., 1972.

Radio Sci., 7, 99.

JOHNSON, F.S., 1973.

Rev. Geophys. and Space Phys., 11, 741.

JONES, V.A., 1971.

Space Res. Sci., 11, 776.

KASPRZAK, W.T., KRANKOWSKY, D., AND NIER, A.O., 1968.

J. Geophys. Res., 73, 6765.

KATO, S., ASO, T., HORIUCHI, T., NAKAMURA, T., AND MATSUAKA, T., 1972.

Radio Sci., 7, 359.

KENESHEA, T., NARCISI, R.S., AND SWIDER, W., 1970.

J. Geophys. Res., 75, 845.

KENESHEA, T.J., AND SWIDER, W., 1972.

J. Atmos. Terr. Phys., 34, 1607.

KISER, R.W., 1960.

Appl. Sci., Res., 8, 183.

KNUDSEN, W.C., AND SHARP, G.W., 1972.

J. Geophys. Res., 77, 1221.

KORFF, S.A., 1948.

'Electron and Nuclear Counters': D. Van Nostrand Co., N.Y.

KOSHELEV, V.V., AND BELINSKAYA, S.I., 1974.

J. Atmos. Terr. Phys., 36, 315.

KRANKOWSKY, D., ARNOLD, F., WIEDER, H., KISSEL, J., AND ZAHRINGER, J., 1972.

Radio Sci., 7, 93.

KREPLIN, R.W., 1961.

Ann. Geophys., 17, 151.

KREPLIN, R.W., CHUBB, T.A., AND FRIEDMAN, M.P., 1962.
J. Geophys. Res., 67, 2231.

KRINBERG, I.A., GARIFULLINA, L.A., AND AKATOVA, L.A., 1974.
J. Atmos. Terr. Phys., 36, 1727.

LAGOS, C.P., AND MAHONEY, J.R., 1967.
J. Atmos. Sci., 24, 88.

LAKE, L.R., AND NIER, A.O., 1973.
J. Geophys. Res., 78, 1645.

LAKE, L.R., AND MAUERSBERGER, K., 1974.
Int. J. Mass Spectrom. Ion Phys., 13, 425.

LAPSON, L.B., AND TIMOTHY, J.G., 1976.
Applied Optics, 15, 1218.

LAYZER, D., 1972.
Radio Sci., 7, 385.

LEHMANN, H.R., AND WAGNER, C.U., 1966.
J. Atmos. Terr. Phys., 28, 617.

LeLEVIER, R.E., AND BRANSCOMB, L.M., 1968.
J. Geophys. Res., 73, 27.

LEVENTHAL, J.J., AND NORTH, G.R., 1971.
Rev. Sci. Instrum., 42, 120.

LOUBET, D., AND BARAT, C., 1973.
Nuclear Instrum. and Methods, 3, 441.

McCORMAC, B.M., AND OMHOLT, A:
editors of 'Atmospheric Emission':
Van Nostrand Reinhold Co., 1969.

MacLEAD, M.A., KENESHEA, T.J., AND NARCISI, R.S., 1975.
Radio Sci., 10, 371.

McLACHLAN, N.W., 1947.
'Theory and Application of Mathieu Functions':
Clarendon Press, Oxford. U.K.

MAIER, E.J., AND RAO, B.C.N., 1972.
J. Atmos. Terr. Phys., 34, 689.

MANDEL'STAM, S.L., 1965.
Space Sci. Rev., 4, 587.

MANSON, A.H., 1971.
Planet. Space Sci., 19, 270.

MANSON, A.H., AND MERRY, M.W.J., 1971.
Atmos. Terr. Phys., 33, 413.

MANSON, J.E., 1972.
Solar Phys., 27, 107.

MANSON, J.E., 1974.
AFCRL-TR-74-006, Research paper No 546.

MANTAS, G.P., 1974.
J. Atmos. Terr. Phys., 36, 1587.

MANTAS, G.P., AND BOWHILL, S.A., 1975.
Planet. Space Sci., 23, 355.

MARMET, P., AND KERWIN, L., 1960.
Can. J. Phys., 38, 787.

MAUERSBERGER, K., MULLER, D., OFFERMANN, D., AND VON ZAHN, U., 1967.
Space Res., 7, 1150.

MAUERSBERGER, K., KAYSER, D.C., POTTER, W.E., AND NIER, A.O., 1976.
J. Geophys. Res., 81, 7.

MAY, B.R., 1973.
Space Res., 13, 243.

MEIRA, L.G., 1971.
J. Geophys. Res., 76, 202.

MELFI, L.T., AND BROCK, F.J., 1973.
Rev. Sci. Instrum., 44, 1524.

MEWE, R., 1972.
Solar Phys., 22, 459.

MITRA, A.P., 1968.
J. Atmos. Terr. Phys., 30, 1065.

MITRA, A.P., AND BANERJEE, P., 1972.
Space Res., 12, 1315.

MITRA, A.P., AND ROWE, J.N., 1974.
J. Atmos. Terr. Phys., 36, 1797.

MOE, K., 1973.
J. Geophys. Res., 78, 1633.

MONRO, P.E., 1970.
J. Atmos. Terr. Phys., 32, 373.

MUKAI, T., AND HIRAO, K., 1973.
J. Geophys. Res., 78, 8395.

MULLER, D., AND HARTMANN, G., 1969.
J. Geophys. Res., 74, 1287.

NARCISI, R.S., SCHIFF, H.I., MORGAN, J.E., AND COHEN, H.A., 1962.
Space Res., 2, 1156.

NARCISI, R.S., AND BAILEY, A.D., 1965.
J. Geophys. Res., 70, 3687.

NARCISI, R.S., 1970.
Trans. Am. Geophys. Union, 51, No 4.

NARCISI, R.S., BAILEY, A.D., DELLA LUCCA, L., SHERMAN, C., AND THOMAS, D.M., 1971.
J. Atmos. Terr. Phys., 33, 1147.

NARCISI, R.S., BAILEY, A.D., WLODYKA, L.E., AND PHILBRICK, C.R., 1972.
J. Atmos. Terr. Phys., 34, 647.

NICOLET, M., AND AIKIN, A.C., 1960.
J. Geophys. Res., 65, 1469.

NIEMANN, H.B., AND KENNEDY, B.C., 1966.
Rev. Sci. instrum., 37, 722.

NIEMANN, H.B., 1972.
Rev. Sci. Instrum., 43, 1151.

NIEMANN, H.B., SPENCER, N.W., AND SCHMITT, G.A., 1973.
J. Geophys. Res., 78, 2265.

NIER, A.O., HOFFMAN, J.H., JOHNSON, C.Y., AND HOLMES, J.C., 1964.
J. Geophys. Res., 69, 4629.

NIER, A.O., POTTER, W.E., KAYSER, D.C., AND FINSTAD, R.G., 1974.
Geophys. Res. Letters, 1, 197.

NIER, A.O., 1972.

Space Res., 12, 881.

NIER, A.O., POTTER, W.E., AND KAYSER, D.C., 1976.

J. Geophys. Res., 81, 17.

NILES, F.E., HEIMERL, J.M., KELLER, G.E., AND PUCKETT, L.J., 1972.

Radio Sci., 7, 117.

NISBET, J.S., 1968.

J. Atmos. Terr. Phys., 30, 1257.

NORTON, R.B., AND WARNOCK, J.M., 1968.

J. Geophys. Res., 73, 5798.

NORTON, R.B., AND ROBLE, R.G., 1974.

J. Geophys. Res., 79, 3876.

NOXON, J.F., AND JOHANSON, A.E., 1972.

Planet. Space Sci., 20, 2125.

O'BOYLE, D., 1965.

J. Appl. Phys., 36, 2849.

OFFERMANN, D., AND TRINKS, H., 1971.

Rev. Sci. Instrum., 42, 1836.

OFFERMANN, D., AND VON ZAHN, U., 1971.

J. Geophys. Res., 76, 2520.

OFFERMANN, D., PELKA, K., AND VON ZAHN, U., 1972.

Int. J. Mass Spectrom. Ion Phys., 8, 391.

OFFERMANN, D., AND DRESCHER, A., 1973.
J. Geophys. Res., 78, 6690.

OFFERMANN, D., AND GROSSMANN, K.U., 1973.
J. Geophys. Res., 78, 8296.

OFFERMANN, D., AND SCHOLZ, T.G., 1973.
Rev. Sci. Instrum., 44, 1573.

OFFERMANN, D., AND TATARCZYK, H., 1973.
Rev. Sci. Instrum., 44, 1569.

OFFERMANN, D., 1974.
J. Geophys. Res., 79, 4281.

OGAWA, T., AND TOHMATSU, T., 1966.
Rep. Ionosphere Space Res.(Japan), 20, 395.

OGAWA, T., AND TOHMATSU, T., 1971.
J. Geophys. Res., 76, 6136.

OLIVER, W.L., 1974.
J. Atmos. Terr. Phys., 36, 801.

OPPENHEIMER, M., DALGARNO, A., AND BRINTON, H.C., 1976.
J. Geophys. Res., 81, 4678.

ORAN, E.S., AND STROBEL, D.F., 1976.
J. Geophys. Res., 81, 257.

PARESCE, F., BOWYER, S., AND KUMAR, S., 1973.
J. Geophys. Res., 78, 71.

PARKER, A.E., AND STEWART, K.H., 1972.
J. Atmos. Terr. Phys., 34, 1223.

PASCHMANN, G., SHELLEY, E.G., CHAPPELL, C.R., SHARP, R.D., AND SMITH, L.F., 1970.
Rev. Sci. Instrum., 41, 1706.

PAUL, W., AND STEINWEDEL, H., 1953.
Z. Naturforsch, A8, 448.

PAUL, W., AND RAETHER, M., 1955.
Z. Physik, 140, 262.

PAUL, W., REINHARD, H.P., AND VON ZAHN, U., 1958.
Z. Physik, 152, 143.

PEARCE, J.B., 1969.
J. Geophys. Res., 74, 853.

PHILBRICK, C.R., GOLOMB, D., ZIMMERMAN, S.P., KENESHEA, T.J., MacLEAD, M.A., GOOD, R.E., DANDEKAR, B.S., AND REINISCH, B.W., 1974.
Space Res., 14, 89.

PONTECORVO, B., 1950.
Helvetica Physica Acta, Suppl., 3, 112.

POTEMRA, T.A., AND ZMUDA, A.J., 1970.
J. Geophys. Res., 75, 7161.

POTTER, W.E., AND MAUERSBERGER, K., 1972.
Rev. Sci. Instrum., 43, 1327.

PRASAD, S.S., AND FURMAN, D.R., 1974.
J. Geophys. Res., 79, 2463.

PRINCE, R.H., AND CROSS, J.A., 1971.
Rev. Sci. Instrum., 42, 66.

RADICELLA, S.M., 1968.
J.Atmos. Terr. Phys., 30, 1745.

RATCLIFFE, J.A., AND WEEKS, K., 1960.
'Physics of the Upper Atmosphere': ed. R.A. Ratcliffe: Academic Press, N.Y.

REBER, C.A., AND HARPOLD, D.N., 1967.
Trans. Am. Geophys. Union, 48, 75.

RICHARDS, J.A., HUEY, R.M., AND HILLER, J., 1973.
Int. J. Mass Spectrom. Ion Phys., 12, 317.

RICHARDS, J.A., HUEY, R.M., AND HILLER, J., 1974a.
Int. J. Mass Spectrom. Ion Phys., 15, 379.

RICHARDS, J.A., HUEY, R.M., AND HILLER, J., 1974b.
Int. J. Mass Spectrom. Ion Phys., 15, 417.

RICHARDS, J.A., AND MCLELLAN, R.N., 1975.
Int. J. Mass Spectrom. Ion Phys., 17, 17.

RILEY, J.A., AND GIESE, C.F., 1970.
J. Chem. Phys., 53, 146.

RISHBETH, H., 1968.
Rev. Geophys., 6, 33.

RISHBETH, H., 1974.
'Structure and Dynamics of the Upper Atmosphere': ed. F. Verniani: Elsevier Scientific Co.

ROBLE, R.G., AND NORTON, RB., 1972.
J. Geophys. Res., 77, 3524.

ROBLE, R.G., AND DICKINSON, R.E., 1973.
J. Geophys. Res., 78, 249.

ROEMER, M., 1971.
Space Res., 11, 965.

ROEMER, M., 1974.
Radio Sci., 9, 223.

ROGERS, F.T., AND HORTON, C.W., 1943.
Rev. Sci. Instrum., 14, 216.

ROSE, M.E., AND KORFF, S.A., 1941.
Phys. Rev., 50, 850.

ROSENBERG, N. W., GOLOMB, D., ZIMMERMAN, W.K., VICKERY, W.K., AND THEON, J.S., 1973.
Space Res., 13, 435.

ROSSI, B.B., AND STAUB, H.H., 1949.
'Ionization Chambers and Counters, Experimental Techniques': Mc Graw-Hill.

ROWE, J.N., MITRA, A.P., FERRARO, A.J., AND LEE, H.S., 1974.
J. Atmos. Terr. Phys., 36, 755.

ROY, D., AND CARETTE, J.D., 1970.
Appl. Phys. Letters, 16, 413.

ROY, D., AND CARETTE, J.D., 1971.
J. Appl. Phys., 42, 3601.

RUDD, M.E., 1972.
'Low Energy Electron Spectroscopy': ed. K.D. Sevier.

RUTHERFORD, E., AND GEIGER, H., 1908.
Proc. Roy. Soc., A81, 141.

SAKUDO, N., AND HAYASHI, T., 1975.
Rev. Sci. Instrum., 46, 1060.

SCHAEFFER, E.J., AND NICHOLS, M.H., 1964.
J. Geophys. Res., 69, 4649.

SCHAEFFER, R.C.
(Private communication).

SCHLEGEL, K., 1974.
J. Atmos. Terr. Phys., 36, 183.

SCHLIER, R.E., 1958.
J. Appl. Phys., 29, 1162.

SCHMIDT, C., 1972.
J. Phys. E: Sci. Instrum., 5, 1063.

SCHMIDT, K.C., AND HENDEE, C.F., 1966.
I.E.E.E. Trans. Nucl. Sci., NS-13, 100.

SCHUNK, R.W., AND HAYS, P.B., 1971.
Planet. Space Sci., 19, 113.

SCHUNK, R.W., AND WALKER, J.C.G., 1973.
Planet. Space Sci., 21, 1875.

SCIALOM, G., 1974.
Radio Sci., 9, 253.

SHEA, M.F., SHARP, R.D., AND McELROY, M.B., 1968.
J. Geophys. Res., 73, 4199.

SHIMAZAKI, T., 1968.

J. Atmos. Terr. Phys., 30, 1270.

SINGLETON, J.H., 1966.

J. Chem. Phys., 45, 2819.

SMITH, D., AND FOURACRE, R.A., 1968.

Planet. Space Sci., 16, 243.

SNYDER, H.S., 1947.

Phys. Rev., 72, 181.

SPENCER, N.W., NIEMANN, H.B., AND CARIGNAN, G.R., 1973.

Radio Sci., 8, 287.

SPIELBERG, N., 1967.

Rev. Sci. Instrum., 38, 291.

STOLARSKI, R.S., AND JOHNSON, N.Y., 1972.

J. Atmos. Terr. Phys., 34, 1691.

STUBBE, P., AND VARNUM, W.S., 1972.

Planet. Space Sci., 20, 1121.

SUBBARAYA, B.H., SATYA, P., AND PAREEK, P.N., 1972.

J. Atmos. Terr. Phys., 34, 1141.

SWIDER, W., 1964.

Planet. Space Sci., 12, 761.

SWIDER, W., 1965.

J. Geophys. Res., 70, 4859.

SWIDER, W., 1968.

Nature, 217, 438.

SWIDER, W., 1972.

J. Atmos. Terr. Phys., 34, 1615.

THOMAS, L., 1971.

J. Atmos. Terr. Phys., 33, 157.

TIMOTHY, A.F., TIMOTHY, J.G., AND WILLMORE, A.D., 1972.

J. Atmos. Terr. Phys., 34, 969.

TISONE, G.C., 1973.

J. Geophys. Res., 78, 746.

TOHMATSU, T., AND WAKAI, N., 1970.

Ann. Geophys., 26, 209.

TRINKS, H., 1973.

AFCL-TR-73-0319, Translations, No 103.

TRINKS, H., AND VON ZAHN, U., 1975.

Rev. Sci. Instrum., 46, 213.

TULINOV, V.F., SHIBAEVA, L.V., AND JAKOVLEV, S.G., 1969.

Space Res., 9, 231.

TURCO, R.P., AND SECHRIST, C.F., 1972.

Radio Sci., 7, 725.

U.S. STANDARD ATMOSPHERE, 1962.

(U.S. Government Printing Office, Washington, D.C.)

U.S. STANDARD ATMOSPHERE, SUPPLEMENTS, 1966.

(U.S. Government Printing Office, Washington, D.C.)

VICTOR, G.A., KIRBY-DOCKEN, K., AND DALGARNO, A., 1976.
Planet. Space Sci., 24, 679.

VOLLAND, H., AND MAYR, H.G., 1970.
Ann. Geophys., 26, 907.

VOLLAND, H., AND MAYR, H.G., 1972.
Planet. Space Sci., 34, 1745, 1769, 1797.

VON ZAHN, U., 1967.
J. Geophys. Res., 72, 5933.

VON ZAHN, U., AND GROSS, J., 1969.
J. Geophys. Res., 74, 4055.

VON ZAHN, U., 1970.
J. Geophys. Res., 75, 5517.

WAGENER, J.S., AND MARTH, P.T., 1957.
J. Appl. Phys., 28, 1027.

WALDTEUFEL, P., BAUER, P., AND McCLURE, J.P., 1972.
Space Res., 12, 899.

WALKER, A.B.C., 1972.
Space Sci. Rev., 13, 672.

WALKER, J.C.G., AND McELROY, M.B., 1966.
J. Geophys., 71, 3779.

WALLACE, L., AND McELROY, M.B., 1966.
Planet. Space Sci., 14, 677.

WEEKS, L.H., AND SMITH, L.G., 1968.
J. Geophys. Res., 73, 4835.

WEEKS, L.H., 1974.

AFCL-TR-74-0109, Environmental Research Paper, No 469.

WEEKS, L.H., 1975.

J. Geophys. Res., 80, 3661.

WHITEHEAD, J.D., 1961.

J. Atmos. Terr. Phys., 20, 20.

WHITEHEAD, J.D., 1967.

Space Res., 7, 9.

WHITTEN, R.C., AND POPPOFF, I.G., 1965.

'Physics of the Lower Ionosphere': Prentice-Hall, New Jersey.

WHITTEN, R.C., AND POPPOFF, I.G., 1971.

'Fundamental of Aeronomy': Wiley and Sons, Inc.

WILKINSON, D.H., 1950.

'Ionization Chambers and Counters': University Press, Cambridge.

WOLFF, R.S., 1974.

Solar Physics, 34, 163.

WOLLNIK, H., AND EWALD, H., 1965.

Nuclear Instrum., and Methods, 36, 93.

WOLLNIK H., 1967.

'Focusing of Charged Particles': Ed. A. Septier: Academic Press, N.Y.

WOOD, B.J., 1971.

J. Chem. Phys., 75, 2186.

YELLIN, E., YIN, L.I., AND ADLER, I., 1970.

Rev. Sci. Instrum., 41, 18.

YONEZAWA, T., 1966.

Space Sci. Rev., 5, 3.

YOUNG, J.M., WELLER, C.S., JOHNSON, C.Y., AND HOLMES, J.C., 1971.

J. Geophys. Res., 76, 3710.

ZALPURI, K.S., AND SOMAYAJULU, Y.V., 1974.

J. Atmos. Terr. Phys., 36, 1789.

ZASTAWNY, A., 1966.

J. Sci. Instrum., 43, 179.

ZBINDEN, P.A., HIDALGO, M.A., EBERHARDT, P., AND GEISS, J., 1975.

Planet. Space Sci., 23, 1621.

ZHLOOD'KO, A.D., AND KLYUEVA, N.M., 1970.

Space Res., 10, 746.

ZHLOOD'KO, A.D., 1971.

Space Res., 11, 1051.

ZIMMERMAN, S.P., AND MARCOS, F.A., 1967.

AFCRL-TR-67-0131, Environmental Research Paper, No 266.

ZIPF, E.C., 1970.

Bull. Am. Phys. Soc., 15, 418.